CENTRAL LIBRARY

SCHOLARLY ARTICLES

A CURRENT AWARENESS BULLETIN OF ARTICLES BY FACULTY, STUDENTS AND ALUMNI

~ *DECEMBER 2013* ~

DELHI TECHNOLOGICAL UNIVERSITY

(FORMERLY *DELHI COLLEGE OF ENGINEERING)*

GOVT. OF N.C.T. OF DELHI

SHAHBAD DAULATPUR, MAIN BAWANA ROAD

DELHI 110042

PREFACE

This is the Twelfth Issue of Current Awareness Bulletin for the year 2013, started by Delhi Technological University Library. The aim of the bulletin is to compile, preserve and disseminate information published by the Faculty, Students and Alumni for mutual benefits. The bulletin also aims to propagate the intellectual contribution of DTU as a whole to the academia. It contains information resources available in the internet in the form of articles, reports, presentation published in international journals, websites, etc. by the faculty and students of Delhi Technological University in the field of science and technology. The publication of Faculty and Students, which are not covered in this bulletin, may be because of the reason that the full text either was not accessible or could not be searched by the search engine used by the library for this purpose. To make the bulletin more comprehensive, the learned faculty and Students may provide their uncovered publication to the library either through email or in CD, etc.

This issue contains the information published during December 2013. The arrangement of the contents is alphabetical wise starting from A-Z. The Full text of the article, which is either subscribed by the University or available in the web, is provided in this Bulletin.

CONTENTS

11. Point Based Features for Contact-less Palm print Images ***Anil Singh Parihar***, Amoiy Kumar, ***Om Prakash Verma***, ***Ankita Gupta***, ***Prerana Mukherjee***, and ***Deepika Vatsa,*** Department of Information Technology

12. Pr3þ doped lead tungsten tellurite glasses for visible red lasers M. Venkateswarlu, M.V.V.K.S. Prasad, K.Swapna, Sk.Mahamuda, ***A. SrinivasaRao,*** Department of Applied Physics, A.MohanBabu and D.Haranathd

13. Prediction of Resonant Frequencies of Rectangular, Circular and Triangular Microstrip Antennas using a Generalized RBF Neural Model ***Taimoor Khan*** and ***Ashok De***, Electronic and Communication Engineering

14. Preparation and characterization of self-assembled layer by layer NiCo2O4-reduced graphene oxide nano composite with improved electro catalytic properties Manish Srivastava, Md. Elias Uddin, ***Jay Singh***, Department of Applied Chemistry, Nam Hoon Kim and Joong Hee Lee

15. Realization of CDTA Based Frequency Agile Filter ***Neeta Pandey, ***Rajeshwari Pandey***, Department of Electronics and Communication Engineering ***Richa Choudhary***, ***Aseem Sayal, *Manan Tripathi***, Department of Electrical Engineering

16. Retrieval of FAQs based on SMS-input through phonetic equivalence ***Akhil Lohchab, *Amanpreet Singh, *Ashish Mahajan*** and ***Ritu Agarwal***

17. Total Productive Maintenance Review: A Case Study in Automobile Manufacturing Industry Jagtar Singh, ***Vikas Rastogi,*** Department of Mechanical & Production Engineering and Richa Sharma

*** Faculty**
~ Ex Faculty
< Ex Research Scholar

Volume 3 (2013) 77-87 ISSN 2347 - 3258
International Journal of Advance Research and Innovation

A Delphi Study of the Vehicular Emissions Control Strategies for the Capital City Delhi

Amit Pal
Department of Mechanical Engineering, Delhi Technological University, Delhi, India

Article Info

Article history:
Received 1 November 2013
Received in revised form
20 November 2013
Accepted 30 November 2013
Available online 15 December 2013

Keywords
Emissions control
Traffic management
Delphi study

Abstract

In present work a Delphi study was commissioned to obtain the feedback and suggestions of the experts, having technical backgrounds, such as industrial, scientific, transport administration, engineering academics and engineering studies. The questionnaire was designed including a wide spectrum of different modes of transportation, beginning with bicycles and cycle rickshaws, encompassing all the prevalent modes of automobiles being used and including up to electric and solar powered vehicles. The collected data was analysed using the MATLAB software and the results have been used to estimate and then propose future emission modification factors. It is found that a large majority of experts were in favour of improving and subsidizing the public transportation system, enhancing the traffic management and accelerating the infra-structure projects. The preferences of the experts were given due consideration while proposing the future emission control strategies and making the estimates of the vehicle emissions in the next chapter.

1. Introduction

Today, the capital of India, Delhi is one of the most polluted cities in the world, which has been caused by phenomenal vehicular growth primarily during the past two-three decades. Incidentally, only a few decades earlier Delhi was acclaimed as one of the greenest capitals in the world. In order to restore the air quality and refurbish its image, a number of plans have been prepared and implemented in Delhi during the past few years. The related externalities like traffic congestion, quality of available fuel quality, extent of overloading or over speeding, and maintenance, have a definite impact on the environmental degradation. Although the statistical data for the vehicular pollution of Delhi is available, a comprehensive planning and optimization strategy to overcome the above problem is yet to be formulated. Controlling the vehicular emissions of a metro city public transportation system need an honest approach to incorporate the judgment, critical comments and suggestions by the people who use these systems and who also know the technical aspects of these systems. The Delphi methodology enables one to incorporate the opinions of a large number of experts/participants, about the present public transportation system and their preferences, without creating any conflict or wide disagreements.

Delphi is one of the most widely used techniques for creative exploration of ideas for the production of suitable information for the decision making or future planning applications. The Delphi study or technique was used to determine if there are emerging patterns or consensus on leadership practices and information technologies used in leading virtual teams. The purpose of the Delphi technique is to elicit information and judgments from participants to facilitate problem-solving, planning, and decision-making. Why Delphi was used in this study is explained in the chapter 3 on the selection of the research methodology.

2. The History of Delphi

The Delphi technique was developed during the 1950s by the workers at the RAND Corporation while operating on a U.S. Air Force sponsored project. The aim of the project was the application of expert opinion to the selection – from the point of view of a Soviet strategic planner – of an optimal U.S. industrial target system, with a corresponding

Corresponding Author,
E-mail address: amitpal@dce.ac.in

estimation of the number of atomic bombs required to reduce armaments output by a prescribed amount. More generally, the technique is seen as a procedure to ‘‘obtain the most reliable consensus of opinion of a group of experts by a series of intensive questionnaires interspersed with controlled opinion feedback’’ (Dalkey & Helmer, 1963). In particular, the structure of the technique is intended to allow access to the positive attributes of interacting groups (knowledge from a variety of sources, creative synthesis, etc.), while pre-empting their negative aspects (attributable to social, personal and political conflicts etc.), from a practical perspective, the method allows input from a larger number of participants that could feasibly be included in a group or committee meeting and from members who are geographically dispersed.

Delphi is not a procedure intended to challenge statistical or model-based procedures, against which human judgment is generally shown to be inferior. It is intended for use in judgment and forecasting situations in which pure model-based statistical methods are not practical or possible because of the lack of appropriate historical / economic / technical data, and thus where some form of human judgmental input is necessary (Wright et al., 1996). Such input needs to be used as efficiently as possible, and for this purpose the Delphi technique might serve a role.

Four key features may be regarded as necessary for defining a procedure as a ‘Delphi’. These are: Anonymity, Iteration, Controlled feedback, and Statistical aggregation of group response.

Anonymity is achieved through the use of questionnaires. By allowing the individual group members an opportunity to express their opinions and judgments privately, undue social pressures – as from dominant or dogmatic individuals or from a majority – should be avoided. Ideally, this should allow the individual group members to consider each idea on the basis of merit alone, rather than on the basis of potentially invalid criteria (such as the status of an idea’s proponent).

Furthermore, with the **iteration** of the questionnaire over a number of rounds, the individuals are given the opportunity to change their opinions and judgments without fear of losing face in the eyes of the others in the group.

Between questionnaire iterations, **controlled feedback** is provided, through which the group members are informed of the opinions of their anonymous colleagues. Often feedback is presented as a simple statistical summary of the group response, usually comprising a mean or median value, such as the average ‘group’ estimate of the date by when an event is forecast to occur.

Occasionally, additional information may also be provided, such as arguments from individuals whose judgments fall outside certain pre specified limits. In this manner, feedback comprises the opinions and judgments of all group members and not just the most vocal. At the end of the polling of participants (i.e., after several rounds of questionnaire iteration), the group judgment is taken as the **statistical average** (mean / median) of the panelists' estimates on the final round.

The above four characteristics are necessary defining attributes of a Delphi procedure, although there are numerous ways in which they may be applied. The first round of the classical Delphi procedure (Martino, 1983) is unstructured, allowing the individual experts relatively free scope to identify, and elaborate on, those issues they see as important. These individual factors are then consolidated into a single set by the monitor team, who produce a structured questionnaire from which the views, opinions and judgments of the Delphi panelists may be elicited in a quantitative manner on subsequent rounds.

After each of these rounds, responses are analyzed and statistically summarized (usually into medians plus upper and lower quartiles), which are then presented to the panelists for further consideration, if panelists' assessments fall outside the upper or lower quartiles, they may be asked to give reasons, why they believe their selections are correct against the majority opinion? This procedure continues until stability in panelists' responses is achieved. The forecast or assessment for each item in the questionnaire is typically represented by the median on the final round. An important point to note here is that variations from the above Delphi model do exist (Martino, 1983). Most commonly round one is structured in order to make the application of the procedure simpler for the monitor team and panelists; the number of rounds is variable, though seldom goes beyond one or two iterations (during which time most change in panelists' responses generally occurs).

Often, panelists may be asked for just a single statistic – such as the date by when an event has a 50% likelihood of occurring – rather than for multiple figures or dates representing degrees of confidence or likelihood (e.g., the 10% and 90% likelihood dates), or for written justifications of extreme opinions or judgments. These simplifications are particularly common in laboratory studies and have important consequences for the generalize ability of research endings.

One of the aims of using Delphi is to achieve greater consensus amongst panelists. Empirically, consensus has been determined by measuring the

variance in responses of Delphi panelists over rounds, with a reduction in variance being taken to indicate that greater consensus has been achieved. Results from empirical studies seem to suggest that variance reduction is typical, although claims tend to be simply reported unanalyzed (Dalkey & Helmer, 1963), rather than supported by analysis (Jolson & Rossow, 1971). Indeed, the trend of reduced variance is so typical that the phenomenon of increased 'consensus', per se, no longer appears to be an issue of experimental interest. Where some controversy does exist, however, it is in whether a reduction in variance over rounds reflects true consensus (reasoned acceptance of a position).

Delphi has, after all, been advocated as a method of reducing group pressures to conform (Martino, 1983) and both increased consensus and increased conformity will be evident as a convergence of panelist's estimates over rounds (i.e., these factors are confounded). It is seen in the literature that reduced variance has been interpreted according to the position on Delphi held by the particular author/s, with proponents of Delphi arguing that results demonstrate consensus, while critics have argued that the 'consensus' is often only 'apparent', and that the convergence of responses is mainly attributable to other social-psychological factors leading to conformity (Stewart, 1987).

Clearly, if panelists are being drawn towards a central value for reasons other than a genuine acceptance of the rationale behind that position, then inefficient process-loss factors are still present in the technique. Alternative measures of consensus have been taken, such as 'post-group consensus. This concerns the extent to which individuals – after the Delphi process has been completed – individually agree with the final group aggregate, their own final round estimates, or the estimates of other panelists.

Rohrbaugh (1979) compared individuals' post-group responses to their aggregate group responses, and seemed to show that reduction in 'disagreement' in Delphi groups was significantly less than the reduction achieved with an alternative technique (Social Judgment Analysis). Furthermore, he found that there was little increase in agreement in the Delphi groups. This latter finding seems to suggest that panelists were simply altering their estimates in order to conform to the group without actually changing their opinions (i.e., implying conformity rather than genuine consensus).

An alternative slant on this issue has been provided by Bardecki (1984), who reported – in a study not fully described – experts with more extreme views were more likely to drop out of a Delphi procedure than those with more moderate views (i.e., nearer to the group average). This suggests that consensus may be due – at least in part – to attrition. Further empirical work is needed to determine the extent to which the convergence of those who do not (or cannot) drop out of a Delphi procedure are due to either true consensus or to conformity pressures.

3. The Delphi versus other Statistical Procedures

The average estimate of Delphi panelists on the first round – prior to iteration or feedback – is equivalent to that from a statistical sized group. Comparing a final round Delphi aggregate to that of the first round is thus, effectively, a within-subjects comparison of techniques (Delphi versus statistical sized group). Although the comparison of round averages should be possible in every study considering Delphi accuracy/quality, a number of evaluative studies have omitted to report round differences [Fischer (1981) and Riggs (1983)]. Many studies have reported significant increase in accuracy over Delphi rounds [Erffmeyer et al. (1986), and Rowe & Wright (1996)]. Some other studies have reported Delphi to be better than statistical or first round aggregates more often than not, or to a degree that does not reach.

4. Application of Delphi to the Public Transportation System of Delhi

Although evidence suggests that Delphi does generally lead to improved judgments over statistical sized groups and unstructured interacting groups, it is clearly of interest to see how Delphi performs in comparison to groups using other structured procedures. The Delphi survey conducted in this research work included the people chosen mainly from technical background such as:

Transportation Planning related Departments like Delhi Transport Corporation (DTC), Department of Science and Technology (DST), Defense Research and Development Organization (DRDO), State Transport Authority (STA), Central Road Research Institute (CRRI), Delhi Metro Rail Corporation (DMRC) etc.

Automobile manufacturers like Maruti Udyoog Limited, Hyundai Motors, Ashok Leyland, Honda and their vendors.

Indian fuel refinery personals from Indian Oil Corporation (IOCL), Bharat Petroleum Corporation Limited (BPCL), Hindustan Petroleum Corporation Limited (HPCL), Indraprastha Gas India Limited (IGIL)

Engineering academicians from Delhi College of Engineering (DCE), Indian Institute of Technology Delhi (IITD), Maharaja Agrasen Institute of Technology (MAIT), Delhi, Directorate of Training and Technical education (DTTE) Delhi and Engineering students from DCE, NSIT, MAIT etc.

The Delphi questionnaire was designed using guidelines of Sharma (2000) and Pal (2004), included a wide spectrum of different modes of transportation, beginning with bicycles and cycle rickshaws, encompassing all the prevalent modes being used of automobiles, and extending up to electric and solar powered vehicles, including advanced forms of fuel cells, hybrid vehicles etc. for planning an appropriate strategy to optimize the vehicular emissions of the capital city of Delhi. The experts have been asked to rate the suggested strategies for the reduction of the vehicular emissions from the transport system of the city of Delhi on a scale of 10 and they were also been asked to give their narrative suggestion and remarks to control the vehicular emissions.

In the first round of Delphi, about 300 participants were approached, roughly fifty plus from each category i.e. Automobile industry, Petroleum oil industry, Transport Department, Engineering Academia's and Engineering Students, out of which 138 responded, spending on an average of 30 to 45 minutes of their precious and rationed time.

5. Investigations of the Delphi Study

Various methods were used to contact the experts for the survey, maximum experts were contacted personally. A sizable number of experts were contacted through various other means of communications such as internet, post/courier, phone calls etc. The respondent's work experience average is more than 8 years which is reasonably good (Assigning the experience of one year to all the students as most of them were already graduate i.e. Post Graduate students), whereas the group's average for experts stay in Delhi is about 10 years. The group's average annual income is more than rupees two lakh, here for students their family income is considered and only final year engineering students (both full time and part time) are approached for the study. The survey experts stay duration in Delhi is also considered and ensured that the experts have reasonable stay duration in Delhi, so as to ensure that they are fully aware of the transportation problem of Delhi. The groups average stay duration in Delhi is more than 8 years.

The responses of above questionnaire were analyzed using statistical tools and processed with MATLAB program me. The STATISTICALLY ACCEPTABLE RANGE followed here to ascertain the agreement of majority of the group, for Delphi first and second round are as following:

RANGE (Higher /Lower) = AVERAGE ± 1.5 STDV, IF STDV d<2.0,

RANGE (Higher /Lower) = AVERAGE ± 2.0 STDV, IF STDV >2.0

The responses of 36 experts were found to be out of acceptable range; they were again contacted and requested to participate in the second round, with a view to arrive at a consensus worthy of framing a feasible solution/policy framework. All the responses of second round were within statistical limits. Further their replies to some specific questions on how to control the vehicular emissions, suitability of the alternative fuels, how to improve the Public Transportation System, steps to control the number of vehicles and their awareness level on alternative propulsion systems are presented in the form of bar chart in Figure 1 to 5.

It is worth to mention that all the experts have rated our suggested measures more than 6. The opinion of the participants is given due consideration in proposing the future emission control strategies. It is observed that they have given a very high rating (i.e. about 8-10) to the practically feasible options like improvement in fuel quality, augmentation of Delhi metro, promoting CNG as fuel, augmentation of PTS, enforcement of strict emission norms etc., while control actions such as removing the encroachment from roads, improving the infrastructure, adding the hydrogen in CNG fuel, strengthening the ring rail, restructuring the tax on vehicles taxes, among others were rated low because their implementation is not practically easy.

Experts reply were also analyzed with MATLAB software, various statistical parameters like average, coefficient of variance, standard deviation etc were determined and they are represented in graphical images in Figure 6 to 8. Different colored lines are used for different experts groups (such as Engg. Acamadiations-ACAD-dark blue. Engg. Students-STUD-blue, Automobile engineers-AIE-green, Transport officials- TRPS-orange, Oil industry personals-OIE-red, group averages are also shown in different column heights. These graphs show the various statistical parameters for the survey data such as standard deviation (SD), mean, coefficient of variance (CV), inter quartile range (IQR) etc. with different types and colored lines with the reply of the different expert groups for various questionnaire entries.

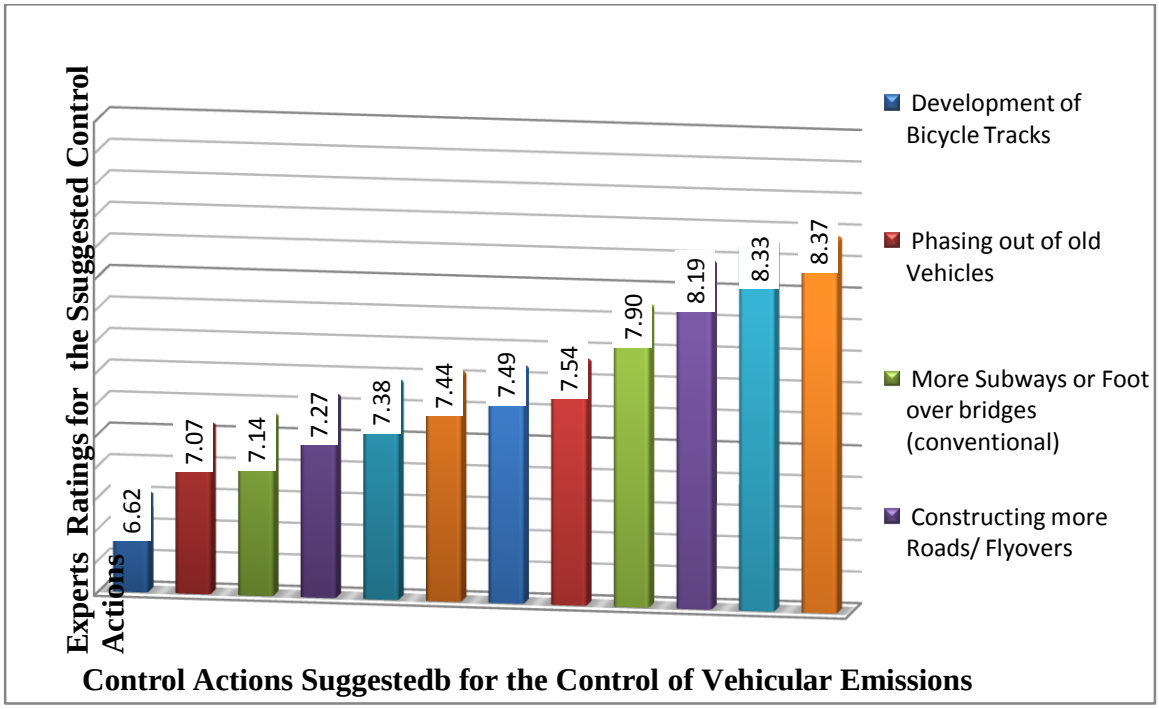

Fig: 1. Experts Preferences to Control Vehicle Emissions

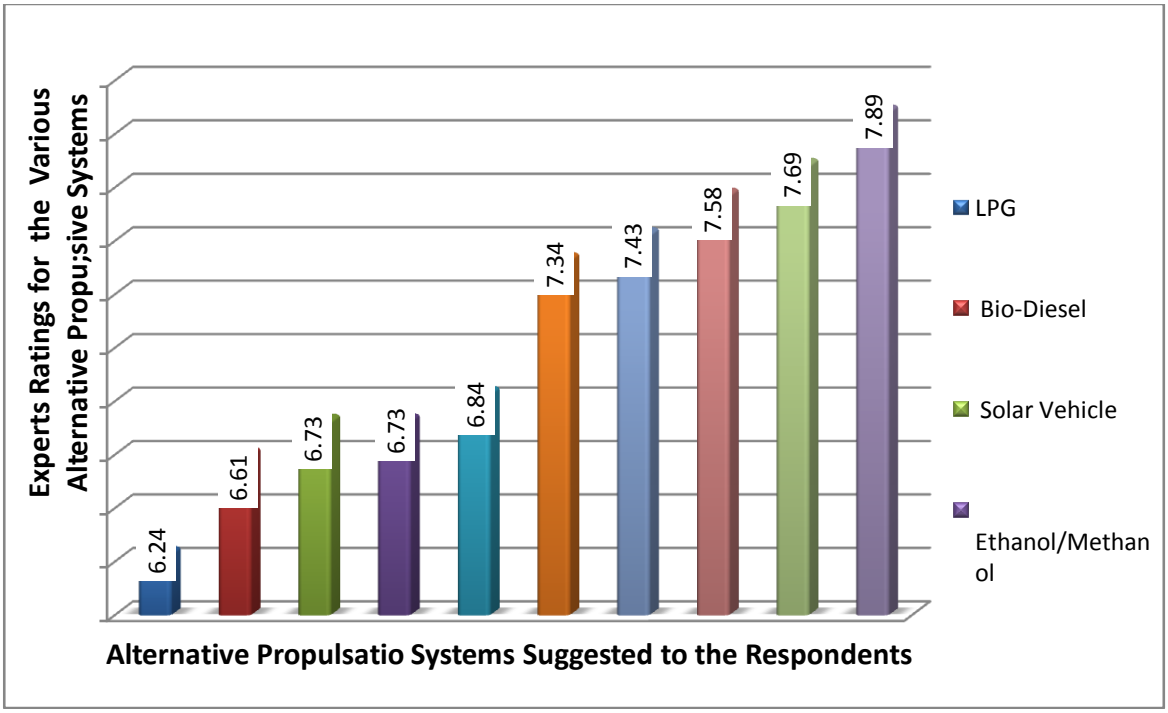

Fig: 2. Experts preferences for the Alternative Fuels

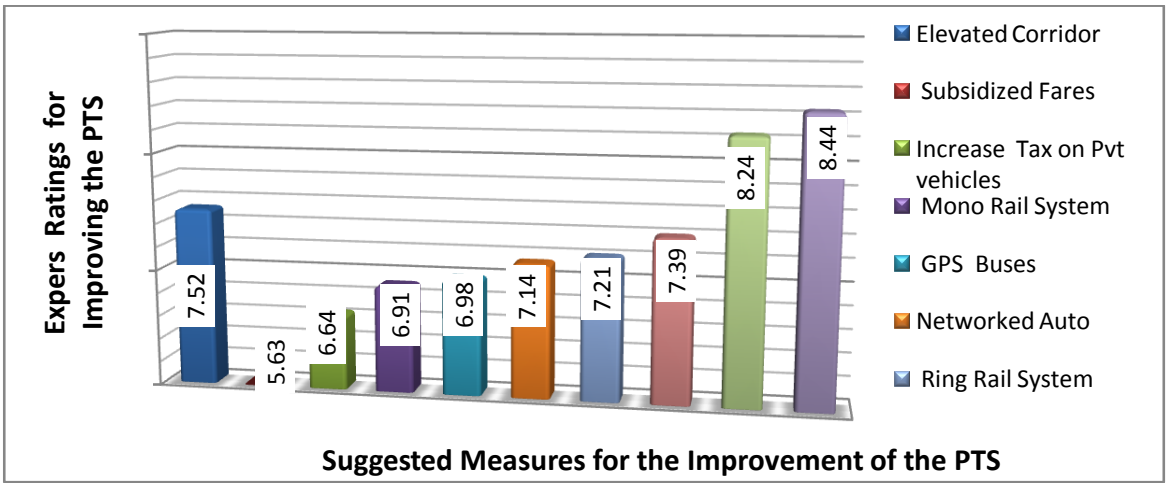

Fig: 3. Experts Suggestions to Improve Public Transport

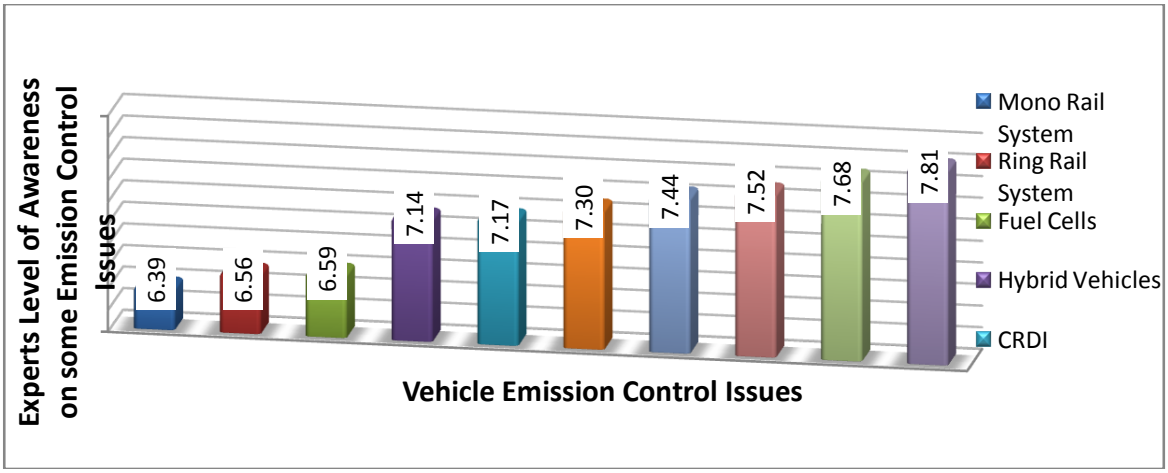

Fig: 4. Experts' Level of Awareness about Alternative Propulsion Systems

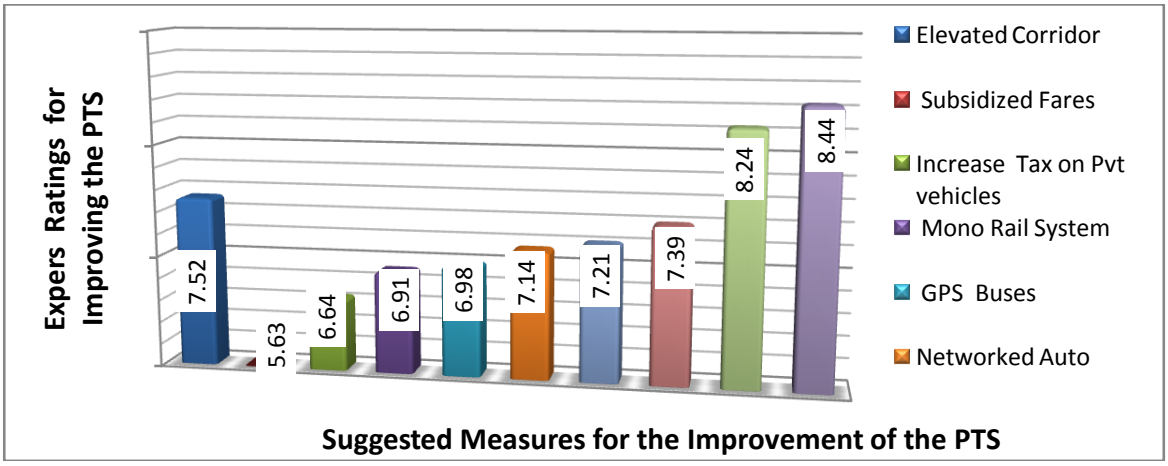

Fig: 5. Experts' Suggestions to Control the Number of Vehicles

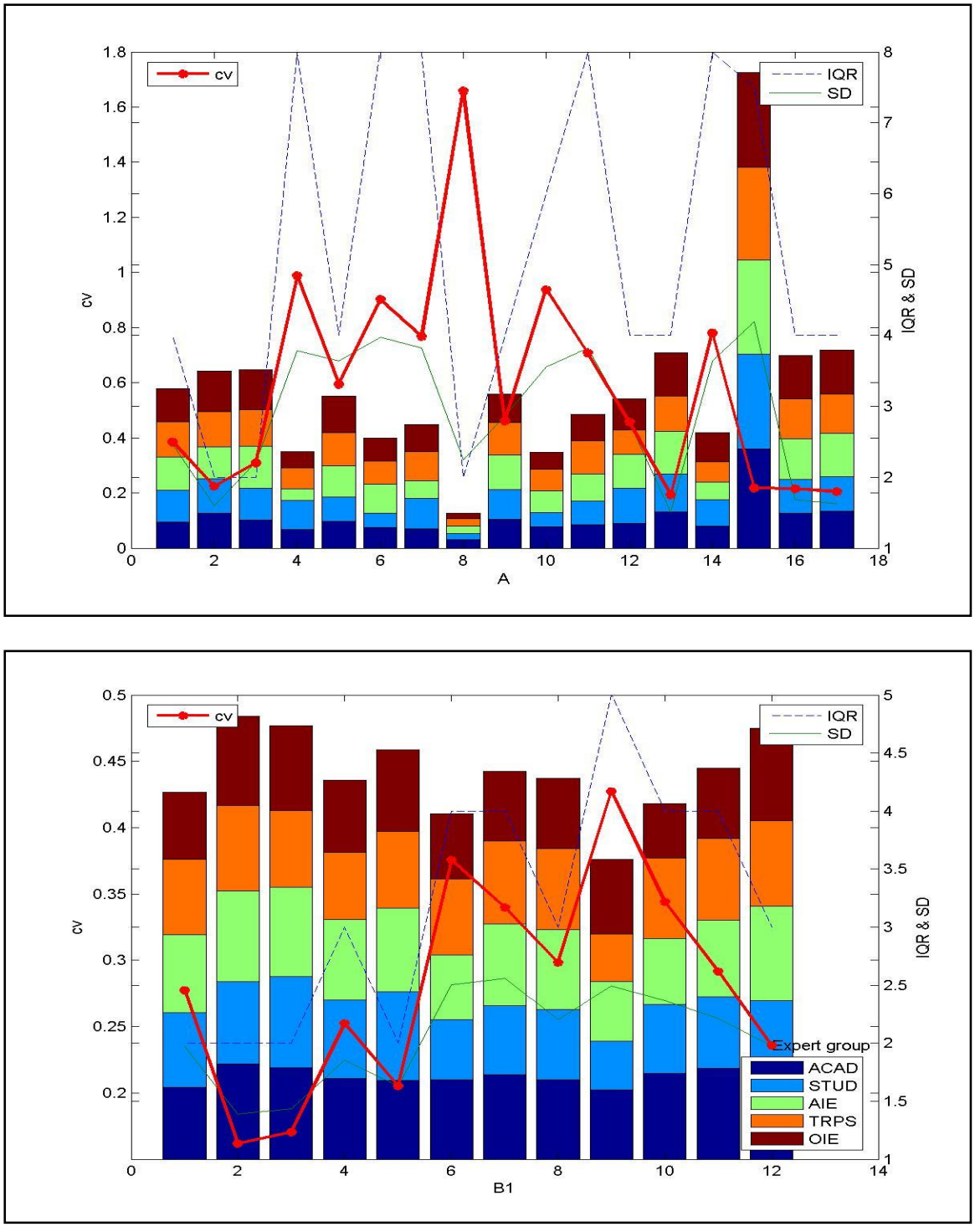

Fig: 6. MATLAB Statistical Results for the Survey Section A & B1

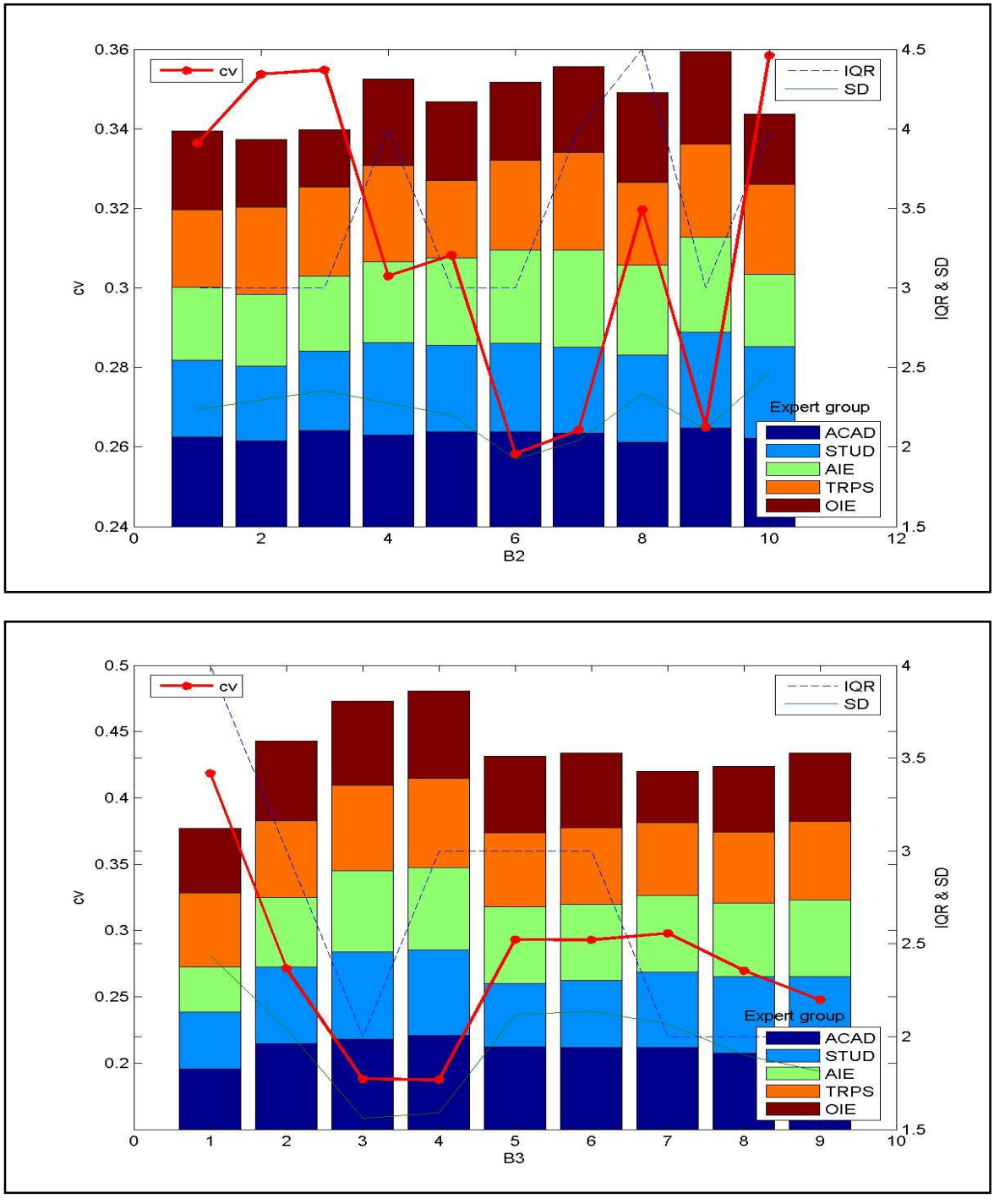

Fig: 7. MATLAB Statistical Results for the Survey Section B2 (Experts' Level of Awareness on Related Topics) and B3 (Experts' Preferences to Control the Growth of Private Vehicles)

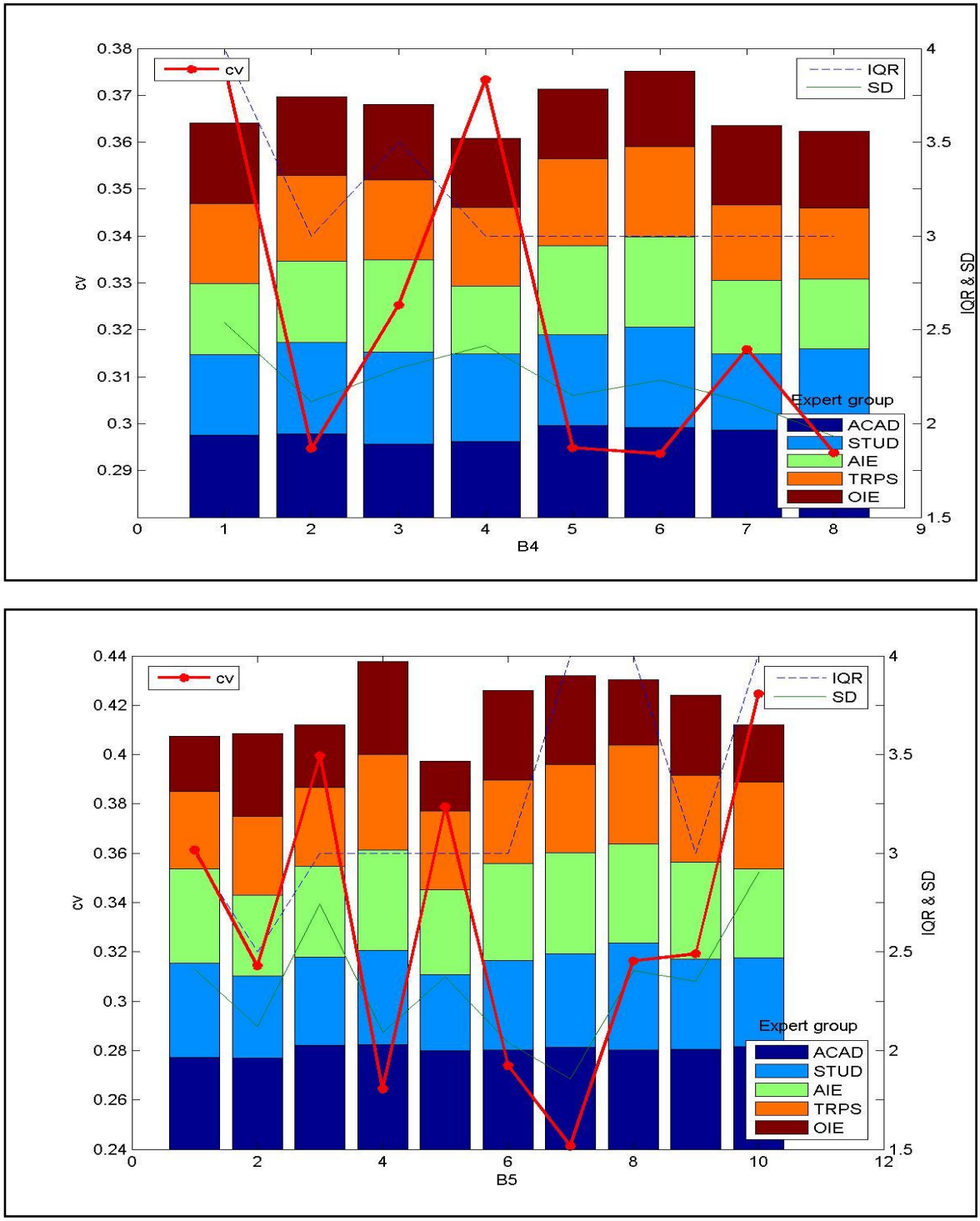

Fig: 8. MATLAB Statistical Results for the Survey Section B4 (Experts' Opinion on Vehicle Taxation) and B5 (Experts' Opinion on Various Alternative Fuels/Technology)

6. Conclusions

The survey results shown above are an indication that though people are well aware about the advanced alternatives like Hydrogen, Hybrid, Solar and Fuel Cell etc. but as their success history is not proven thus they are ranked, marginally lower than that of well established and familiar alternative fuels like CNG/LPG/Ethanol and Bio-diesel etc. We noticed some very much important and interesting suggestion from the experts. Some of them valuable to be referred are:

- There should be a system in which or a method has to be developed so that only a particular lot of vehicle (like odd or even numbered) can operate on some decided day of work.
- Strict rule for no use of private vehicles, for at least one day /week
- Advanced and classified PTS for different section of people
- Campaign on public awareness for lane driving to avoid traffic jams
- Endorse employee car pool as a part of corporate social responsibility
- To control higher fuel consumption and aldehyde emission
- Hydrogen technology is in nascent stage.
- For CNG safety aspects need to be taken care of.
- Motor vehicle licensing system should be strict and linked to awareness for emission control and driving training, and advance driver licensing system like graduated licensing system must be promoted.
- Create a phool (ideates) lane for fast movers, let live others.
- Reliable integration of different modes of public transport.
- Tax Free, State owned buses, to subsidize public transport.
- Making turbocharger mandatory in standard design in diesel engine.
- Delhi metro should be linked possibly by small PTS vehicle under one ticket scheme.
- Amendment should be made in Central Motor Vehicle Rule (CMVR) to restrict entry of other state private vehicle in Delhi. Otherwise due to heavy tax in Delhi people are lured top get their vehicles registered outside Delhi and use in Delhi.
- Substantially subsidized fare passes of PTS for the School/College/Office goers.
- Incentive for accident /challenge free vehicle
- Public walk way (footpath to be made encroachment free) elevated, made to cater up to 1km walk
- Limiting the number of vehicle per family, and enforcing higher tax for the subsequent vehicles.
- Tax to the number of vehicle per floor of a house.
- Heavy duty vehicle should not be allowed from 6AM to 11PM.
- Public Transport Systems routes should be increased connecting residential and industrial area.
- High penalty for environment enemy vehicle.

References

[1] M. J. Bardecki, “Participants’ Response to the Delphi Method: An Attitudinal Perspective”, Journal of Technological Forecasting and Social Change; 25 pp281–292, 1984.

[2] K. Brockhoff, H A. Linstone, M. Turoff, “The Performance of Forecasting Groups in Computer Dialogue and Face-to-Face Discussion", The Delphi Method, Addison-Wesley, Reading, MA, pp291-322, 1975

[3] N. C. Dalkey and O. Helmer, “An Experimental Application of the Delphi Method to the Use of Experts”, Management Science; 9 pp 458–467, 1963

[4] R. C. Erffmeyer, E. S. Erffmeyer and I. M. Lane, “The Delphi Technique: An Empirical Evaluation of The Optimal Number of Rounds”, Group and Organization Studies 11(1): 120–128, 1986

[5] G. W. Fischer, “When oracles fail – a comparison of four procedures for aggregating subjective probability forecasts”, Organizational Behavior and Human Performance, 28: 96–110, 1981

[6] M. A. Jolson & G. Rossow “The Delphi Process in Organization Marketing Decision Making”, Journal of Marketing Research, 8: pp 443–448, 1971

[7] J. Martino, “Technological Forecasting for Decision Making”, 2nd ed., American Elsevier, New York, 1983

[8] W. E. Riggs, “The Delphi Method: An Experimental Evaluation”, Technological

Forecasting and Social Change, 23: pp 89–94, 1983

[9] J. Rohrbaugh, "Improving the Quality of Group Judgment Social Judgment Analysis and the Delphi Technique", Organizational Behavior and Human Performance, 24: pp 73–92, 1979

[10] G. Rowe, and G. Wright, "The Delphi Technique as a Forecasting Tool: Issues and Analysis", International Journal of Forecasting, 15, pp 353 –375, 1983

[11] T. R. Stewart, "The Delphi Technique and Judgmental Forecasting", Climatic Change 11: pp 97–113, 1987

[12] G. Wright, M. J. Lawrence and F. Collopy, "The Role and Validity of Judgment in Forecasting", International Journal of Forecasting, 12: pp 1–8, 1996.

International Journal of Current Engineering and Technology
ISSN 2277 - 4106

Available at http://inpressco.com/category/ijcet

Research Article

An Experimental Investigation of Jatropha Biodiesel Blends in a Multi Cylinder CI Engine: Performance and Emissions Study

Amit Pal[Á*]

[Á]Department of Mechanical Engineering, Delhi Technological University, Formerly Delhi College of Engineering, Delhi-110042, India

Accepted 05 November 2013, Available online 01 December 2013, **Vol.3, No.5 (December 2013)**

Abstract

There is tremendous increase in transportation activities in recent times. Petroleum fuels are the key energy source in India and preferred as automotive fuel. Their use has been increasing continuously from 3.5 MMT (Million Metric Tons) in the year 1950-51 to 84.3 MMT in 1997-98 and about 113 MMT in 2001 and it were about 148 MMT in 2011-12. Petroleum based fuels are obtained from limited reserves which are highly intense in certain regions of the world. Therefore, those countries that do not have these resources and facing a foreign exchange crisis are looking for alternative fuels, which can be produced from materials available inside the country. Biodiesel is considered as clean fuel since it has almost no sulphur, no aromatics and has about 10 % built in oxygen, which helps it to burn fully. In present paper the engine performance and exhaust emissions of jatropha oil biodiesel blends, were investigated on a 39 kW multi cylinder engine, in B10 to B30 percent blends and compared with the petroleum diesel fuel. The experimental results show that the engine power and torque of the mixture of oil–diesel fuel are close to the values obtained from diesel fuel and the amounts of smoke, CO and HC exhaust emissions are lower than those of diesel fuel, except slight increase of NOx emissions at higher loads.

Keywords*: Diesel Engine, Performance testing, Emissions, Smoke, jatropha, biodiesel*

1. Introduction

The world is presently facing the twin problems of fossil fuel depletion and severe environmental degradation. Haphazard extraction and lavish consumption of fossil fuels resulted in reduction of underground carbon resources. The search for alternative fuels, which promise a melodious correlation with sustainable development, energy preservation, efficiency and environmental protection, has become highly prominent in the present context. In the last decade, several researchers have been examined that vegetable oils may be proved as one such alternative fuel and their potential. Vegetable oils are renewable and eco-friendly to the environment, and they are free of sulphur content in them. This makes vegetable fuel studies become current issue among the various popular investigations. Bio-diesel have many advantages over petroleum diesel fuel; produce less smoke and particulates, have high cetane number, produce lower carbon monoxide and hydrocarbon emissions, renewable, biodegradable and non-toxic. In India, with abundance of forest resources, there are a number of other non-edible tree borne oilseeds with an estimated annual production of more than 20 million tones, which have large potential for making biodiesel to supplement other conventional sources. Biodiesel is considered as clean fuel since it has almost no sulphur, no aromatics and has about 10 % built in oxygen, which helps it to burn fully. Hebbal et al. (2006) have presented the investigation on deccan hemp, a non-edible vegetable oil in a diesel engine for its suitability as an alternate fuel.

Agarwal and Agarwal (2007) conducted experiments using various blends of Jatropha oil with mineral diesel to study the effect of reduced blend viscosity on emissions and performance of diesel engine. The acquired data were analyzed for various parameters such as thermal efficiency, brake specific fuel consumption (BSFC), smoke opacity, CO_2, CO and HC emissions. While operating the engine on Jatropha oil (preheated and blends), performance and emission parameters were found to be very close to mineral diesel for lower blend concentrations. Purushothaman and Nagarajan (2009) presented work on the performance, emission and combustion characteristics of a single cylinder, constant speed, direct injection diesel engine using orange oil as an alternate fuel and the results are compared with the standard diesel fuel operation. Results indicated that the brake thermal efficiency was higher compared to diesel throughout the load spectra. Carbon monoxide (CO) and hydrocarbon (HC) emissions were lower and oxides of nitrogen (NOx) were higher compared to diesel operation. Labeckas and Slavinskas (2006) reported the comparative bench testing results of a four stroke Diesel engine when operating on neat rapeseed oil methyl ester and it's 5 %,

*Corresponding author: **Amit Pal**

10 %, 20 % and 35 % blends with Diesel fuel. The brake specific fuel consumption at maximum torque and rated power found to be higher for rapseed oil by 18.7 % and 23.2 % relative to Diesel fuel. The maximum brake thermal efficiency is higher for rapseed oil at higher load. The maximum NOx emissions increase proportionally with the mass percent of oxygen in the bio-fuel and engine speed. The carbon monoxide emissions and visible smoke emerging from the biodiesel over all load and speed ranges are lower by up to 51.6 % and 13.5 % to 60.3 %, respectively. The carbon dioxide (CO_2) is slightly higher in case of biodiesel. The emissions of unburned hydrocarbons for all bio-fuels are reported low.

In the study of Altuna et al. (2008) a blend of 50 % sesame oil and 50 % diesel fuel was used as an alternative fuel in a direct injection diesel engine. The experimental results show that the engine power and torque of the mixture of sesame oil–diesel fuel are close to the values obtained from diesel fuel and the amounts of exhaust emissions are lower than those of diesel fuel. Suresh kumar et al. (2008) presented the results of performance and emission analyses of an unmodified diesel engine fuelled with Pongamia Pinnata Methyl Ester (PPME) and its blends with diesel. Engine tests were conducted to get the comparative measures of brake specific fuel consumption (BSFC), brake specific energy consumption (BSEC) and emissions such as CO, CO_2, HC and NOx to evaluate the behaviour of PPME and diesel in varying proportions. BSFC and BSEC for all the fuel blends and diesel tested decrease with increase in load. This is due to higher percentage increase in brake power with load as compared to increase in the fuel Consumption. For the blends B20 and B40, the BSFC is lower than and equal to that of diesel respectively and the BSEC is less than that of diesel at all loads. This could be due to the presence of dissolved oxygen in the PPME that enables complete combustion; engine emits more CO for diesel as compared to PPME blends under all loading conditions. The CO_2 emission increased with increase in load for all blends. The lower percentage of PPME blends emits less amount of CO_2 in comparison with diesel. Blends B40 and B60 emit very low emissions. This is due to the fact that biodiesel in general is a low carbon fuel and has a lower elemental carbon to hydrogen ratio than diesel fuel. HC emission decreases with increase in load for diesel and it is almost nil for all PPME blends except for B20 where some traces are seen at no load and full load. The NOx emission for all the fuels tested followed an increasing trend with respect to load. The reason could be the higher average gas temperature, residence time at higher load conditions.

In an experiment on a kirloskar single cylinder diesel engine with 10-20 % palm oil bio-diesel, Naveen and Dhuwe (2004) reported significant reduction in smoke level. Lapuerta et al. (2007) analyzed diesel engine emissions when using biodiesel fuels as opposed to conventional diesel fuels. The engine emissions from biodiesel and diesel fuels are compared, paying special attention to the most concerning emissions, nitric oxides and particulate matter. Some of the important outcomes are: at part load operation, no differences in power output, since an increase in fuel consumption in the case of biodiesel would compensate its reduced heating value. There is slight increase of NO_X with biodiesel because of more oxygen content of biodiesel and at higher temperature it leads to increase NO_x. There is a sharp reduction in particulate emissions with biodiesel as compared to diesel fuel. CO is usually found to significantly decrease with biodiesel. A more complete combustion caused by the increased oxygen content in the flame coming from the biodiesel molecules has been pointed out as the main reason.

Some researchers worked to find the effect of viscosity on emissions and performance of diesel engine Agarwal et al. (2001), Gangwar et al. (2008) and Choudhary et al. (2008). Emission parameters such as smoke NOx and CO_2 were found to have increased with increasing proportion of Jatropha oil in the blends compared to diesel. They found Jatropha oil to be a promising alternative fuel for compression ignition engines. Thermal efficiency was lower for unheated Jatropha oil compared to heated Jatropha oil and diesel. CO_2, CO, HC, and smoke opacity were slightly higher for neat Jatropha oil compared to that of diesel, but it were significantly less with Jatropha and other specie's bio-diesel. These emissions were found to be close to diesel for preheated Jatropha oil.

2. Experimental setup for performance testing

The setup consists of four cylinders, four stroke, Tata Indica diesel engine connected to eddy current type dynamometer for loading. The engine test setup specifications are given in Table 1, actual test setup is shown in Figure 1. The setup enables study of engine performance for various parameters such as torque, brake power, specific fuel consumption, brake thermal efficiency, opacity and p-θ diagram. The main aim of this experiment is to investigate the suitability and effect on performance of blending of biodiesel with gasoline diesel fuel.

Preparation of biodiesel blends

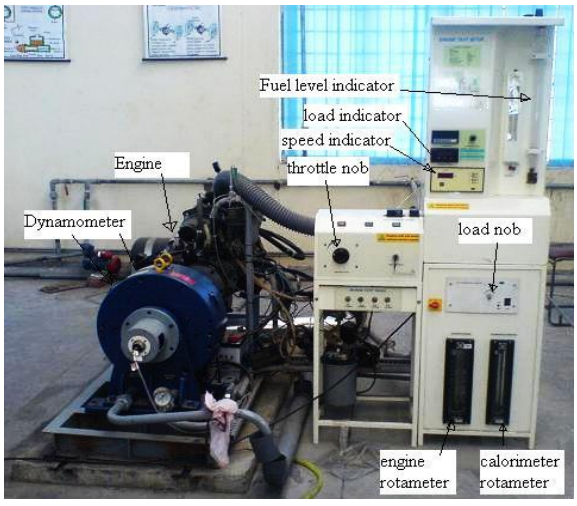

Figure 1: Actual Experimental setup.

Calorific value of petroleum diesel = 42000 kJ/kg.
Calorific value of biodiesel = 37000 kJ/kg.
Density of petroleum diesel = 800 kg/m^3.
Density of biodiesel = 891 kg/m^3.

Table 1: Specifications of the engine test setup

S.No.	Component	Specifications
1	Engine	Tata Indica, 4 Cylinder, 4 Stroke, water cooled, Power 39kW at 5000 rpm, Torque 85 NM at 2500 rpm, stroke 79.5mm, bore 75mm, 1405 cc, CR22
2	Dynamometer	eddy current, water cooled
3	Temperature	Input RTD PT100,Range 0–100 ^{0}C,
	transmitter	Output 20 mA and , Input Thermocouple, Range 0–1200 ^{0}C,
4	Piezo sensor	Range 5000 PSI,
5	Air box	M S fabricated with orifice meter and manometer
6	Load indicator	Digital, Range 0-50 Kg, Supply 230VAC
7	Engine	Input Piezo sensor,crank angle sensor, Input Piezo sensor, Communication RS 232, Crank angle sensor, No. No. of channel 2,
	indicator	
8	Software	Enginesoft
9	Temperature	Type RTD, PT100 and
	sensor	Thermocouple Type K
10	Fuel flow	DP transmitter, Range 0-500 mm
	transmitter	
11	Air flow	Pressure transmitter,
	transmitter	Range (-) 250 mm WC
12	Load sensor	Load cell, type strain gauge,
		Range 0-50 Kg

Table 2: Description of different blends of biodiesel

Blend	Amount of Diesel (ml)	Amount of Bio diesel (ml)	Calorific value of blend (kj/kg)	Resultant Density (kg/m^3)
Diesel	2000	0	42000	800
B-10	1800	200	41500	809
B-20	1600	400	41000	818
B-30	1400	600	40500	827

On this engine experiments are performed with different blends of biodiesel (pure diesel, B-10, B-20, and B-30). Jatropha biodiesel were prepared in our IC Engines laboratory. These blends are prepared in quantity of 2 liter each by mixing required quantity of biodiesel in petroleum diesel. There description of biodiesel blends is shown in Table 2.

3. Result and discussions on performance testing

Variation of Torque v/s Engine Speed

Figure 2 shows the variation of torque with speed for pure diesel and biodiesel blends of jatropha biodiesel. Variation of torque for different blends and pure diesel at a particular engine speed is within a very narrow range. In case of both biodiesel blends and pure diesel, initially the torque rises sharply with increase in engine speed up to 2500 rpm. Between speed 2500 to 4000 rpm the variation or torque with speed remain almost constant. Further increase in speed causes decrease in torque. The pattern is almost same for all blends. At initial speed biodiesel have more torque especially jatropha biodiesel has more torque. Almost similar pattern has obtained for all percentage of blends.

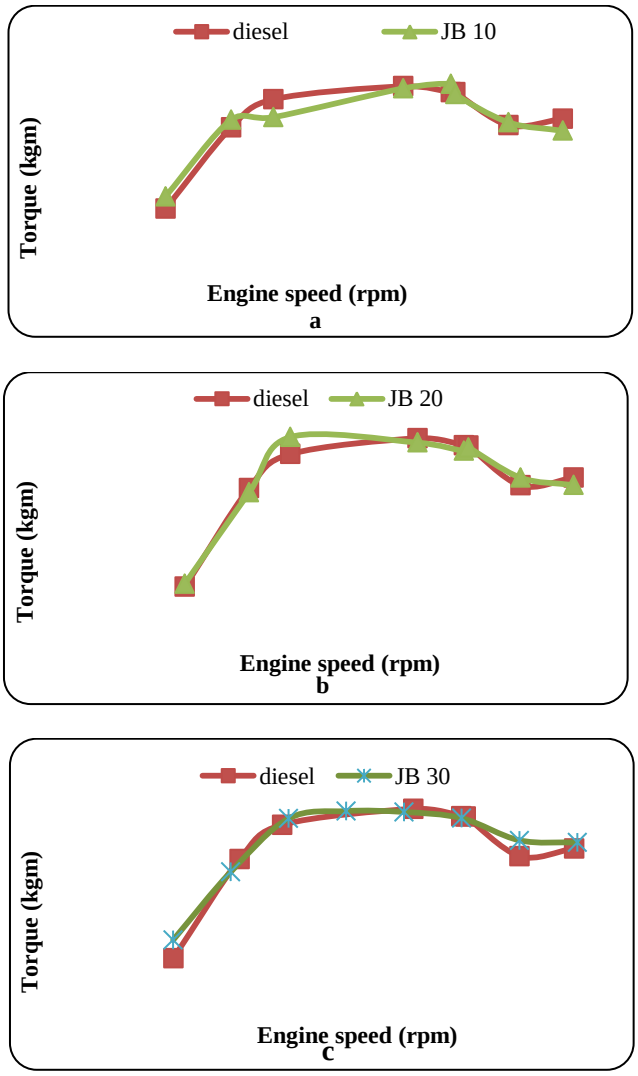

Figure 2: Comparison of Torque v/s Speed for different biodiesel blends of Jatropha oil

Variation of Brake Power v/s Speed

The variation of brake power vs. speed for both blends in comparison to pure diesel is shown in Figure 3. The Brake Power increases proportionally to engine speed in the range of 2000 to 4000 rpm. In this speed range variation of brake power is between 6-32 kW. For more than 4000 rpm there is fluctuating variation in brake power among the biodiesel blends. The variation of brake power is almost negligible for all types of blends and pure diesel for upto 4000 engine rpm. Between 4000 to 5000 rpm biodiesel

blends are having slightly higher brake power as compared to pure diesel. At initial speed break power obtained is more in case of biodiesel. Except initial speed thumba biodiesel has more power compare to jatropha biodiesel.

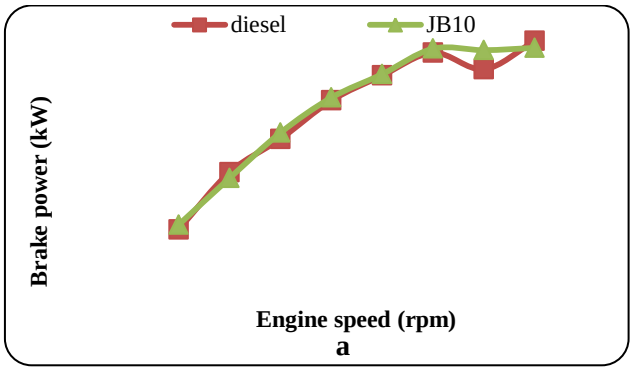

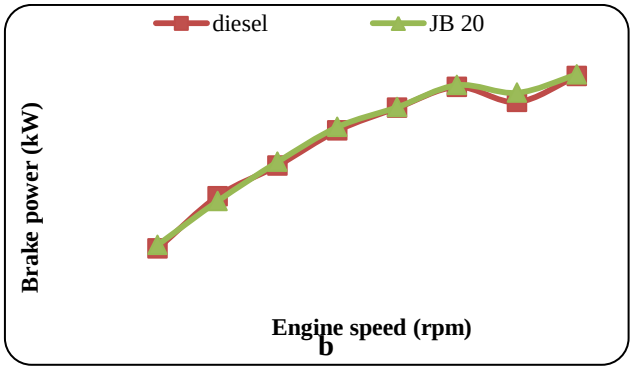

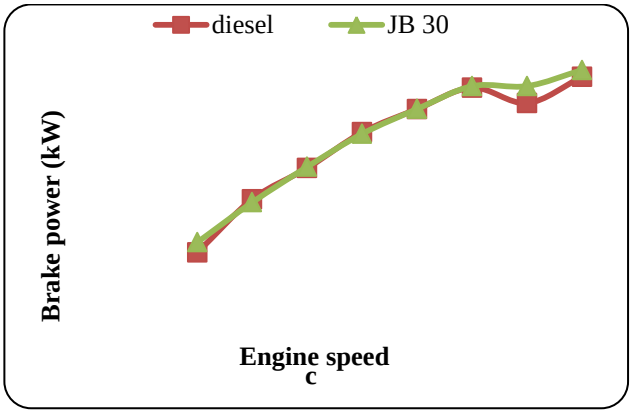

Figure 3: Comparison of Brake Power v/s Speed for different biodiesel blends of Jatropha oil

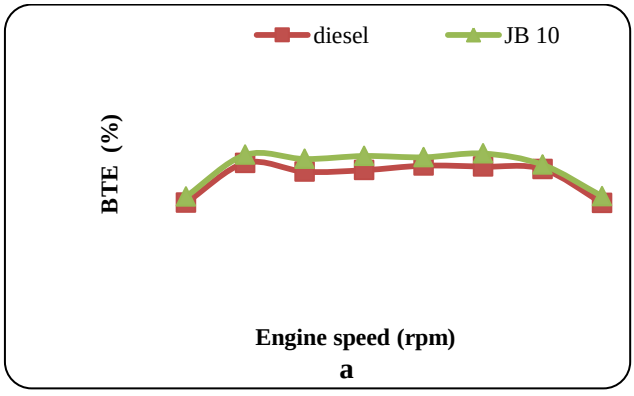

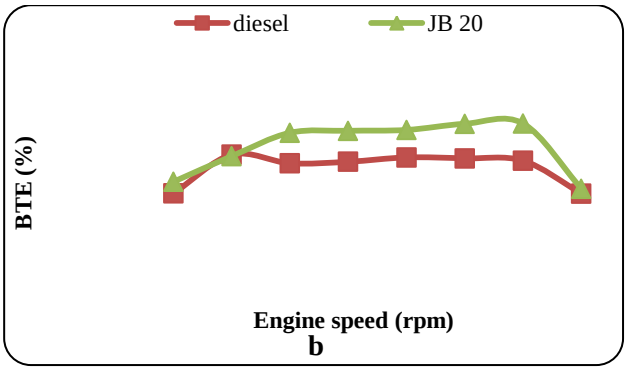

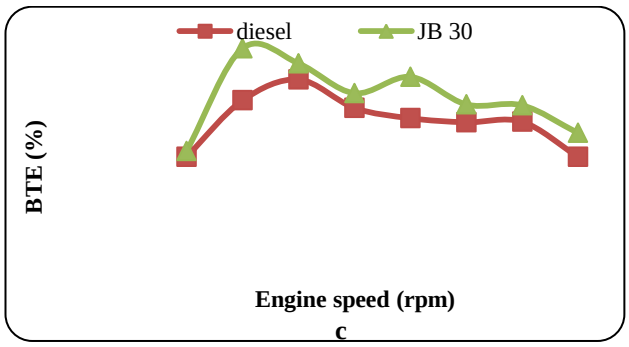

Figure 4: Brake Thermal Efficiency v/s Speed for different biodiesel blends of Jatropha oil

Brake Thermal Efficiency v/s Speed

Figure 4 shows comparison of Brake thermal efficiency vs. speed for different biodiesel blends of jatropha oil in comparison to diesel respectively. The maximum value of brake thermal efficiency for all blends & pure diesel is at 2000 rpm. For all blends of both oils variation of brake thermal efficiency is higher as compared to pure diesel for wide range of engine speed. The maximum thermal efficiency is achieved by using JB-30 blend is around 26.9 % at 2000 rpm which is 5 % higher as compared to pure diesel. The brake thermal efficiency is almost constant between rpm range of 2000 to 4000, and it decreases sharply with further increase in rpm and with increase in percentage of biodiesel blending the brake thermal efficiency increase for wide range of engine rpm. Jatropha oil exhibits comparatively higher efficiency for all speed range than pure diesel with all blends. Biodiesel blend of 30% shows much higher efficiency than diesel fuel.

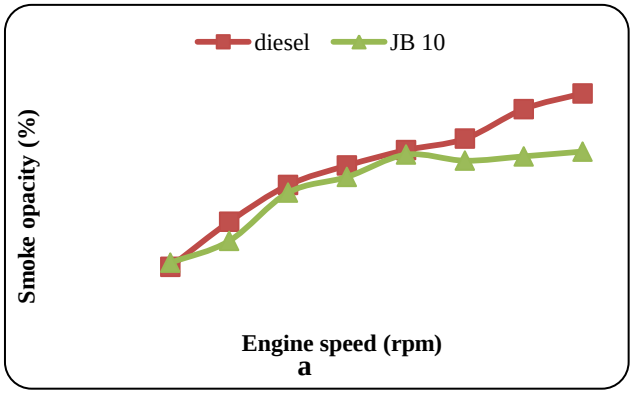

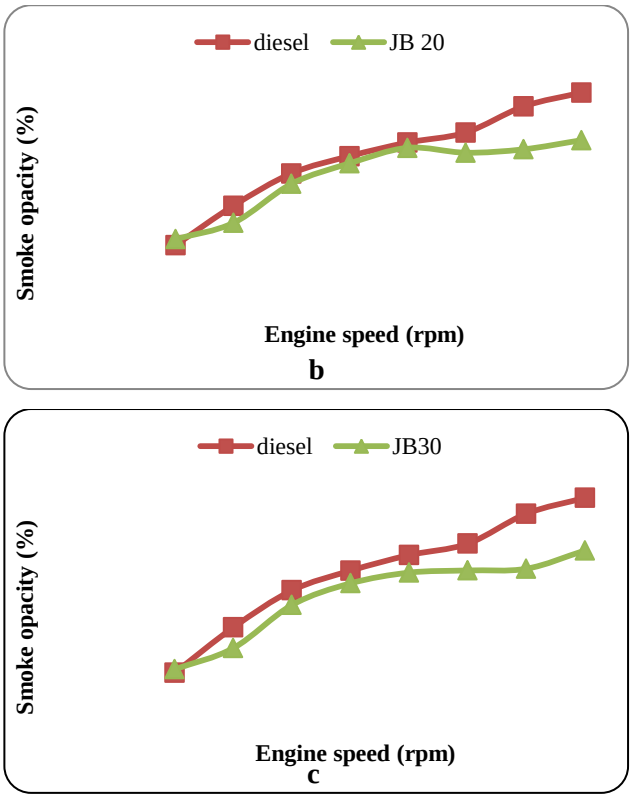

Figure 5: Comparison of Opacity v/s Speed for different biodiesel blends of Jatropha oil

Smoke Opacity v/s. Speed

To understand the pollution aspect of biodiesel the variation of opacity vs. speed are shown in Figure 5. The smoke opacity value for pure diesel is slightly higher as compared to all type of blends for wide range of engine rpm. For all biodiesel blends the opacity value increases from 10 to 60 % between the speed ranges of 2000 to 3500 rpm. There is no significant change in opacity value for above 4000 rpm engine speed. The trend regarding variation of opacity with respect to speed is almost similar for all type of blends and further the variation of opacity value of different blend at a particular rpm is almost negligible. Except initial speed opacity of biodiesel blends have less value than diesel oil. This is due to better combustion property of biodiesel.

4. Conclusions

From the engine performance testing it can be concluded that the performance parameters and emission characteristics for biodiesel (jatropha) are better results than the diesel oil. In this work performance of biodiesel is compared by the parameters like brake power, torque, brake thermal efficiency, specific fuel consumption and emission are characterized by opacity measurement. Some advantages obtained for biodiesel are:

At low speed more torque is obtained for biodiesel and torque almost constant for wide range of speed for both diesel and biodiesel blends. Maximum torque obtained for jatropha oil is 7.5 kg-m at 2500 rpm and maximum percentage increase in torque is 30% more than the diesel oil which is obtained for 30% blend at 1500 rpm.

More brake power is obtained at initial speed and it is nearly constant for 2500 to 4000 rpm. The maximum brake power achieved is 35 kW at 5000 rpm for biodiesel a blend of 10%. Maximum percentage increase obtained for biodiesel of 30% blend is 3.5% at 1500 rpm.

Except at starting speed more brake thermal efficiency has obtained for higher speeds. For 10% blend of biodiesel there is not much difference in diesel and biodiesel. For higher blend biodiesel has much better efficiency than diesel oil. Maximum brake thermal efficiency increased is 1.98% for biodiesel at 2000 rpm.

Lower value of opacity has obtained for biodiesel than diesel oil at higher speeds. Maximum reduction in opacity obtained is about 35 % for biodiesel.

References

Ministry of Petroleume and Naturale Gas, Government of India, New Delhi,(Economic Division) report, Basic Statistics on Indian Petroleum & Natural Gas, 2011-12, Available at www. http://petroleum.nic.in/petstat.pdf, Accessed on 04-11-2013 20:30 PM

O. D., Hebbal, V. K., Reddy and K Rajagopal, 2006. Performance characteristics of a diesel engine deccan hemp oil. Fuel 85, 2187–2194.

Deepak Agarwal and Avinash Kumar Agarwal, 2007, Performance and Emissions Characteristics of Jatropha Oil (Preheated And Blends) in A Direct Injection Compression Ignition Engine, *Applied Thermal Engineering*; 27: pp 2314–2323.

K Purushothaman, and G Nagarajan, 2009, Performance, Emission and Combustion Characteristics of a Compression Ignition Engine Operating on Neat Orange Oil. *Renewable Energy*; 34 pp 242–245.

Labeckas Gvidonas and Slavinskas Stasys, 2006, The Effect of Rapeseed Oil Methyl Ester on Direct Injection Diesel Engine Performance and Exhaust Emissions, *Energy Conversion and Management*; *47*: pp1954–1967.

Altuna Sehmus, Bulut Husamettin and Oner Cengiz, 2008, The Comparison of Engine Performance and Exhaust Emission Characteristics of Sesame Oil–Diesel Fuel Mixture with Diesel Fuel in A Direct Injection Diesel Engine, *Renewable Energy*;33 pp 1791–1795.

Suresh Kumar.R Velraj , R Ganeshan, 2008 Performance and Exhaust Emission Characteristics of a C I Engine Fuelled with Pongamia Pinnata Methyl Ester (PPME) and its Blends with Diesel. *Renewable Energy*; 33: pp 2294–2302.

Naveen kumar and Abhay Dhuwe, (2004). Fuelling an Agricultural Diesel Engine with Derivatives of Palm Oil, *SAE International2004, Paper no.* 2004-28-0039.

Lapuerta Magin**,** Octavio Armas and Jose Rodriguez, Effect of Biodiesel Fuels on Diesel Engine Emissions. *Progress in Energy and Combustion Science* 2008; *34*: pp198–223.

Avinash Agarwal, and L M Das, 2001, Biodiesel Development and Characterization for Use as A Fuel in C. I. Engine, *Journal of Engineering for Gas Turbines and Power ASME transaction*; 123, number 2 pp 440-447.

Harish Kumar Gangwar, and Avinash Kumar Agarwal, 2008, Emission and Combustion Characteristics of Vegetable Oil Blends in an Indirect Ignition Transportation Engine, *SAE International; Paper no. 2008-28-0034*

S Choudhury, P K Bose., 2008 *Jatropha derived Biodiesel and its Suitability as C. I. Engine Fuel*, *SAE International*; paper no. 28-0040

Volume 3 (2013) 98-106 ISSN 2347 - 3258
International Journal of Advance Research and Innovation

An Investigation of the Combustion and Emission Characteristics of Compression Ignition Engines in Dual-Fuel Mode

Amit Pal *, Abhishek Tiwari
Department of Mechanical Engineering, Delhi Technological University, Delhi, India

Article Info

Article history:
Received 15 November 2013
Received in revised form
30 November 2013
Accepted 05 December 2013
Available online 15 December 2013

Keywords
Combustion
Dual fuel mode
Soot emissions

Abstract

Nowadays automobiles have become significantly essential to our modern life style. On the other hand, future of automobiles, built on the internal combustion engines, has been badly hit by the twin problems due to diminishing fuel supplies and environmental degradation. Thus, it is very important to identify some clean-burning, renewable, alternative fuels to ensure the safe survival of internal combustion engines. However, it is not possible to have a common alternative fuel for universal application in the existing engines that have been designed to operate on petroleum-based fuels. Towards this, scientists have proposed a range of solutions for diesel engines, one of which is the use of gaseous fuels as a complement for liquid diesel fuel. These engines, which use conventional diesel fuel and gaseous fuel, are referred to as 'dual-fuel engines'. In this work an attempt is made to find the role of various operating parameters in optimizing engine operating and design parameters, and the effect of the type of gaseous fuel on the performance and emissions of the gas diesel engines. The 'dual fuel concept' is a promising technique for controlling both NOx and soot emissions even on existing diesel engine. But, HC, CO emissions and 'bsfc' are higher for part load gas diesel engine operations.

1. Introduction

National interest in generating alternative fuels for internal combustion (IC) engines continues to be strong due to environmental concerns and/or the uncertainties associated with the future availability of fossil fuel. Mostly, the interest lies in identifying alternative sources of fuel energy supply. Natural gas, bio-derived gas and liquids appear more attractive in view of their friendly environmental nature [1,2].The gaseous fuels are getting more positive response from researchers and end-users compared to past because of current unfolding developments. Gas is clearly the fossil fuel of least environmental impact. When burnt, it produces virtually insignificant SOx and relatively little NOx, the main constituents of acid rain, and substantially less CO_2, a key culprit in the greenhouse debate, than most oil products and coal [3].

Gaseous fuels have high octane numbers, and therefore, suitable for engines with relatively high compression ratio. Gaseous fuels also promise to be suitable for higher compression engines, since it is known that they resist knock more than conventional liquid fuels, as well as producing less polluting exhaust gases if appropriate conditions are satisfied for its mixing and combustion. Therefore, it is more economical and of environmental advantage to use gaseous fuel in diesel engines that use the 'dual-fuel concept' [4, 5]. Due to limited resources of fossil fuels, alternative solutions have been proposed by many scientists. In 1939, the first commercial dual-fuel engine, fuelled by town gas or other types of gaseous fuels, was produced by the National Gas and Oil Engine Company in Great Britain. This type of

*** Corresponding Author,**
E-mail address: amitpal@dce.ac.in

engine was relatively simple in operation and was mainly employed in some areas where cheap stationary power production was required. During the Second World War, scientists in Great Britain, Germany and Italy paid more attention to the possible application of dual-fuel engines in civil and military areas due to the shortage of liquid fuels. Some vehicles with diesel engines were successfully converted to dual-fuel running. Different kinds of gaseous fuels, such as coal gas, sewage gas or methane, were employed in conventional diesel engines [6-7]. After the Second World War, due to economical and environmental reasons, dual-fuel engines have been further developed and employed in a very wide range of applications from stationary power production to road and marine transport, such as in long and short haul trucks and buses. Some conversions from the original compression ignition diesel engines to dual-fuel operation are made by manufacturers utilizing a double plunger system or two pumps in the injection system of the engine to handle the small quantity of diesel fuel required for ignition [8].

Diesel engines, with appropriate relatively simple conversion can be made to operate on gaseous fuels efficiently. Such engines usually have the gaseous fuel mixed with the air in the engine cylinders, either through direct mixing in the intake manifold with air or through injection directly into the cylinder. The resulting mixture after compression is then ignited through the injection of a small amount of diesel fuel (the pilot) in the usual way. This pilot liquid fuel auto-ignites to provide ignition sources for subsequent flame propagation within the surrounding gaseous fuel mixture. Unlike the spark ignited gas engine, which requires an adequate and uninterrupted gas supply, most current dual-fuel engines are made to operate interchangeably, either on gaseous fuels with diesel pilot ignition or wholly on liquid fuel injection as a diesel engine. Accordingly, a dual-fuel engine tends to retain most of the positive features of diesel operation [9]. Even it surpasses occasionally those of the diesels, producing higher power outputs and efficiencies. This is achieved without significant smoke or particulates emission and with reduced NOx production [10], while having reduced peak cylinder pressures and quieter operation. When considering a gaseous fuel for use in existing diesel engines, a number of issues are important. These issues include the engine operating and design parameters, and type of gaseous fuel supply to the engine.

2. Literature Review

2.1 Dual-fuel concept

Available technologies for reciprocating IC engines are generally divided in two categories: compression-ignition (CI) and spark-ignition (SI) engines. In CI engines (diesel engines), air is compressed at pressures and temperatures at which the injected liquid fuel fires easily and burns progressively after ignition. Whereas, SI engines (Otto engines) that runs according to the Beau de Rochas cycle [11], the carbureted mixture of air and vaporized fuel (high octane index) is compressed under its ignition point and then fired at a chosen instant by an independent means. In a dual-fuel engine, both types of above combustion coexist together, i.e. a carbureted mixture of air and high octane index gaseous fuel is compressed like in a conventional diesel engine. The compressed mixture of air and gaseous fuel does not auto-ignite due to its high auto-ignition temperature. Hence, it is fired by a small liquid fuel injection which ignites spontaneously at the end of compression phase. The advantage of this type of engine is that, it uses the difference of flammability of two used fuels. Again, in case of lack of gaseous fuel, this engine runs according to the diesel cycle by switching from dual-fuel mode. The disadvantage is the necessity to have liquid diesel fuel available for the dual-fuel engine operation [12].

2.2 Modification in internal combustion gas engines

In dual-fuel gas diesel engines, the normal diesel fuel injection system still supplies a certain amount of diesel fuel. The engine however induces and compresses a mixture of air and gaseous fuel that is prepared in the external mixing device. The compressed mixture is then ignited by energy from the combustion of the diesel fuel spray, which is called pilot fuel. The amount of pilot fuel needed for this ignition is between 10% and 20% of the operation on diesel alone at normal working loads and the amount differs with the point of engine operation and its design parameters. During part load engine operation, the fuel gas supply is reduced by means of a gas control valve. However, a simultaneous reduction of the air supply decreases the air quantity induced. Hence, the compression pressure and the mean effective pressure of the engine are decreased. This would eventually lead to a drop in power and efficiency. The drastic reduction in the compression conditions might even become too weak for the mixture to effect self-ignition.

Therefore, dual-fuel engines should not to be throttled/ controlled on the air side.

Ideally, there is a need for optimum variation in the liquid pilot fuel quantity used any time in relation to the gaseous fuel supply so as to provide for any specific engine the best performance over the whole load range desired [12]. Usually, the main goal, for both emissions and economic reasons, is to minimize the use of the diesel fuel and maximize its replacement by the cheaper gaseous fuel throughout the whole engine load range. Normally, the change over from dual-fuel to diesel operation and vice versa can be made automatically, even under load conditions [3].

2.3 Combustion processes in gas diesel engine and conventional diesel engine

The combustion processes in CI engines running on pure diesel fuel can be divided into four stages as shown in Fig. 1. They are, A–B: period of ignition delay; B–C: premixed (rapid pressure rise) combustion; C–D: controlled (normal) combustion; and D–E: late combustion. Point 'A' is the start of fuel injection and 'B' for start of combustion.

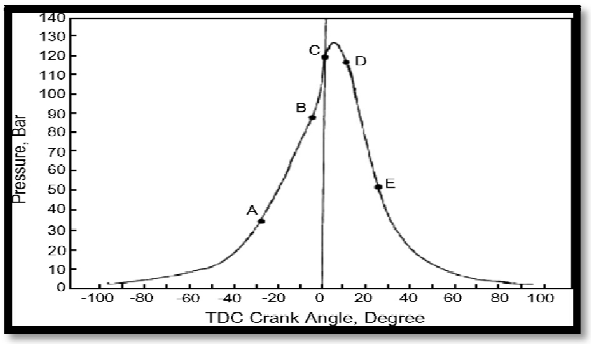

Fig: 1. Details of combustion processes in diesel engine [13]

However, the combustion processes in gas-fumigated dual-fuel engines using pilot injection have been identified to take place in five stages as shown in Fig. 2. They are the pilot ignition delay (AB), pilot premixed combustion (BC), primary fuel ignition delay (CD), rapid combustion of primary fuel (DE) and the diffusion combustion stage (EF).

Ignition delay (AB) of injected pilot fuel exists longer than the pure diesel fuel operation. This is due to the reduction in oxygen concentration resulting from gaseous fuel substitution for air. The pressure rise (BC) is moderately low as compared to pure diesel fuel operation due to the ignition of small quantity of pilot fuel.

Again, there is a finite time lag between the development of the first and second pressure rises due to a longer ignition delay of gas– air mixture, a

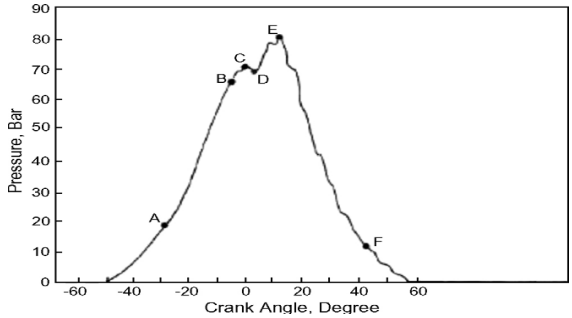

Fig: 2. Dual-fuel pilot injection pressure–crank angle diagram [13]

result of the high self-ignition temperature. However, this ignition delay is short as compared with the initial delay period due to the pilot fuel injection. The pressure decreases slowly (CD) until the actual combustion of the fumigated gas starts. The phase of combustion (DE) is very unstable because it started with flame propagation that has been initiated by the spontaneous ignition of pilot fuel. The pressure rise here does not cause any operating problem since it occurs in an increasing cylinder volume. Diffusion combustion stage (EF) starts at the end of rapid pressure rise and continues well into the expansion stroke. The success of this phase primarily depends on the length of ignition delay [13].

3. Performance of ''gas diesel engines''

Gaseous fuels are considered to be good alternative fuels for passenger cars, truck transportation and stationary engines that can provide both good environmental effect and energy security [4]. However, as some of the engine operating and design parameters namely, load, speed, compression ratio, pilot fuel injection timing, pilot fuel mass, inlet manifold condition, composition of gaseous fuel candidates vary, the performance of the dual-fuel gaseous engines are affected.

3.1 Effect of engine load

The effect of load on combustion noise for the diesel and dual fuel engine (Fig. 3), at an engine speed of 1200 rpm is examined by Selim [14]. The pressure rise rate (combustion noise) for the diesel engine increases slightly when the load increases. For the dual-fuel mode, the combustion noise also increases when the load increases and is always higher than that for the diesel fuel case. Increasing

the load at constant speed results in an increase in the mass of gaseous fuel admitted to the engine, since the pilot mass injected remains constant at all loads. This increase in the mass of methane then causes an increase in the ignition delay period of pilot diesel which then auto-ignites and starts burning the gaseous fuel at a higher rate of pressure rise. This is also shown by Nielsen et al. [15] on dual-fuel engine where natural gas is admitted in the inlet air manifold.

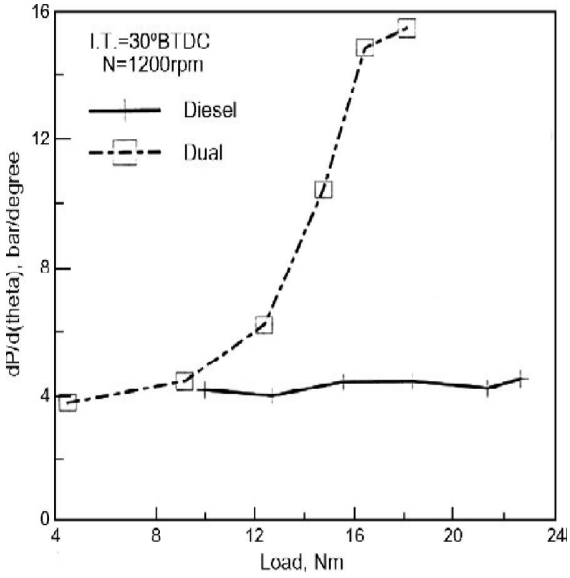

Fig: 3. Effect of engine load on pressure rise rate for the diesel and dual-fuel engines [14]

Concentration of pollutants is investigated with diesel alone and dual-fuel mode (producer gas) at different loads (10, 20, 30 and 40 kW) and is given in Table 1. NOx emissions in dual-fuel mode are lower than the emissions from diesel engine in diesel alone mode. SO2 levels are low in dual fuel mode. This is due to low sulphur content in biomass fuel. The CO emission in dual fuel mode is higher than that of diesel alone. High concentration of CO in the dual-fuel exhaust is an indication of incomplete combustion. At part load condition, concentration of CO increases.

An experimental investigation has been conducted by Papagiannakis and Hountalas [19] to examine the effect of dual fuel combustion on the performance and pollutant emissions of a DI diesel engine. The engine has been properly modified to operate under dual-fuel operation. Under dual-fuel operation, an effort has been made to keep the pilot amount of diesel fuel constant, while the power output of the engine is adjusted through the amount of gaseous fuel. Referring to Fig. 4, the term 'z' refers to the percentage of gaseous fuel. At part engine load, cylinder pressure under dual-fuel operation diverges from the respective values under normal diesel operation. The lower cylinder pressures observed under dual-fuel operation during the compression stroke are the result of the higher specific heat capacity of the NG–air mixture. The total heat release rate under dual-fuel operation is slightly higher compared to the one under normal diesel operation; revealing late combustion of the gaseous fuel. But, the effect on the cylinder pressure is small since it is in the expansion stroke. At high engine load (Fig. 5), the cylinder pressure traces under dual-fuel operation diverge again from the respective values under normal diesel operation during the compression stroke and the initial stages of combustion. This difference is again more evident at low engine speed where the combustion rate under dual-fuel operation during the premixed controlled combustion phase is significantly lower compared to the one under normal diesel operation. It is revealed that the total rate of heat release under dual-fuel operation is obviously higher compared to the one under normal diesel operation. The effect is stronger at low engine speed, revealing later combustion of the gaseous fuel and this obviously has an effect on the 'bsfc'.

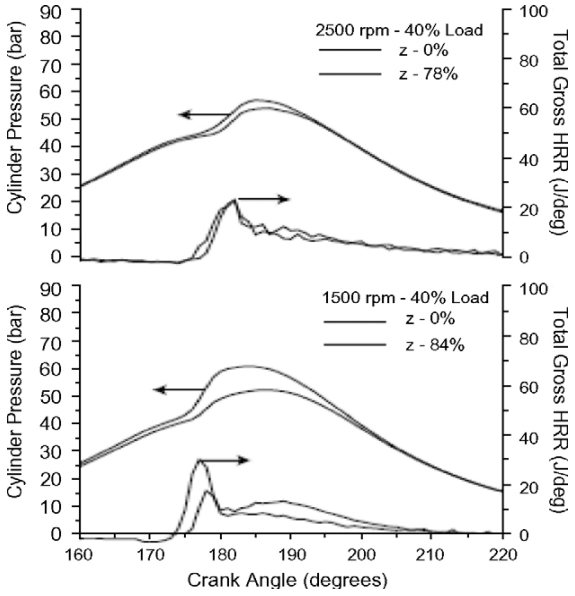

Fig: 4. Cylinder pressure and total heat release traces under normal diesel (z=0%) and dual-fuel (z > 0%) operation for 1500 and 2500 rpm engine speed at 40% load [19]

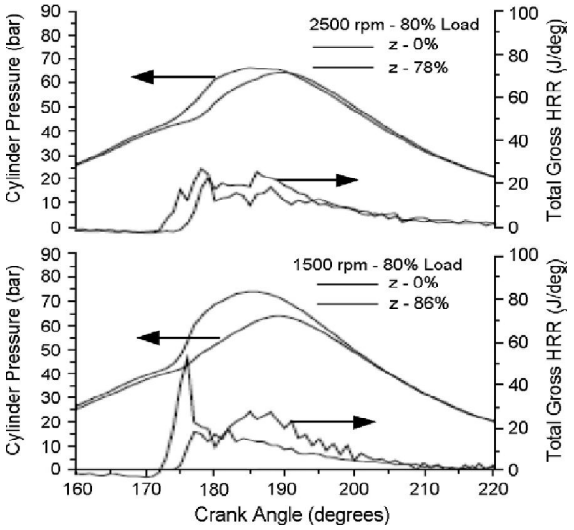

Fig: 5. Cylinder pressure and total heat release traces under normal diesel (z = 0%) and dual-fuel (z > 0%) operation for 1500 and 2500 rpm engine speed at 80% load [19].

3.2 **Dual-Fuel engine emissions**

The formation of nitric oxide (NO) is favored by high oxygen concentration and high charge temperature [11, 21, 22]. NOx concentration is affected considerably by the presence of gaseous fuel–air mixture. The concentration of NOx under dual-fuel operation is lower compared to the one under normal diesel operation at the same engine operating conditions (i.e. engine speed and load). At low engine loads, the NOx concentration under dual-fuel operation is slightly lower compared to the one under normal diesel operation (Fig. 6).This is mainly as a result of the lower rate of premixed controlled combustion of the gaseous fuel, which results in lower charge temperature inside the combustion chamber compared to normal diesel operation. At higher load, the NOx concentration under dual-fuel operation is considerably lower compared to the one under normal diesel operation.

The rate of CO formation is a function of the unburned gaseous fuel availability and mixture temperature which controls the rate of fuel decomposition and oxidation [21,23]. The CO emissions under dual-fuel operation are significantly higher as shown in Fig. 7. At low engine speed, CO concentration under dual-fuel operation clearly decreases with the increase of engine load. This is the result of the improvement of gaseous fuel utilization especially during the second phase of combustion. At high engine speed, the increase of engine load does not seem to affect the concentration of CO due to the less time available for combustion.

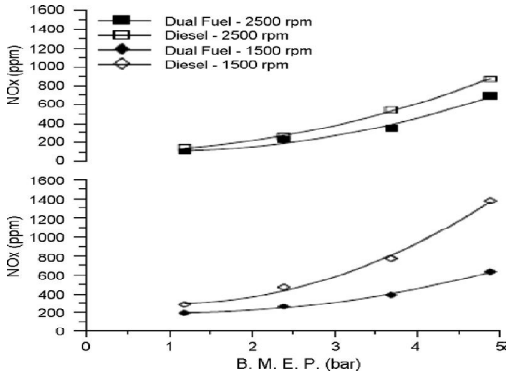

Fig: 6. Variation of nitric oxide under normal diesel and dual-fuel operation versus load at 1500 and 2500 rpm engine speed [19]

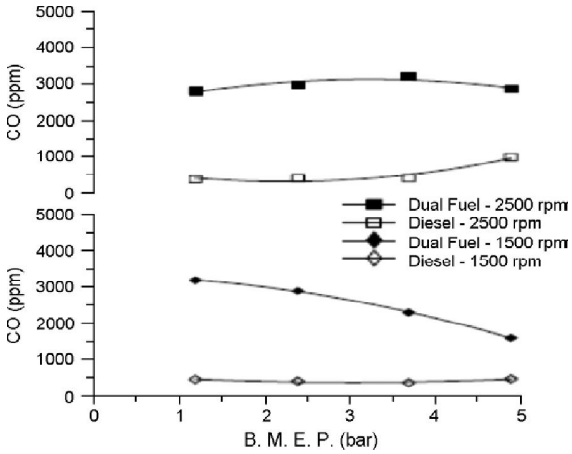

Fig: 7. CO under normal diesel and dual-fuel operation versus load at 1500 and 2500 rpm engine speed [19]

At low engine load, HC emissions under dual-fuel operation are considerably higher compared to the ones under normal diesel operation (Fig. 8). With the increase of engine load, there is a sharp decrease of HC emissions under dual-fuel operation. This is the result of the increase of burned gas temperature that helps oxidize efficiently the UBHCs. But for all cases examined, the HC emissions are considerably higher under dual-fuel operation compared to normal diesel operation.

Soot emissions under dual-fuel operation are considerably lower compared to the ones under normal diesel operation for all cases examined as it is

shown in Fig. 9. It can be seen that under normal diesel operation, soot emissions increase with increasing engine load.

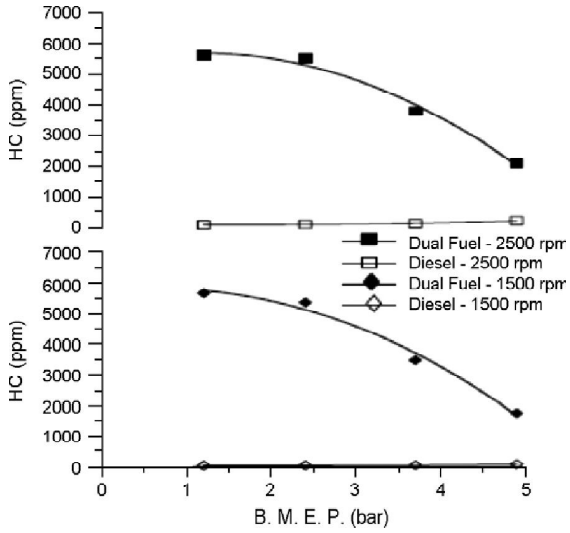

Fig: 8. UBHC under normal diesel and dual-fuel operation versus load at 1500 and 2500 rpm engine speed [19]

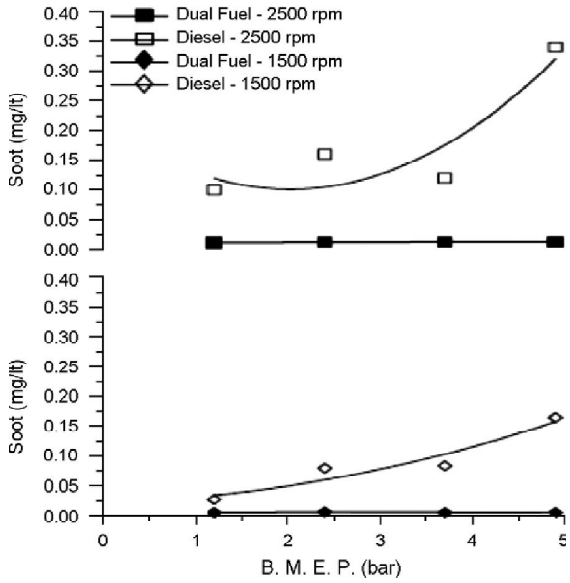

Fig: 9. Soot emissions under normal diesel and dual-fuel operation versus load at 1500 and 2500 rpm engine speed [19]

3.3 Effect of pilot fuel injection timing

The injection timing of the pilot fuel is an important factor that influences the performance of dual-fuel engines. For a fixed total equivalence ratio, advancing the injection timing increase the peak cylinder pressure because more fuel is burned before TDC and the peak pressure moves closer to TDC. Retarding the injection timing decreases the peak cylinder pressure because more of the fuel burns after TDC. This is because, the pilot fuel combustion is delayed and thus, the temperature of the mixture is not enough to propagate the flame in the whole gaseous fuel–air mixture; and consequently, incomplete combustion of the gaseous fuel mixture takes place. The charge temperature increases with advancing the injection timing of the pilot fuel and the associated higher energy release rates of the mixture. Similarly, the rates of pressure rise during the combustion of the gaseous fuel increases with advancing the injection timing of the pilot fuel.

The effect of advanced injection timing on the performance of NG used as primary fuel in dual-fuel combustion has been examined by Nwafor [2]. The injection is first advanced by 5.58 (i.e. 35.58 BTDC). The engine runs for about 5 min at this timing and then stops and with subsequent attempts, he fails to start the engine. But after changing the injection to 33.58 BTDC, the engine runs smoothly, but seems to incur penalty on fuel consumption especially at high load levels. The poor performance of gas engines at low load levels is due to the effect of gas residuals and low cylinder temperature. It is also due to the reduction in combustion efficiency caused by reduced flame propagation speed and increased compression work resulting from the large amount of air–gas inducted. The diesel fuel operation produces the highest BTE at the two speeds (Fig. 10a and b). Standard timing shows little improvement over the advanced system at 3000 rev/min. However, at 2400 rev/min the dual-fuel mode standard and advanced timing show similar trends at low and intermediate load levels. Fig. 13(a) and (b) shows that diesel fuel operation produces the shortest delay periods at both test speeds.

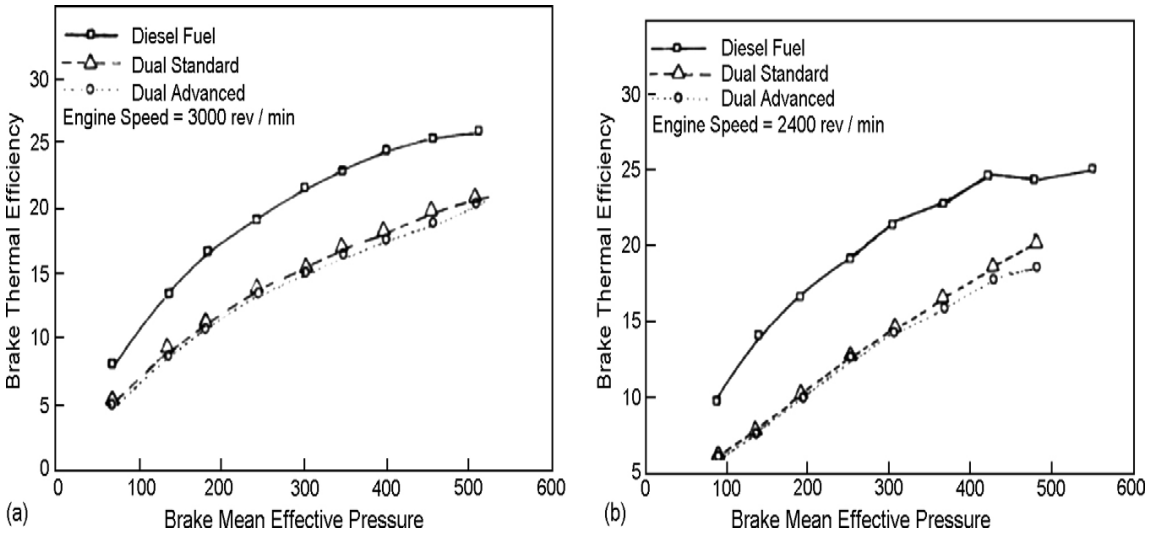

Fig: 10. Injection advanced effect on gas combustion—BMEP (kN/m2) versus BTE (%) [2]

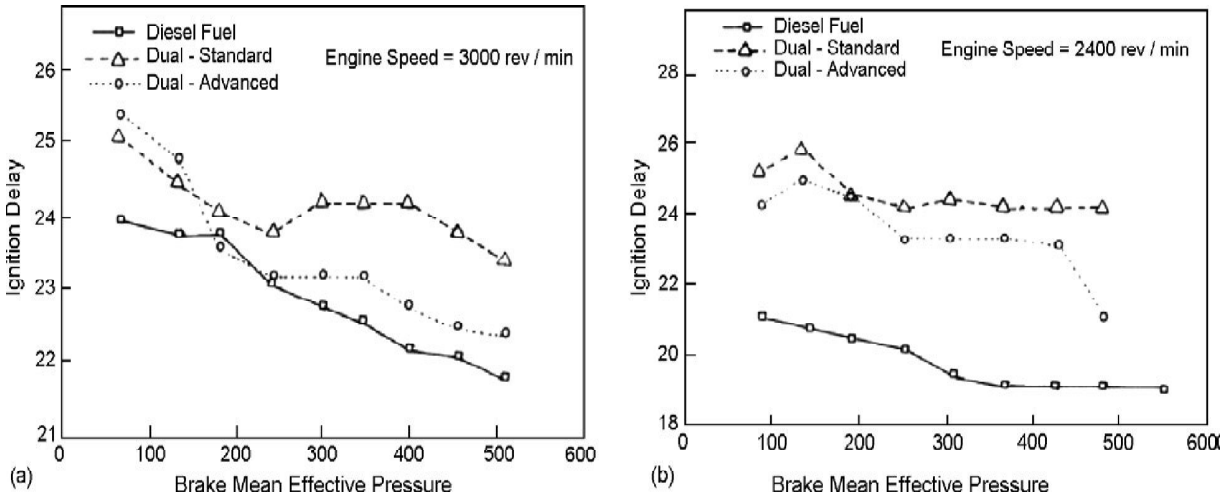

Fig: 11. Injection advanced effect on gas combustion—BMEP (kN/m2) versus ignition delay (deg.) [2]

Standard dual-fuel timing at 3000 rev/min shows longer delay periods at high loads than the advanced injection timing operation. There is a very significant difference between the ignition delays of diesel fuel and dual-fuel operations at 2400 rev/min. Standard dual-fuel timing also shows the longest delay period. At high loads and combustion temperatures, the ignition delay is reduced and combustion is dominated by the system temperature. At low loads with longer delay periods, greater proportion of pilot fuel takes part in premixed combustion, thus increases the tendency of diesel to knock. Very poor atomization results in a relatively long delay period, due to the slow development of very fine droplets. Dual fuel operation with advanced timing shows the highest exhaust temperatures at 3000 rev/min (Fig. 11a and b). The dual-fuel mode with the standard timing also shows a marginal increase over the operation on pure diesel fuel. The standard timing dual-fuel unit produced the highest cylinder wall temperatures while the advanced system showed the lowest values at this speed.

However, the diesel fuel operation produces the lowest cylinder wall temperatures, whereas the standard unit offers the highest values. The best fuel economy is realised when running on pure diesel fuel

and hence, the thermal efficiency of the gas engine is less than that of pure diesel fuel case. The results from Fig. 12(a) and (b) indicate that the HC emissions of the gas-fuelled engine are higher than that in pure diesel fuel operation. Diesel fuel operation gives the lowest HC emissions at both speeds. Dual-fuel standard timing shows higher concentration of HC in the exhaust at low load levels over the advanced injection unit. HC emissions increase due to several factors, including quenching, lean combustion, wall wetting, cold starting and poor mixture preparation. For both test conditions, the HC levels are relatively high in dual-fuel operations and stay reasonably high throughout the load range.

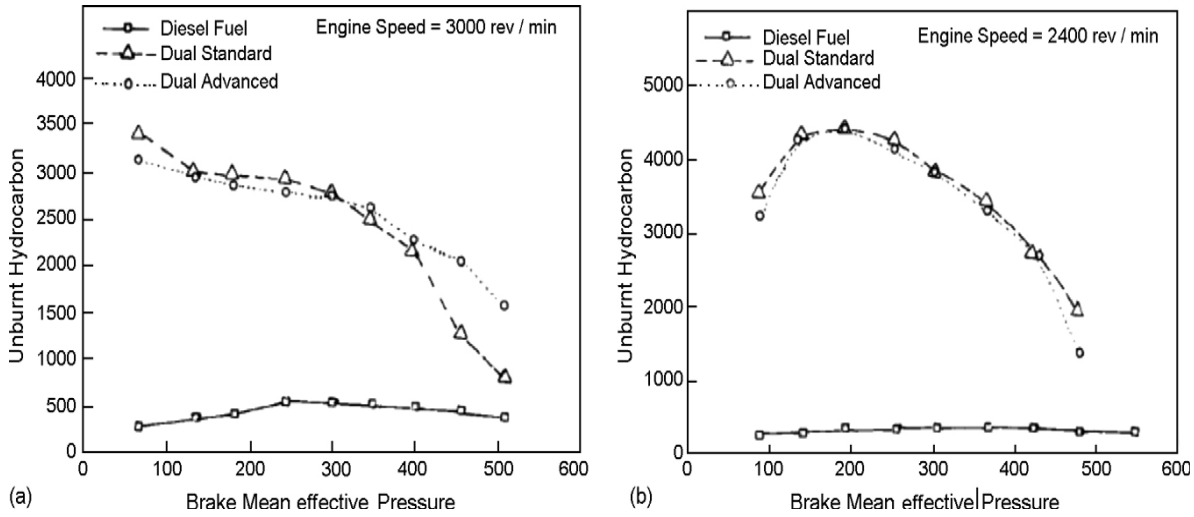

Fig: 12. Injection advanced effect on gas combustion—BMEP (kN/m2) versus UBHC (ppm) [2]

4. Conclusions

Researchers in various countries have carried out many experimental works using gaseous fuels as diesel engine fuel substitute in a dual-fuel mode of operation. An attempt has been made here to review the previous studies on dual-fuel concept. The overall observation from these experimental results is that the engine operating and design parameters, namely, load, speed, pilot fuel injection timing, pilot fuel mass, compression ratio, inlet manifold conditions and type of gaseous fuel play an important role in the performance and exhaust emissions of dual-fuel diesel engines. The ignition characteristics of the gaseous fuels need further more experimental research for a long-term use in a dual-fuel engine.

References

[1] OMI Nwafor. "Effect of choice of pilot fuel on the performance of natural gas in diesel engines Renewable Energy" 21(3/4):495–504, 2000
[2] OMI Nwafor. "Effect of advanced injection timing on the performance of natural gas in diesel engine.Sadhana" 25(1):11–20, 2000
[3] A Henham, MK Makkar. "Combustion of simulated biogas in a dual-fuel diesel engine" Energy Conversion and Management 1998; 39(16–18):2001–9
[4] MYE Selim. "Sensitivity of dual fuel engine combustion and knocking limits to gaseous fuel Composition". Energy Conversion and Management; 45(3): 411–25, 2004
[5] TR White, BE Milton, M Behnia, "Direct injection of natural gas/liquid diesel fuel sprays". In: Proceedings of the 15th Australasian fluid mechanics conference; 2004
[6] Rajesh Kumar, Manish Kumar Chauhan, Naveen Sharma and Amit Pal. "Performance and Emissions Analysis of a Multi Cylinder CI Engine Fulled with Diesel-CNG Dual Fuel" Int. J. S & T Review, Vol. 1, No. 1, 2011, pp 55-62
[7] GA Karim. "The dual fuel engine In: Evans RL, editor. Automotive engine alternatives New York": Plenum Press; 1987
[8] V Thyagarajan, MKG Babu. "A combustion model for a dual fuel direct injection diesel engine, diagnostics and modelling of combustion

in reciprocating engine" In: Proceedings of the Comodia symposium; .p. 607, 1985
[9] O Badr, GA Karim, B Liu. "An examination of the flame spread limits in a dual fuel engine". Applied Thermal Engineering; 19(10):1071–80, 1999
[10]SH Turner, CS Weaver. "Dual fuel natural gas/diesel engines: technology, performance and emissions". Gas Research Institute Technical Report no. 94/ 0094; 1994
[11]JB Heywood. "Internal combustion engine fundamentals, New York": McGraw- Hill Book Co.; 1988
[12] C Mansour, A Bounif, A Aris, F Gaillard. "Gas–diesel (dual-fuel) modelling in diesel engine environment" International Journal of Thermal Science; 40(4):409–24, 2001
[13]B.B. Sahoo, N. Sahoo, U.K. Saha. "Effect of engine parameters and type of gaseous fuel on the performance of dual-fuel gas diesel engines—A critical review". Renewable and Sustainable Energy Reviews 13, 1151–1184, 2009
[14] MYE Selim. "Pressure–time characteristics in diesel engine fuelled with natural gas". Renewable Energy; 22(4):473–89, 2001
[15] OB Nielsen, B Qvale, S Sorenson. "Ignition delay in the dual fuel engine". SAE paper 870589; 1987
[16] R Uma, TC Kandpal, VVN Kishore. "Emission characteristics of an electricity generation system in diesel alone and dual fuel modes", Biomass & Bioenergy; 27(2):195–203, 2004
[17] PP Parikh, AG Bhave, DV Kapse, Shashikantha. "Study of thermal and emission performance of small gasifier-dual-fuel engine systems". Biomass; 19:75– 97, 1989
[18]G Sridhar, PJ Paul, HS Mukunda. "Biomass derived producer gas as a reciprocating engine fuel—an experimental analysis". Biomass & Bioenergy; 21(1): 61–72, 2001
[19] RG Papagiannakis, DT Hountalas. "Combustion and exhaust emission characteristics of a dual fuel compression ignition engine operated with pilot diesel fuel and natural gas". Energy Conversion and Management; 45(18/19):2971–87, 2004
[20]DT Hountalas. "The effect of operating parameters on the net and gross heat release rates of a direct injection diesel engine. In: Proceedings of the second biennial ASME-ESDA international conference on design of energy systems"; 63(3), 1994
[21]RS Benson, ND Whitehouse, "Internal combustion engines", Oxford: Pergamon Press; 1973
[22]GA Lavoie, JB Heywood, JC Keck. "Experimental and theoretical study of nitric oxide formation in internal combustion engines", Combustion Science Technology; 1:313–26, 1970
[23]DA Kouremenos, CD Rakopoulos, DT Hountalas. "Experimental investigation of the performance and exhaust emissions of a swirl chamber diesel engine using JP-8 aviation fuel" In: International journal of energy research, vol. 21. John Wiley & Sons; 1997

Optik xxx (2013) xxx–xxx

Contents lists available at ScienceDirect

Optik

journal homepage: www.elsevier.de/ijleo

Demonstration of temperature resilient properties of 2D silicon carbide photonic crystal structures and cavity modes

Jiten Boruah*, Yogita Kalra, R.K. Sinha

TIFAC-Centre of Relevance and Excellence in Fiber Optics and Optical Communication, Department of Applied Physics, Delhi Technological University (Formerly Delhi College of Engineering, Faculty of Technology, University of Delhi), Bawana Road, Delhi 110042, India

ARTICLE INFO

Article history:
Received 24 April 2013
Accepted 5 September 2013
Available online xxx

Keywords:
Photonic crystal
Photonic band gap
Photonic crystal cavity
Plane wave expansion (PWE) method
Finite difference time domain (FDTD) method

ABSTRACT

In this paper, photonic crystal (PhC) based on two dimensional (2D) square and hexagonal lattice periodic arrays of Silicon Carbide (SiC) rods in air structure have been investigated using plane wave expansion (PWE) method. The PhC designs have been optimized for telecommunication wavelength ($\lambda = 1.55\ \mu m$) by varying the radius of the rods and lattice constant. The result obtained shows that a photonic band gap (PBG) exists for TE-mode propagation. First, the effect of temperature on the width of the photonic band gap in the 2D SiC PhC structure has been investigated and compared with Silicon (Si) PhC. Further, a cavity has been created in the proposed SiC PhC and carried out temperature resiliency study of the defect modes. The dispersion relation for the TE mode of a point defect A1 cavity for both SiC and Si PhC has been plotted. Quality factor (Q) for both these structures have been calculated using finite difference time domain (FDTD) method and found a maximum *Q* value of 224 for SiC and 213 for Si PhC cavity structures. These analyses are important for fabricating novel PhC cavity designs that may find application in temperature resilient devices.

1. Introduction

Photonic Crystals exhibit photonic band gaps (PBG) in which electromagnetic fields cannot propagate in given directions, if the geometrical parameters and dielectric contrast of the photonic lattices are chosen appropriately [1]. Photonic Crystals can be used to control light propagation through it by using different geometry and dielectric contrast. Because of the strong photon confinement shown by these crystals they can be used in variety of applications. A special attractive application of PhCs is to construct localized electromagnetic modes by introducing defects in the periodic structure. These confined modes could be used in optical resonators, laser cavities, etc.

Investigating photonic structures which are less sensitive to environmental fluctuations is a valuable area of research, hence, we here propose to design photonic crystals using silicon carbide [2] and investigate the variation of width of photonic band gaps in SiC photonic crystals with change in temperature and a comparison with Silicon (Si) photonic crystals [3,4]. Further, analysis of the SiC photonic crystal cavity defect modes using plane wave expansion (PWE) method and finite difference time domain (FDTD) method has been done. However the most widely used materials to design photonic crystal devices are silicon and gallium arsenide because of the available and mature technology of fabrication and optimum refractive index contrast offered by these materials for the existence of the photonic band gaps. We here propose to design photonic crystals using silicon carbide which is one of the hardest materials known and further the creation of photonic crystal cavity in SiC photonic crystal. The reason for using silicon carbide is its high mechanical strength, large thermal conductivity and small thermo optic coefficient.

In this paper, a 2D SiC PhC composed of square lattice of SiC rods in air is realized and the PhC structures are optimized by varying different parameters like radius of the nanopillars, period of the lattice etc. for telecommunication applications [5]. Further, defect cavities have been created in the optimized PhC structures and analysis of the cavity defect modes using plane wave expansion (PWE) method and finite difference time domain (FDTD) method has been done. The defect A1 cavity has been created in the periodic lattice of photonic crystal by removing one central dielectric rod completely from the unperturbed lattice structure that result in localization of light in the specified defect space in the frequency range lying within the PBG of the optimized PhC [6]. The localized defect modes of these A1 defect cavity structures have been extracted and the dispersion relations plotted to investigate the temperature resilient property of the localized defect modes of these structures. Also Quality factor (Q) for both these structures have been calculated using finite difference time domain (FDTD) method for different temperatures ranging from 25 to 200 °C

* Corresponding author. Tel.: +91 11 27871017; fax: +91 11 27871023.
E-mail addresses: jitenboruah1@rediffmail.com (J. Boruah), dryogitakalra@gmail.com (Y. Kalra), dr_rk_sinha@yahoo.com (R.K. Sinha).

0030-4026/$ – see front matter © 2013 Elsevier GmbH. All rights reserved.
http://dx.doi.org/10.1016/j.ijleo.2013.09.063

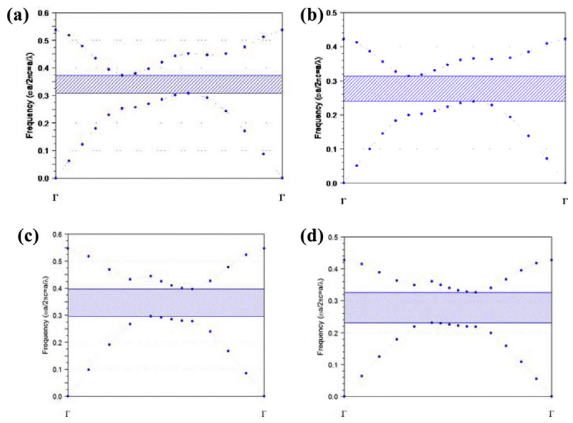

Fig. 1. (a) TE band gap of square lattice of SiC rods in air. (b) TE band gap of square lattice of Si rods in air. (c) TE band gap of hexagonal lattice of SiC rods in air. (d). TE band gap of hexagonal lattice of Si rods in air.

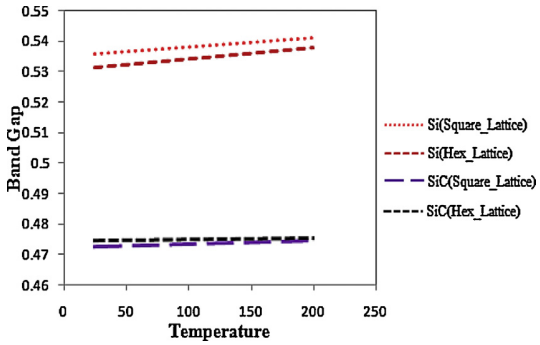

Fig. 2. Variation of band gap width with temperature in square and hexagonal lattice SiC and Si PhC.

and studied resonant wavelength peak shift for the temperature range.

2. Design of SiC photonic crystals

A 2D PhC composed of square lattice of SiC rods ($n = 2.64$) in air with radius of dielectric nanopillars, $r = 0.16\,\mu m$ and lattice

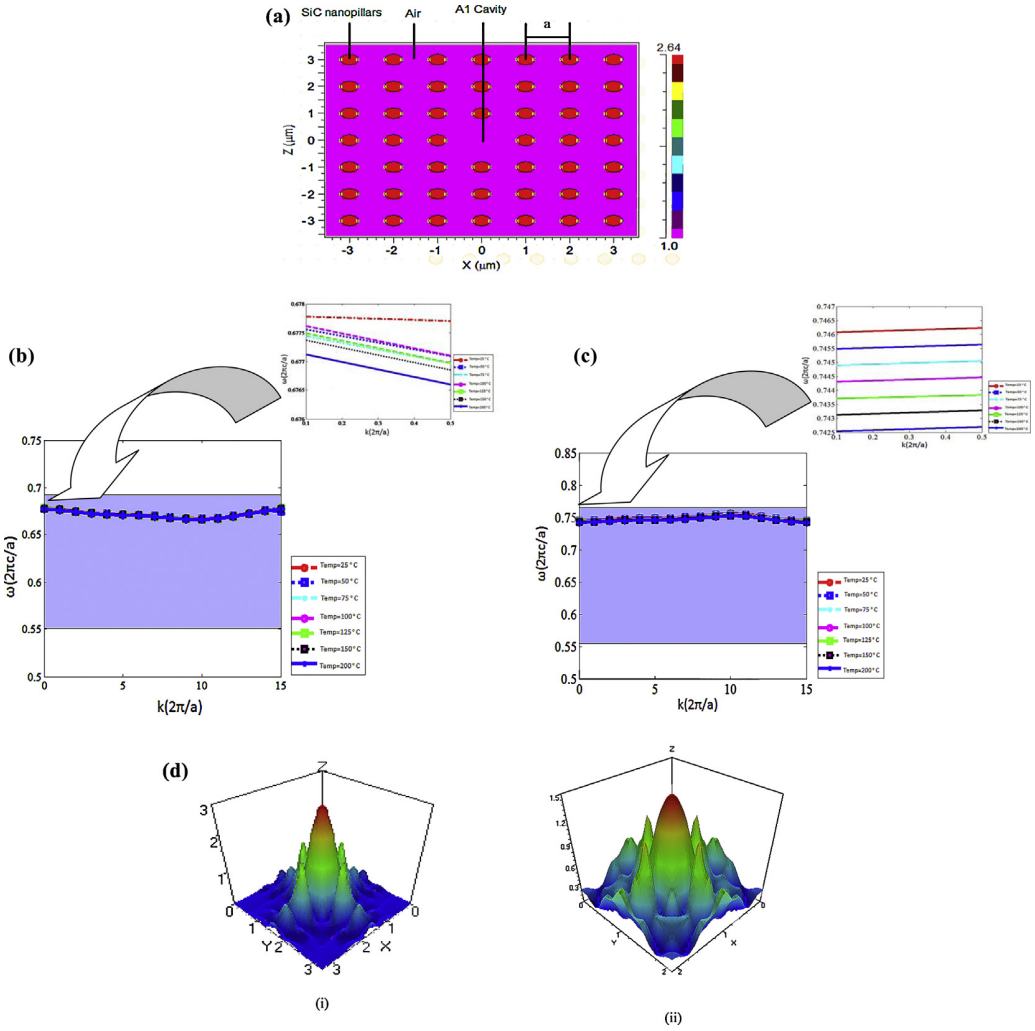

Fig. 3. (a) Schematic diagram of SiC PhC A1 cavity having lattice constant, $a = 0.55\,\mu m$. (b) Dispersion graph of localized defect mode of SiC PhC A1 cavity at different temperatures: the blue line is the dispersion curve. Inset: shift in the resonant wavelength of the A1 SiC rods in air PhC micro cavity structures for different temperatures. (c) Dispersion graph of localized defect mode of Si PhC A1 cavity at different temperatures: the blue line is the dispersion curve. Inset: Shift in the resonant wavelength of the A1 Si rods in air PhC micro cavity structures for different temperatures. (d)(i and ii). Localized defect modes of a square lattice of SiC and Si dielectric cylinders in air PhC A1 cavity: Y – component of electric field (E) amplitude. (For interpretation of the references to color in this figure legend, the reader is referred to the web version of the article.)

Please cite this article in press as: J. Boruah, et al., Demonstration of temperature resilient properties of 2D silicon carbide photonic crystal structures and cavity modes, Optik - Int. J. Light Electron Opt. (2013), http://dx.doi.org/10.1016/j.ijleo.2013.09.063

constant, $a = 0.55$ μm has been considered, whose PBG for TE mode lies in the range of 1.46–1.80 μm as shown in the Fig. 1(a). Similarly, a 2D Si rods in air PhC with a square lattice is created with $r = 0.12$ μm and $a = 0.42$ μm, whose PBG for TE mode is in between 1.34 and 1.77 μm as shown in the Fig. 1(b). Further, point defect is created in the proposed design of SiC and Si photonic crystal to form PhC cavity.

Again, a 2D PhC composed of hexagonal lattice of SiC rods ($n = 2.64$) in air with radius of dielectric nanopillars, $r = 0.16$ μ m and lattice constant, $a = 0.55$ μm has been considered, whose PBG for TE mode lies in the range of 1.38–1.85 μm as shown in the Fig. 1(c). Similarly, a 2D Si rods in air PhC with a hexagonal lattice is created with $r = 0.12$ μm and $a = 0.42$ μm, whose PBG for TE mode is in between 1.28 and 1.81 μm as shown in the Fig. 1(d). Further, point defect is created in the proposed design of SiC and Si photonic crystal to form PhC cavity.

2.1. Temperature resiliency study of band gap of 2D SiC PhC

To study the effect of temperature on the photonic crystal structures, the temperature of the designed structures has been raised from 25 to 200 °C [7–9] and the band gap width has been calculated at various temperatures for both SiC PhC and Si PhC. The variation of photonic band gap with temperature for both Si and SiC based square and hexagonal lattice PhC has been shown in Fig. 2. Fig. 2 indicates that the SiC based photonic crystal exhibited a very small variation or shallow shift in the width of the band gap with change in temperature as compared to the Si based PhC. For the operational wavelength of 1550 nm, the SiC based square lattice PhC exhibited a shift of around 2.2 nm in the operational range (band gap width) while the temperature is varied from 25 °C to 200 °C, whereas the Si based photonic crystal, exhibits a shift of around 5.5 nm in the same operational window, which is around three times the variation observed with respect to the SiC based PhC. Also the SiC based hexagonal lattice PhC exhibited a shift of 1 nm in the operational range (band gap width) while the temperature is varied from 25 to 200 °C, whereas the Si based photonic crystal, exhibits a shift of around 8.2 nm in the same operational window, which is around eight times the variation observed with respect to the SiC based PhC. Thus, the results indicate that the SiC based photonic crystals are nearly three times more resilient than Si based photonic crystals over a given temperature range and hexagonal lattice SiC PhC structures are more resilient than its square counterpart. This variation in the operational range of the SiC and Si PhC indicate the difference in the thermo optic effect of SiC and Si photonic crystal. Thus, the SiC PhCs are less susceptible to the temperature fluctuations in comparison to Si PhCs that lead to the instability of the optical properties of the opto-elctronic systems and hence SiC PhCs find application in making photonic crystal nanophotonic devices almost independent of the temperature of their environment.

3. Defect mode analysis of 2D SiC square lattice cavity

Photonic crystals have the potential of realizing nanoscale optical components and devices. Since the PBG structures strongly control the flow of light, therefore various types of defect cavities can be created in periodic lattice of PhC's by changing the radius of rods or holes or by removing them completely that result in confinement or localization of light in a specified defect space [10]. These cavities support localized modes in the frequency range lying within the PBG of the PhC. These localized modes are horizontally confined by PBG of the photonic crystal and vertically by total internal reflection because of the refractive index contrast between the dielectric and the cladding [11,12].

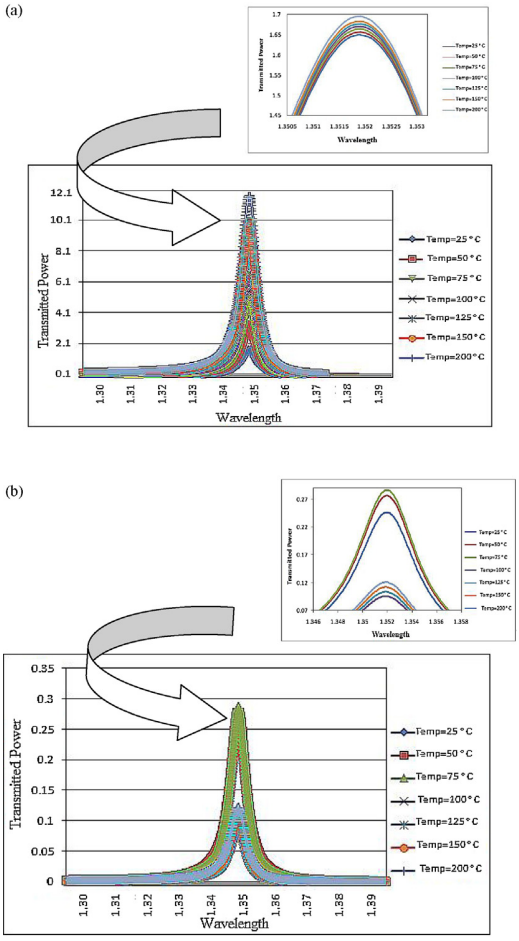

Fig. 4. (a) Transmitted power versus wavelength graph for localized defect mode of SiC PhC A1 defect cavity at different temperatures. Inset: Shift in the resonant peak of the A1 SiC rods in air PhC micro cavity structures for different temperatures. (b) Transmitted power versus wavelength graph for localized defect mode of Si PhC A1 defect cavity at different temperatures. Inset: Shift in the resonant peak of the A1 Si rods in air PhC micro cavity structures for different temperatures.

3.1. Analysis of A1 defect cavity mode

A defect A1 cavity has been created by removing a silicon carbide dielectric rod from the square lattice of the proposed design as shown in the Fig. 3(a). It has been found that the PWE TE solutions exhibit a band gap in the range between 1.49 and 1.81 μm. When a point defect is created in a photonic crystal, the defect can pull light mode into the band gap. As such a state is forbidden from propagating in the bulk crystal, it is trapped. Localized defect modes have been extracted from the structure by varying the temperature from 25°C to 200°C and plotted as shown in the dispersion diagram in Fig. 3(b). Fig. 3(c) shows the dispersion diagram for Si 2D PhC cavity. The corresponding defect mode profile of SiC and Si PhC cavity is shown in Fig. 3 (d)(i and ii), which indicates that modes get localized in both 2D SiC and Si PhC A1 cavity i.e. the modes are confined vertically by total internal reflection and horizontally by the photonic band gap of the PhC.

The dispersion graph of localized defect mode of SiC PhC A1 cavity in Fig. 3(b) shows a shift of around 3.6 nm for the temperature range from 25 to 200 °C whereas the Si PhC A1 cavity in Fig. 3(c) exhibits a shift of around 37 nm in the same operational window, which is around ten times the variation observed with respect to the SiC based PhC A1 cavity. The result depicts that the SiC cavity

Please cite this article in press as: J. Boruah, et al., Demonstration of temperature resilient properties of 2D silicon carbide photonic crystal structures and cavity modes, Optik - Int. J. Light Electron Opt. (2013), http://dx.doi.org/10.1016/j.ijleo.2013.09.063

structures are more temperature resilient as compared to Si based PhC cavity.

3.1.1. Q factor and its optimization

The Q factor or Q of the cavity is defined as the ratio of the cavity resonance and is a measure of the ratio of the optical energy stored in the micro cavity to the cycle average power radiated out of the cavity. The resonant mode is strongly confined in the micro cavity. Q can be calculated from relative power versus distance curve using transmission function based on the point or transmission function based on the area.

$$\text{i.e.} \quad Q = \frac{\lambda}{\Delta\lambda} = \frac{f_0}{f_2 - f_1}$$

where, f_0 is the center frequency or the resonant frequency and f_2 and f_1 are upper and lower cut off frequencies, $(f_2 - f_1)$ is the band width of the resonant system. Quality factor or Q factor is a measure of quality of performance of a resonant system. It indicates the ability of the system to produce a large output at the resonant frequency. Hence, the quality factor for the above mentioned structures has been found out and a maximum value of 224 is obtained for SiC A1 PhC cavity and 213 for Si A1 PhC cavity. It has been found that there is a shift of about 0.3 nm in the resonant wavelength peak of the SiC A1 PhC cavity structures when the temperature is varied from 25 to 200 °C as shown in Fig. 4(a). Whereas the Si PhC A1 cavity in Fig. 4(b) exhibits a resonant wavelength peak shift of around 2 nm in the same operational window, which is around seven times the variation observed with respect to the SiC based PhC A1 cavity. The result indicates that the SiC cavity structures are more temperature resilient as compared to Si based PhC cavity structures.

4. Conclusion

We have designed an optimized cavity in temperature resilient material (SiC) and analyzed its PBG and cavity mode characteristics using PWE and FDTD techniques. The SiC PhC devices can be used for high temperature and power transmission which is difficult to achieve with Si or GaAs based photonic crystals and devices. Apart from applications in optical communication, various other SiC based devices such as optical filters, switches and lasers etc. can be designed which are stable at high power and high temperature, at which the silicon photonics fails, which can lead to the era of silicon carbide power photonics analogous to silicon carbide power electronics.

Acknowledgements

The authors gratefully acknowledge the initiatives and support toward establishment of the "TIFAC-center of Relevance of Excellence" in Fiber Optics and Optical Communication at Delhi College of Engineering now Delhi Technological University, Delhi, through the "Mission REACH" program of Technology Vision-2020 of the Government of India.

References

[1] J.D. Joannapolous, R.D. Meade, J.N. Winn, Photonic Crystals:, Moulding the flow of light, second ed., Princeton University Press, New Jersey, 2008.
[2] G.L. Harris, Properties of Silicon Carbide, INSPEC, Institution of Electrical Engineers, London, 1995.
[3] J. Zhou, H. Li, L. Ye, J. Liu, J. Wang, T. Zhao, L. Jiang, Y. Song, Facile fabrication of tough SiC inverse opal photonic crystals, J. Phys. Chem. C114 (2010) 22303.
[4] B.S. Song, S. Yamada, T. Asano, S. Noda, Demonstration of two-dimensional photonic crystals based on silicon carbide, Opt. Express 19 (2011) 11084–11089.
[5] R.K. Sinha, Y. Kalra, Photonic band gap engineering in 2D photonic crystals, Pramana J. Phys. India 67 (6) (2006) 1155–1164.
[6] M. Ziaei-Moayyed, M.F. Su, C.M. Reinke, I. El-Kady, R.H. Olsson, Silicon carbide phononic crystals for high f.Q micromechanical resonators, in: IEEE IUS Proceedings, ULTSYM, 2010, pp. 162–166.
[7] S. Yamada, B.S. Song, T. Asano, S. Noda, Experimental investigation of thermo-optic effects in SiC and Si photonic crystal nanocavities, Opt. Lett. 36 (2011) 3981–3983.
[8] B. Wild, R. Ferrini, R. Houdré, M. Mulot, S. Anand, C.J.M. Smith, Temperature tuning of the optical properties of planar photonic crystal micro cavities, Proc. SPIE 5450 (2004) 311–317.
[9] S.M. Weiss, M. Molinari, P.M. Fauchet, Temperature stability for silicon-based photonic band-gap structures, Appl. Phys. Lett. 83 (10) (2003) 1980–1982.
[10] J.S. Foresi, P.R. Villeneuve, J. Ferrera, E.R. Thoen, G. Steinmeyer, S. Fan, J.D. Joannopoulos, et al., Photonic-band gap microcavities in optical waveguides, Nature 390 (1997) 143–145.
[11] S.G. Johnson, S. Fan, P.R. Villeneuve, J.D. Joannopoulos, Guided modes in photonic crystal slabs, Phys. Rev. B 60 (1999) 5751–5758.
[12] E. Chow, S.Y. Lin, S.G. Johnson, P.R. Villeneuve, J.D. Joannopoulos, Three-dimensional control of light in a two-dimensional photonic crystal slab, Nature 407 (2000) 983–986.

Please cite this article in press as: J. Boruah, et al., Demonstration of temperature resilient properties of 2D silicon carbide photonic crystal structures and cavity modes, Optik - Int. J. Light Electron Opt. (2013), http://dx.doi.org/10.1016/j.ijleo.2013.09.063

Enhanced Fano resonance in silver ellipsoidal plasmonic crystal cavity

Venus Dillu and R. K. Sinha

Citation: Journal of Applied Physics **114**, 234305 (2013); doi: 10.1063/1.4851775
View online: http://dx.doi.org/10.1063/1.4851775
View Table of Contents: http://scitation.aip.org/content/aip/journal/jap/114/23?ver=pdfcov
Published by the AIP Publishing

JOURNAL OF APPLIED PHYSICS **114**, 234305 (2013)

Enhanced Fano resonance in silver ellipsoidal plasmonic crystal cavity

Venus Dillu and R. K. Sinha[a)]
Department of Applied Physics, TIFAC—Centre of Relevance and Excellence in Fiber Optics and Optical Communication, Delhi Technological University (Formerly: Delhi College of Engineering), Bawana Road, Delhi 110042, India

(Received 2 August 2013; accepted 2 December 2013; published online 19 December 2013)

Enhancement in the asymmetric line shape of Fano resonance is observed and extensively examined for cavities in plasmonic crystals of ellipsoidal silver nanoparticles with hexagonal arrangement. Scattering models for ellipsoidal and cylindrical nanoparticles are compared and it is found that the spectral interference between the cavity mode and the background scattering mode results in a sharp asymmetric peak, which is the defining characteristic of Fano resonance. It is found that the cavity in ellipsoidal nanoparticles yields high transmission at a wavelength of 1600 nm compared with its cylindrical counterpart. Higher harmonic generation is also observed, which confirms the ultrahigh cavity response in ellipsoidal nanoparticles. The effect of power variation on the Fano resonance profile is described, and its application in the field of switching is explored. In addition, the influence of mutual interparticle coupling on Fano line shapes for transverse electric and transverse magnetic polarization is reported. The extraordinary rise in asymmetric line shapes of the Fano resonance promises profound applications in the field of sensing, switching, and lasing devices.
 [http://dx.doi.org/10.1063/1.4851775]

I. INTRODUCTION

Fano resonance, discovered by Ugo Fano, is a resonant scattering phenomenon that gives rise to asymmetric line shapes due to the interaction of discrete excited states with continuum excited states sharing same energy level.[1] The response of an oscillating system driven at an external frequency, ω, about its resonant frequency, ω_0, is symmetric and the intensity, I, for the system is approximated by the universally accepted Lorentzian function given below

$$I(\omega) \propto \frac{\left(\frac{\gamma}{2}\right)^2}{(\omega-\omega_0)^2+\left(\frac{\gamma}{2}\right)^2}, \tag{1}$$

where γ is the width of resonance about resonant frequency, ω_0.

In contrast to the Lorentzian function, the distinct asymmetric Fano resonance shape is given by the following function:

$$I \propto \frac{(F\gamma+\omega-\omega_0)^2}{(\omega-\omega_0)^2+\gamma^2}, \tag{2}$$

where F is the Fano parameter describing the degree of asymmetry.[2] Fano resonance is generally specific to quantum systems that involve auto-ionization of atoms due to interference of excited leaky modes with incoming continuum radiation. This interference (or auto-ionization) gives rise to asymmetric profile characteristics of the Fano resonance. By using the comprehensive approach developed by Fano, it is possible to predict the position as well as the width of the Fano resonance.[2,3] Fano resonance was first observed in 1902 as Wood's anomalies in gratings.[4] Subsequently, this phenomenon has been meticulously studied and had been observed in quantum dots, quantum wires,[5,6] dielectric and metallic photonic crystals,[7,8] prism-coupled micropillars,[9] plasmonic nanostructures,[2] metamaterials,[10] self-assembled nanoparticle clusters,[11] individual plasmonic nanocavities,[12] and symmetry breaking disk-ring nanostructures,[13] among others. Because this unique resonance arises from the interference between two or more oscillators, the system has intrinsic sensitivity towards local changes,[2] making it well suited for application in chemical and biological sensors. Large shifts in the resonance frequency of the system are the basis of its sensing capability. The characteristic Fano resonance profile also has promising applications in lasing, switching, slow-light devices, and plasmon-induced transparency. To realize these prospective applications, novel plasmonic designs with improved properties are required, for example, with respect to transmission, propagation, and loss characteristics.

Clusters of strongly interacting metallic nanoparticles support strong Fano resonance arising owing to the interference between the superradiant bright mode and the subradiant dark mode of the quantum system, which can be designed to achieve the desired optical response. The electromagnetic interactions within such a quantum system influence the line shape of the resultant plasmonic Fano profile. Plasmonic dimers, dolmen structures, metallic double gratings, quadrumers, and heptamers with different cross-sectional areas have been found to exhibit Fano resonance, which can be manipulated by tailoring the number and position of the monomeric units.[11,14–17] However, in simpler clusters like dimers and trimers, the electric dipole resonance subdues the Fano resonance.[11] This limitation is addressed

[a)]Author to whom correspondence should be addressed. Electronic mail: dr_rk_sinha@yahoo.com

by adding structural complexity or breaking the symmetry to induce bright and dark modes available for interaction to produce Fano resonance. Oligomers such as heptamers promote Fano resonance owing to electromagnetic coupling within the particles without breaking the symmetry of the system, because the dark and bright modes are not completely orthogonal in Oligomers.[11,14] Notwithstanding earlier work done in this field, different types of metal nanoparticles need to be studied to ascertain the factors that control and influence Fano resonance in these systems. Therefore, we explore herein the Fano behavior of the plasmonic crystal cavity formed in silver ellipsoidal nanoparticles and its cylindrical counterpart. We report an enhancement and shape dependence of the asymmetric Fano line shape and the observation of higher harmonic generation (HHG), which leads to ultrahigh transmission. Further, the power dependence of the Fano line shape was shown to be suitable for switching applications and the influence of transverse electric (TE) and transverse magnetic (TM) polarization on the Fano resonance profile was investigated. The study was conducted using a scattering model along with the finite difference time domain (FDTD) method.

II. SCATTERING MODEL FOR SILVER ELLIPSOIDAL AND CYLINDRICAL PLASMONIC CRYSTAL

We observed remarkable enhancement in asymmetric Fano resonance line shape, exhibited by the nanocavity introduced in hexagonally arranged ellipsoidal silver nanoparticles [see Figure 1 inset (iii)] as compared to cylindrical silver nanorods (CSNs). We have used the following scattering model to validate this observation.

Particles having ellipsoidal shape are smooth with no edges or corners which result into in-phase scattering of incident light unlike that of their cylindrical counterparts. The surface of an ellipsoid is defined by the following standard equation:

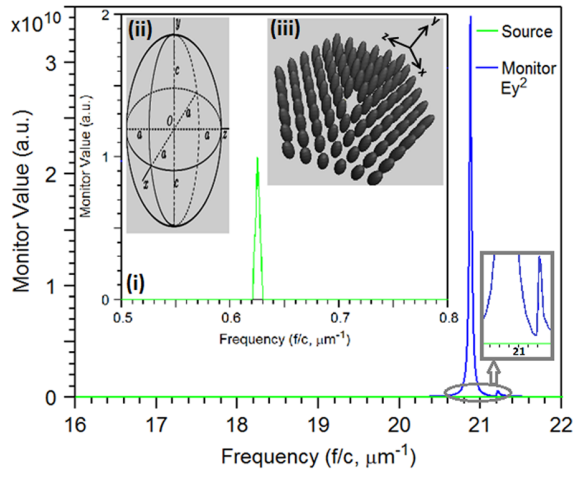

FIG. 1. Cavity response of hexagonally arranged ESN, the zoomed out illustration shows the asymmetry in the output response. Inset (i) displays the symmetric input source profile; inset (ii) presents the semi-axes "a," "b," and "c" of the ellipsoid and inset (iii) presents cavity in the hexagonal arrangement of the silver ellipsoids.

$$\frac{x^2}{a^2}+\frac{y^2}{b^2}+\frac{z^2}{c^2}=1, \tag{3}$$

where a, b, and c are the semi-principle axes of the ellipsoid in Cartesian coordinates (x, y, z) system.[15] However, ellipsoidal coordinates (ξ, η, ζ) are preferred to determine the dipole moment and potential of an ellipsoidal particle in a uniform electric field. Therefore the surface of an ellipsoid in ellipsoidal coordinates (ξ, η, ζ) is defined as

$$\frac{x^2}{a^2+\xi}+\frac{y^2}{b^2+\xi}+\frac{z^2}{c^2+\xi}=1, \quad -c^2<\xi<\infty \tag{4a}$$

$$\frac{x^2}{a^2+\eta}+\frac{y^2}{b^2+\eta}+\frac{z^2}{c^2+\eta}=1, \quad -b^2<\eta<-c^2 \tag{4b}$$

$$\frac{x^2}{a^2+\zeta}+\frac{y^2}{b^2+\zeta}+\frac{z^2}{c^2+\zeta}=1, \quad -a^2<\zeta<-b^2. \tag{4c}$$

Also to any point (x, y, z) in Cartesian coordinates, there corresponds one set of ellipsoidal coordinates (ξ, η, ζ) which determine eight points, symmetrically located in each of the octants as given below[15]

$$x^2=\frac{(a^2+\xi)(a^2+\eta)(a^2+\zeta)}{(b^2-a^2)(c^2-a^2)}, \tag{4d}$$

$$y^2=\frac{(b^2+\xi)(b^2+\eta)(b^2+\zeta)}{(a^2-b^2)(c^2-b^2)}, \tag{4e}$$

$$z^2=\frac{(c^2+\xi)(c^2+\eta)(c^2+\zeta)}{(a^2-c^2)(b^2-c^2)}. \tag{4f}$$

Now, for a homogeneous ellipsoid placed in a uniform electric field aligned along z-axis, the potential Φ has symmetric properties as shown below

$$\Phi(x,y,z)=\Phi(-x,y,z)=\Phi(x,-y,z)=\Phi(-x,-y,z)$$

and

$$\Phi(x,y,-z)=\Phi(-x,y,-z)=\Phi(x,-y,-z)=\Phi(-x,-y,-z). \tag{5a}$$

Therefore, potential in only two octants having positive and negative z values is to be considered with the required condition that potential and its derivative are continuous on the plane $z=0$. So, we choose the octant in which the value of x, y, z is positive. Let Φ_0 denote the potential due to the external field E_0, whereas Φ_1 and Φ_2 denote the potential inside and outside the ellipsoid, respectively. Further, let Φ_p be the perturbing potential caused by the ellipsoid. Then, Φ_2 can be expressed as the superposition of Φ_0 and $\Phi_{p,}$ with Φ_0 given as

$$\Phi_0=-E_0\left[\frac{(c^2+\xi)(c^2+\eta)(c^2+\zeta)}{(a^2-c^2)(b^2-c^2)}\right]^{1/2}. \tag{5b}$$

At sufficiently large distance from the ellipsoid the perturbing potential Φ_p is negligible and we observe that when $\xi \gg a^2$ the limit,

$$\lim_{\xi\to\infty}\Phi_p = 0. \tag{5c}$$

Also, it is required that at the boundary of the ellipsoid, the potential should be continuous

$$\Phi_1(0,\eta,\zeta) = \Phi_0(0,\eta,\zeta) + \Phi_p(0,\eta,\zeta). \tag{5d}$$

Hence, the Laplace's equation to accurately describe the electric potential Φ in ellipsoidal coordinates is obtained and given as follows:

$$\begin{aligned}\nabla^2\Phi = {} & (\eta-\zeta)f(\xi)\frac{\partial}{\partial\xi}\left\{f(\xi)\frac{\partial\Phi}{\partial\xi}\right\} \\ & + (\zeta-\xi)f(\eta)\frac{\partial}{\partial\eta}\left\{f(\eta)\frac{\partial\Phi}{\partial\eta}\right\} \\ & + (\xi-\eta)f(\zeta)\frac{\partial}{\partial\zeta}\left\{f(\zeta)\frac{\partial\Phi}{\partial\zeta}\right\} = 0,\end{aligned} \tag{5e}$$

where Φ is the scalar potential and expression f is defined for a variable q as

$$f(q) = \left\{(q+a^2)(q+b^2)(q+c^2)\right\}^{1/2}. \tag{5f}$$

Now in order to solve the Laplace's equation (5e), using Eq. (5b) we assumed that the potentials Φ_1 and Φ_p are of the form

$$\Phi(\xi,\eta,\zeta) = F(\xi)\left\{(c^2+\eta)(c^2+\zeta)\right\}^{1/2} \tag{5g}$$

and it follows from Eq. (5e) that the function $F(\xi)$ satisfies the ordinary differential equation,

$$f(\xi)\frac{d}{d\xi}\left\{f(\xi)\frac{dF}{d\xi}\right\} - \left(\frac{a^2+b^2}{4}+\frac{\xi}{2}\right)F(\xi) = 0, \tag{5h}$$

yielding a solution of the form

$$F_1(\xi) = (c^2+\xi)^{1/2}, \tag{5i}$$

which is verified by substituting it in Eq. (5h) and follows from the fact that Eq. (5b) satisfies the Laplace's equation (5e).

A second linear independent solution to Eq. (5h) is obtained by integrating Eq. (5i),

$$F_2(\xi) = F_1(\xi)\int_\xi^\infty \frac{dq}{F_1^2(q)f(q)}, \tag{5j}$$

with the property $\lim_{\xi\to\infty}F_2(\xi) = 0$.

The function F_1 is not compatible with the required condition given in Eq. (5c); therefore, the perturbing potential of the ellipsoidal particle is given as

$$\boldsymbol{\Phi_p}(\boldsymbol{\xi},\boldsymbol{\eta},\boldsymbol{\zeta}) = \boldsymbol{C_2F_2}(\boldsymbol{\xi})\left\{(\boldsymbol{c}^2+\boldsymbol{\eta})(\boldsymbol{c}^2+\boldsymbol{\zeta})\right\}^{1/2} \tag{5k}$$

and for the potential inside the particle to be finite at the origin, we must have

$$\boldsymbol{\Phi_1}(\boldsymbol{\xi},\boldsymbol{\eta},\boldsymbol{\zeta}) = \boldsymbol{C_1F_1}(\boldsymbol{\xi})\left\{(\boldsymbol{c}^2+\boldsymbol{\eta})(\boldsymbol{c}^2+\boldsymbol{\zeta})\right\}^{1/2}, \tag{5l}$$

where C_1 and C_2 are constants. Therefore, we get the field inside the particle to be uniform and aligned parallel to the applied field.

The boundary condition given in (5d) yields an equation in constants C_1 and C_2 as mentioned below

$$C_2\int_0^\infty \frac{dq}{(c^2+q)f(q)} - C_1 = \frac{E_0}{\left\{(a^2-c^2)(b^2-c^2)\right\}^{1/2}}. \tag{5m}$$

And the requirement that the normal component of the displacement vector be continuous at the boundary of the particle and the medium yields the second equation,

$$\begin{aligned}&\varepsilon_m C_2\left[\int_0^\infty \frac{dq}{(c^2+q)f(q)} - \frac{2}{abc}\right] - \varepsilon_1 C_1 \\ &\quad = \frac{\varepsilon_m E_0}{\left\{(a^2-c^2)(b^2-c^2)\right\}^{1/2}}.\end{aligned} \tag{5n}$$

This gives us the required potential inside and outside the particle as follows:

$$\Phi_1 = \frac{\Phi_0}{1+\dfrac{L_3(\varepsilon_1-\varepsilon_m)}{\varepsilon_m}}, \tag{5o}$$

$$\Phi_p = \Phi_0\frac{\dfrac{abc}{2}\dfrac{(\varepsilon_m-\varepsilon_1)}{\varepsilon_m}\displaystyle\int_\xi^\infty \frac{dq}{(c^2+q)f(q)}}{1+\dfrac{L_3(\varepsilon_1-\varepsilon_m)}{\varepsilon_m}}, \tag{5p}$$

where

$$L_3 = \frac{abc}{2}\int_0^\infty \frac{dq}{(c^2+q)f(q)}. \tag{5q}$$

Equations (5o) and (5p) give the potential at all points in space and is a consequence of the particle symmetry.

In a similar way, the solution for potential inside and outside the cylindrical particles can be obtained at all points in space. The details have been exhaustively given in Bohren and Huffman[15] which also describes the polarizability tensor and the scattering matrix. It is inferred from the scattering matrix that scattering is attributed to the particles which are not spherically symmetric and an ellipsoid can be easily approximated to sphere for a = b = c, unlike cylinders.[15] Therefore, ellipsoidal particles are more likely to result into in-phase scattering as compared to cylindrical particles.

The inference of the scattering model discussed above is that the shapes of the particles have noteworthy influence on the scattered waves. The resultant wave scattered in a given direction by a particle is due to the interference of the scattered waves from the entire volume. Thus we conclude that the maximum scattered intensity is obtained when angle between the scattering surface and the incident field is small.

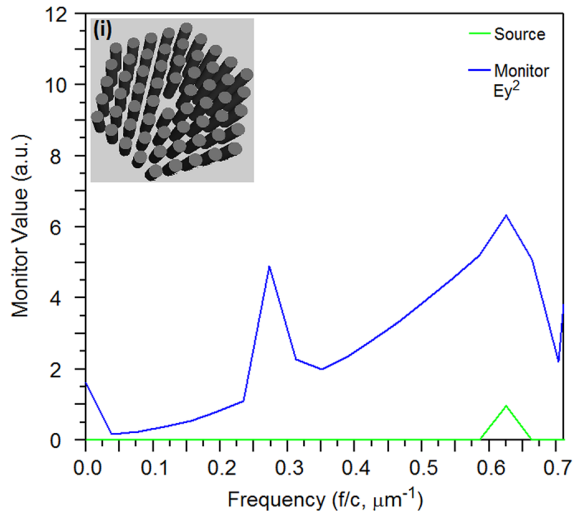

FIG. 2. Cavity response of hexagonally arranged CSN with inset (i) presenting the arrangement of the cylindrical nanorods.

With this qualifier, we compare and study the in-phase scattering in ellipsoidal geometry vis-à-vis cylindrical geometry.

III. FDTD METHOD

Maxwell's equations are solved to obtain resultant electromagnetic field for a plasmonic system, as usually followed for the photonic structures. Mie scattering theory is often used for providing rigorous solution for the Maxwell's equation for spherical nanoparticles, but to model non-spherical geometries and nanostructures of different shapes, FDTD method is employed. This method helps in evaluating the electromagnetic fields within a given structure as a function of time, in a finite domain, on a spatial grid. As our structure comprises of nanorod geometry, we have applied three-dimensional FDTD computational method to numerically assess the temporal evolution of electromagnetic field. The FDTD simulations were performed using perfectly matched layer (PML) boundary conditions with PML width of 200, 500, and 175 nm and average grid size of 25.0, 62.5, and 20.0 nm along the x, y, and z axes, respectively.

IV. STRUCTURE

We considered hexagonally-arranged prolate ellipsoids with axes $a = b = 130$ nm, and $c = 500$ nm (with a dielectric constant $\varepsilon = \varepsilon_i + i\varepsilon_r = -110.143 + 8.807i$, corresponding to the input wavelength of 1600 nm). The background index (n) was 1 and ε varies with the wavelength. The ellipsoids were arranged to have a semi-axis c oriented along the vertical plane of the cavity located at the center of the plasmonic crystal [see Figure 1, inset (ii)]. This arrangement increases the coherent electromagnetic coupling within the particles that interferes destructively with the cavity mode resulting in Fano resonance. We used the technique of adding identical ellipsoidal silver nanoparticles with periodicity of 400 nm. This leads to the formation of large clusters, which creates dark modes that intensify the Fano resonance.[16] The extinction properties and transmission characteristics of the cavity were then explored. The dependence of the Fano line shape on the shape of the nanoparticles is discussed and compared for ellipsoidal silver nanorods (ESN) and CSNs. We assess the important observation of distinct wavelength bands sustaining Fano resonance in the ESN cavity and report the application of switching in the proposed geometry. We further examine the effect of light polarization on the line shape of Fano resonance, taking into account TE and TM polarized light.

V. RESULTS AND DISCUSSION

A. Ultrahigh transmission in the ellipsoidal silver nanorod cavity

The asymmetry observed in the response of the cluster results from the introduction of the nanocavity and the characteristic ellipsoid shape. The output can be tuned from the visible to the IR regime of the electromagnetic spectrum. The asymmetric line shape of the observed plasmonic Fano resonance can be described by a general formula based on Maxwell's equation derived by Gallinet and Martin,[18] which includes the contribution of electromagnetic interactions

$$\sigma_a(\omega) = \frac{\left(\frac{\omega^2 - \omega_a^2}{2W_a\omega_a} + q\right)^2 + b}{\left(\frac{\omega^2 - \omega_a^2}{2W_a\omega_a}\right)^2 + 1}, \tag{6}$$

where ω_a is the resonance frequency, W_a is the spectral width in frequency units, q is the asymmetry parameter, and b is the damping parameter. This equation describes Fano resonance for lossy materials in defined plasmonic nanostructures.

We first examined the response of a cavity introduced in CSNs with a hexagonal arrangement [Figure 2 inset (i)] using the FDTD method for scattered waves, which was successfully employed by Powell *et al.* for controlling the scattering of plasmonic nanoparticles.[19] We now compare these results with those obtained from the cavity in the ESNs [Figure 1 inset (iii)] using the 3D FDTD computational

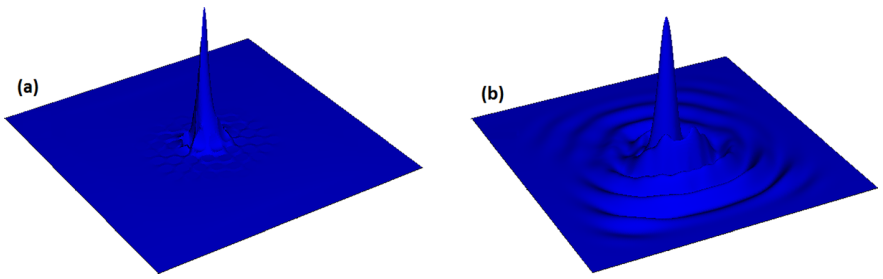

FIG. 3. 3D contour plot of the field distribution in the cavity formed in (a) ESN and (b) CSN.

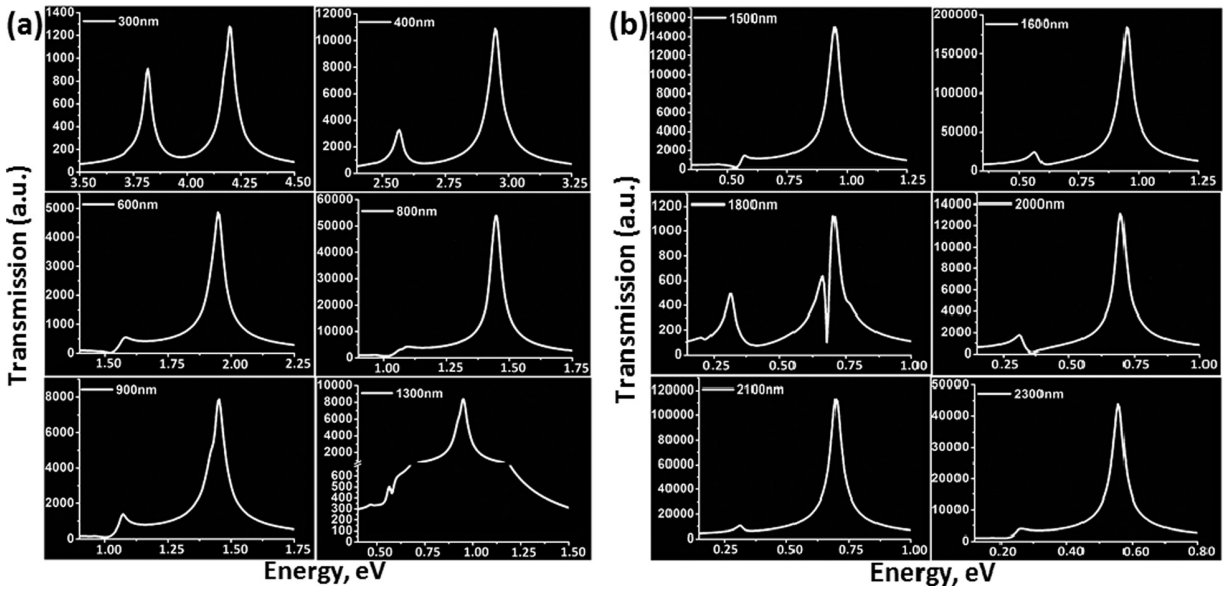

FIG. 4. (a) and (b) Transmission characteristics (1-Extinction; for normalized output) of the ESN cavity for different input wavelength presenting the variation in Fano lineshapes.

method. In both cases, asymmetric output curves are observed (blue curves in Figures 1 and 2), in contrast to the symmetric source profile shown as the green curves in Figure 1 (inset (i)) and Figure 2. These output asymmetric curves represent the unique characteristic of Fano resonance.

Now, we define the transmission $T = 1 - E$, where T is the transmission and E is the extinction, which includes losses due to absorption A and scattering S of the cavity. It is observed that the transmission in the case of ESNs is extraordinarily high (Figure 1) in comparison to CSN (Figure 2). This ultrahigh transmission can be attributed to the geometry of ESNs, the cross-sectional area ($\sigma_{\text{prolate ESN}} = \pi a^2$) of which varies smoothly as semi-axis $a = b$ decreases gradually from $a = a_{\max}$ to $a = 0$ and semi-axis c varies from $c = 0$ to $c = c_{\max}$. This is in contrast to the sudden boundary change in the case of CSNs at $c = c_{\max}$, which causes extreme scattering losses. The absorption losses are negligible in both cases, thereby making scattering the main factor that contributes to the extinction. Therefore, these observations validate the distinct shape enhancement of the asymmetric line shape of Fano resonance in ESNs, in contrast to CSNs, due to the interference of the superradiant bright cavity mode and the subradiant dark mode. This is also evident in the 3D contour plots of the field distribution in the cavities formed in ESNs and CSNs [see Figures 3(a) and 3(b)]. We studied the transmission characteristics of the ESN nanocavity extensively for input wavelengths ranging from the ultraviolet to infrared domains of the electromagnetic spectrum, to

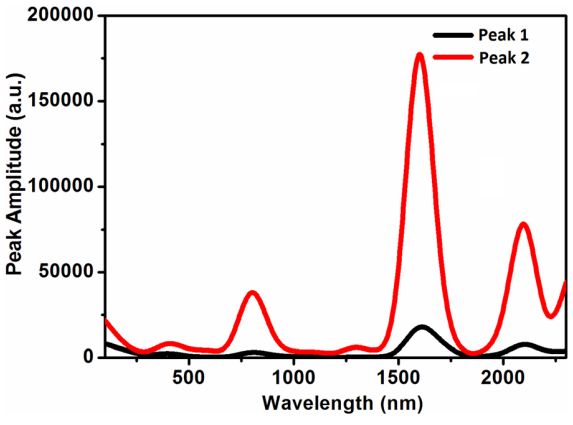

FIG. 5. Spectral variation of peak amplitude for the ESN cavity highlighting switching application.

TABLE I. Peak amplitude values obtained for peaks 1 and 2.

Wavelength (nm)	Peak 1 (a.u.)	Peak 2 (a.u.)
100	8195.91	21637.04
200	4150.61	6232.61
300	910.58	1277.39
400	3284.35	10887.45
500	534.00	4001.24
600	551.93	4861.58
700	231.15	1519.85
800	4238.18	54694.67
900	1382.95	7869.13
1000	716.09	2776.31
1100	414.84	3917.64
1200	332.44	1322.46
1300	502.39	8409.09
1400	332.27	1248.81
1500	1412.12	15042.29
1600	23699.73	184840.60
1700	9740.62	29054.09
1800	631.10	1120.83
1900	758.33	2368.74
2000	1758.96	13138.58
2100	10367.99	113064.20
2200	3028.58	3360.73
2300	3861.49	43866.16

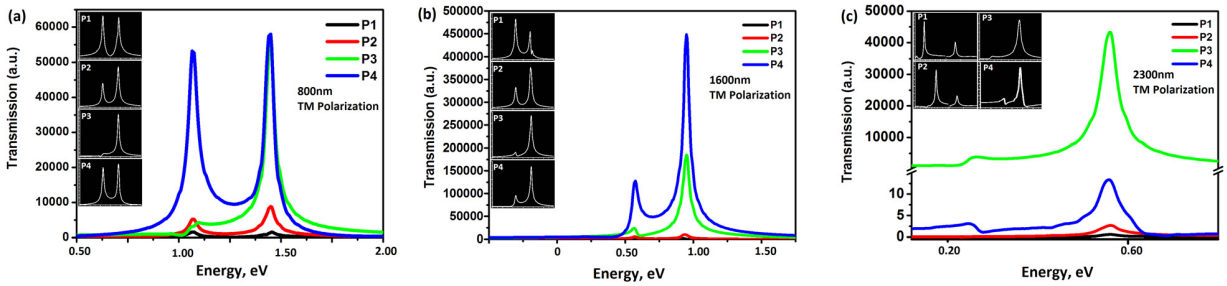

FIG. 6. (a), (b), and (c) Power dependence of Fano lineshapes showing the adaptation of resonance profile with varying input power. TM polarization establish strong mutual coupling resulting in distinct Fano profile.

determine the decisive and controlling parameters in this system. Characteristic Fano curves are obtained for different input wavelengths, as shown in Figures 4(a) and 4(b). These curves reveal interesting behavior of the ESN cavity: as the input wavelength increases, the transmission through the cavity also increases until 800 nm, after which it decreases until 1300 nm. Between 1300 and 1600 nm, there is a steep rise in transmission, which is followed by a fall at 1800 nm and again a rise at 2100 nm. This behavior is discussed in further detail with respect to Figure 5 later in Sec. V B. All the curves are characterized by a short peak (Peak 1) followed by a central peak (Peak 2); these peaks represent the asymmetric Fano profile. The maximum transmittance is obtained at 1600 nm with peak values of 23699.73 and 184840.60 (arbitrary units) for Peak 1 and Peak 2, respectively [see Table I and Figure 4(b)]. This indicates that the considered ESN is suitable for applications in lasing and for plasmon-induced transparency. The peak values obtained in each case are tabulated in Table I and the variation of peak amplitude with wavelength is presented in Figure 5.

B. HHG

The ESN cavity response demonstrated in Figure 5 reveals bands which reflect significant Fano resonance centered at $\lambda_1 = 800$ nm, $\lambda_2 = 1600$ nm, and $\lambda_3 = 2100$ nm. Upon closer inspection, these central wavelengths reveal an important result. The peak wavelengths of the second and third bands (λ_2 and λ_3) are exactly twice and approximately three times that of the first band (λ_1). The formation of bands at regular intervals appears to be related to geometry-dependent nonlinear optical phenomena such as sum/difference frequency generation, that is, frequency mixing processes,[20,21] which lead to significant Fano resonance. Moreover, when we closely analyze the response of the ESN cavity shown in Figure 1, we find that for an input frequency of $1.875 \times 10^8\,s^{-1}$ (corresponding to $0.625\,\mu m^{-1}$; green curve in the inset (i) of Figure 1), the cavity transmits a frequency of $62.7 \times 10^8\,s^{-1}$ (corresponding to $20.9\,\mu m^{-1}$; blue curve in Figure 1). Thus, the output frequency is approximately 33 times the input frequency, confirming the occurrence of HHG[22,23] and the storing of energy at higher frequencies. Therefore, we infer that HHG also contributes to ultrahigh amplification of the input signal in ESNs but not for CSNs (see Figure 2) resulting in the shape-enhanced Fano resonance in ESN cavity.

C. Power dependence and switching application in the ESN cavity

Now we turn our attention to an important application of the power-dependent behavior of the ESN cavity. The difference in the amplitudes of Peak 1 and Peak 2 can be exploited for switching applications. From the curves in Figure 5, we identify three peaks (i.e., 800, 1600, and 2300 nm) suitable for switching applications because of their different peak amplitudes. We varied the input power of the ESN cavity because increasing the power leads to remarkable nonlinear transitions. By varying the power, the line shape of the Fano resonance can also be controlled by enhancing the continuum transition rate to match the saturated discrete level transition.[24] Four different input powers viz. 0.01, 0.1, 1.0, and 10 mW termed P_1, P_2, P_3, and P_4, respectively, were applied in the ESN cavity. The effect of the input power on the transmission spectrum at the wavelengths $\lambda = 800$, 1600, and 2300 nm is shown in Figures 6(a)–6(c), respectively. The ratios of the peak amplitudes, i.e., $\Gamma =$ Peak 2/Peak 1, are summarized in Table II. At 800 nm for power P_1, Peak 1 is larger than Peak 2 (i.e., $\Gamma < 1$) but as the input power is increased to P_2 and above, the amplitude of Peak 1 decreases and the amplitude of Peak 2 increases, such that $\Gamma > 1$. The maximum value of Γ (12.91) is obtained for input power P_3, thereby making this the optimum operating power to achieve maximum switching efficiency in the proposed ESN. The lower switching efficiency for power P_4 may have been due to the power applied to the cavity being exceeding the tolerance limit of the structure. At power P_3, the values of Γ obtained at 1600 and 2300 nm were 7.79 and 11.36, respectively. From these observations we conclude that the best switching capability of the ESN cavity is obtained for a wavelength of 800 nm at a power of 1.0 mW.

TABLE II. Ratio of peak amplitudes $\Gamma =$ Peak 2/Peak 1 for different input power P_1, P_2, P_3, and P_4.

Wavelength (nm)	P_1	P_2	P_3	P_4
800	0.95	1.71	12.91	1.05
1600	0.68	1.80	7.79	3.52
2300	0.43	0.22	11.36	3.85

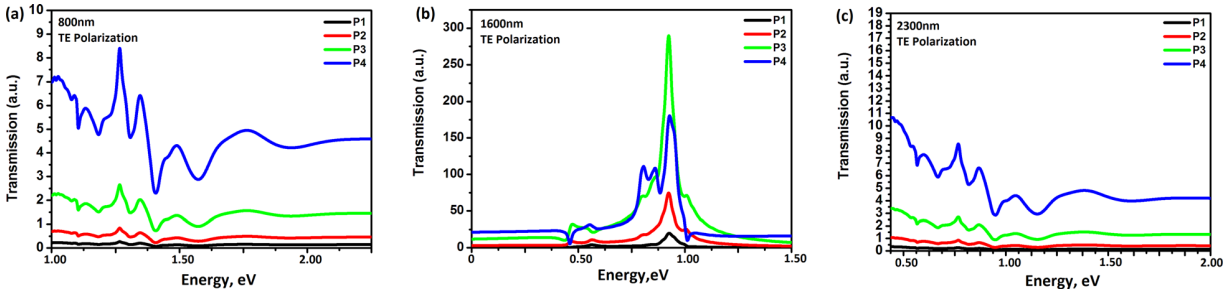

FIG. 7. Effect of TE polarization on the Fano lineshapes validating weak mutual coupling.

D. Effect of polarization

Finally, we discuss the dependence of polarization of the incident light on the line shape of Fano resonance. Plots for TM and TE polarized light at different input powers for $\lambda = 800$, 1600, and 2300 nm are given in Figures 6 and 7, respectively. For TM polarization, the electric field component is parallel to the longitudinal semi-axis "c" of the ellipsoids resulting in the alignment of the charges along the y axis. This, in turn, results in strong mutual coupling of the electrical field components between the ellipsoids and, hence, coherent coupling to the radiation continuum. Accordingly, for TM polarization, well-defined, distinct Fano resonance line shapes are obtained, as illustrated in Figures 6(a)–6(c). However, for TE polarization, the electric field is parallel to the shorter semi-axis "a," which is transverse to the longitudinal direction. This results in weak mutual coupling and multiple random peaks in the transmission response of the cavity, as presented in Figures 7(a)–7(c). These results have therefore demonstrated that the Fano line shape is polarization dependent.

VI. CONCLUSION

We have extensively investigated the Fano resonance in an ellipsoidal nanoparticle cavity. A scattering model was used to gain an understanding of how the structural symmetry controls the in-phase scattering. The FDTD method was used to model and analyze the results. The influence of the ellipsoidal shape on the Fano profile was discussed by means of comparison with its cylindrical counterpart with respect to the spectral interference of superradiant bright and subradiant dark modes. The ESN cavity, which exhibits ultrahigh transmission at 1600 nm because of HHG, can be used for applications in lasing and plasmon-induced transparency. The influence of input power and its application in switching was demonstrated with the maximum efficiency displayed in the visible region. The dependence of Fano line shapes on the light polarization was also assessed. The Fano response of the proposed system revealed that different wavelength regimes are suitable for different applications, thereby highlighting the potential of the ESN cavity in a broad range of applications including lasing, switching, sensing, and design of surface plasmon polariton-based filters.

ACKNOWLEDGMENTS

We greatly acknowledge the initiative and support towards establishment of TIFAC—Center of Relevance and Excellence in Fiber Optics and Optical Communication at Delhi College of Engineering now Delhi Technological University, Delhi through Mission Reach Program of Technology Vision 2020, Government of India.

[1]U. Fano, Phys. Rev. **124**, 1866 (1961).
[2]B. Lukyanchuk, N. I. Zheludev, S. A. Maier, N. J. Halas, P. Norlander, H. Geissen, and C. T. Chong, Nature Mater. **9**, 707 (2010).
[3]A. E. Miroshnichekno, S. Flach, and Y. S. Kivshar, Rev. Mod. Phys. **82**, 2257 (2010).
[4]M. Sarrazin, J. P. Vigneron, and J. M. Vigoureux, Phys. Rev. B **67**, 085415 (2003).
[5]A. C. Johnson, C. M. Marcus, M. P. Hanson, and A. C. Gossard, Phys. Rev. Lett. **93**, 106803 (2004).
[6]K. Kobayashi, H. Aikawa, A. Sano, S. Katsumoto, and Y. Iye, Phys. Rev. B **70**, 035319 (2004).
[7]S. Fan and J. Joannopoulos, Phys. Rev. B **65**, 235112 (2002).
[8]A. Christ, S. Tikhodeev, N. Gippius, J. Kuhl, and H. Giessen, Phys. Rev. Lett. **91**, 183901 (2003).
[9]H. Lee and A. W. Poon, Opt. Lett. **29**, 5 (2004).
[10]A. Christ, O. J. F. Martin, Y. Ekinci, N. A. Gippius, and S. G. Tikhodeev, Nano Lett. **8**, 2171 (2008).
[11]J. A. Fan, C. Wu, K. Bao, J. Bao, R. Bardhan, N. J. Halas, V. N. Manoharan, P. Norlander, G. Shvets, and F. Capasso, Science **328**, 1135 (2010).
[12]N. Verellen, Y. Sonnefraud, H. Sobhani, F. Hao, V. V. Moshchalkov, P. Van. Dorpe, P. Norlander, and S. A. Maier, Nano Lett. **9**, 1663 (2009).
[13]F. Hao, Y. Sonnefraud, P. Van. Dorpe, S. A. Maier, N. J. Halas, and P. Norlander, Nano Lett. **8**, 3983(2008).
[14]B. Gallinet and O. J. F. Martin, ACS Nano **5**, 8999–9008 (2011).
[15]C. F. Bohren and D. R. Huffman, "Absorption and Scattering of Light by Small Particles" (Wiley-Interscience Publications, 1983).
[16]J. A. Fan, K. Bao, C. Wu, J. Bao, R. Bardhan, N. J Halas, V. N. Manoharan, G. Shvets, P. Norlander, and F. Capasso, Nano Lett. **10**, 4680 (2010).
[17]D. Wu, S. Jiang, and X. Liu, J. Phys. Chem. C **116**, 13745–13748 (2012).
[18]B. Gallinet and O. J. F. Martin, Phys. Rev. B **83**, 235427 (2011).
[19]A. W. Powell, M. B. Wincott, A. A. R. Watt, H. E. Assender, and J. M. Smith, J. Appl. Phys. **113**, 184311 (2013).
[20]S. Baldelli, A. S. Eppler, E. Anderson, Y. Shen, and G. A. Somorjai, J. Chem. Phys. **113**, 5432–5438 (2000).
[21]O. Levi, T. J. Pinguet, T. Skauli, L. A. Eyres, K. R. Parameswaran, J. S. Harris, M. M. Fejer, T. J. Kulp, S. E. Bisson, B. Gerard, E. Lallier, and L. Becouarn, Opt. Lett. **27**, 2091 (2002).
[22]S. Kim, J. Jin, Y. Kim, I. Park, Y. Kim, and S. Kim, Nature **453**, 757 (2008).
[23]A. Husakou and J. Herrmann, Phys. Rev. A **83**, 043839 (2011).
[24]M. Kroner, A. O. Govorov, S. Remi, B. Biedermann, S. Seidl, A. Badolato, P. M. Petroff, W. Zhang, R. Barbour, B. D. Gerardot, R. J. Warburton, and K. Karrai, Nature **451**, 311 (2008).

Journal of Energy Technologies and Policy
ISSN 2224-3232 (Paper) ISSN 2225-0573 (Online)
Vol.3, No.12, 2013

Hybrid Micro Grid Systems - Drivers & Challenges

Palak Kalra
Department of Electrical Engineering, Delhi Technological University
(formerly known as Delhi College of Engineering) New Delhi, India
Palak.kalra1311@gmail.com

Abstract
Increasing environmental concerns, consumer expectations in terms of reliability & better quality of power supply and improving economics of distributed energy resources (DER) based on renewable, is making Micro Grid a viable proposition. Hybrid Micro grid utilising diversity of various energy resources including Wind, Solar, Biomass, and Energy Storage Batteries is found to be a better solution than single source Micro grid system. However, integration of multiple resources poses many issues & challenges. Moreover, present distribution system offers many technical & operational glitches for successful integration of Micro Grid Technologies. Paper addresses such challenges, issues and solutions. The Micro Grid resources optimization is generally being done based on self-sufficiency criterion which utilizes the grid support only in the event of contingencies like fault, generation disruptions (DER) etc. Paper also discusses various resources optimization techniques to serve the net load requirements in all time of the Day (TOD).
Keywords: Distributed Energy, Black Start, net load, Islanding, MGCC, PSO, Genetic Algorithm

1. Introduction

The growing energy demand in developing nations has triggered the issue of energy security which has made essential to utilise the untapped potential of renewable resources. As a result, the solar photovoltaic and wind generation technologies have made significant progress in the last decade and many megawatt scale solar parks and wind farms have been added to the Grids.

In the view of increasing environmental concerns and consumer expectations in terms of reliability & satisfactory power quality, energy access to farthest located consumers, increasing technical & commercial losses (AT&C) etc. is indicating need of paradigm shift from centralized electricity system to decentralised & distributed electricity system. These challenges give a thrust to Micro grid Concepts. Micro Grid is realised through utilizing the potential of distributed renewable energy resources where various small power systems working as independent "Micro Grids" may be established which can cater to several consumers' loads through small size distributed energy resources. In other means, Micro grids are modern, small-scale version of centralized electricity systems which generates, distributes and regulates the flow of electricity to a set of consumers at the local level itself. From generation point of view, with the advancement of renewable generation technologies, small generating units exploiting renewable sources through Solar PV panels, wind turbines or biomass plants have already been commercialised at distribution level. However, at most of the places Micro Grids are realised through Single resources generation like Solar PV along with Battery Storage systems.

As the renewable resources generally suffers with the limitations of intermittency and variability, use of more than one distributed resource i.e. resource diversity, improves reliability and security of power supply. Thus hybrid Microgrid system is preferred over the use of single resource Microgrid System, but challenge lies in integration of all such resources based generations to meet consumer demand with reliability, security and best of quality.

The hybrid Microgrid may consists of Solar Photovoltaic array (PV), Wind turbine (WT), Biomass Gassifier (BG) and Battery Energy Storage (BES). The figure1 shows grid-interfaced Hybrid Microgrid architecture. In such systems, two types of control i.e. sources control and load control is designed. Source control is achieved primarily through generation control of Biomass Gassifier or Battery energy storage systems which serves as flexible generation whereas Solar PV and Wind, considering its nature of resources, is never controlled or backed down. At the time of supply exceeding demand, flexible resources like Biomass is asked to back down/shut down and balance excess energy is used to charge the batteries for utilisation in times of lower generation by other resources like Wind/Solar. Thus energy storage batteries provide an economical and/or logistical advantage by making better use of off-peak hours to supply the daily energy needs in peak hours. In case of demand exceeding the generation, batteries provide immediate power response dynamically to the net load fluctuations as Biomass Gassifier gives comparatively slower responses, but longer duration support. Moreover in case of further deficit, demand side management through Advanced Metering Infrastructure (AMI) controlling consumer non-critical load is achieved. In real terms, design of Microgrid should be based on self-sufficiency criterion that means in normal scenario, energy is not drawn from the main grid. In such concepts, grid interfacing is provided only to support Microgrid in case of contingencies or unforseen eventualities' so that consumers are not deprived off the electricity.

The distributed generators (DG) in Microgrid are generally inverter-based that has very low inertia. Unlike, rotating DGs, the low inertial inverter based DGs have tendency to respond very quickly causing large transients. These transients of high magnitude are not favourable for stable operation of Microgrid. However, due to their fast response, the inverter based sources ensure the supply of dynamic load regardless of slow rotating machines which requires seconds of response time to transients [11]. Therefore, this aspect needs to be taken care while designing architecture of Microgrid.

Considering different characteristics of various distributed resources, their optimal sizing & selection requires judicious choices based on techno-economic considerations. The choices of DGs are based on case to case basis which also require detailed study of historical data of resource availability of Wind/Solar. However, the unit sizing/optimisation is done by various optimisation methodologies which are discussed in section II. In section III, the paper outlines some technical and operational challenges for Microgrid interface into present power system.

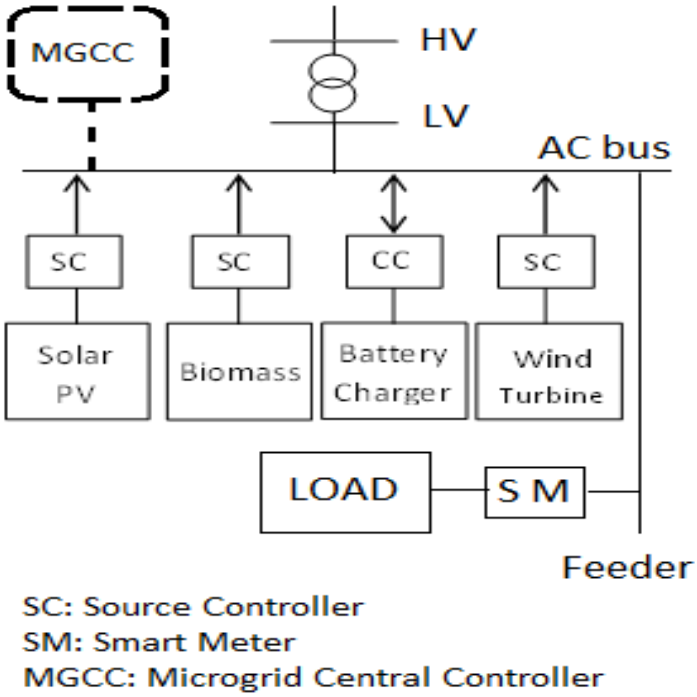

Fig. 1 Grid-interfaced Microgrid architecture

2. Resources optimization techniques

Resource optimisation is carried out with objective of fitting the load curve at any point of time which means providing reliable power supply to the consumers all the time of the day. Apart from technical considerations, economical aspects including capital cost as well as operation cost of DGs is also given due weightage.

For standalone hybrid system, typical tangent method is used to fix size of wind generator, PV panels and the capacity of the battery [1]. Recently, various optimization methodologies are being exploited for unit sizing in Microgrid system. In research work by Xu et al, the Genetic Algorithm (GA) has been used to optimize the size of PV panels, wind generator and capacity of battery. In some research works, Evolution strategy and Particle Swarm Optimisation (PSO) techniques have also been used to arrive at minimum cost [3, 4]. The references [1, 2] show GA technique provides better performance as compared to other literature. These optimization methods need mathematical formulation of non-linear cost minimising objective function and constraints achieving certain reliability conditions.

3. Technical hallenges

Microgrid, as a new field of research, is in the evolutionary stage. Many pilot projects have been tested in laboratories worldwide but very few have been replicated in the field. In field, apart from technical challenges, regulatory barriers are also present which makes commercialization of Microgrid model implementation quite difficult then as imagined [5].

In Micro Grid System, the Microgrid Central Controller (MGCC) resides at the centre of Microgrid architecture, acting as a brain of the entire system. MGCC monitors and controls the operations over SCADA network

utilising Information and Communication Technologies (ICT). MGCC facilitates all the functions of Sources as well as Load control to achieve load-generation balance all the time.
However to improve reliability, the Microgrid system is grid interfaced even if the unit sizing of distributed generations large enough to make Microgrid system autonomous. As a result, the increased flexibility in grid interfaced Microgrid architecture using advanced features of the Information and Communication Technologies (ICTs) for controls and operations creates huge complexities and technical challenges in the Microgrid system. Moreover, Micro Grid being much weaker in terms of short circuit strength, as compared to conventional grid, any parameter variation may lead to have big impact on health of the system.
The intentional islanding required in grid interfaced Microgrid system requires DGs to operate in dual mode of operations i.e. PQ mode and PV mode. The hybrid system having DGs located at different locations must also be equipped with black start capability. The fault current observed in the system also varies with grid-tied and off-grid conditions which makes the protection strategy for Microgrid architecture to be different from one in present power system. Given these limitations and requirements in Microgrids, the three major technical challenges are identified in Microgrid systems which are discussed as under:

4. Operation support in Grid tied and islanded conditions

In grid-tied condition, the DG has to work in PQ mode where the source controller of DG controls the output current. In this condition, Voltage and frequency of Micro grid is governed by grid parameters and therefore DGs have to follow the Superior Grid. In islanded condition, when the Microgrid is in isolated state from the utility grid, DG has to transition in PV mode controlling Voltage & frequency of its own autonomous mode. In hybrid system, where more than one DG is present, all DGs are operated in parallel in master-slave configuration. A Microgrid following master-slave strategy needs only one energy source to operate in PV mode when utility grid is absent. However, the master slave configuration makes all other DGs dependent on a single source acting as master. The highly centralized controlled system is always vulnerable because in case the master fails, the whole Microgrid could suffer collapse. The solution is to make other DGs also capable of taking over the role of master in such situations. The transition between the modes is needed to be seamless in order to improve the quality of power supply. The Microgrid system consists of two types of DGs: inverter-based DGs and rotational-machine-based DG. The Inverter based DG has low output impedance and can change between modes – current and voltage modes very fast but produces large transients during mode transfer [6]. However, the rotational-machine-based DGs balance the voltage and to adjust current sharing, by using droop control method. Therefore, the challenge is to operate hybrid system with inverter based DGs by utilising fast inverters while avoiding large transients during mode transfer.

5. Black start capability

Black start phenomenon is to start the Microgrid system from complete shutdown state. It is a challenging task to black start a Microgrid system because it requires complete analysis of system's state. Moreover start of DGs and connection of loads requires certain procedure to be followed. It involves step-by-step connection of DGs and loads to the LV grid on the basis of overload capacity. However, in comparison to conventional power restoration, the Microgrid restoration process is much simpler due to reduced number of variables (switches, DGs, and loads) [6].
The capability of black start is needed in remote areas where utility grid is absent and where utility grid outages are very frequent.
In Microgrid system, bottom-up approach to black start is more preferred as it reduces the restoration times [6]. The MGCC equipped with black start software plays central role by registering conditions of system and following a set of rules during the restoration period. The rules and conditions define a sequence of control actions to be carried out.
The DGs in Microgrid system always need reference voltage and frequency to operate. So, DG acting as master needs to produce reference voltage and frequency for other DGs must be present. The bottom-up approach includes building up of low voltage network, connecting DG, controlling voltage and frequency, connecting controllable loads and MG synchronization with upstream grid, when it is available, in sequence.

6. Protection strategy

The protection scheme of Microgrid is much more complex and challenging than conventional power system because of the requirements of both grid-interfaced and grid-isolated modes in Microgrid and also, the existence of the two types of faults - internal and external faults. The need of differentiation between the types of faults demands the formulation of overall new protection strategy for the Microgrids. The Microgrid system has load current/fault current ratio smaller in comparison to the conventional system [6]. The conventional power systems comprising of synchronous generators provide large fault currents that are helpful for fast and efficient fault

protection. Whereas, the inverter based DG can provide fault current up to only two –three times the rated current which is insufficient when fault is in upstream network. For this, it needs oversizing of inverters but it is not a preferred option due to economic reason. If the protective relay designed for small fault currents has to satisfy the Microgrid operation, this might lead to nuisance tripping. To avoid this problem, following protection strategies are under research for Microgrid.

Adaptive protection schemes which can change relay settings in real time [10]. This would ensure the protection of Microgrid but it requires very fast communication network. The other way is to design Microgrid to enter it in island mode before any protection action could take place in response to an internal fault [5]. This strategy would eliminate the need of adaptive relay setting but it creates heavy dependence on correct and timely opening of Point of Common Coupling (PCC) switch. The malfunctioning of communication link to PCC might lead to selectivity issue of nuisance tripping from internal protection devices in response to an external fault. So, neither of these two solution appears to be the direct solution to protection of Microgrid.

However, the protection scheme using differential relays in place of overcurrent relay is seen by many researchers to be a more promising solution [8]. The difference between the two transformers across the device passing through the relay, when get exceeds a certain threshold value, the line gets tripped. Under this scheme, the fault location identification with different fault types (earth fault, phase to phase fault, etc.) and the line fault differentiation from DG faults can be achieved. The differential relays show highest selectivity and operate only for internal faults but they also require reliable communication for instantaneous data transfer between terminals of the protected element.

Although Differential relay scheme is suitable scheme to Microgrids but differential relays are too costly to deploy for all equipment. The differential relays are generally used to protect important piece of equipment such as distributed generators and transformers [9]. So, any single scheme will not address the protection system requirement of Microgrid. It should be mix of at least two of above proposed to improve the reliability of operation keeping as low as possible. One common requirement of almost all protection mechanism is a high speed communication network to enable the communication of devices with each other and determine the location of fault and nature of the fault.

The limitation of overcurrent relays in Microgrid and high cost associated with differential relays has opened scope for voltage based protection mechanism in Microgrid. The voltage based protection relays trips in the case of overvoltage and under voltage scenario.

7. Conclusions

The paper investigates technical & operational challenges and probable solutions for Hybrid Microgrid systems comprising various distributed energy resources. The load -generation balance in such system is achieved through Source control as well as Load control through AMI solutions. Various algorithms can also be used towards resource optimization for evolving best solutions based on techno-economic considerations.

8. References

[1] T. Logenthiran, D. Srinivasan, A. M. Khambadkone and T. Sundar Raj, “Optimal Sizing of an Islanded Microgrid Using Evolution Strategy” in IEEE Conference, 2010, p. 12-17

[2] S. M. M. Tafreshi, H. A. Zamani, M. Baghdadi and H. Vahedi. “Optimal Unit Sizing of Distributed Energy Resources in Microgrid Using Genetic Algorithm”, ” in IEEE Conference, 2010, p. 836 – 841.

[3] F. Tooryan, S. M. Moghaddas-tafreshi, S. M. Bathaee, and H. Hassanzadehfard, “Assessing the reliable size of Distributed Energy Resources in Islanded Microgrid Considering Uncernainty”, in WREC, 2011, p. 2969 - 2976.

[4] JoydeepMitra, Shahsi B. patra, M. R. Vallem, and S. R. Ranade,”Optimization of Generation and Distribution Expansion in Microgrid Architectures”, in WSEAS Conf. on Power System, 2006 .

[5] L. Tao, C. Schwaegerl, S. Narayanan, and J. H. Zhang, “From Laboratory Microgrid to Real Markets – Challenges and Opportunities”, 8th International Conference on Power Electronics – ECCE Asia, 2011, p. 264 – 271.

[6] Jinwei Li, Jianhui Su, Xiangzhen Yang and Tao Zhao. “Study on Microgrid Ooperation Control and Black Start,” in Power System Conference, 2006, p. 1652 - 1655.

[7] A. A. Salam, A. Mohamed and M. A. Hannan, “Technical Challenges on Microgrid,”*ARPN Journal of Engineering and Applied Sciences,* vol. 03, pp. 64–69, Dec. 2008.

[8] Zeineldin. H.H., El-Saadany E.F. and Salama M.M.A. “Distributed Generation Micro-Grid Operation: Control and Protection,” in Power System Conference, 2006, p. 105 - 111.

[9] *Novel protection systems for Microgrids,* CERTS, 11/11/2009.

[10] A. Oudalov, and A. Fidigatti, “Adaptive Network Protection in Microgrids”.

[11] *Integration of Battery-Based Energy Storage Element in the CERTS Microgrid,* CERTS, 27/10/2009

Label-free detection of cardiac troponin-I using gold nanoparticles functionalized single-walled carbon nanotubes based chemiresistive biosensor

Rajesh, Vikash Sharma, Nitin K. Puri, Rajiv K. Singh, Ashok M. Biradar, and Ashok Mulchanadani

Citation: Applied Physics Letters **103**, 203703 (2013); doi: 10.1063/1.4830223
View online: http://dx.doi.org/10.1063/1.4830223
View Table of Contents: http://scitation.aip.org/content/aip/journal/apl/103/20?ver=pdfcov
Published by the AIP Publishing

Label-free detection of cardiac troponin-I using gold nanoparticles functionalized single-walled carbon nanotubes based chemiresistive biosensor

Rajesh,[1,a)] Vikash Sharma,[1,2] Nitin K. Puri,[2] Rajiv K. Singh,[1] Ashok M. Biradar,[1] and Ashok Mulchanadani[3,b)]
[1]*CSIR-National Physical Laboratory, Dr. K.S. Krishnan Road, New Delhi 110012, India*
[2]*Department of Applied Physics, Delhi Technological University, Bawana Road, Delhi 110042, India*
[3]*Department of Chemical and Environmental Engineering, University of California, Riverside, California 92521, USA*

(Received 21 June 2013; accepted 28 October 2013; published online 13 November 2013)

We report a specific and ultrasensitive, label-free chemiresistive biosensor based on mercaptopropionic acid capped gold nanoparticles (GNP) functionalized single walled carbon nanotube (SWNT) hybrid for the detection of cardiac specific biomarker troponin-I (cTnI). GNPs were attached to SWNTs through a molecular linker 1-pyrenemethylamine. The highly specific cTnI antibody was covalently immobilized on GNPs through capping agent using carbodiimide coupling reaction. The cTnI interaction to its corresponding antibody was studied with respect to changes in conductance in SWNTs channel, and a detailed field-effect transistor characteristic was delineated. The device exhibited a linear response to cTnI from 0.01 to 10 ng ml^{-1}. © *2013 AIP Publishing LLC*.
[http://dx.doi.org/10.1063/1.4830223]

Cardiovascular disease (CVD) is the leading cause of morbidity and mortality worldwide and accounts for approximately half of all the deaths within the western world. Coronary ischemia is the root cause of acute myocardial infarction (AMI). As MI causes irreversible damage to the heart, a patient suspected of MI must be diagnosed quickly, efficiently, and comprehensively based on the information obtained from the readings of the electrocardiogram (ECG) and the measurement of cardiac specific biomarkers within the patient's blood. Hence, cardiac markers continue to play a major role in the diagnosis and management of patients suspected of having myocardial damage or AMI. Previously, the commonly used biomarkers for early detection of CVD included the MB isoenzyme of creatine kinase (CK-MB) and myoglobin.[1,2] However, in the recent years, CK-MB has been replaced by cardiac troponin I (cTnI), a more specific biomarker. cTnI is a subunit of cardiac troponin complex, which is broken up during the myocardial damage, and the individual protein components are released in the blood stream.[3] The cTnI has high tissue specificity and virtually absent in skeletal muscle tissue. cTnI levels are measurable in serum within 4–6 h after the onset of AMI. The serum concentrations peaks at about 12 h, and remain diagnostic for at least 7 days post-AMI,[4,5] hence provides a long window of detection of cardiac injury allowing for reliable point-of-care detection. Therefore, cTnI in the human serum has been considered as the "gold standard" for diagnosis of myocardial injury.[6] Based on literature data and clinical assessments, cTnI levels greater than 0.1 ng/ml places a patient with unstable angina in the high-risk category for short-term risk of death or non-fatal MI. A cut-off value of greater than 1.2 ng/ml is taken as the definition of AMI, making a cut off value of 0.1 ng/ml of cTnI to identify patients at higher risk for very early adverse outcomes. This underlines the need to develop a rapid, sensitive, and cost effective point-of-care device for quantitative detection of cardiac biomarker cTnI for the diagnosis of AMI. Various instrumentation methods[7,8] and diagnostic techniques, including conventional enzyme-linked immunosorbent assay (ELISA)[9] and radioimmunoassay (RIA),[10] are currently used for the detection of cTnI. However, these techniques suffer from disadvantages of long diagnostic time, multiple steps process, and requirement of labeled reagents and bulky instrumentation.

Chemiresistor/field-effect transistor (FET) transducers based on one-dimensional (1-D) nanostructure (nanowire, nanotube, and nanorod) have attracted a great deal of attention because of their superior biosensing performance. The single walled carbon nanotubes (SWNTs) based chemiresistive/FET devices are extremely sensitive to the variant surrounding environment as the electrical current flows through the outermost layer of SWNT which is in direct contact with the analyte. The surface modification of carbon nanotubes (CNTs) with metal nanoparticles (NPs) has recently shown considerable interest from both the fundamental and technological points of view.[11] Gold nanoparticles (GNPs) have a wide range of applications in sensors, biosensors, and many emerging areas of nanotechnology[12–14] due to their electronic, optical, and magnetic properties.

Here, we demonstrate the fabrication of SWNTs/NPs hybrids based nanoelectronic chemiresistive/FET device for the quantitative detection of cTnI. These GNPs capped with 3-mercaptopropionic acid (MPA) are attached to SWNT through an organic molecular bilinker 1-pyrenemethylamine. The capping of MPA provided the carboxyl functional groups for the covalent immobilization of cTnI specific protein antibody, Ab-cTnI, through carbodiimide linkage. This strong bonding together with the high surface-to-volume

a)Electronic mail: rajesh_csir@yahoo.com
b)Electronic mail: adani@engr.ucr.edu

ratio of the GNPs resulted in a sufficiently high loading of Ab-cTnI, which acted as a probe for immunoreaction with the target cTnI. The sensor fabrication, performance, and the sensing mechanism were investigated by the measurement of $I-V$ and FET transfer characteristics.

Anti-cardiac troponin, Ab-cTnI (Cat 4T21 MAb 19C7) and human cardiac troponin I, cTnI (Cat 8T53) were obtained from Hytest (Turku, Finland). Mouse IgG was obtained from Bangalore Genei, India. N-(3-dimethylaminopropyl)-N′-ethyl carbodiimide hydrochloride (EDC), N-hydroxy succinimide (NHS), sodium tetrahydroboride ($NaBH_4$), and MPA were obtained from Sigma-Aldrich Corp. Tetrachloroauric (III) acid ($HAuCl_4$) was obtained from Himedia, Pvt Ltd., India. The SWNTs (SWNT-COOH, 80%–90% purity; bundle diameter: 4–5 nm) were purchased from Carbon Solution, Inc. (Riverside, CA). All the chemicals used were as purchased without further purification.

1.0 μl drop of SWNTs suspended in *N*,*N*-dimethylformamide (DMF) were aligned across a pair of 3 μm apart microfabricated gold electrodes by ac dielectrophoresis by applying an AC voltage at a frequency of 4 MHz and 1.5 V peak-to-peak amplitude. The aligned SWNTs were then annealed at 300 °C for 1 h in an inert flow environment (95% N_2 and 5% H_2). The aligned SWNTs were modified with bilinker, 1-pyrenemethylamine hydrochloride (PyMe-NH_2), by incubation with 6 mM PyMe-NH_2 in DMF, for 2 h, at room temperature, washed with DMF, and dried under N_2 flow. The gold microelectrodes surface of the device was then passivated by incubation with 6 mM 6-mercapto-1-hexanol (MCH) in DMF for 1 h to block the nonspecific binding sites. For making SWNTs/GNPs hybrids, MPA capped GNPs were prepared by a procedure as reported earlier.[15] In brief, 6 mg of $HAuCl_4$ was dissolved in 15 ml ethanol. To this solution, 0.35 mg of MPA was added and the mixture was vigorously stirred for 15 min. After this, a solution containing 5 mg $NaBH_4$ in 10 ml ethanol was added drop wise to the above mixture and left aside for stirring for 1 h. A dark brown colloidal suspension was obtained which was washed with ethanol and centrifuged at 14 000 rpm for 30 min. The black precipitate so obtained was then dried in vacuum and re-dissolved in water to obtain aqueous MPA capped gold solution of desired concentration.

A 0.5 mg ml^{-1} aqueous solution of GNPs (MPA) containing 0.1M EDC and 0.05M NHS was dispensed on PyMe-NH_2 functionalized aligned SWNTs for 2 h, rinsed thoroughly with double distilled water and dried under N_2 flow to obtain the desired GNPs (MPA)/SWNTs hybrids. This was followed by covalent immobilization of antibody, Ab-cTnI, on GNPs (MPA)/SWNTs hybrids by overnight incubation with 100 μg ml^{-1} Ab-cTnI in phosphate buffer solution (PBS; pH 7.4) at 4 °C to obtain the Ab-cTnI-GNP/SWNTs. The device was then repeatedly washed with PBS to remove the unbound protein molecules and dried under N_2 flow. This was further treated with 1.0% bovine serum albumin (BSA) in PBS to block the possible nonspecific binding of target cTnI to residual free carboxyl groups of GNPs, as well as to GNPs and SWNTs in Ab-cTnI-GNPs/SWNTs hybrid. Ab-cTnI-GNPs/SWNTs hybrid FET was formed by using the highly doped silicon substrate as a back gate. The stepwise fabrication process is schematically represented in Fig. 1

The fabrication of the device at each step of surface modification of the aligned SWNTs was monitored by recording the current-voltage (I-V) characteristics from −0.5 V to +0.5 V (Fig. 2(a)) measured on PGSTAT302N, AUTOLAB instrument from Eco Chemie, The Netherlands, connected to a Micromanipulator model 450PM-B probe station that makes electrical contact to the source and drain electrodes. To understand the charge transfer mechanism, corresponding field dependence electron transfer characteristic (FET) study was carried out before and after the chemical and biological modification of the SWNT device in dry conditions. Figure 2(b) shows the dependence of the source-drain current, I_{sd}, on the back gate voltage, V_g, of the SWNTs FET after each surface modification steps in the range −40 to +40 V, at a bias drain voltage (V_d) of 0.1 V measured on a Keithley semiconductor characterization system 2420.

Fig. 2(b) shows a p-type behavior for the pristine SWNT due to the electron withdrawal of adsorbed oxygen molecules

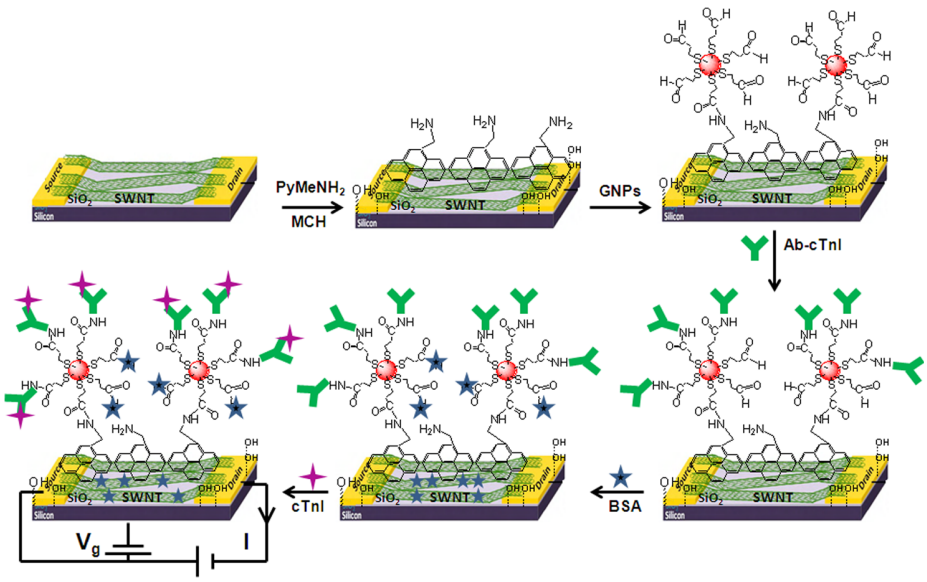

FIG. 1. Schematic illustration of the different stages of device fabrication.

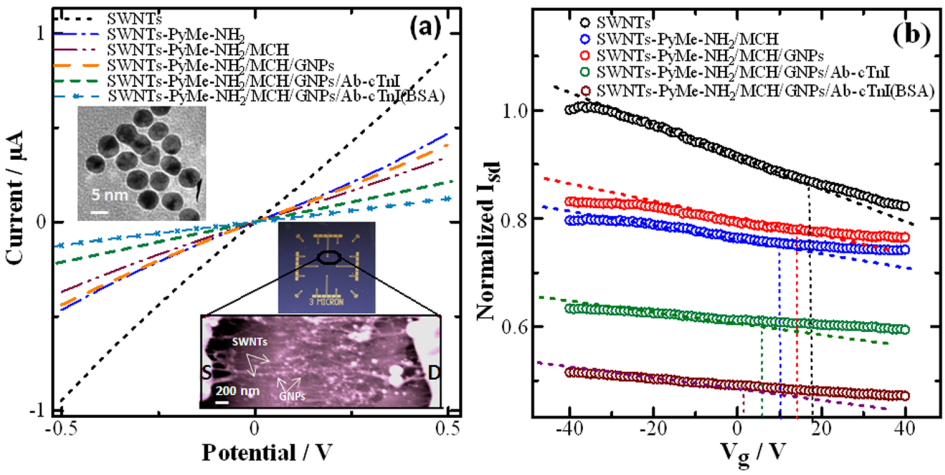

FIG. 2. (a) Current versus voltage (I–V) curves and (b) typical gate voltage dependence of the normalized source-drain current (I_{sd}) at V_d of 0.1 V of SWNTs chemiresistive device at different stages of fabrication.

from the air.[16] A decrease in current at a given voltage was obtained upon functionalization of SWNTs with bilinker PyMe-NH_2 due to a π-π stacking interaction of the SWNTs with pyrene ring moiety. A subsequent decrease in the current was observed after the passivation of gold microelectrodes with MCH. This is attributed to MCH adsorption on gold electrodes shifting the Au Fermi level towards valence band of CNTs and therefore decreasing the carrier injection barrier.[17] The hole density in SWNT was calculated by using the expression $C\Delta V_T/eL$ and the field-effect mobility of the holes was calculated in the linear regime by the equation, $\mu = (L)^2$ $(dI_{sd}/dV_g)/CV_d$ (where C is the approximate capacitance, ΔV_T is the shift in threshold voltage, e is the electron charge, and L is the channel length)[18] and the field-effect holes mobility (μ) was calculated in the linear regime by the equation, $\mu = (L)^2$ $(dI_{sd}/dV_g)/CV_d$,[19] where dI_{sd}/dV_g is the slope of a plot between the source-drain current (I_{sd}) and applied back gate voltage (V_g), and V_d is the drain voltage. A negative shift in V_T ($\Delta V_T = 7.09$ V) with respect to the pristine SWNT was observed after the successive treatment of the device with PyMe-NH_2 and MCH, respectively, due to electron charge transfer from these electron donor molecules to SWNTs, which corresponded to a total decrease of $\sim 10 \times 10^6\,cm^{-1}$ holes concentration in SWNT with a charge mobility of $\sim 1.3 \times 10^2\ cm^2\ V^{-1}\ s^{-1}$. However, a significant increase in the current with a positive shift in V_T ($\Delta V_T = 3.99$ V) was seen after the covalent attachment of GNPs (MPA) over the SWNTs, leading to an increased hole charge density of $6.0 \times 10^6\,cm^{-1}$ with respect to PyMe-NH_2/MCH/SWNT with a charge mobility of $\sim 1.6 \times 10^2\ cm^2\ V^{-1}\ s^{-1}$. This may be explained on the basis of work functions of the gold (5.1–5.47 eV)[20] and SWNTs (4.3–4.9 eV),[21] where the comparatively high work function of gold facilitate the charge transfer of electrons from the SWNT to GNP. Subsequently, the current decreased drastically after the covalent immobilization of cardiac protein antibody, Ab-cTnI, with GNP(MPA)/PyMe-NH_2/MCH/SWNT and on treatment with a blocking protein reagent (BSA), respectively. The covalent attachment of 5–7 nm size GNP(MPA) (TEM image shown in top inset of Fig. 2(a)) over the SWNTs was also confirmed by the scanning electron microscope (SEM, LEO 440 PC, UK) image (bottom inset of Fig. 2(a)) of the hybrid device. A negative shift in V_T of 8.27 V and a further shift of 4.8 V revealed an overall decrease in the hole density of $\sim 12.5 \times 10^6\,cm^{-1}$ and $\sim 7.3 \times 10^6\,cm^{-1}$ after successive modification of GNP(MPA)/PyMe-NH_2/MCH/SWNT with proteins Ab-cTnI and BSA, respectively. This may be attributed to the electron charge transfer process in which the amino acids with base containing residues (arginine, histidine, and lysine) located on the protein backbone structure provide electrons, where each adsorbed amine donates 0.04 electrons[22] to the SWNTs leading to the depletion of hole charge density. However, the transconductance (dI_{sd}/dV_g) does not show any significant change after successive modifications with Ab-cTnI and BSA, and nearly identical charge mobilities of 0.8×10^2 and $0.9 \times 10^2\ cm^2\ V^{-1}\ s^{-1}$ were obtained, respectively. This indicated that the charge transfer characteristic in SWNT hybrid device upon biomolecular functionalization is governed by the electrostatic gating effect without showing much change in the charge mobility.

To investigate the sensitivity of the hybrid device, it was exposed to varying concentrations of target antigen cTnI in the PBS buffer (pH 7.4). Fig. 3 shows the normalized response of the cTnI-GNP/SWNTs hybrid [$(R-R_0)/R_0$, where R_0 and R is the resistance of the device measured before and after exposure to cTnI in PBS, respectively] as a function of cTnI concentration in PBS. The resistance was calculated as the inverse of the slope of the *I–V* plot between 0.5 and +0.5 V (linear range). The device was exposed to 2 μl aliquot of each concentration of cTnI for 10 min, at room temperature, rinsed thoroughly with distilled water, dried with N_2 gas flow before electrically characterized by measuring *I-V* characteristics. It was observed that the conductance of the SWNT hybrid device continued to decrease, i.e., the resistance increased with increasing concentrations of cTnI. The device exhibited a linear response (normalized resistance change) to target cTnI from 0.1 to 10 ng ml^{-1} concentrations with sensitivity (slope of the calibration curve) of about 20% per decade ng ml^{-1} cTnI. The error bars (which correspond to the range of the resistance measured for the three replicates) show that the variability in the resistance was within a range of 6%–15% at individual cTnI concentration. We note

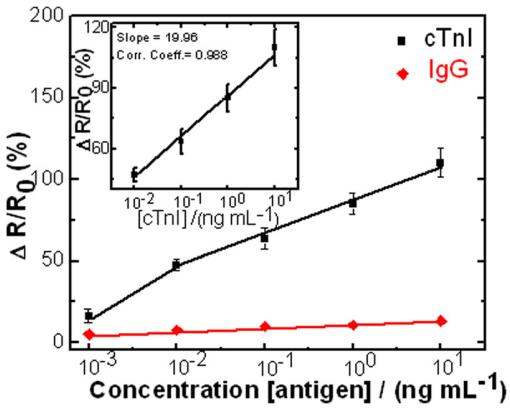

FIG. 3. Calibration curve of cTnI and mouse IgG detection on Ab-cTnI-GNP/SWNTs chemiresistive biosensor. Each data point is an average of the measurements from 3 independent sensors prepared at different time and error bars represent ±1 standard deviation.

that the exposure of even 0.001 ng ml^{-1} cTnI to the device makes a significant change in the resistance ($\Delta R/R_0$) ~ 14%, indicated a low detection of cTnI down up to 0.001 ng ml^{-1} concentration. This detection limit of the SWNTs hybrid device towards cTnI is lower than those of recently reported capacitance[23] and impedance based sensors.[24]

Since specificity of a device is a critical factor in sensing, it was investigated by checking the response of the cTnI−GNP/SWNTs hybrid device to a varying concentration of a non-specific protein, mouse IgG, in PBS (Fig. 3). The resistance of the device was found to increase with increasing concentration of IgG with a minimum to maximum change in resistance from 3.3% to 12.4% to a range of 0.001 to 10 ng ml^{-1} IgG in PBS. This change in resistance was significantly smaller in comparison to a change in resistance (14.0% to 109.4%) for the same concentration range of cTnI in PBS. This demonstrated the specificity of the Ab-cTnI-GNP/SWNTs hybrid device to cTnI causing a change in resistance due to antibody-antigen immunoreaction only.

In conclusion, we demonstrated a facile method of ultrasensitive detection of cTnI using MPA capped GNPs-SWNT hybrid device. The free carboxyl groups of the capping agent provided binding sites for the efficient biomolecular immobilization of cTnI specific antibody, Ab-cTnI, for the construction of a label-free chemiresistive biosensor. The specificity of the device was determined by exposing it to mouse IgG and was found to be specific only to cTnI based on antibody-antigen interaction. The device exhibited a linear response to cTnI in the range of 0.01 to 10 ng ml^{-1} with a sensitivity of about 20% change in resistance per decade cTnI concentration in PBS. The high sensitivity and specificity of the device together with a label-free detection makes it a better method than the current techniques.

We are grateful to Professor R. C. Budhani, Director, National Physical Laboratory, New Delhi, India for providing facilities.

[1]J. E. Adams, G. S. Bodor, V. G. Davila-Roman, J. A. Delmez, F. S. Apple, J. H. Ladenson, and A. S. Jaffe, Circulation **88**, 101 (1993).
[2]A. S. Jaffe, L. Babuin, and S. F. S. Fred, J. Am. Coll. Cardiol. **48**, 1 (2006).
[3]M. C. Fishbein, T. Wang, M. Matijasevic, L. Hong, and F. S. Apple, Cardiovasc. Pathol. **12**, 65 (2003).
[4]L. Babuin and A. S. Jaffe, Can. Med. Assoc. J. **173**, 1191 (2005).
[5]S. E. F. Melanson, M. J. Conrad, N. Mosammaparas, and P. Jarolim, Clin. Chim. Acta **395**, 57 (2008).
[6]E. Antman, J.-P. Bassand, W. Klein, M. Ohman, J. L. L. Sendon, L. Rydén, M. Simoons, and M. Tendera, J. Am. Coll. Cardiol. **36**, 959 (2000).
[7]J. Wei, Y. Mu, D. Song, X. Fang, X. Liu, L. Bu, H. Zhang, G. Zhang, J. Ding, W. Wang, Q. Jin, and G. Luoa, Anal. Biochem. **321**, 209 (2003).
[8]Y. Lin, Q. Fu, J. Zhu, J. M. Miller, and J. E. Eyk, Clin. Chem. **56**, 1307 (2010).
[9]J. Wang, A. Ibanez, M. P. Chatrathi, and A. Escarpa, Anal. Chem. **73**, 5323 (2001).
[10]F. S. Apple, A. Falahati, P. R. Paulsen, E. A. Miller, and S. W. Sharkey, Clin. Chem. **43**, 2047 (1997).
[11]G. G. Wildgoose, C. E. Banks, and R. G. Compton, Small **2**, 182 (2006).
[12]M. C. Daniel and D. Astruc, Chem. Rev. **104**, 293 (2004).
[13]T. Taniguchi, T. Inada, T. Kashiwakura, F. Murakami, M. Kohri, and T. Nakahira, Colloids Surf., A **377**, 63 (2011).
[14]T. Ishida, K. Kuroda, N. Kinoshita, W. Minagawa, and M. Haruta, J. Colloid Interface Sci. **323**, 105 (2008).
[15]S. T. Liu, T. Zhu, Y. C. Wang, and Z. F. Liu, Mol. Cryst. Liq. Cryst. **337**, 245 (1999).
[16]A. Star, J. C. Gabriel, K. Bradley, and G. Gruner, Nano Lett. **3**, 459 (2003).
[17]X. Tang, S. Bansaruntip, N. Nakayama, Y. Yenilmez, Y. L. Chang, and Q. Wang, Nano Lett. **6**, 1632(2006).
[18]C. Li, B. Lei, D. Zhang, X. Liu, S. Han, T. Tang, M. Rouhanizadeh, T. Hsiai, and C. Zhou, Appl. Phys. Lett. **83**, 4014 (2003).
[19]Rajesh, B. K. Das, S. Srinives, and A. Mulchandani, Appl. Phys. Lett. **98**, 013701 (2011).
[20]*CRC Handbook of Chemistry and Physics, Version 2008*, edited by D. R. Lide (CRC Press, USA, 2008).
[21]P. Liu, Q. Sun, F. Zhu, K. Liu, K. Jiang, L. Liu, Q. Li, and S. Fan, Nano Lett. **8**, 647 (2008).
[22]K. Bradley, M. Briman, A. Star, and G. Gruner, Nano Lett. **4**, 253 (2004).
[23]A. Periyakaruppan, R. P. Gandhiraman, M. Meyyappan, and J. E. Koehne, Anal. Chem. **85**, 3858 (2013).
[24]V. Bhalla, S. Carrara, P. Sharma, Y. Nangia, and C. R. Suri, Sens. Actuators, B **161**, 761(2012).

ISSN (Print) : 2320 – 3765
ISSN (Online): 2278 – 8875

International Journal of Advanced Research in Electrical, Electronics and Instrumentation Engineering

(An ISO 3297: 2007 Certified Organization)

Vol. 2, Special Issue 1, December 2013

Load Modeling of Broadband Power Line Communication (BPLC) Network

Mini S. Thomas[1], Senior Member, IEEE,Vinay Kumar Chandna[2], Senior Member, IEEE and Seema Arora[3], Student Member, IEEE

Professor, Department of Electrical Engineering, Jamia Millia Islamia, New Delhi, India[1]

Professor, Department of Electrical Engineering, JSS College of Engineering, Noida, India[2]

Research Scholar, Department of Electrical Engineering, Jamia Millia Islamia, New Delhi, India[3]

***Abstract*:** Power line communication technology uses power lines for its data communication. This technology takes profits from the advantage of not requiring any additional wiring and thus offers an inexpensive medium for data transmission. For data communication, it is necessary to determine the characteristics of the Powerline channel which has been considered as a medium not only for low-rate, control purpose communication, but also for high-speed data communication. However, the power line channel is extremely difficult to model as it is a very noisy transmission medium. For creating a complete PLC communication system, there is necessity to create model of channels. The simulations and analysis carried out in this work will help in characterization of broadband power line communication (BPLC) network. The paper also provides insight into the laboratory facilities for research in performance analysis of BPLC network at Jamia Millia Islamia.

Keywords: Channel modeling, broadband power line communication communications, Multipath, BER.

I. INTRODUCTION

BROADBAND OVER POWER LINE COMMUNICATIONS (BPLC) is a term used to identify technologies, set of equipments, applications and software and management services that allow users to communicate over already existing power lines. The advantage of using this technology is that the power-line network is the most pervasive and accessible network. It reaches every power socket in every home. Since the power-line network is already installed, there is no need to lay new cables. The technology operates in the 1-30 MHz and can deliver data rates up to 200Mbps. The logic behind providing high bit-rate data services exploiting the power grid rests in the fact that vast infrastructure already exists in place for power distribution, and hence the penetration of the service could be much higher than any other wire line alternative [1].

To analyze the performance and to access the possibilities of optimization of transmission systems, a reasonably accurate channel model is needed [2]. With this aim, various models of a power-line network for broadband data transmission have been derived in the recent past. Some of those models can be found in Phillips [3], Zimmermann and Dostert [4], and Gali and Banwell [5], etc. However, a widely accepted channel model has not yet been presented, since models based on either experimental results or obtained from specific network topologies or boundary conditions are not general and incomplete, for predicting the behavior of power-line networks. The powerline medium is an unstable transmission channel owing to the variance of impedance caused by variety of appliances that could be connected to the power outlets, and these impedance fluctuations lead to multipath of BPLC channel [4, 6]. The noise present in the BPLC environment makes the communication over power lines further more difficult.

For the communication engineers, BPLC represents the formidable challenge of transmitting data along a communication media that was originally designed for the electrical energy delivery and not for communication purpose. Since home networking transcends the simply data communication between computers or Internet access,

ISSN (Print) : 2320 – 3765
ISSN (Online): 2278 – 8875

International Journal of Advanced Research in Electrical, Electronics and Instrumentation Engineering

(An ISO 3297: 2007 Certified Organization)

Vol. 2, Special Issue 1, December 2013

BPLC technology appears as a potential way to become the smart home concept, and the indoor multimedia data interchange, in a reality. Although the performance of BPLC technology supporting multimedia applications with quality service at bit rates of up to 200 Mbps has been proved, it is reasonable to consider BPLC as a complementary technology and not as a competitor for the other home-networking technologies; both wired and wireless [7].

II. BPLC CHANNEL MODELING

BPLC channel modeling work can be categorized as BPL communication model, Models of power lines and Source of Interference (Noise) model [2, 8 and 9]. The focus of our work presented in this paper is on the load modeling of indoor BPLC, and in particular, calculation of effects of load on the BER rate. The most representative indoor BPL modeling approaches have been proposed based on the recent literature. Fig 1 shows the block diagram of BPLC channel model.

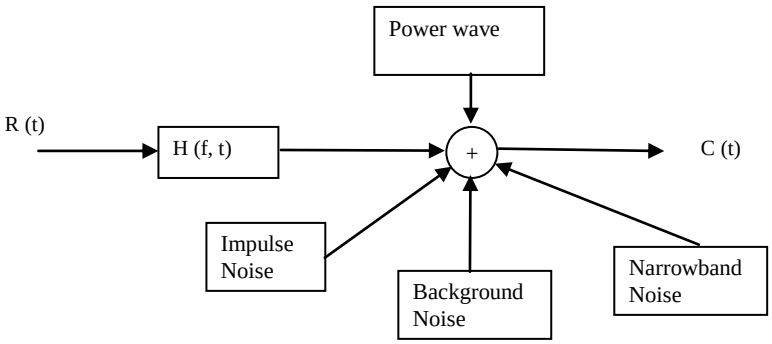

Fig 1. PLC Channel Model

The model can be created by using transmission line theory, which applies chain parameter matrices or scattering parameters to describe the relation between input and output voltage and current by two-port network [2,10,11and 12]. Power line model can also be created by using the concept of environment of multipath signal propagation [4 and 6]. The parameters of this line are obtained from a distribution network topology or based on metering and measurements.

III. MODELING THE INDOOR POWERLINE BASED ON TRANSMISSION LINE THEORY

The indoor power cables (fig.2) are approximated to be a two-wire transmission line with solid core conductor for software simulation. The line voltage V(x) and the current I(x) with x as displacement can be expressed in the frequency domain.

$$\frac{\partial V(x)}{\partial x} = -(R + j\omega L)I(x) \quad (1)$$

$$\frac{\partial I(x)}{\partial x} = -(G + j\omega C)V(x) \quad (2)$$

Differentiating both equations (1) and (2), we get:

$$\frac{\partial^2 V(x)}{\partial x^2} = \gamma^2 V(x) \quad (3)$$

ISSN (Print) : 2320 – 3765
ISSN (Online): 2278 – 8875

International Journal of Advanced Research in Electrical, Electronics and Instrumentation Engineering

(An ISO 3297: 2007 Certified Organization)

Vol. 2, Special Issue 1, December 2013

$$\frac{\partial^2 I(x)}{\partial x^2} = \gamma^2 I(x) \qquad (4)$$

The propagation of signals over power lines introduces an attenuation, which increases with the length of the line and the frequency. The line attenuation is caused by the heat loss and radiation on the power line and is a function of characteristic impedance Z_0 and transmission line complex valued propagation constant γ. These two intrinsic line parameters dominate the wave behavior along the power line.

$$\gamma = \sqrt{((R + j\omega L)(G + j\omega C))} \qquad (5)$$

$$Z_0 = \sqrt{((R + j\omega L)/(G + j\omega C))} \qquad (6)$$

R, L, G and C are the resistance, inductance, conductance and capacitance per unit length of the power line conductor respectively. In order to derive γ and Z_0, the four primary line constants have to be derived first.

$$R = 1 / \pi (\sqrt{\pi f \mu_c/\sigma_c}) \qquad (7)$$

$$G = \pi \sigma / (\cosh^{-1}(D/2a)) \qquad (8)$$

$$L = \mu / \pi \cosh^{-1}(D/2a) \qquad (9)$$

$$C = \pi \varepsilon / \cosh^{-1}(D/2a) \qquad (10)$$

A solution for V (x) and I (x) is:

$$V_x = V_f e^{\gamma x} + V_r e^{-\gamma x} \qquad (11)$$

$$I_x = I_f e^{\gamma x} - I_r e^{-\gamma x} \qquad (12)$$

where x is the displacement from the load, negative towards the source, and V_f, V_r, I_f and I_r are forward and reflected voltages and currents respectively at the load end of the line. The above expressions can be rewritten as:

$$V_x = V_f (e^{\gamma x} + \Gamma e^{-\gamma x}) \qquad (13)$$

$$I_x = I_f (e^{\gamma x} - \Gamma e^{-\gamma x}) \qquad (14)$$

where Γ is the complex reflection coefficient at the load. Transmission line behavior is described by these equations and the boundary conditions imposed by the load with load impedance given by Z_L=V/I.

$$\Gamma = \frac{Z_L - Z_o}{Z_L + Z_o} \qquad (15)$$

$$\Gamma(x) = \Gamma \frac{e^{\gamma x}}{e^{-\gamma x}} \qquad (16)$$

The equations (1) to (16) fully describe the behavior of a transmission line with a given load impedance. Input impedance Z_{in} of line of length l can be calculated from the load impedance:

ISSN (Print) : 2320 – 3765
ISSN (Online): 2278 – 8875

International Journal of Advanced Research in Electrical, Electronics and Instrumentation Engineering

(An ISO 3297: 2007 Certified Organization)

Vol. 2, Special Issue 1, December 2013

$$Z = Z_o \frac{Z_L + Z_o \tanh(\gamma l)}{Z_o + Z_L \tanh(\gamma l)} \quad (17)$$

If V_1 and I_1 are the voltage and current at the input port, and V_2 and I_2 are the voltage and current at the output port ; the relationships exist (equations 18 and 19) for the two port network equivalent of a transmission line:

$$V_1 = V_2 \cosh(\gamma l) + I_2 Z_0 \sinh(\gamma l) \quad (18)$$

$$I_1 = \frac{V_2}{Z_o} \sinh(\gamma l) + I_2 Z_o \cosh(\gamma l) \quad (19)$$

The dielectric material, between the cable conductors, is inhomogeneous in both space (due to the round shape of the cable conductor) and contents (mixture of insulation and air). But since the cables are of close proximity to each other, the thickness 't' of the insulation is comparable with that of the air space between the conductors. In this model, the dielectric is assumed to be just a mixed content material and the effects of the inhomogeneous in space are neglected to keep the model tractable.

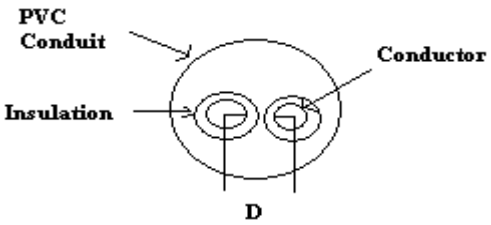

Fig. 2. Approximate model of the power line

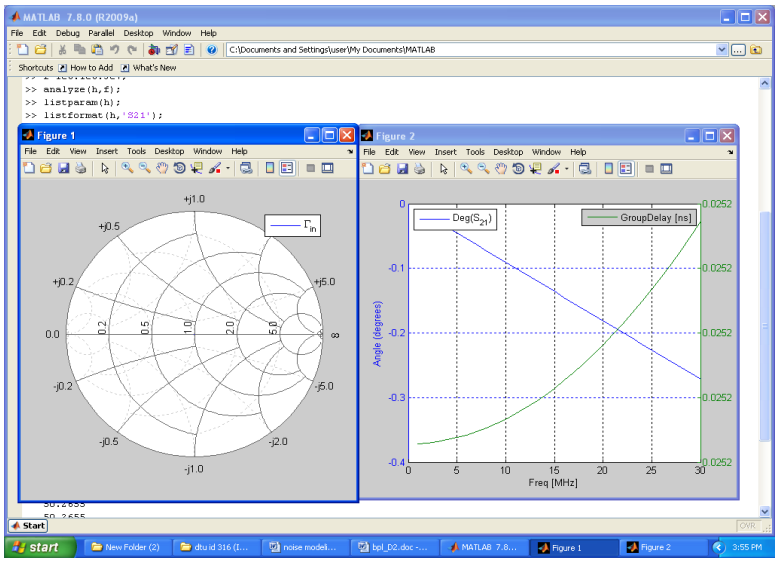

ISSN (Print) : 2320 – 3765
ISSN (Online): 2278 – 8875

International Journal of Advanced Research in Electrical, Electronics and Instrumentation Engineering

(An ISO 3297: 2007 Certified Organization)

Vol. 2, Special Issue 1, December 2013

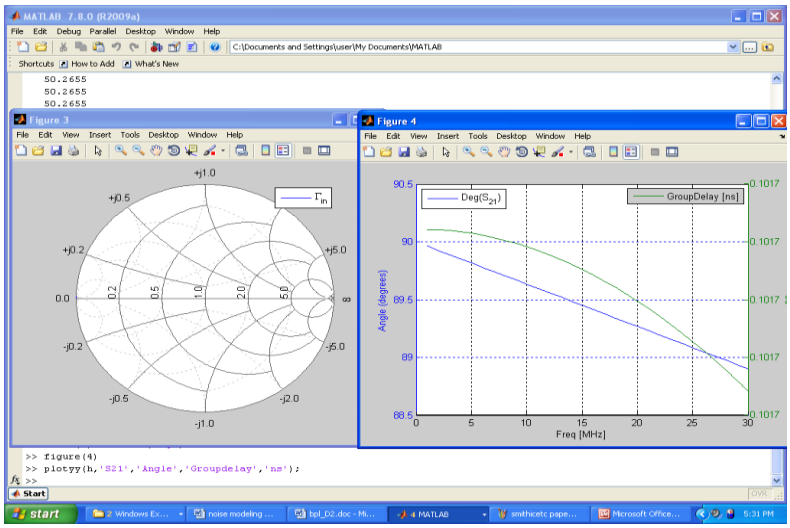

Fig. 3a and 3b .Shunt stub terminated in an open circuit and shunt stub terminated in a short circuit.

The simulations have initially been carried out in MATLAB with the small length of transmission line (taken to be 0.01m length) with shunt stub terminated in an open circuit as shown in fig.3a and shunt stub terminated in a short circuit as shown in fig.3b. The simulations have next been carried out in MATLAB with the length of transmission line taken to be 15 m with shunt stub terminated in an open circuit. The simulation results are revealed in fig.4. The length of transmission line is again taken to be 15 m with shunt stub terminated but short circuit. The simulation results are revealed in fig.5. The distance between the two conductors (Live and Neutral) 'D'= 2t + 2t + 2a = 4.06 mm

t = thickness of insulation = 0.7 mm

a = radius of copper conductor = 0.63 mm

Conductivity of copper $\sigma_C = 5.8 \times 10^7$ S/m

Relative permittivity of dielectric $\varepsilon_r = 0.8$

Conductivity of dielectric $\sigma_d = 1 \times 10^{-5}$ S/m

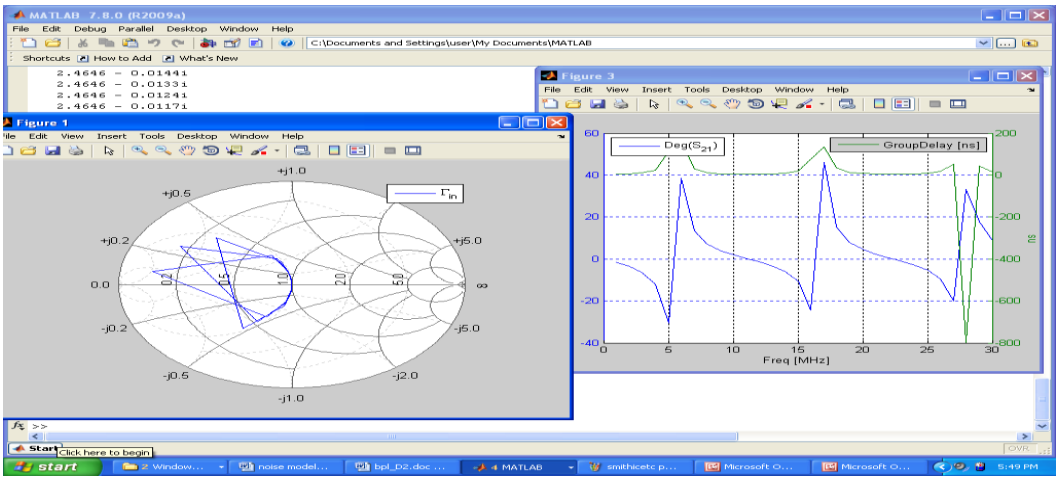

Fig 4. Simulation results for open termination

ISSN (Print) : 2320 – 3765
ISSN (Online): 2278 – 8875

International Journal of Advanced Research in Electrical, Electronics and Instrumentation Engineering

(An ISO 3297: 2007 Certified Organization)

Vol. 2, Special Issue 1, December 2013

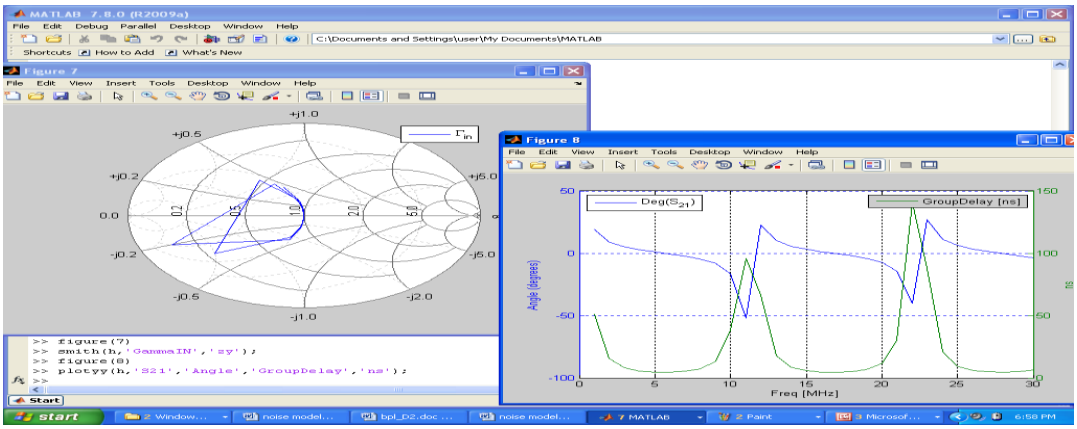

Fig 5. Simulation results for short termination

IV. EFFECT OF VARYING LOADS

Low-voltage power distribution networks (indoor) were designed only for supply of electrical signals at 50 Hz to households. The sockets, or terminal nodes, are considered the access points to the channel where transmitter or receiver equipment or loads can be located. Every device connected to the power network represents a load to the network, whose model includes, besides its impedance value, noise source associated with it. The frequency dependent and time variant values of the loads can be obtained directly from measurements of typical electrical loads. Some loads may have constant impedance value as long as their connection status does not change, but others exist that present a cyclic variation of their value according to the mains frequency.

If a wide range of devices and appliances with variable electrical characteristics are either switched on or off at any location or node and at any time, their variation in the network will lead to strong fluctuations of the impedance. These impedance fluctuations and discontinuity lead to multipath behavior of the BPLC channel, making its utilization for the information transmission more delicate. Model of powerline channel can be expressed as linear combination of a time-varying filter with additive noise and an attenuating multipath channel. The multipath channel with additive noise can be described by an Echo Model [4]. In contrast to the known approaches, a top-down strategy [4] considers the communication channel as a black box and describing its transfer characteristics by a frequency response in the frequency range from 500 kHz up to 20 MHz by very few relevant parameters. The structure of the model is based on fundamental physical effects, which were analyzed during a great number of measurements. However, in contrast to previous approaches, the relevant parameters are not derived from component properties, but from channel measurements.

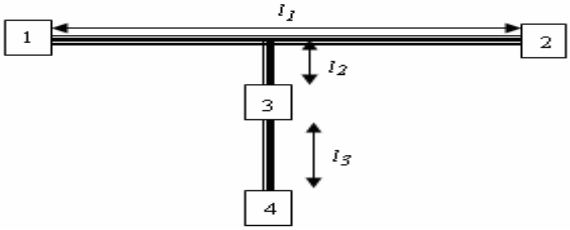

Fig 6. Section of Low voltage power distribution Network (Indoor)

ISSN (Print) : 2320 – 3765
ISSN (Online): 2278 – 8875

International Journal of Advanced Research in Electrical, Electronics and Instrumentation Engineering

(An ISO 3297: 2007 Certified Organization)

Vol. 2, Special Issue 1, December 2013

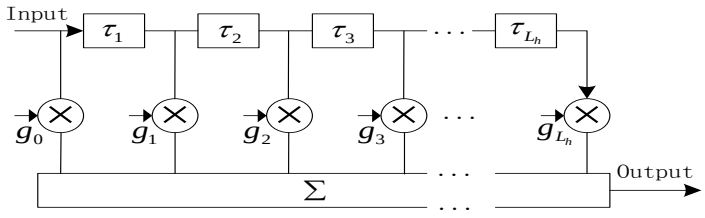

Fig 7. Echo model of power line

The echo model can be described by a discreet time impulse response h (t).

$$h(t) = \sum g_i \delta(t - \tau_i) \quad (19)$$

Considering the effect of line attenuation due to heat loss and radiation and taking the Fast Fourier Transform, the channel response is given by equation (20).

$$H(f) = \sum g_i e^{-\alpha(f) d_i} e^{-2\pi f \tau_i} \quad (20)$$

g_i is the weighting factor and represents the product of the reflection and transmission factors along the path i
d_i is the length of the path.
τ_i is the path delay introduced by path i and is the ratio of the path length (d_i) and phase velocity (v_p) .

$$\tau_i = d_i / v_p \quad (21)$$

The simulation of the BPL system is carried out in MATLAB/SIMULINK with variable number of branches and increasing loads and the BER rate is compared graphically. As observed from fig.8 and fig.9, the effect of changing loads is more on networks with lesser number of branches. With increasing number of branches, the effect of load on the network goes on decreasing. With increase in the number of branches, the impedance of the network decreases because of a large number of impedances in parallel. More the number of branches, lesser is the network impedance.

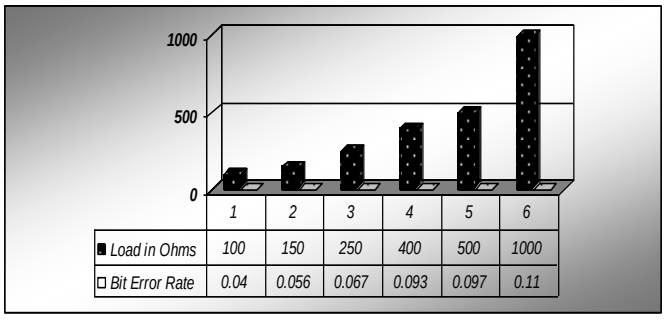

Fig.8 BER and load for one branch

ISSN (Print) : 2320 – 3765
ISSN (Online): 2278 – 8875

International Journal of Advanced Research in Electrical, Electronics and Instrumentation Engineering

(An ISO 3297: 2007 Certified Organization)

Vol. 2, Special Issue 1, December 2013

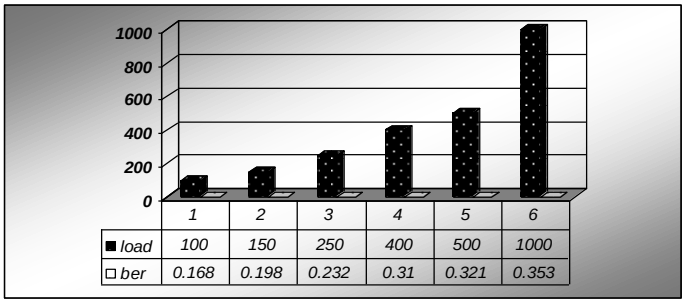

Fig.9 BER and load for three branches

V. BROADBAND PLC EQUIPMENTS FOR INDOOR POWER LINE NETWORK

Network performance analysis of CORINEX Communication, Inc. Broadband PLC equipments (fig10 and fig 11) for indoor power line network using measurements of different network characteristics parameters such as throughput and latency is conducted for the network in Jamia Millia Islamia.

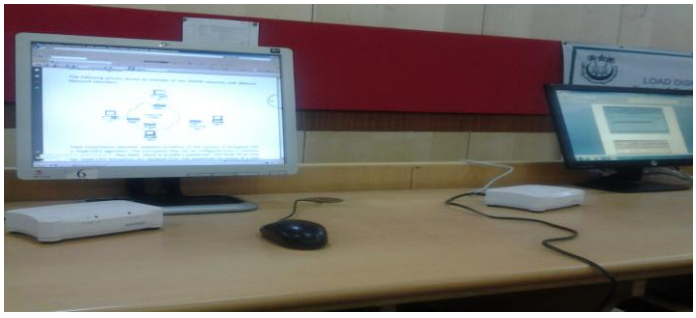

Fig 10. Corinex AV200 Enterprise Powerline Adapters in Jamia Millia Islamia BPL and SCADA Lab.

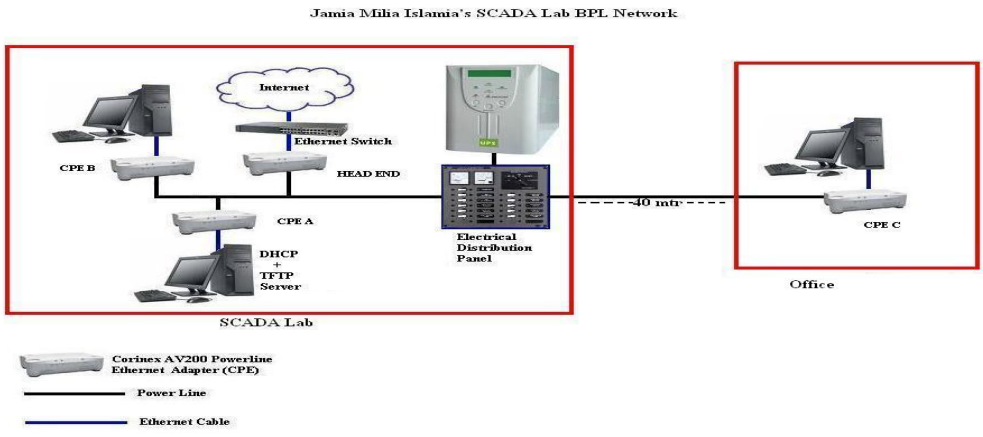

Fig 11. A Typical Layout of BPL Network in Jamia Millia Islamia BPL and SCADA Lab.

The Corinex AV200 Enterprise Power line Adapters [6, 8 and10] installed enable the users to connect individual PCs or other devices with Ethernet communications links into a local area network through existing electric power lines

ISSN (Print) : 2320 – 3765
ISSN (Online): 2278 – 8875

International Journal of Advanced Research in Electrical, Electronics and Instrumentation Engineering

(An ISO 3297: 2007 Certified Organization)

Vol. 2, Special Issue 1, December 2013

(Power line), also enable PC file and application sharing, allow peripheral and printer sharing through the Power line network, enables shared broadband Internet access, enables sharing of bandwidth for multimedia payloads, including voice, data, audio and video, eliminates the need for long network cables running throughout.

VI. CONCLUSION

The simulation results reveal that in a realistic PLC scenario, the transient variations of the nature of termination, value of loads (i.e. transient impulsive noise) and the different network conditions (i.e. different access point with different mismatch), make the PLC transmission channel time-frequency dependent. In principle, channel attenuation depends on the characteristics such as length, per-unit-length parameters, frequency dependence etc. of the cables and of the loads. While the frequency dependence can be mathematically modeled, the load variation cannot be analytically calculated as the loads are applied or disconnected several times a day randomly. The load variations are quite significant. Models of the transfer characteristics of the mains network prove to be significant for design of such future networks.

REFERENCES

[1] T. S. Pang, P. L. So,K. Y. See, and A. Kamarul, "Modeling and Analysis of Common-Mode Current Propagation in Broadband Power-Line Communication Networks," IEEE Transactions on Power Delivery, Vol. 23, No. 1, January 2008, pp.171-179.
[2] P. Mlynek, M. Koutny, and J. Misurec, "Power line Modelling for creating PLC communication system," International Journal of Communications, Issue1, Volume 4, 2010, pp.13-21.
[3] Holger Philipps,"Performance Measurements Of Powerline Channels At High Frequencies," International Conference on PLC, 1 998,pp. 229-237.
[4] Manfred Zimmermann and Klaus Dostert, "A Multipath Model for the Powerline Channel,"IEEE Transactions on Communications, Vol. 50, NO. 4, APRIL 2002, pp. 553-559.
[5] Stefano Galli and Thomas Banwell, "A Novel Approach To The Modeling of the Indoor Power Line Channel—Part II: Transfer Function And Its Properties," IEEE Transactions On Power Delivery, Vol. 20, NO. 3, July 2005 pp. 1869-1878.
[6] Vinay Kumar Chandna , and Mir Zahida, "Effect of Varying Topologies on the Performance of Broadband over Power Line," IEEE Transactions On Power Delivery, Vol. 25, No. 4, October 2010, pp. 2371-2375.
[7] Gerardo Laguna and Ricardo Barr´on, "Survey on Indoor Power Line Communication Channel Modeling," IEEE Electronics, Robotics and Automotive Mechanics Conference 2008,pp.163-168
[8] Seema Arora, Vinay Kumar Chandna and Mini S. Thomas, "Modeling of Broadband Indoor Power Line Channel for Various Network Topologies", IEEE PES Innovative Smart Grid Technologies, ISGT 2011, pp. 229-235.
[9] Sami Barmada, Member, IEEE, Antonino Musolino, and Marco Raugi, "Innovative Model for Time-Varying Power Line Communication Channel Response Evaluation", IEEE Journal On Selected Areas In Communications, Vol. 24, No. 7, July 2006 pp.1317-1326
[10] Shabana Mehfuz, Abhishek Sinha and Mini S. Thomas, "Modeling of Indoor power line for Substation monitoring using Broadband Power line Communications", TENCON, Hyderabad, 2008, pp.1-4.
[11] Er Liu, Yangpo Gao, Osama Bilal and Timo Korhonen, "Broadband Characterization Of Indoor Power line Channel".IEEE International Conference on Communications 2005, VOL 2, pp. 901-905.
[12] Andrea M. Tonello and Tao Zheng, "Bottom-Up Transfer Function Generator for Broadband PLC Statistical Channel Modeling," IEEE Conference 2009, pp.7-12.

BIOGRAPHY

Mini S. Thomas (M-88, SM-99), graduated from University of Kerala in1984, completed her M.Tech from IIT Madras in1986 (both with gold medals) & PhD from IIT Delhi in 1991, all in Electrical Engineering. Her employment experiences include Regional Engineering College, Calicut, Kerala, and Delhi College of Engineering, New Delhi and presently as Professor in the Faculty of Engineering and Technology, Jamia Millia Islamia, New Delhi. Mini S. Thomas received the prestigious 'Career Award' for young teacher, instituted by AICTE, Govt. of India, for the year 1999. She has published over 70 papers in International/National Journals & Conferences. Her current research interests are in SCADA/EMS System and Substation and Distribution Automation.

V. K. Chandna (M-08, SM-11) graduated from Nagpur University in 1994 in electronics & power, completed his M.E.in Power System from Walchand college of Engg. Sangli, Maharashtra and Ph.D. in Electrical engineering, from Delhi College of Engineering. His employment experience includes ITS College of Engineering, Greater Noida, Jamia Millia Islamia, New Delhi, Walchand college of Engg., Nagpur, Raj Kumar Goel institute of technology, Ghaziabad (UP), Maharaja Agarsen Institute of Technology, Delhi, Jamia Millia Islamia (Central University), Delhi. He is presently working as Prof. and Head in Electrical Engg. Department, JSS College of Engineering, Noida. He has more than 20 papers in International Journal / Conferences of repute. His area of interest is Distributed Generation, Smart/ Microgrid, application of soft computing techniques to power system, SCADA, operation, design and control.

Seema Arora (S-10) received her B.Tech (with Honors) in Electrical from PEC, Panjab University, Chandigarh, in 1995, completed her M.E in Power Electronics, Electrical Machines and Drives in 2006 from M.D.University, Rohtak. She worked in a consultancy of Thermal power plants as a Design and Protection Engineer. She is currently working as an Assistant Professor in the Department of Electrical and Electronics Engineering at GCET, Greater Noida. She is also doing PhD from Jamia Millia Islamia, New Delhi and her research area is Broadband over Power Lines. She has published various research papers in International /National Journals & Conferences of repute. Her research interests include Distributed Generation, Smart Grids, Micro grids, and Communication over Power Lines.

Chem. Biol. Lett. 2014, 1, 1, 33-39 Article

Chemical Biology
LETTERS

Monoamine Oxidase Inhibitors for Neurological Disorders: A review

Ram Singh[1]*, Geetanjali[2] and Naveen Sharma[1]

[1]*Department of Applied Chemistry & Polymer Technology, Delhi Technological University, Bawana Road, Delhi – 110042, India*
[2]*Department of Chemistry, Kirori Mal College, University of Delhi, Delhi-110007, India*

Received Date: 04-11-2013

ABSTRACT

Neurological disorders are drawing much attention from scientists in recent times. These disorders are one of the most serious disorders mankind will have to fight against in near future. Monoamine oxidase is one target which is implicated in many neurological disorders. Scientists have studied different molecular entities as monoamine oxidase inhibitors. The MAO-A and MAO-B inhibitors have been developed to increase the available amounts of monoamine neurotransmitters in the brains for the treatment of neurological disorders. In this article, selected classes of compounds like coumarins, chromones, isatins, phthalimides, phthalonitriles and quinolinones have been reviewed as potential inhibitors of human MAO-A and MAO-B.

Keywords: Chromone, Coumarin, Isatin, Phthalonitrile, Quinolinone, MAO-A, MAO-B, FAD, Neurological disorders

INTRODUCTION

Amine oxidases (AOs) are a heterogeneous family of enzymes that catalyze the oxidative deamination of mono-, di-, and polyamines. AOs fall into two classes based on the chemical nature of the cofactors present in them: AOs that contain flavin adenin dinucleotide (FAD, **1**) as a cofactor, and AOs that contain copper II-2,4,5-trihydroxyphenylalanine quinone as a cofactor.[1] Monoamine oxidases (MAOs; EC 1.4.3.4) falls in the first categories and hence are FAD (**1**) containing enzyme which are tightly bounded to the outer membranes of mitochondria through a cysteine residue (**2**).[2] MAOs are present in several living organisms. They are involved in the oxidation of monoamines including monoamine neurotransmitters and hence control the balance of their concentrations in the brain and peripheral tissues.[3-6] Abnormal levels of MAOs in humans are associated with depression, schizophrenia, substance abuse, attention deficit disorder, migraines, irregular sexual maturation and other diseases.[7]

Corresponding Author: Dr. Ram Singh
Tel: 91-11-27871044 (ext. 1913)
Email: singh_dr_ram@yahoo.com

Cite as: *Chem. Biol. Lett., 2014, 1(1), 33-39.*

Mammals contain two isoforms of MAOs: Monoamine oxidase A (MAO-A) and Monoamine oxidase B (MAO-B).[8] The crystal structures of the two isoforms gave information about the interaction of enzyme with substrates and inhibitors.[2] The amino acid sequences of both the forms are 73% identical but they exhibit different substrate and inhibitor specificities.[9,10] The differences between them are due to their amino acid sequences[11], tissue distribution[12], three-dimensional structure[13], inhibitor selectivity[14], and substrate preferences[15]. The MAO-A oxidises serotonin (5-hydroxytryptamine, **3**) and norepinephrine (**4**) under normal physiological conditions. The MAO-B oxidises phenylethylamine (**5**) preferentially, with dopamine (**6**) and tyramine (**7**) being substrates for both isoenzymes irrespective of concentration.[16-18] The active site of MAO-A consists of a single cavity while the active site of MAO-B is comprised of two separate cavities, an entrance cavity and substrate cavity.[19] The MAO-B active site cavities are normally separated by the side chain of Ile-199, but upon binding of larger cavity-filling ligands, the Ile-199 may adopt an alternate conformation which allows for the fusion of the two cavities.[20,21]

According to World Health Organization (WHO), neurological disorders are diseases of the central and peripheral nervous system. These disorders include epilepsy, Alzheimer disease and other dementias, cerebrovascular diseases including stroke, migraine and other headache disorders, multiple sclerosis, Parkinson's disease, neuroinfections, brain tumours,

traumatic disorders of the nervous system.[22] The neurological disorders are an important cause of mortality and estimated to constitute 11.84% of total deaths in 2015 and increase to 12.22% in 2030 globally.[23] Neurological disorders constitute 16.8% of the total deaths in lower middle income countries compared with 13.2% of the total deaths in high income countries.[23] As per a report by WHO published in 2007, about one billion people affected worldwide, 50 million suffer from epilepsy and 24 million from Alzheimer and other dementias.[24]

The development of MAO inhibitors have a range of potential therapeutic uses especially for neurological disorders.[25-33] The first MAO inhibitor discovered was iproniazid (**8**). This compound was antidepressant in nature and initially developed for the treatment of tuberculosis.[34] This was followed by the development of other hydrazine derivative like phenelzine (**9**) as antidepressants. However, reports of liver toxicity, hypertensive crises, and haemorrhage and, in some cases, death resulted in the withdrawal of many MAO inhibitors from the clinic.[34] Since then, scientists have been involved in developing several compounds that can selectively inhibit one isoform of MAO and can act as a efficient therapeutic agent for various neurological disorders.

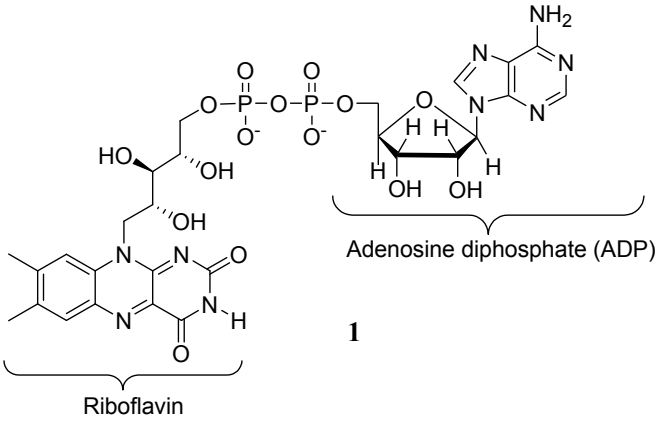

1

MECHANISM OF ACTION BY MAO

The MAOs catalyze the catabolism of amine neurotransmitters and hence are considered as attractive drug targets in the therapy of neurological disorders. Despite considerable progress in understanding their isoforms with respect to their structure, substrates and inhibitors, no general rules have been formulated for the rational design of potent, selective and reversibility based MAO inhibitors.[35,36] In general, the MAO catalyzes oxidative deamination of endogenous or xenobiotic primary amines via oxidative cleavage of the α-CH bond of the substrate to imines which further converted to aldehyde with concomitant reduction of oxygen to hydrogen peroxide (Scheme 1).[37-39] The pathway for this reaction is shown in scheme 2.[39] The cofactor FAD takes an important chemical role in catalysis. This is the most accepted and consistent with the structure mechanism.

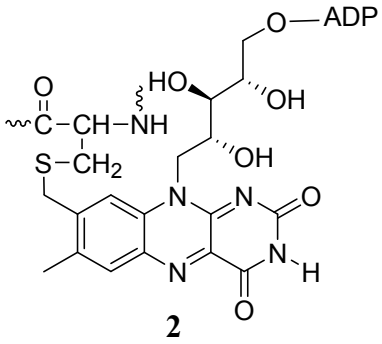

2

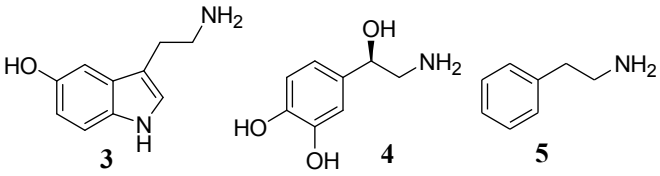

3 **4** **5**

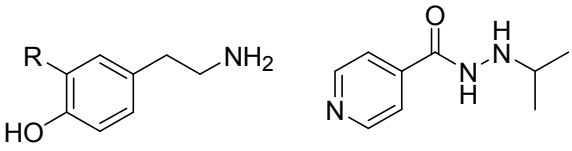

6 R = OH
7 R = H

8

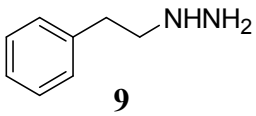

9

$$RCH_2NH_2 + H_2O + O_2 \rightarrow RCHO + NH_3 + H_2O_2$$

Scheme 1

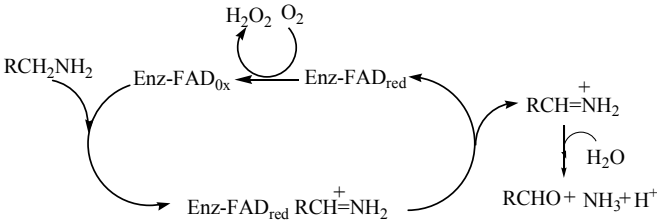

Scheme 2

The isoalloxazine (or flavin)[40-42] moiety in the cofactor FAD gets reduced and acts as a proton acceptor from amine so that it can get converted to an imine (Scheme 3).[43,44] The imine intermediate undergoes immediate hydrolysis by a non-enzymatic pathway into an aldehyde and ammonia in the presence of water. The positioning of the monoamine directly adjacent to flavin in the protein cavity vastly speeds up these reactions.[45] This is because, the precise orientation of the correct chemical groups is always important for the enzymatic efficiency. The enzymes utilize primary amine as substrates and to lesser extent also methyl-substituted secondary amines.

The generated hydrogen peroxide (H_2O_2) from the MAO catalyzed reactions is one aspect responsible for neurodegeneration diseases.[46-48] If this H_2O_2 is not detoxified by

antioxidant systems such as glutathione peroxidase, it may be further converted by iron-mediated Fenton reactions to hydroxyl radicals that can initiate lipid peroxidation and cell death leading to neurological disorders.[46-49]

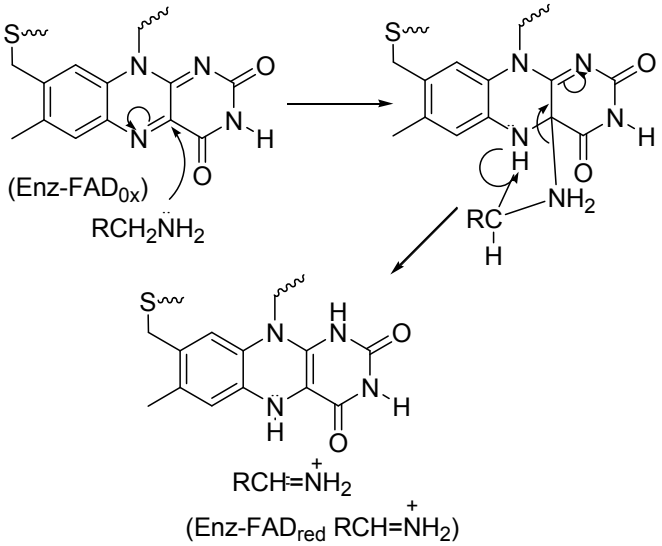

Scheme 3

MAO INHIBITORS

The monoamine oxidase inhibitors are chemicals which inhibit the activity of the monoamine oxidase enzyme family. They were discovered in the 1950s and work by correcting chemical imbalance in the brain. They have a long history of use as medications prescribed for the treatment of depression. The MAO inhibitors have been developed as drugs for treating clinical depression, Parkinson's disease, Alzheimer's disease, and cerebral ischemia and stroke.[50] In the brain, MAO-B comprises 75% of total brain MAO[51] and hence selective MAO-B inhibitors are used clinically to increase dopamine levels in Parkinsonian patients[52]. The MAO-A inhibitors have been prescribed for depression.[53] Following sections highlights the selected potential inhibitors of MAOs.

CHROMONE AND COUMARIN INHIBITORS

Chromone [(4H-1-benzopyran-4-one, **10**] is a member of the benzopyrone class of compounds and a structural isomer of coumarin (1-benzopyran-2-one, **11**). Chromone derivatives have been recognized as potential MAO inhibitors.[54-59] The presence of carboxylic acid (-COOH) derivatives in the γ-pyrone nucleus is very effective in increasing the inhibition properties. Borges et al[39] demonstrated that the chromone carboxamide (-CONHR) is a privileged moiety for the design of potent, selective and reversible MAO inhibitors after careful evaluation of 24 chromone carboxamide compounds.[39] The presence of –COOH derivative at 3-position exert selective inhibition for MAO-B with respect to A-isoform with IC_{50} values in the nanomolar to micromolar range.[39] The chromone 3-caboxamide, 4-Oxo-4H-chromene-3-carboxylic acid (4-chloro-phenyl)-amide (**12**) exhibited the inhibition of MAO-B with IC_{50} value of 63 nM. This compound showed greater than 1000-fold selectivity over MAO-A and found to be a quasi-reversible inhibitor.[39] The reversibility and irreversibility inhibition experiments were performed using the standards R-(-)deprenyl (**13**) for irreversible inhibitor and isatin (**14**) for reversible inhibitor.[60]

The reversible MAO-B inhibitors possess certain advantages over irreversible MAO-B inhibitors. The most notable advantage is an immediate recovery of enzyme activity when the inhibitor has been eliminated from the tissues.[61,62] On the other hand, after termination of treatment with irreversible inhibitors, the rates of recovery of enzyme activity are slow and variable, in part because the turnover rate for the biosynthesis of MAO-B in the human brain may be as much as 40 days.[61,62]

The benzyloxy (-OCH_2Ph) substitution at 6-position in chromones were shown to exhibit high binding affinities for human monoamine oxidase-B (hMAO-B).[63] The reversible MAO-B inhibitor, safinamide (N2-{4-[(3-fluorobenzyl)oxy]benzyl}-L-alaninamide, **15**), a drug candidate in the treatment of Parkinson's disease exhibits an IC_{50} value of 0.08–0.5 μM, whereas 6-benzyloxy chromone inhibits MAO-B with an IC_{50} value of 0.053 μM under similar conditions.[64,65]

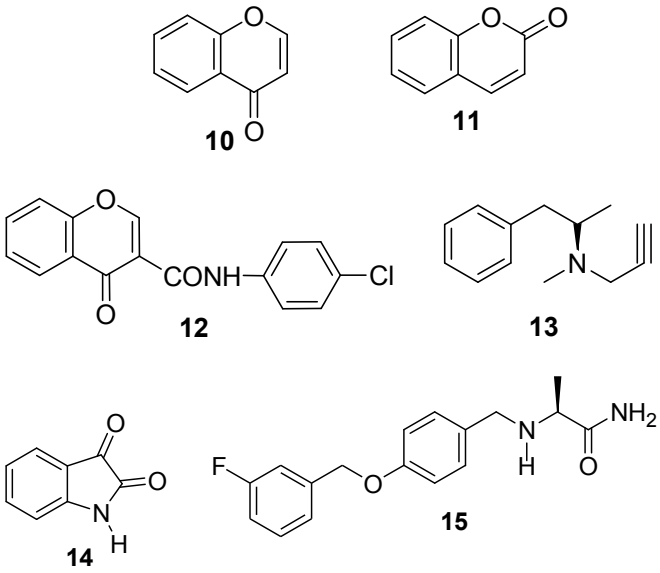

Petzer et al examined the chromone derivatives containing benzyloxy substituents on C6 and a polar substituents on C3.[63] The prepared compounds possessed high affinity for MAO-B, a property imparted by the C6 substituent, as well as improved selectivity for MAO-B, a property imparted by the polar C3 substituent.[63] The results demonstrated that the 6-[(3-bromobenzyl)oxy]chromones (**16**) containing acidic (**17**) and aldehydic (**18**) functional groups on C3 act as potent reversible MAO-B inhibitors with IC_{50} values of 2.8 and 3.7 nM, respectively.[63] However, the benzyloxy substituent on C5 of the chromone ring showed MAO-B inhibition potencies significantly weaker than C6 substitution.[63]

Petzer et al also examined the chromone derivatives containing benzyloxy, phenylethoxy and phenylpropoxy substituents on C7.[66] The substituents and substitution patterns on the benzyloxy ring is suitable for reversible and selective

MAO-B inhibition as per SAR study.[66] The 7-benzyloxychromone derivative was substituted on the benzyloxy phenyl ring with alkyl groups and their derivatives like CH_3, CN, CF_3 and halogens like Cl, Br and F.[66] With the exception of cyano substitution, all substitution and substitution patterns enhanced MAO-B inhibition potency. Substitution on the benzyloxy phenyl ring with halogens and alkyl groups increased the lipophilicity of the C7 side chain, and responsible for enhancements of MAO-B inhibition potencies compared to the unsubstituted homologue.[66]

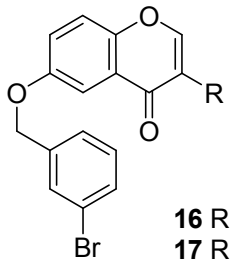

16 R = H
17 R = COOH
18 R = CHO

The introduction of a *p*-methoxy group in coumarin (**11**) increased the MAO inhibitory activity.[67,68] The C7-functionalized coumarin derivatives are found to be reversible inhibitors of both human MAO enzymes.[69] 7-(3,4-difluorobenzyloxy)-3,4-dimethylcoumarin (**19**) was shown to inhibit rat brain MAO-B with an IC_{50} value of 1.14 nM and a 108-fold selectivity for MAO-B over the MAO-A isoform.[69]

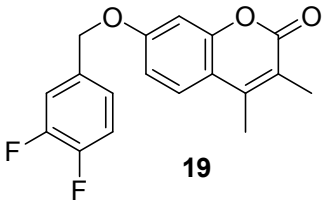

19

ISATIN DERIVATIVES

Isatin or 1H-indole-2,3-dione (**14**) is an indole derivative. The derivatives of this molecule are found to be a reversible inhibitor of both human MAO forms.[70] The enzyme inhibition dissociation constants of MAO-A is 15 µM and MAO-B is 3 µM.[70,71] The three-dimensional structural binding study of human MAO-B with isatin showed that isatin is located in the substrate cavity in close proximity to the FAD co-factor where it is involved in hydrogen bonding with conserved water molecules.[71] The binding of isatin to the substrate cavity leaves the entrance cavity of the enzyme unoccupied. To further enhance the binding affinity of isatin to MAO-B, the two derivatives of isatin (E)-5-styrylisatin (**20**) and (E)-6-styrylisatin (**21**) were synthesized and evaluated.[71,72] Both the compounds were found to posses higher binding affinities because the isatin dioxoindolyl ring bound to the substrate cavity and the styryl side chain extent to the entrance cavity.[71] Out of the two derivatives, the C-5 substituted isomer was found to be more potent inhibitor.[71] The presence of hydroxyl group (-OH) at C-5 of isatin also increased selectivity of MAO-A inhibitor.[73,74] The inhibiting activity is due to both the hydrophobic properties of the molecule and details of electronic structure, especially, the presence of carbonyl group at C-3 and a substitution at C-5.[75]

PHTHALIMIDE AND PHTHALONITRILE DERIVATIVES

The cyclic imide class of compounds generally has an imide ring, with the general structure of CO-N(R)-CO-. They are both hydrophobic and neutral and can cross biological membranes *in vivo*.[76] Phthalimide is a cyclic imide and an isomer of isatin whose potential as MAO inhibitor is well studied.[70-75] Petzer et al has synthesized and evaluated selected 5-alkyloxy- and 5-aryloxyphthalimides as inhibitors of MAO-A and –B.[77] The benzyloxy side chain were found to possess exceptionally potent reversible MAO-B inhibitor properties with most analogues exhibiting IC_{50} values in the lower nM range.[77] Analysis of the structure-activity relationships (SAR) reveals that increasing the length or size of the C5 substituent enhances the MAO-B inhibition potencies of the phthalimide analogues. Halogen substitution on the ring system of the C5 side chain also enhances MAO-B inhibition potency.[77] In addition, certain analogues such as (4-$BrC_6H_4CH_2O$) (**22**) which also possesses potent MAO-A inhibition activities, may act as lead compounds for the design of non-selective reversible MAO-A/B inhibitors.[77]

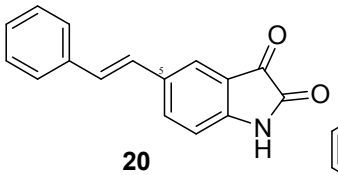

20

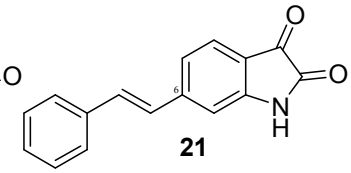

21

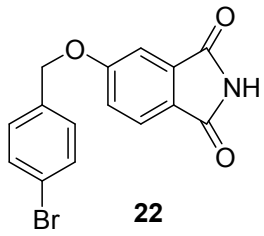

22

The phthalonitriles are the synthetic precursors in the synthesis of the target phthalimides and so these compounds were also evaluated. The nitriles may undergo polar interactions with the active site of MAO and thus facilitate potent inhibition of MAO. The evaluation of a homologous series of benzonitriles established that the phthalonitrile moiety is more optimal for MAO-B inhibition than the corresponding benzonitrile moiety (Figure 1).[21]

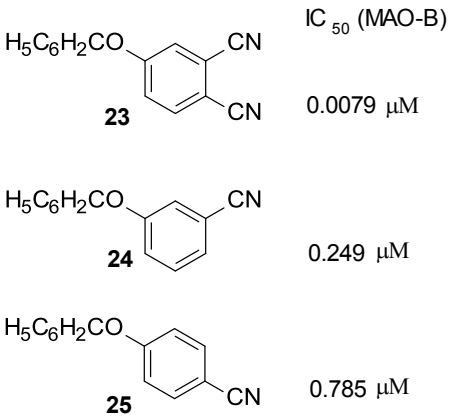

Figure 1: IC_{50} values of three aromatic nitriles

QUINOLINONE DERIVATIVES

The 3,4-dihydro-2(1H)-quinolinone derivatives are found to possess reversible and selective MAO-B inhibitor properties. A series of 3,4-dihydro-2(1H)-quinolinone derivatives were synthesized and evaluated.[78] The alkoxy substituted compounds like benzyloxy, phenylethoxy and phenylpropoxy at the C-6 (**26**) and C-7 (**27**) positions of the 3,4-dihydro-2(1H)-quinolinone moiety was tested.[78] Among these, the benzyloxy side chain has been shown to be the most potent MAO-B inhibitor. The halogen substituents on the benzyloxy phenyl ring further enhances the inhibition properties.[78] The compound **28** was found to posses high MAO-B inhibitor potency with IC_{50} = 2.9 nM and reversible inhibition.[78]

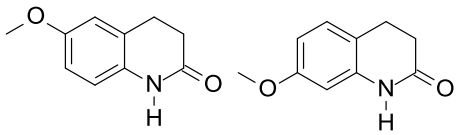

26

27

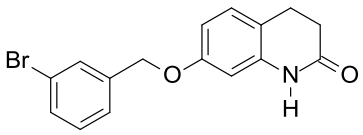

28

SUMMARY AND FUTURE PROSPECTS

MAOs are involved in the oxidation of monoamines neurotransmitters. Hence, their inhibitors are used in the treatment of neurological disorders. The MAOs have two isoenzymes, MAO-A and MAO-B in humans. Many studies have been carried out concerning the physiological importance of these enzymes and potential of their inhibitors. Compounds belonging to different basic moieties like coumarine, chromon, isatin, phthalimide, phthalonitrile etc have been evaluated as potential MAO inhibitors. A wide range of reversible and irreversible inhibitors of MAO-A, MAO-B or both is available. These inhibitors have proved their applications in the diseases like affective disorders, neurodegenerative diseases, stroke and ageing.

Still many questions are remaining to be answered. We still have to understand the complete mechanism of cytoprotective actions. Selection of models is also an important issue. Data obtained with rat as a model for hMAO may not be extrapolated to the human enzymes. Still a long distance has to be covered in the development and continued use of MAO inhibitors as therapeutics.

ACKNOWLEDGMENTS

The author RS is thankful to CSIR, New Delhi, India and G is thankful to UGC, New Delhi, India for financial support.

REFERENCES AND NOTES

1. G.C. Griffith. Amine Oxidase Inhibitors: Their current place in the therapy of cardiovascular diseases. *Circulation* **1960**, 22, 1156-1165.
2. C. Binda, P. Newton-Vinson, F. Hubálek, D.E. Edmondson, A. Mattevi. Structure of human monoamine oxidase B, a drug target for the treatment of neurological disorders. *Nat. Struct. Biol.* **2002**, 9, 22–26.
3. K.F. Tipton, S. Boyce, J. O'Sullivan, G.P. Davey, J. Healy. Monoamine oxidases: certainties and uncertainties. *Curr. Med. Chem.* **2004**, 11, 1965–1982.
4. D.E. Edmondson, A. Mattevi, C. Binda, M. Li, F. Hubálek. Structure and mechanism of monoamine oxidase. *Curr. Med. Chem.* **2004**, 11, 1983–1993.
5. M. Reyes-Parada, A. Fierro, A.P. Iturriaga-Vasquez, B.K. Cassels. Monoamine oxidase inhibition in the light of new structural data. *Curr. Enzyme Inhib.* **2005**, 1, 85–95.
6. S.E. Rigby, J. Basran, J.P. Combe, A.W. Mohsen, H. Toogood, A. van Thiel, M.J. Sutcliffe, D. Leys, A.W. Munro, N.S. Scrutton. Flavoenzyme catalysed oxidation of amines: roles for flavin and proteinbased radicals. *Biochem. Soc. Trans.* **2005**, 33, 754–757.
7. R.H. Haung, R. Faulkner. The role of phospholipid in the multiple functional forms of brain monoamine oxidase. *J. Biol. Chem.* **1981**, 256, 9211-9215.
8. A.W.J. Bach, N.C. Lan, D.J. Bruke, C.W. Abell, M.E. Bembenek, S.W. Kwan, P.H. Seeburg, J.C. Shih. Molecular-cloning of human monoamine oxidase-A and oxidase-B (MAO-A and MAO-B). *FASEB J.* **1988**, 2, A1733-A1733.
9. K. Chen, H.-F. Wu, J.C. Shih. The deduced amino acid sequences of human platelet and frontal cortex monoamine oxidase B are identical. *J. Neurochem.* **1993**, 61, 187-190.
10. T. Okaecwe, A.J. Swanepoel, A. Petzer, J.J. Bergh, J.P. Petzer, Inhibition of monoamine oxidase by 8-phenoxymethylcaffeine derivatives. *Bioorg. Med. Chem.* **2012**, 20, 4336–4347.
11. A.W.J. Bach, N.C. Lan, D.L. Johnson, C.W. Abell, M.E. Bembenek, S.W. Kwan, P.H. Seeburg, J.C. Shih. cDNA cloning of human liver monoamine oxidase A and B: molecular basis of differences in enzymatic properties. *Proc. Natl. Acad. Sci. U.S.A.* **1988**, 85, 4934–4938.
12. J. Wouters. Structural Aspects of Monoamine Oxidase and its Reversible Inhibition. *Curr. Med. Chem*. **1998**, *5*, 137-162.
13. J. Grimsby, N.C. Lan, R. Neve, K. Chen, J.C. Shih. Tissue Distribution of Human Monoamine Oxidase A and B mRNA. *J. Neurochem.* **1990**, *55*, 1166-1169.
14. A.S. Kalgutkar, N. Castagnoli, B. Testa. Selective inhibitors of monoamine oxidase (MAO-A and MAO-B) as probes of its catalytic site and mechanism. *Med. Res. Rev.* **1995**, 15, 325–388.
15. R.M. Geha, I. Rebrin, K. Chen, J.C. Shih. Substrate and inhibitor specificities for human monoamine oxidase A and B are influenced by a single amino acid. *J. Biol. Chem.* **2001**, 276, 9877–9882.
16. P.H. Yu, B.A. Davis, A.A. Boulton. Neuroprotective effects of some monoamine oxidase-B inhibitors against DSP-4-induced noradrenaline depletion in the mouse hippocampus. *J. Neurochem.* **1994**, 63, 1820-1828.

17. T. Thomas. Monoamine oxidase-B inhibitors in the treatment of Alzheimer's disease. *Neurobiol. Aging*. **2000**, 21, 343-348.
18. E.E. Billett. Monoamine Oxidase (MAO) in human peripheral tissues. *NeuroToxicology*. **2004**, 25, 139–148.
19. S.-Y. Son, J. Ma, Y. Kondou, M. Yoshimura, E. Yamashita, T. Tsukihara. Structure of human monoamine oxidase A at 2.2-Å resolution: The control of opening the entry for substrates/inhibitors. *Proc. Natl Acad. Sci. USA*. **2008**, 105, 5739–5744.
20. M.C. Anderson, F. Hasan, J.M. McCrodden, K.F. Tipton. Monoamine oxidase inhibitors and the cheese effect. *Neurochem. Res.* **1993**, 18, 1145–1149.
21. C.I. Manley-King, J.J. Bergh, J.P. Petzer. Monoamine oxidase inhibition by C4-substituted phthalonitriles. *Bioorg. Chem.* **2012**, 40, 114–124.
22. http://www.who.int/features/qa/55/en/ (Accessed on: 01 December 2013)
23. http://www.who.int/mental_health/neurology/chapter_2_neuro_ disorders_public_h_challenges.pdf (Accessed on: 01 December 2013)
24. http://www.who.int/mediacentre/news/releases/2007/pr04/en/ (Accessed on: 01 December 2013)
25. K.C. Teo, S.-L. Ho. Monoamine oxidase-B (MAO-B) inhibitors: implications for disease-modification in Parkinson's disease. *Translat. Neurodegen.* **2013**, 2, 19-28.
26. E.C. Coelho, P.A. Netz, V.P. do Canto, A.P. Cunha, C. Follmer. Beyond topoisomerase inhibition: antitumor 1,4-naphthoquinones as potential inhibitors of human monoamine oxidase (MAO), accepted article **2013**, DOI: 10.1111/cbdd.12255.
27. J. Juárez-Jiménez, E. Mendes, C. Galdeano, C. Martins, D.B. Silva, J. Marco-Contelles, M.C. Carreiras, F.J. Luque, R.R. Ramsay. Exploring the structural basis of the selective inhibition of monoamine oxidase A by dicarbonitrile aminoheterocycles: Role of Asn181 and Ile335 validated by spectroscopic and computational studies**.** *Biochim. Biophys. Acta.* accepted article, **2013**, doi:pii: S1570-9639(13)00378-6. 10.1016/j.bbapap.2013.11.003
28. K.I. Shulman, N. Herrmann, S.E. Walker. Current Place of Monoamine Oxidase Inhibitors in the Treatment of Depression. *CNS Drugs*, **2013**, 27, 789-797.
29. G. Ferino, S. Vilar, M.J. Matos, E. Uriarte, E. Cadoni. Monoamine oxidase inhibitors: Ten years of docking studies. *Curr. Top. Med. Chem.* **2012**, 12, 2145-2162.
30. K.F. Tipton. Enzymology of monoamine oxidase. *Cell. Biochem. Funct.* **1986**, 4, 79–87.
31. H.H. Fernandez, J.J. Chen. Monamine oxidase inhibitors: current and emerging agents for Parkinson disease. *Clin. Neuropharmacol.* **2007**, 30, 150–168.
32. A. Pletscher. The discovery of antidepressants: a winding path. *Experientia*. **1991**, 47, 4–8.
33. P. Dostert, M.S. Benedetti, K.F. Tipton. Interactions of monoamine oxidase with substrates and inhibitors. *Med. Res. Rev.* **1989**, 9, 45–89.
34. M.B.H. Youdim, D. Edmondson, K.F. Tipton. The therapeutic potential of monoamine oxidase inhibitors. *Nat. Rev. Neurosci.* **2006**, 7, 295–309.
35. P. Pacher, V. Kecskemeti. Trends in the development of new antidepressants. Is there a light at the end of the tunnel? *Curr Med. Chem.* **2004**, 11, 925–943.
36. P. Riederer, L. Lachenmayer, G. Laux. Clinical applications of MAO-inhibitors. *Curr. Med. Chem.* **2004**, 11, 2033–2043.
37. E.B. Kearney, J.I. Salach, W.H. Walker, R. Seng, T.P. Singer. Structure of the covalently bound flavin of monoamine oxidase. *Biochem. Biophys. Res. Commun.* **1971**, 42**,** 490–496.
38. M. Naoi, W. Maruyama. Monoamine oxidase inhibitors as neuroprotective agents in age-dependent neurodegenerative disorders, *Curr. Pharmaceut. Des.* **2010**, 16, 2799-2817.
39. A. Gaspar, T. Silva, M. Yanez, D. Vina, F. Orallo, F. Ortuso, E. Uriarte, S. Alcaro, F. Borges. Chromone, a privileged scaffold for the development of monoamine oxidase inhibitors. *J. Med. Chem.* **2011**, 54, 5165–5173.
40. S.M.S. Chauhan, Geetanjali, R. Singh. A mild and efficient synthesis of 10-substituted isoalloxazines in the presence of solid acids. *Ind. J. Heterocycl. Chem.* **2000**, 10, 157-158.
41. S.M.S. Chauhan, R. Singh, Geetanjali. Microwave assisted synthesis of 10-substituted isoalloxazines in the presence of solid acids. *Synth. Commun*. **2003**, 33, 1179-1184.
42. Geetanjali, R. Singh. Effect of intramolecular hydrogen bonding on biomimetic reactions by flavins. *Heterocyclic Commun.* **2013**, 19, 261-263.
43. D.E. Edmondson, A. Mattevi, C. Binda, M. Li, F. Hubálek. Structure and mechanism of monoamine oxidase. *Burger's Medicinal Chemistry, Drug Discovery and Development* , John Wiley & Sons: New York, **2005**.
44. S.S. Erdem, Ö. Karahan, İ. Yıldız, K. Yelekçi. A computational study on the amine-oxidation mechanism of monoamine oxidase: Insight into the polar nucleophilic mechanism. *Org. Biomol. Chem.* **2006**, 4, 646-658.
45. J.R. Miller, D.E. Edmondson. Influence of flavin analogue structure on the catalytic activities and flavinylation reactions of recombinant human liver Monoamine Oxidases A and B. *J. Biol. Chem.* **1999**, 274, 23515–23525.
46. H. Sies. Strategies of antioxidant defense. *Eur. J. Biochem. FEBS*. **1993**, 215, 213-219.
47. Y. Zhu, P.M. Carvey, Z. Ling. Age-related changes in glutathione and glutathione-related enzymes in rat brain. *Brain Res*. **2006**, 1090, 35-44.
48. X. Cao, Z. Wei, G.G. Gabriel, X.M. Li, D.D. Mousseau. Calcium-regulation of monoamine oxidase-A contributes to the production of peroxyradicals in hippocampal cultures: implications for Alzheimer disease-related pathology. *BMC Neuroscience*. **2007**, 8, 73-83.
49. J.C. Shih, K. Chen, M.J. Ridd. Monoamine oxidase: from genes to behavior. *Ann. Rev. Neurosc.* **1999**, 22, 197-217.
50. S. Mandel, O. Weinreb, T. Amit, M.B. Youdim. Mechanism of neuroprotective action of the anti-Parkinson drug rasagiline and its derivatives. *Brain Res. Rev.* **2005**, *48,* 379-387.
51. J. Saura Marti, R. Kettler, M. Da Prada, J.G. Richards. Molecular neuroanatomy of MAO-A and MAO-B. *J. Neural. Transm. Suppl.* **1990**, 32, 49–53.
52. O. Weinreb, T. Amit, O. Bar-Am, M.B. Youdim. Rasagiline: a novel anti-Parkinsonian monoamine oxidase-B inhibitor with neuroprotective activity. *Prog Neurobiol*. **2010**, 92, 330–344.
53. F. Lopez-Munoz, C. Alamo. Monoaminergic neurotransmission: the history of the discovery of antidepressants from 1950s until today. *Curr. Pharm. Des*. **2009**, 15, 1563–1586.
54. M.P.S. Ishar, G. Singh, S. Singh, K.K. Sreenivasan, G. Singh. Design, synthesis, and evaluation of novel 6-chloro-fluorochromone derivatives as potential topoisomerase inhibitor anticancer agents. *Bioorg. Med. Chem. Lett*. **2006**, 16, 1366–1370.
55. S. Alcaro, A. Gaspar, F. Ortuso, N. Milhazes, F. Orallo, E. Uriarte, M. Yanez, F. Borges. Chromone-2- and -3-carboxylic acids inhibit differently monoamine oxidases A and B. *Bioorg. Med. Chem. Lett.* **2010**, 20, 2709–2712.
56. N. Desideri, A. Bolasco, R. Fioravanti, L. Proietti Monaco, F. Orallo, M. Yanez, F. Ortuso, S. Alcaro. Homoisoflavonoids: natural scaffolds with potent and selective monoamine oxidase-B inhibition properties. *J. Med. Chem.* **2011**, 54, 2155–2164.
57. A. Gaspar, J. Reis, A. Fonseca, N. Milhazes, D. Vina, E. Uriarte, M.F. Borges. Chromone 3-phenylcarboxamides as potent and selective MAO-B inhibitors. *Bioorg. Med. Chem. Lett.* **2011**, 21, 707–709.
58. P.O. Patil, S.B. Bari, S.D. Firke, P.K. Deshmukh, S.T. Donda, D.A. Patil. A comprehensive review on synthesis and designing aspects of coumarin derivatives as monoamine oxidase inhibitors for depression and Alzheimer's disease. *Bioorg Med Chem.* **2013**, 21, 2434-2450.
59. L. Pisani, M. Catto, O. Nicolotti, G. Grossi, M. Di Braccio, R. Soto-Otero, E. Mendez-Alvarez, A. Stefanachi, D. Gadaleta, A. Carotti. Fine molecular tuning at position 4 of 2H-chromen-2-one derivatives in the search of potent and selective monoamine oxidase B inhibitors. *Eur. J. Med. Chem.* **2013**, 70, 723-739.

60. M. Gerlach, P. Riederer, M.B.H. Youdim. The molecular pharmacology of L-deprenyl. *Eur. J. Pharmacol.* **1992**, 226, 97–108.
61. K.F. Tipton, S. Boyce, J. O'Sullivan, G.P. Davey, J. Healy. Monoamine Oxidases: Certainties and Uncertainties. *Curr. Med. Chem.* **2004**, 11, 1965-1982.
62. J.S. Fowler, N.D. Volkow, J. Logan, G.J. Wang, R.R. MacGregor, D. Schlyer, A.P. Wolf, N. Pappas, D. Alexoff, C. Shea, E. Dorflinger, L. Kruchowy, K. Yoo, E. Fazzini, C. Patlak. Slow recovery of human brain MAO B after L-deprenyl (Selegeline) withdrawal. *Synaps*. **1994**, 18, 86-93.
63. L.J. Legoabe, A. Petzer, J.P. Petzer. Selected chromone derivatives as inhibitors of monoamine oxidase. *Bioorg. Med. Chem. Lett.* **2012**, 22, 5480–5484.
64. L.J. Legoaba, A. Petzer, J.P. Petzer, Inhibition of monoamine oxidase by selected C6-substituted chromone derivatives. *Eur. J. Med. Chem.* **2012**, 49, 343–353.
65. C. Binda, J. Wang, L. Pisani, C. Caccia, A. Carotti, P. Salvati, D.E. Edmondson, A. Mattevi, Structures of human monoamine oxidase B complexes with selective noncovalent inhibitors: safinamide and coumarin analogs. *J. Med. Chem.* **2007**, 50, 5848–5852.
66. L.J. Legoabe, A. Petzer, J.P. Petzer. Selected C7-substituted chromone derivatives as monoamine oxidase inhibitors. *Bioorg. Chem.* **2012**, 45, 1–11.
67. Y. Zhang, Y. Xu, S. Tan, L. Xu, X. Qian. Rapid and sensitive fluorescent probes for monoamine oxidases B to A at low concentration. *Tetrahedron Lett.* **2012**, 53, 6881-6884.
68. M.J. Matos, D. Vina, E. Quezada, C. Picciau, G. Delogu, F. Orallo, L. Santana, E. Uriarte. A new series of 3-phenylcoumarins as potent and selective MAO-B inhibitors. *Bioorg. Med. Chem. Lett.* **2009**, 19, 3268-3270.
69. C. Gnerre, M. Catto, F. Leonetti, P. Weber, P.-A. Carrupt, C. Altomare, A. Carotti, B. Testa. Inhibition of monoamine oxidases by functionalized coumarin derivatives: biological activities, QSARs, and 3D-QSARs. *J. Med. Chem.* **2000**, 43, 4747–4758.
70. F. Hubálek, C. Binda, A. Khalil, M. Li, A. Mattevi, N. Castagnoli, D.E. Edmondson. Demonstration of Isoleucine 199 as a Structural Determinant for the Selective Inhibition of Human Monoamine Oxidase B by Specific Reversible Inhibitors. *J. Biol. Chem.* **2005**, 280, 15761-15766.
71. C.I. Manley-King, J.J. Bergh, J.P. Petzer. Inhibition of monoamine oxidase by selected C5- and C6-substituted isatin analogues. *Bioorg. Med. Chem.* **2011**, 19, 261–274.
72. E.M. Van der Walt, E.M. Milczek, S.F. Malan, D.E. Edmondson, N. Castagnoli Jr, J.J. Bergh, J.P. Petzer. Inhibition of monoamine oxidase by (*E*)-styrylisatin analogues. *Bioorg. Med. Chem. Lett.* **2009**, 19, 2509-2513.
73. V Raj. Review on CNS activity of isatin derivatives. *Int. J. Curr. Pharmaceut. Res.* **2012**, 4, 1-9.
74. A.E. Medvedev, A.S. Ivanov, N.S. Kamyshanskaya, A.Z. Kirkel, T.A. Moskvitina, V.Z. Gorkin, N.Y. Li, VYu, Marshakov. Interaction of indole derivatives with monoamine oxidase A and B. Studies on the structure-inhibitory activity relationship. *Biochem. Mol. Biol. Int.* 1995, 36, 113-122.
75. I. Virsis, B.A. Grinberg, D.G. Tsedere, A.A. Prinkulis. Relationship between the structure of 2-indolinones and 2, 3-indolinediones and their biological activity. *Pharmaceut. Chem. J.* **1985**, 19, 554-557.
76. M.K. Haergreaves, J.G. Pritchard, H.R. Dave. Cyclic carboxylic monoimides. *Chem. Res*. **1970**, 70, 439–469.
77. C.I. Manley-King, J.J. Bergh, J.P. Petzer. Inhibition of monoamine oxidase by C5-substituted phthalimide analogues. *Bioorg. Med. Chem.* **2011**, 19, 4829–4840.
78. L. Meiring, J.P. Petzer, A. Petzer. Inhibition of monoamine oxidase by 3,4-dihydro-2(1H)-quinolinone derivatives. *Bioorg. Med. Chem. Lett.* **2013**, 23, 5498–5502.

Journal of
Materials Chemistry B

RSC Publishing

PAPER

View Article Online
View Journal | View Issue

Phase control of nanostructured iron oxide for application to biosensor†

Cite this: *J. Mater. Chem. B*, 2013, **1**, 464

Rachna Sharma,[ac] Ved Varun Agrawal,*[a] A. K. Srivastava,[a] Govind,[a] Lata Nain,[b] Mohd Imran,[a] Soumya Ranjan Kabi,[b] R. K. Sinha[c] and Bansi D. Malhotra*[d]

Received 1st October 2012
Accepted 9th October 2012

DOI: 10.1039/c2tb00192f

www.rsc.org/MaterialsB

We report results of the studies relating to the phase transformation of bare Fe_3O_4 nanoparticles (NPs) to α-Fe_2O_3 NPs obtained during electrophoretic film deposition onto indium-tin oxide coated glass plates. The *in situ* oxidation of NPs during electrophoretic deposition can be circumvented using surface passivation of the Fe_3O_4 NPs with an organic shell (carbon) as well as an inorganic shell (silica), while retaining the biocompatibility of the Fe_3O_4 NPs. XRD and XPS studies reveal the transformation of Fe_3O_4 NPs to α-Fe_2O_3 NPs upon electrophoretic deposition, and the retention of the phase of the Fe_3O_4 NPs upon encapsulation with carbon and silica, respectively. The results of SEM studies indicate decreased agglomeration of the Fe_3O_4 NPs upon encapsulation during film deposition. Attempts have been made to compare the characteristics of cholesterol biosensors fabricated using Fe_3O_4@C and α-Fe_2O_3 NPs, respectively. The Fe_3O_4@C NPs based cholesterol biosensor shows response time of 60 s, a linearity range of 25–500 mg dl^{-1}, a sensitivity of 193 nA mg^{-1} dl cm^{-2} and a Michaelis–Menten constant of 1.44 mg dl^{-1}.

Introduction

Nanostructured iron oxides (Fe_3O_4, γ-Fe_2O_3 and α-Fe_2O_3) owing to their multifunctional properties, such as small size, superparamagnetism, low toxicity *etc.*, are being widely investigated for applications in high-density information storage,[1] electronic devices,[2] ferrofluid technology,[3] catalysis,[4] pharmaceuticals[5] and biotechnology.[6] Among these, the application of nanostructured iron oxides in clinical diagnostics and biomedicine have aroused much interest because of their biocompatibility and stability under physiological conditions.[7,8] They can also be used as contrast agents in magnetic resonance imaging,[9,10] as mediators in hyperthermia,[11] as carriers for guided drug delivery[12–14] and as immobilization supports for desired biomolecules for the diagnosis of various pathogens and diseases, and estimation of various biochemical analytes such as glucose, urea *etc.*[15–17] Besides this, the particle size of the nanostructured iron oxide can be controlled to a similar size as that of a biomolecule (protein 5–50 nm; virus 20–450 nm; cell 10–100 μm).[18]

Despite several advantages, the susceptibility of Fe_3O_4 NPs towards oxidation and their tendency to agglomerate due to strong dipole–dipole attractions between particles, have limited their applications to date.[19] It is anticipated that encasing colloids in a shell of a different material may perhaps protect the core from extraneous chemical and physical changes. Core–shell nanostructures are known to exhibit improved physical and chemical properties over their single-component counterparts, and hence are potentially useful for a range of applications. To improve the stability of the deposited NPs, many molecules, such as carbon and silica, have been considered as interesting encapsulants.[20–22] Compared to polymer and inorganic shells, carbon shells exhibit much higher stability in various chemical and physical environments such as acid or base media, as well as at high temperatures and pressures.[23] Thus, carbon coated Fe_3O_4 NPs may perhaps ensure prolonged activity of the biomolecules and enhanced stability of the biosensors.

Among various methods, the formation of nanocrystalline films using electrophoretic deposition has recently gained much interest since it is cost effective[24] and can be used to obtain uniform thin films by optimizing parameters such as solution concentration, applied potential, pH of the solution *etc.*[24,25] The fabrication of nanostructured iron oxide films using electrophoretic deposition and its characterization may perhaps yield important information relating to the phase change of nanostructured iron oxide. Also, the utilization of

[a]*National Physical Laboratory, New Delhi-110012, India. E-mail: agrawalvv@nplindia.org; Tel: +91-11-45609489*

[b]*Division of Microbiology, Indian Agricultural Research Institute, New Delhi-110012, India*

[c]*Department of Applied Physics, Delhi Technological University, New Delhi-110042, India*

[d]*Department of Biotechnology, Delhi Technological University, New Delhi-110042, India. E-mail: bansi.malhotra@gmail.com*

† Electronic supplementary information (ESI) available: SEM studies showing the immobilization of cholesterol oxidase onto nanostructured iron oxide films, shelf life, reproducibility and response time studies of the fabricated cholesterol biosensors. See DOI: 10.1039/c2tb00192f

nanostructured iron oxide films for the fabrication of biosensors may perhaps result in enhanced electrocatalytic activity of the given biomolecule and improved sensitivity for detection of the desired analyte.

We report a novel method of controlling the phase of iron oxide NPs obtained during electrophoretic deposition. It is shown that the phase of the nanostructured iron oxide during electrophoretic deposition can be tuned to the desired requirements by using bare Fe_3O_4 NPs or capped Fe_3O_4 NPs as the starting material. The nanocrystalline films of Fe_3O_4@C and α-Fe_2O_3 NPs have been employed for the fabrication of a biosensor using cholesterol oxidase as a model enzyme and the biosensing characteristics have been investigated using electrochemical techniques such as cyclic voltammetry and electrochemical impedance spectroscopy. To the best of our knowledge, there is as yet no report on the phase transformation of Fe_3O_4 NPs during electrophoretic deposition, its prevention and further application in biosensing.

Experimental methods

Materials and methods

Ferrous sulphate heptahydrate ($FeSO_4 \cdot 7H_2O$), ferric chloride ($FeCl_3$), sodium hydroxide (NaOH), fructose ($C_6H_{12}OH$) powder and tetraethyl orthosilicate ($Si(OC_2H_5)_4$) have been purchased from Sigma-Aldrich. All reagents are of analytical grade and have been used without further purification. De-ionized water (Milli-Q 10 TS) with resistivity >18.2 MΩ cm has been used for preparing all aqueous solutions. Indium-tin-oxide (ITO) coated glass plates have been obtained from Balzers, UK, (Baltracom 247 ITO, 1.1 mm thick) with a sheet resistance and transmittance of 25 Ω sq^{-1} and 90%, respectively. Cholesterol powder and cholesterol oxidase (EC 1.1.36 from *Pseudomonas fluorescens*) with a specific activity of 26 U mg^{-1} have been purchased from Sigma-Aldrich (USA). The stock solution of cholesterol has been prepared in 10% triton X-100 and stored at 4 °C.

(a) Preparation of Fe_3O_4, Fe_3O_4@C and Fe_3O_4@SiO_2 NPs

(i) Fe_3O_4 NPs. The Fe_3O_4 NPs have been prepared *via* hydrolytic reaction based on chemical co-precipitation of metal salts with an alkali, as reported earlier.[26] Briefly, 0.32 M $FeSO_4 \cdot 7H_2O$ and 0.64 M $FeCl_3$ are added to 10 mL of deoxygenated water (containing 12.1 N HCl) with continuous stirring at 30 °C. The solution containing iron salts is dropwise added to 100 mL of NaOH solution (1.5 M) with vigorous stirring at 30 °C. The mixture is then stirred for an additional 30 min, resulting in the appearance of a black precipitate. The particles are washed by centrifugation at 3500 rpm for 30 min and the supernatant is removed by decantation. The particles are then redispersed in 200 mL of deoxygenated water and are stabilized by making the pH of the sol 3.5 using HCl.

Furthermore, the Fe_3O_4 NPs are subjected to high temperature and pressure using autoclaves. 30 mL of the above synthesized NPs are autoclaved at 180 °C for 4 h.[27]

(ii) Fe_3O_4@C NPs. Carbon capped Fe_3O_4 NPs have been prepared *via* hydrothermal carbonization reaction. For this purpose, 10 mmol of fructose powder is added to 30 mL of Fe_3O_4 NPs sol[23,28,29] and the mixture is autoclaved at 180 °C for 4 h. At this temperature, fructose melts and carbonization of fructose occurs, resulting in a carbon shell over the Fe_3O_4 NPs.[30] The reaction mixture is cooled under ambient conditions. The synthesized product is washed by centrifugation at 3500 min^{-1} and the supernatant is removed by decantation. No change in color of the sol is observed and the pH of the NPs redispersed in water is recorded as 8.0.

(iii) Fe_3O_4@SiO_2 NPs. To 10 mL of Fe_3O_4 NPs sol (diluted with 40 mL of iso-propanol) are added 1 mL of ammonia and 1 mL of tetraethyl orthosilicate (TEOS).[31] The mixture is stirred at 30 °C for 4 h and a change in colour from dark brown to light brown is observed upon completion of the reaction. The synthesized NPs are collected by centrifugation at 3500 min^{-1} and the pH of the NPs redispersed in water is recorded as 9.6.

(b) Preparation of nanostructured iron oxide films

The nanocrystalline films of iron oxide are deposited onto ITO coated glass plates using a two-electrode system with platinum as the auxiliary electrode and an ITO-coated glass plate as the deposition electrode. The electrophoretic deposition involves charged particles in a suspension being deposited onto an electrode under the influence of an applied electric field. Thus, the use of surfactant is avoided and the charge on the surface of the NPs is introduced by adjusting the pH of the suspension to obtain a stable sol. The Fe_3O_4 NPs carry a positive charge at pH 3.5 since the isoelectric point of Fe_3O_4 is 6–7.[32–34] Cationic NPs are deposited onto the ITO-coated glass plate at the cathode terminal. Application of even a small voltage leads to electrolysis of water, producing hydrogen and oxygen gas, which hinder continuous flow of the NPs and affect the film uniformity.[25] Thus, a mixture of methanol–water (2 : 1) is utilized for deposition of the desired nanocrystalline film. The conditions for obtaining uniform films have been optimized for various parameters such as applied potential, concentration, deposition time, *etc.*, and uniform films of Fe_3O_4 NPs and Fe_3O_4 NPs (autoclaved) are obtained upon application of a 5 V potential for 30 s (Scheme 1).

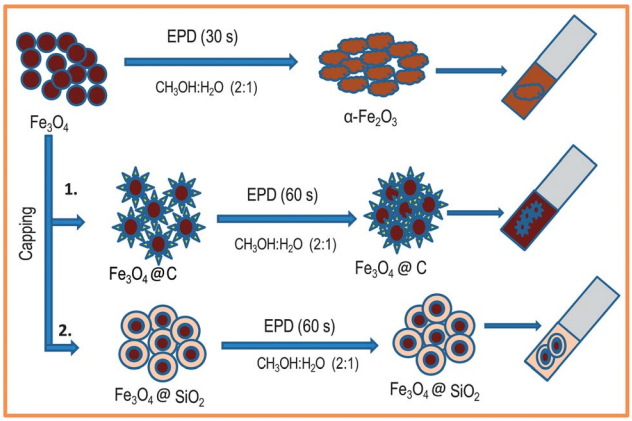

Scheme 1

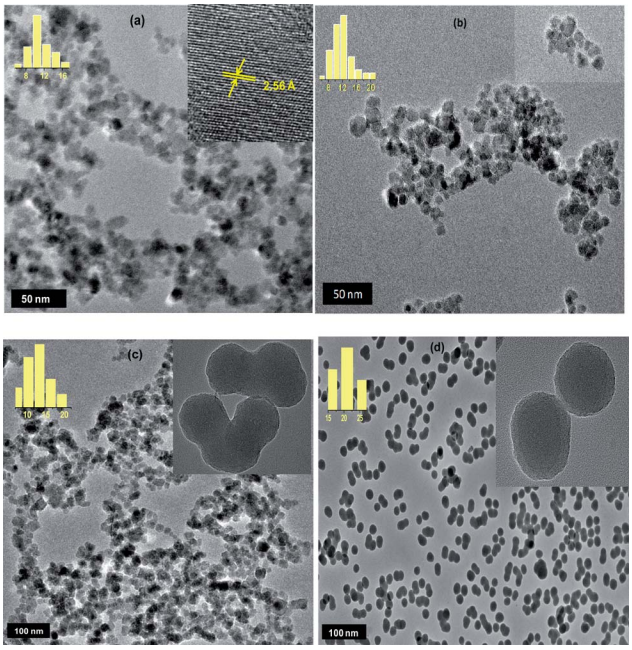

Fig. 1 TEM micrographs of: (a) Fe_3O_4 NPs (inset: high-resolution image of a single particle); (b) Fe_3O_4 NPs (autoclaved); (c) Fe_3O_4@C NPs; (d) Fe_3O_4@SiO_2 NPs.

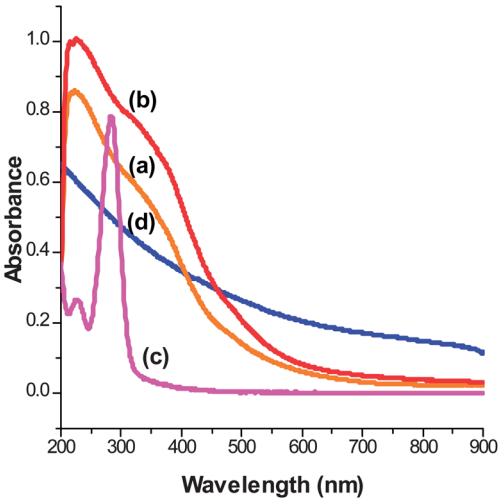

Fig. 2 UV-vis absorption spectra of: (a) Fe_3O_4 NPs; (b) Fe_3O_4 NPs (autoclaved); (c) Fe_3O_4@C NPs; (d) Fe_3O_4@SiO_2 NPs.

The Fe_3O_4@C and Fe_3O_4@SiO_2 NPs have been deposited in a methanol–water (2 : 1) mixture. Although the Fe_3O_4@C NPs are stable at 8.0 pH, no deposition occurs, indicating that the NPs carry negligible charge. A positive charge on the NPs is then introduced by adjusting the pH to 3.5 and a nanocrystalline film is deposited onto the ITO-coated glass plate at the cathode terminal by applying an optimized potential of 10 V for 60 s. Interestingly, the Fe_3O_4@SiO_2 NPs carry negative charge at pH 9.6 (as the iso-electric point of SiO_2 NPs is ~2),[35] thus a nanocrystalline film is deposited onto the ITO-coated glass plates at the anode terminal upon application of a 10 V potential for 60 s.

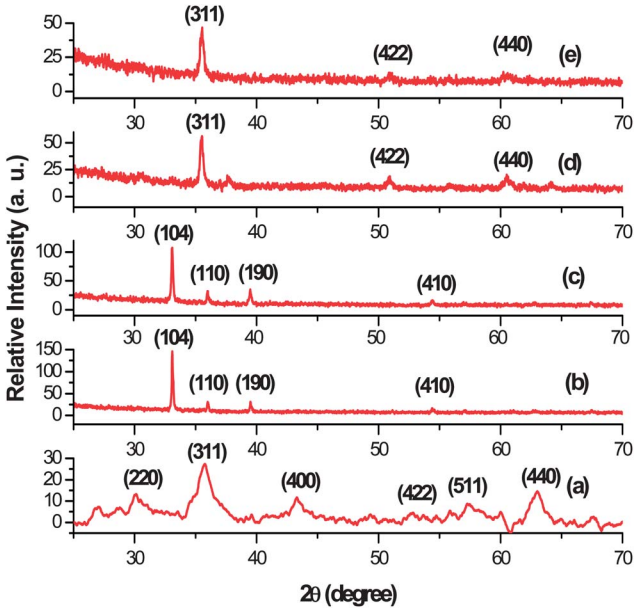

Fig. 3 XRD spectra of: (a) Fe_3O_4 NPs; (b) film obtained from Fe_3O_4 NPs; (c) film obtained from Fe_3O_4 NPs (autoclaved); (d) film obtained from Fe_3O_4@C NPs; (e) film obtained from Fe_3O_4@SiO_2 NPs.

(c) Fabrication of nanostructured iron oxide film based bioelectrodes

ChOx is physisorbed onto the nanostructured iron oxide films. For this purpose, 20 μL of freshly prepared ChOx solution (1 mg mL^{-1}) is spread onto the α-Fe_2O_3 and Fe_3O_4@C nanocrystalline films. ChOx immobilized iron oxide films are incubated at 27 °C for 2 h and at 4 °C for 12 h.[36] Later, weakly bound ChOx are removed by washing these films with 100 mM PBS buffer containing 0.05% Tween-20.[37] These films are stored at 4 °C when not in use. The fabricated ChOx/Fe_3O_4@C film/ITO and ChOx/α-Fe_2O_3 film/ITO bioelectrodes have been characterized *via* SEM, CV and EIS studies and the enzyme activity measurements for the fabricated bioelectrodes have been carried out using CV and EIS techniques.

(d) Characterization

TEM micrographs have been recorded using a high-resolution transmission electron microscope (HR-TEM, Tecnaii-G2F30 STWIN). Samples for TEM are prepared on 200 mesh carbon coated copper grids. A drop of iron oxide NPs sol is carefully placed on the copper grid surface and is then dried under ambient conditions. The structure of the powder samples and nanostructured iron oxide films have been analyzed using X-ray powder diffraction (XRD, Cu-Kα radiation, Rigaku) over the 2θ range from 25–70° using a monochromatized X-ray beam with Cu-Kα radiation (λ = 1.54 Å). XPS measurements have been carried out in a Perkin Elmer XPS chamber (PHI 1257) with a base pressure of 5×10^{-9} torr. The chamber is equipped with a dual anode Mg-K_α (energy 1253.6 eV) and Al-K_α (energy 1486.6 eV) X-ray source and a high-resolution hemispherical energy analyzer for energy resolved electron detection. An Mg-K_α X-ray source has been used for this study. The samples are

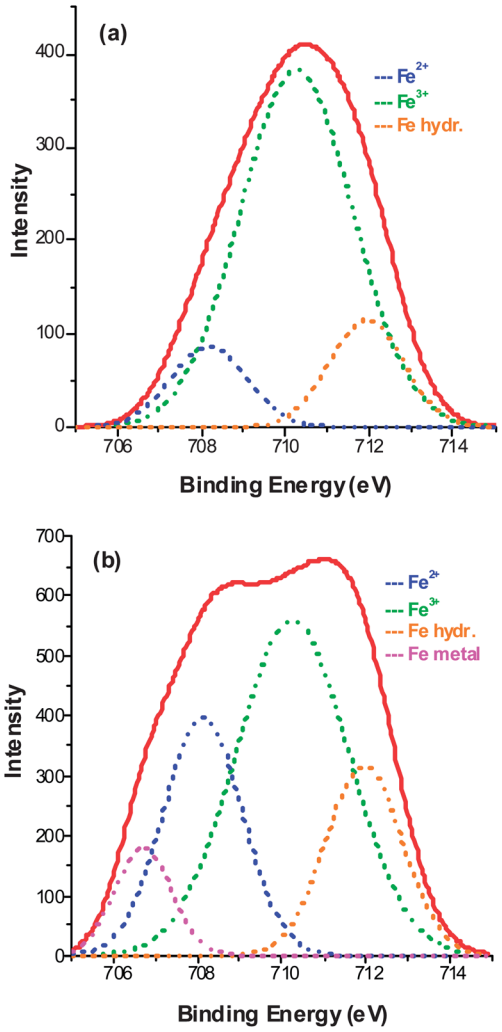

Fig. 4 Deconvoluted XPS spectra of Fe $2p_{3/2}$ acquired for: (a) α-Fe_2O_3 film, and (b) Fe_3O_4@C film.

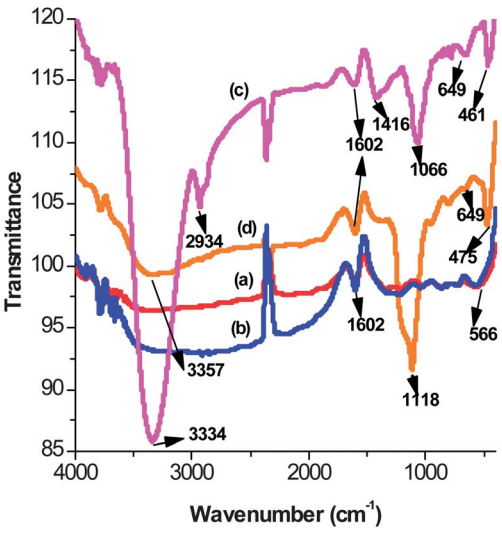

Fig. 5 FTIR spectra of: (a) α-Fe_2O_3 NPs film obtained from Fe_3O_4 NPs; (b) α-Fe_2O_3 NPs film obtained from Fe_3O_4 NPs (autoclaved); (c) film of Fe_3O_4@C NPs; (d) film of Fe_3O_4@SiO_2 NPs.

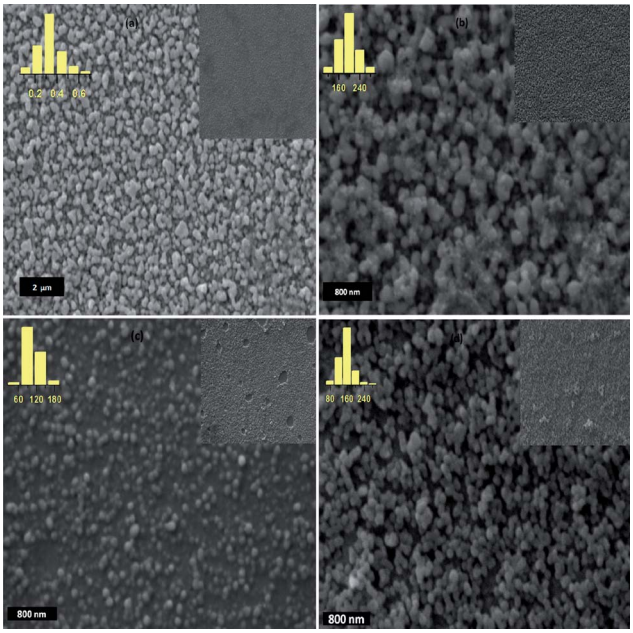

Fig. 6 SEM micrograph of: (a) α-Fe_2O_3 NPs film obtained from Fe_3O_4 NPs; (b) α-Fe_2O_3 NPs film obtained from Fe_3O_4 NPs (autoclaved); (c) film of Fe_3O_4@C NPs; (d) film of Fe_3O_4@SiO_2 NPs.

sputtered with 4 keV argon ions to remove surface contamination prior to XPS studies. The absorption studies of the bare and encapsulated NPs have been conducted on a Phoenix–2200 DPCV UV-Vis spectrophotometer in the wavelength range 200–900 nm. The transmission studies of the nanostructured iron oxide films in the infrared region have been carried out on a Perkin Elmer, Spectrum BX II spectrophotometer in the wavenumber range of 400–4000 cm^{-1}. The morphological changes of the nanocrystalline films upon enzyme immobilization have been studied using SEM (LEO 440 scanning electron microscope).

The electrochemical experiments have been conducted on an Autolab PGSTAT 302N System (Ecochemie, The Netherlands) in a three electrode system. All electrochemical experiments have been carried out in a cell containing 15 mL of 100 mM phosphate buffer solution (PBS) containing 0.9% NaCl and 5 mM $K_3/K_4[Fe(CN)_6]$ as a redox probe and using a platinum wire as auxiliary, a Ag/AgCl wire as reference, and the nanostructured iron oxide films on ITO as the working electrode.

Results and discussion

(a) TEM studies of iron oxide NPs

Fig. 1(a) shows a TEM micrograph of the Fe_3O_4 NPs, indicating formation of nearly monodispersed nanocrystals with an average diameter of 10 nm. The lattice spacing of ~2.56 Å obtained from the fringe pattern (Inset Fig. 1(a)), matches with the *d*-value (2.56 Å), corresponding to the (311) *hkl* plane of the Fe_3O_4 nanocrystals (JCPDS file: 890951). However, after hydrothermal treatment, the average size of the NPs increases by about two nm (Fig. 1(b)). The increase in the average particle size of autoclaved NPs and the decrease in the number of

Table 1 Optical density of Gram positive (*Providencia* sp.) and Gram negative (*Bacillus* sp.) bacteria as a function of time in the presence of Fe_3O_4@C and α-Fe_2O_3 films

		Optical density						
Nanostructured film	Bacteria	0 h	2 h	4 h	6 h	8 h	10 h	12 h
Fe_3O_4@C film	*Providencia* sp.	0.01	0.03	0.07	0.15	0.28	0.43	0.56
Fe_3O_4@C film	*Bacillus* sp.	0.02	0.09	0.24	0.57	0.68	0.73	0.89
α-Fe_2O_3 film	*Providencia* sp.	0.03	0.06	0.09	0.14	0.19	0.54	0.63
α-Fe_2O_3 film	*Bacillus* sp.	0.02	0.08	0.26	0.58	0.65	0.82	0.85

smaller NPs indicates the growth of NPs at the expense of smaller NPs, suggesting Ostwald ripening[38] of NPs. Also, the edges and roughness observed on the NPs' surfaces are reduced upon hydrothermal treatment, and the NPs assume a spherical shape. Thus, the size and smoothness of the NPs can be tailored using hydrothermal treatment.

Upon capping the Fe_3O_4 NPs with carbon and silica, the average particle size of the Fe_3O_4 NPs increased to 14 nm and 20 nm (Fig. 1(c) and (d)) suggesting the formation of a carbon and silica shell, respectively, over the Fe_3O_4 NPs. Due to the formation of the thick shell of silica, the Fe_3O_4 NPs are well separated and uniform (inset Fig. 1(d)) while some agglomeration has been observed in the case of the Fe_3O_4@C NPs (inset Fig. 1(c)).

(b) UV-visible studies of Fe_3O_4, Fe_3O_4 (autoclaved), Fe_3O_4@C and Fe_3O_4@SiO_2 NPs

Fig. 2 shows absorption spectra of the Fe_3O_4 NPs, Fe_3O_4 NPs (autoclaved), Fe_3O_4 NPs capped with carbon and Fe_3O_4 NPs capped with silica in the UV-Vis wavelength range. The absorption onset of the Fe_3O_4 NPs is at ~600 nm (Fig. 2(a)). Because of the quantum size effect, this onset value is blue-shifted by 100 nm as compared to that of the bulk Fe_3O_4.[39] The band near 300 nm corresponds to ligand field transitions of Fe^{3+} and the shoulder peak around 480 nm corresponds to excitation of the Fe–Fe pair.[40] A similar spectrum is observed for the autoclaved Fe_3O_4 NPs (Fig. 2(b)). The higher absorption for the autoclaved NPs for the same concentration may be due to an increase in particle size of the NPs upon hydrothermal treatment.

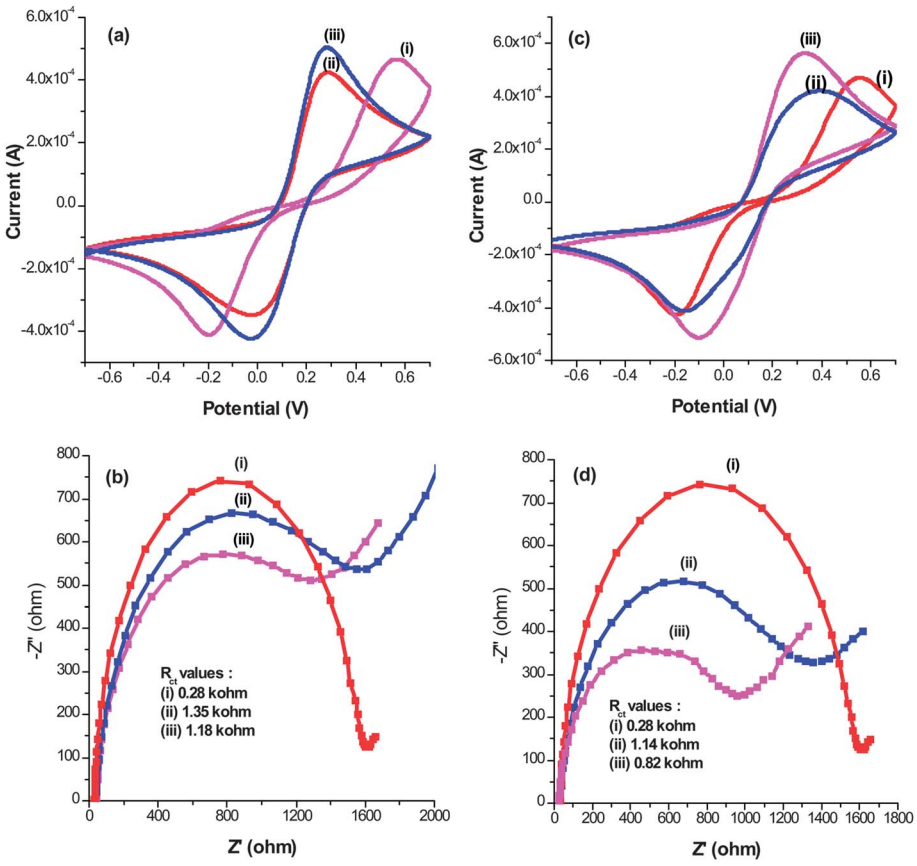

Fig. 7 (a) CV curves for the ITO electrode (i), Fe_3O_4@C film/ITO electrode (ii), and ChOx/Fe_3O_4@C film/ITO bioelectrode (iii); (b) Nyquist plots for the ITO electrode (i), Fe_3O_4@C film/ITO electrode (ii), and ChOx/Fe_3O_4@C film/ITO bioelectrode (iii); (c) CV curves for the ITO electrode (i), α-Fe_2O_3 film/ITO electrode (ii), and ChOx/α-Fe_2O_3 film/ITO bioelectrode (iii); (d) Nyquist plots for the ITO electrode (i), α-Fe_2O_3 film/ITO electrode (ii), and ChOx/α-Fe_2O_3 film/ITO bioelectrode (iii).

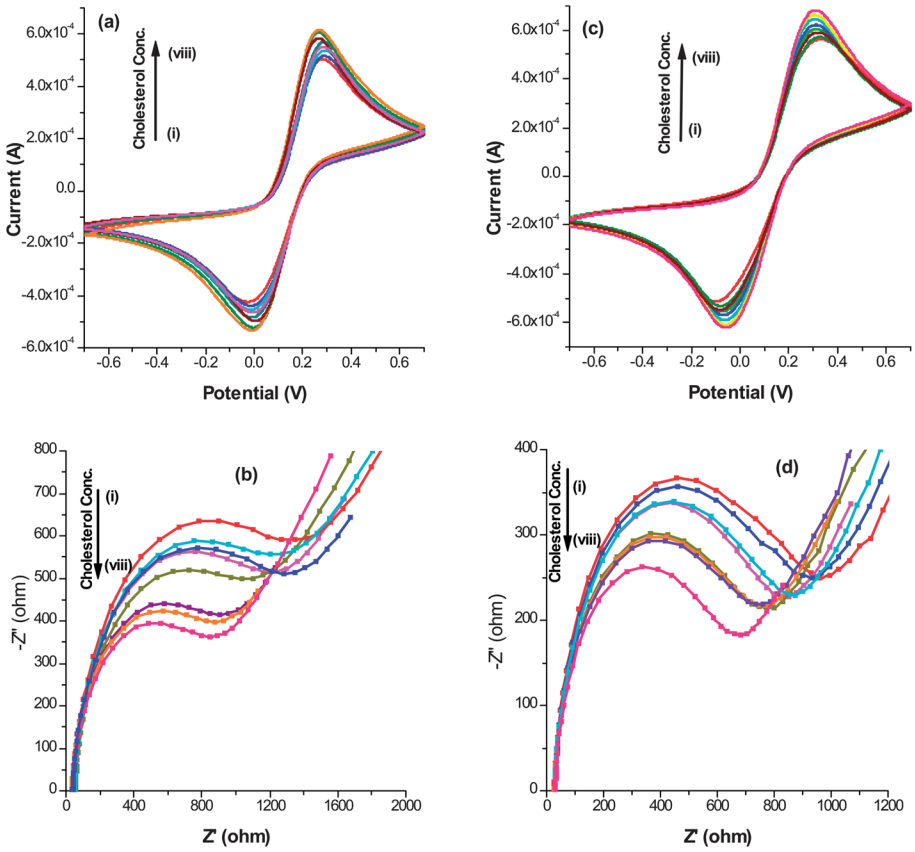

Fig. 8 (a) CV response studies of ChOx/Fe_3O_4@C film/ITO bioelectrode; (b) EIS response studies of ChOx/Fe_3O_4@C film/ITO bioelectrode; (c) CV response studies of ChOx/α-Fe_2O_3 film/ITO bioelectrode and (d) EIS response studies of ChOx/α-Fe_2O_3 film/ITO bioelectrode with different cholesterol concentrations (mg dl^{-1}): (i) 10; (ii) 25; (iii) 50; (iv) 100; (v) 200; (vi) 300; (vii) 400 and (viii) 500.

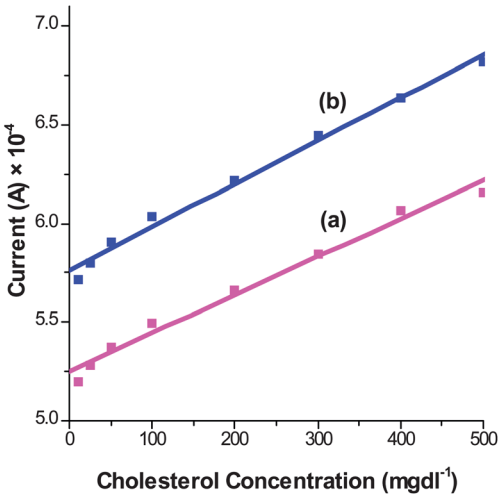

Fig. 9 Linear calibration plots obtained using CV data for: (a) ChOx/Fe_3O_4@C film/ITO bioelectrode and (b) ChOx/α-Fe_2O_3 film/ITO bioelectrode.

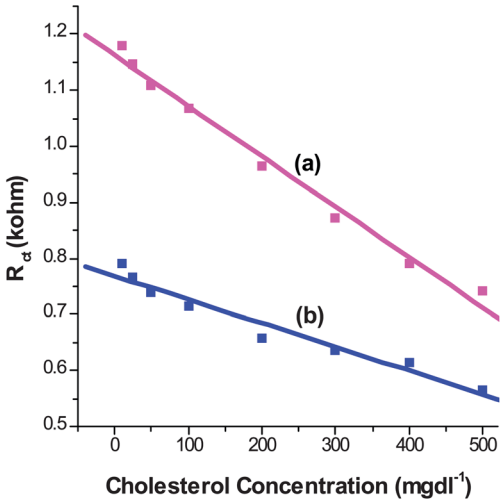

Fig. 10 Linear calibration plots obtained using EIS data for: (a) ChOx/Fe_3O_4@C film/ITO bioelectrode and (b) ChOx/α-Fe_2O_3 film/ITO bioelectrode.

Upon encapsulation of the Fe_3O_4 NPs with carbon and silica shells, the scattering from the NPs increases due to an increase in particle size.[41] Importantly, this increase in scattering is specific to the wavelength range of 500–900 nm. On the contrary, the absorption at lower wavelengths is suppressed due to capping of the Fe_3O_4 NPs. Such crossover in absorption spectra for the same concentration suggests surface modification of the Fe_3O_4 NPs. For the carbon capped Fe_3O_4 NPs, the characteristic spectrum from the Fe_3O_4 NPs is retained (Fig. 2(c)), but the partial suppression of the absorption

Table 2 Comparison table summarizing the characteristics of cholesterol biosensors based on nanostructured metal oxide films

Electrode	Transducer	Linear range (mg dL^{-1})	Sensitivity	K_m value	Response time (s)	Reproducibility	Shelf life (days)	Ref.
CeO_2/ITO	Cyclic voltammetry	10–400	—	2.08 mM	15	—	—	62
Chitosan–SnO_2/ITO	Cyclic voltammetry	5–400	34.7 μA mg^{-1} dl cm^{-2}	3.8 mM	5	—	80	63
ZnO/Au	Cyclic voltammetry	25–400	45.7 nA mg^{-1} dl cm^{-2}	2.1 mM	15	—	70	64
ZnO/ITO	Cyclic voltammetry	5–400	59.0 nA mg^{-1} dl cm^{-2}	0.03 mM	10	20	85	65
Fe_3O_4 NPs	Spectroscopy	50–200	—	0.45 mM	—	—	10	66
Fe_3O_4@C/ITO	Cyclic voltammetry Impedance spectroscopy	25–400	193 nA mg^{-1} dL cm^{-2} 0.90 Ω mg^{-1} dL cm^{-2}	0.03 mM	60	25	70	Present work
α-Fe_2O_3/ITO	Cyclic voltammetry Impedance spectroscopy	50–400	218 nA mg^{-1} dL cm^{-2} 0.42 Ω mg^{-1} dL cm^{-2}	0.04 mM	60	20	56	

intensity suggests the capping of the Fe_3O_4 NPs with a thin layer of carbon. Upon capping the Fe_3O_4 NPs with silica, an absence of the characteristic absorption from Fe_3O_4 NPs (200–450 nm) can be seen[42,43] (Fig. 2(d)). This suggests complete coverage of the Fe_3O_4 NPs with a thick shell of silica, which increases the overall scattering from the NPs, while on the contrary, it completely suppresses the absorption from the Fe_3O_4 NPs.

(c) X-Ray diffraction studies of Fe_3O_4 NPs and nanostructured iron oxide films

Fig. 3(a) shows an XRD pattern of the bare Fe_3O_4 NPs. The diffraction peaks obtained correspond to the cubic spinel structure of Fe_3O_4.[44,45] The average particle diameter of 10.6 nm calculated using the Debye–Scherrer formula (from the most intense peak at $2\theta = 35.57^\circ$) is in agreement with the particle size determined by statistical analysis of the TEM images, indicating that each individual particle is a single crystal.[46]

Fig. 3(b) and (c) show XRD spectra of the iron oxide films prepared from the Fe_3O_4 NPs and Fe_3O_4 NPs (autoclaved), respectively. The diffraction peaks of the films match α-Fe_2O_3 (JCPDS file: 890599-96). In spite of the Fe_3O_4 NPs being the starting material for the film deposition, the XRD spectra obtained from the deposited film corresponds to that of α-Fe_2O_3. This change of phase can be ascribed to the oxidation of NPs during electrophoretic deposition in the water–methanol mixture. The hydroxyl (OH) groups resulting from the dissociation of water and methanol molecules get adsorbed on the surface of magnetite NPs and catalyze their oxidation process.[47] In addition, the application of a potential above the oxidation potential of Fe^{2+} (*i.e.* 0.77 V) results in the modified nucleation rate (kinetics), enhanced diffusion of species and gradient of the lattice constant, which drives the nucleation of α-Fe_2O_3 NPs.[47,48] Also, uncapped Fe_3O_4 NPs undergo rapid agglomeration during deposition, their large size favors the oxidation to hematite over magnetite.[49] To the best of our knowledge, a change in phase of Fe_3O_4 NPs obtained during electrophoretic deposition occurring in such a short span of time (30 s) has not been reported in the literature.

To control this oxidation step, the Fe_3O_4 NPs have been encapsulated with an organic carbon shell and an inorganic silica shell, as mentioned in the preceding section. Fig. 3(d) and (e) show XRD spectra of the films obtained from the Fe_3O_4@C NPs and Fe_3O_4@SiO_2 NPs, respectively. The diffraction peaks obtained from the films of the encapsulated NPs match those of Fe_3O_4 (with a slight shift), indicating that no oxidation occurs during the deposition of films upon capping the Fe_3O_4 NPs with organic and inorganic shells. After capping, the surface of the Fe_3O_4 NPs has been passivated, which circumvents the adsorption of hydroxyl groups onto their surface and thus prevents their phase change. Thus, an additional oxidation step during electrophoretic deposition of Fe_3O_4 NPs can be circumvented using surface passivation.

(d) X-Ray photoelectron studies of α-Fe_2O_3 and Fe_3O_4@C films

To further confirm the phase of the NPs before and after electrophoretic deposition, XPS core level spectra of α-Fe_2O_3 and Fe_3O_4@C films have been acquired for Fe 2p and the deconvoluted Fe $2p_{3/2}$ spectra are shown in Fig. 4. Background subtraction and peak fitting of the spectra have been done using the Shirley function and Gaussian function, respectively, and the spectra have been referenced to the C 1s main peak at 284.6 eV. A considerable difference can be seen in the two spectra for the α-Fe_2O_3 and Fe_3O_4@C films.

Fig. 4(a) shows the deconvoluted XPS Fe $2p_{3/2}$ spectra of the α-Fe_2O_3 film. The peak fitting of the spectra reveals that Fe^{2+} and Fe^{3+} ions are present in the ratio of 1 : 6.7. This shows that the film mostly contains Fe_2O_3 with traces of Fe_3O_4, which suggests the *in situ* oxidation of uncapped Fe_3O_4 NPs during electrophoretic deposition. However, the deconvolution and peak fitting of the Fe $2p_{3/2}$ spectra obtained for the Fe_3O_4@C film reveals that the ratio of Fe^{2+} and Fe^{3+} ions is 1 : 2 (Fig. 4(b)). This shows that the Fe_3O_4 NPs retain their phase upon encapsulation with carbon and the film consists of Fe_3O_4 NPs. Thus, surface passivation restricts the *in situ* oxidation of Fe_3O_4 NPs during electrophoretic deposition. The presence of metal Fe has also been noticed in Fe_3O_4@C film, while hydrated Fe is present in both the films, as expected.[50,51]

(e) FTIR studies of nanostructured iron oxide films

Fig. 5 shows the transmittance spectra of the nanostructured iron oxide films. In the case of the α-Fe_2O_3 NPs film (Fig. 5(a) and (b)) (obtained from Fe_3O_4 NPs and Fe_3O_4 NPs (autoclaved),

respectively), the peak seen at 566 cm^{-1} corresponds to the vibrations of Fe–O.[19] However, upon capping of the Fe_3O_4 NPs with carbon and silica, the Fe–O vibration peak at 566 cm^{-1} disappears and two additional peaks at 649 cm^{-1} and 465 cm^{-1} (Fig. 5(c) and (d)) have been obtained.

In the case of the carbon capped Fe_3O_4 NPs (Fig. 5(c)), the peak at 2934 cm^{-1} refers to the C–H stretching vibrations, the peak at 1416 cm^{-1} refers to the C–H bending vibrations and the peak at 1066 cm^{-1} refers to the C–O stretching vibrations. All these peaks indicate the presence of aliquots of fructose, since fructose molecules present in the hydrated state are unlikely to decompose completely,[52–54] but as a convention adopted by previous reports, we label these nanoparticles as carbon capped Fe_3O_4 NPs.[23,29]

In the case of silica capped Fe_3O_4 NPs (Fig. 5(d)), a sharp peak at 1118 cm^{-1} corresponds to characteristic Si–O vibrations, revealing the capping of the Fe_3O_4 NPs with silica.[55,56] The broad band found at 3300–3400 cm^{-1} and the peak at 1602 cm^{-1} present in all the films correspond to the O–H stretching mode and the H–O–H bending mode, respectively, indicating the presence of interstitial water molecules in the films.[44]

(f) Morphological studies of nanostructured iron oxide films and bioelectrodes

Fig. 6 shows the SEM micrographs of the nanostructured iron oxide films. It can be seen that the α-Fe_2O_3 films obtained from Fe_3O_4 NPs and Fe_3O_4 NPs (autoclaved) have an average particle size of 300 nm and 200 nm, respectively (Fig. 6(a) and (b)). The observed increase in particle size and deformation in shape indicate agglomeration of the uncapped NPs upon deposition. The agglomeration is more prominent for the as-prepared Fe_3O_4 NPs owing to their surface roughness. The electrical double layer gradient is maximum at the edges of the NPs, which results in the electrostatic attraction of the NPs and the growth in their size.[57] However, due to the removal of edges and surface smoothing of the NPs upon hydrothermal treatment, the autoclaved NPs undergo reduced aggregation.

Upon capping of the Fe_3O_4 NPs with carbon and silica, the agglomeration has been further restricted. A radical decrease of the average particle size to 100 nm (Fig. 6(c)) and 160 nm (Fig. 6(d)) is observed in the case of the carbon capped NPs and silica capped NPs, respectively. Also, the capped NPs retain their initial spherical shape upon deposition, as compared to the film of uncapped NPs. The reduction in size and retention of spherical shape indicate a considerable decrease in the agglomeration of NPs upon capping. Further, the immobilization of cholesterol oxidase onto the nanostructured iron oxide films has been confirmed using SEM (Fig. S1, ESI†). The change in morphology from a dense uniform distribution of NPs in the nanoscale to the globular structure of ChOx at the micron scale is attributed to the physical adsorption of ChOx molecules onto nanostructured iron oxide films.[58]

(g) Biocompatibility of Fe_3O_4@C and α-Fe_2O_3 films

The biocompatibility of the Fe_3O_4@C and α-Fe_2O_3 films has been investigated using bacterial systems *i.e.* Gram positive (*Bacillus* sp.) and Gram negative (*Providencia* sp.) bacteria. Two methods have been utilized to examine the biocompatibility of nanostructured iron oxide films. Firstly, cultures of Gram positive and Gram negative bacteria are spread on nutrient agar plates and Fe_3O_4@C and α-Fe_2O_3 films are kept on these plates under optimum growth conditions (28 °C and 150 rpm). No zone of inhibition is observed for the nanostructured iron oxide films. Secondly, side arm flasks are prepared with nutrient broth and both the bacteria are inoculated. Films are kept in the nutrient broth and grown under optimum conditions (28 °C and 150 rpm). Colorimetric readings recorded at intervals of 2 h are summarized in Table 1, which clearly indicates the biocompatibility of the Fe_3O_4@C and α-Fe_2O_3 films as the optical density of Gram positive and Gram negative bacteria increases with time in the presence of nanostructured iron oxide films.

(h) Electrochemical characterization of ChOx immobilized iron oxide electrodes

(i) ChOx/Fe_3O_4@C film/ITO bioelectrode. Fig. 7(a) shows the cyclic voltammograms of the ITO electrode, Fe_3O_4@C film/ITO electrode and ChOx/Fe_3O_4@C film/ITO bioelectrode in the potential range of −0.7 V to +0.7 V at a scan rate of 30 mV s^{-1}. The decrease in anodic peak current obtained for the Fe_3O_4@C film/ITO electrode (Fig. 7(a), (ii)) compared to that of the ITO electrode (Fig. 7(a), (i)) reveals the formation of a layer of Fe_3O_4@C NPs on the ITO surface. Furthermore, the increase in oxidation current obtained for the ChOx/Fe_3O_4@C film/ITO bioelectrode (Fig. 7(a), (iii)) compared to that of the Fe_3O_4@C film/ITO electrode (Fig. 7(a), (ii)) is attributed to electron transfer facilitated by redox moieties at the active sites (FAD centres) of the enzyme at the electrode surface.

Fig. 7(b) shows the Nyquist plots obtained for the ITO electrode, Fe_3O_4@C film/ITO electrode and ChOx/Fe_3O_4@C film/ITO bioelectrode. The increased R_{ct} value of 1.35 kΩ for the Fe_3O_4@C film/ITO electrode (Fig. 7(b), (ii)) compared to the R_{ct} value of 0.28 kΩ for the ITO electrode (Fig. 7(b), (i)) indicates formation of a Fe_3O_4@C NPs layer on the ITO surface. The presence of the Fe_3O_4@C NPs layer impedes the flow of electrons, resulting in an increased value of R_{ct}. Furthermore, a decrease in R_{ct} value from 1.35 kΩ for the Fe_3O_4@C film/ITO electrode to 1.18 kΩ for the ChOx/Fe_3O_4@C film/ITO bioelectrode (Fig. 7(b), (iii)) reveals the ChOx immobilization onto the Fe_3O_4@C film/ITO electrode. This decrease in R_{ct} value is ascribed to the facile electron transfer aided by the redox moieties of the enzyme at the electrode surface.

According to Laviron's theory, the slope of the linear curve between the anodic peak potential and the logarithm of scan rate represents $RT/\alpha nF$ (α: transfer coefficient). This can be used to calculate the surface concentration of the ionic species of the bioelectrodes using the following equation:

$$i_p = n^2F^2\nu CA(4RT)^{-1} \quad (1)$$

where, i_p/ν can be calculated from the i_p *vs.* ν plot[58] (i_p: anodic peak current; ν: scan rate).

The slope of the linear plot of anodic peak potential *vs.* logarithm of scan rate for the ChOx/Fe_3O_4@C film/ITO

bioelectrode gives $RT/\alpha nF = 0.23$. Using eqn (1), the surface concentration on the ChOx/Fe_3O_4@C film/ITO bioelectrode has been found to be 2.52×10^{-11} mol cm^{-2}.

(II) ChOx/α-Fe_2O_3 film/ITO bioelectrode. Fig. 7(c) shows the cyclic voltammograms obtained for the ITO electrode, α-Fe_2O_3 film/ITO electrode and ChOx/α-Fe_2O_3 film/ITO bioelectrode in the potential range of -0.7 V to +0.7 V at a scan rate of 30 mV s^{-1}. The oxidation peak seen at 0.38 V is attributed to the oxidation of the redox couple $K_3/K_4[Fe(CN)_6]$, present in the buffer.[58] The decrease in the oxidation current obtained for the α-Fe_2O_3 film/ITO electrode (Fig. 7(c), (ii)) compared to that of the ITO electrode (Fig. 7(c), (i)) indicates formation of a layer of α-Fe_2O_3 NPs on the ITO surface. Furthermore, the increase in oxidation current obtained for the ChOx/α-Fe_2O_3 film/ITO bioelectrode (Fig. 7(c), (iii)) compared to that of the α-Fe_2O_3 film/ITO electrode (Fig. 7(c), (ii)) is attributed to the presence of redox moieties at active sites (FAD centres) of the enzyme, leading to fast electron transfer between the enzyme and the electrode surface.[37]

Fig. 7(d) shows the Nyquist plots obtained for the ITO electrode, α-Fe_2O_3 film/ITO electrode and ChOx/α-Fe_2O_3 film/ITO bioelectrode. The increased R_{ct} (charge transfer resistance) value of 1.14 kΩ obtained for the α-Fe_2O_3 film/ITO electrode (Fig. 7(d), (ii)) compared to the R_{ct} value of 0.28 kΩ for the ITO electrode (Fig. 7(d), (i)) is attributed to the formation of a layer of α-Fe_2O_3 NPs on the ITO surface. Formation of an α-Fe_2O_3 NPs layer results in decreased interfacial electron transfer, thereby causing an increase in the R_{ct} value. Furthermore, the observed decrease in R_{ct} value from 1.14 kΩ for the α-Fe_2O_3 film/ITO electrode (Fig. 7(d), (ii)) to 0.82 kΩ for the ChOx/α-Fe_2O_3 film/ITO bioelectrode (Fig. 7(d), (iii)) is attributed to facile electron transfer mediated by the redox centres of the enzyme.

The surface concentration of ionic species on the ChOx/α-Fe_2O_3 film/ITO bioelectrode has been found to be 1.81×10^{-11} mol cm^{-2} (using $RT/\alpha nF = 0.16$). The higher concentration of ionic species on the ChOx/Fe_3O_4@C film/ITO bioelectrode compared to the ChOx/α-Fe_2O_3 film/ITO bioelectrode is attributed to the larger surface area provided by the Fe_3O_4@C nanocrystalline film owing to the smaller particle size of the NPs as compared to the α-Fe_2O_3 nanocrystalline film for enzyme immobilization.

(i) Electrochemical response of ChOx immobilized iron oxide electrodes

(I) ChOx/Fe_3O_4@C film/ITO bioelectrode. Fig. 8(a) shows the response of the ChOx/Fe_3O_4@C film/ITO bioelectrode obtained as a function of cholesterol concentration using cyclic voltammetry. The bioelectrode exhibits a response time of 60 s (Fig. S4(a)†). The anodic peak current of the ChOx/Fe_3O_4@C film/ITO bioelectrode plotted as a function of cholesterol concentration (Fig. 9(a)) reveals the linearity range as 25–500 mg dl^{-1} with a standard deviation and correlation coefficient of 4.82 μA and 0.99, respectively. The sensitivity of the ChOx/Fe_3O_4@C film/ITO bioelectrode exhibited by the slope of the linear regression curve is 193 nA mg^{-1} dl cm^{-2}. The value of the Michaelis–Menten constant of the ChOx immobilized Fe_3O_4@C film has been found to be 1.44 mg dl^{-1}.

The Nyquist plots for the ChOx/Fe_3O_4@C film/ITO bioelectrode as a function of cholesterol concentration have been investigated to obtain the impedimetric response of the biosensor (Fig. 8(b)). The linear calibration curve obtained by plotting the R_{ct} value for the ChOx/Fe_3O_4@C film/ITO bioelectrode as a function of cholesterol concentration (Fig. 10(a)) reveals a linearity range of 25–500 mg dl^{-1} with standard deviation and regression coefficient of 0.02 kΩ and 0.99, respectively. The sensitivity of 0.90 Ω mg^{-1} dl cm^{-2} is obtained from the slope of the linear regression curve of the ChOx/Fe_3O_4@C film/ITO bioelectrode.

The shelf life and reproducibility of the ChOx/Fe_3O_4@C film/ITO bioelectrode have been investigated using cyclic voltammetry. The activity of the bioelectrode is monitored at regular intervals of seven days. The bioelectrode exhibits only 6% reduction in peak current after 10 weeks for 100 mg dl^{-1} cholesterol concentration when stored at 4 °C (Fig. S2(a)†). The reproducibility of the sensing parameters of the bioelectrode has been studied with a cholesterol concentration of 25 mg dl^{-1} and it has been found that the bioelectrode can be used up to 25 times without significant decrease (40 μA) of the response signal (Fig. S3(a)†).

(II) ChOx/α-Fe_2O_3 film/ITO bioelectrode. Fig. 8(c) shows the response of the ChOx/α-Fe_2O_3 film/ITO bioelectrode obtained as a function of cholesterol concentration using the cyclic voltammetric technique. The response time of this electrode is found to be 60 s (Fig. S4(b)†). The magnitude of the amperometric current of the ChOx/α-Fe_2O_3 film/ITO bioelectrode plotted as a function of cholesterol concentration (Fig. 9(b)) shows linearity in the range 25–500 mg dl^{-1} with standard deviation and correlation coefficient of 4.52 μA and 0.99, respectively. The sensitivity of the ChOx/α-Fe_2O_3 film/ITO bioelectrode exhibited by the slope of linear calibration curve is found to be 218 nA mg^{-1} dl cm^{-2}. The value of the Michaelis–Menten constant of the ChOx immobilized α-Fe_2O_3 film has been found to be 1.46 mg dl^{-1}.

The electrochemical impedimetric response of the ChOx/α-Fe_2O_3 film/ITO bioelectrode has been investigated as a function of cholesterol concentration using Nyquist plots (Fig. 8(d)). The linear calibration curve obtained by plotting the R_{ct} values for the ChOx/α-Fe_2O_3 film/ITO bioelectrode as a function of cholesterol concentration (Fig. 10(b)) reveals a linearity range of 50–500 mg dl^{-1} with standard deviation and regression coefficient of 0.02 kΩ and 0.97, respectively. The value of sensitivity exhibited by the slope of the linear regression curve for the ChOx/α-Fe_2O_3 film/ITO bioelectrode is 0.42 Ω mg^{-1} dl cm^{-2} (Table 2).

The shelf-life of the ChOx/α-Fe_2O_3 film/ITO bioelectrode has been investigated for a 100 mg dl^{-1} cholesterol concentration using cyclic voltammetry. The bioelectrode exhibits a 6% decrease in the peak current for the first 8 weeks, but a sudden decrease in the signal has been observed afterwards and the current reduced by 11.5% after 10 weeks (Fig. S2(b)†). The ChOx/α-Fe_2O_3 film/ITO bioelectrode can be used up to 20 times with insignificant loss (66 μA) of the signal (Fig. S3(b)†).

Conclusions

Nanocrystals of Fe_3O_4 with an average particle diameter of 10 nm have been synthesized. The electrophoretic deposition of bare Fe_3O_4 NPs in a methanol–water mixture results in oxidation and phase transformation of NPs and a film of α-Fe_2O_3 NPs has been obtained. The phase transformation of the Fe_3O_4 NPs can be circumvented using surface passivation of Fe_3O_4 NPs with an organic carbon shell and an inorganic silica shell. Encapsulation of the Fe_3O_4 NPs restricts agglomeration of NPs during film deposition and retains a high surface to volume ratio for enzyme loading. Due to the non-conducting nature of silica, Fe_3O_4@SiO_2 NPs show poor electrochemical response. However, these can be utilized for applications in drug delivery,[21] biocatalysis and bioseparation,[20,59] magnetic resonance imaging,[60] determination of metal ion concentration,[61] *etc.* Growth of Gram positive and Gram negative bacteria in contact with the Fe_3O_4@C and α-Fe_2O_3 films reveals the biocompatible nature of the nanostructures, which is suitable for prolonged activity of enzymes and thus, stability of biosensors. The fabricated cholesterol biosensors employing Fe_3O_4@C and α-Fe_2O_3 nanocrystalline films show sensitivities of 193 nA mg^{-1} dl cm^{-2} and 218 nA mg^{-1} dl cm^{-2}, respectively, from cyclic voltammetric studies and sensitivities of 0.42 Ω mg^{-1} dl cm^{-2} and 0.90 Ω mg^{-1} dl cm^{-2}, respectively, from electrochemical impedance spectroscopic studies. The low values of the Michaelis–Menten constant reveals the enhanced enzymatic activity of ChOx on nanostructured iron oxide films. The comparable sensitivities for biosensors obtained using Fe_3O_4@C and α-Fe_2O_3 NPs suggests that encapsulation of Fe_3O_4 NPs with carbon does not significantly affect the electrocatalytic activity of Fe_3O_4 NPs, while it adds to the stability of the NPs. However, the encapsulation of Fe_3O_4 NPs with conjugated carbon molecules, conducting polymers like polypyrrole, polyaniline, *etc.*, may result in improved sensitivity of the biosensor.

Acknowledgements

We thank Prof. R. C. Budhani, Director, National Physical Laboratory, New Delhi, India for providing facilities. R. S. is thankful to the UGC-CSIR for the award of a Junior Research Fellowship. The authors thank Dr K. N. Sood, NPL for SEM measurements, Dr S. M. Shivprasad, JNCASR for XPS measurements and Dr Kavita Arora, JNU for TEM studies. Financial support received from the Department of Science and Technology (DST) centre on biomolecular electronics and CSIR Empower projects is sincerely acknowledged. Thanks are due to Dr Pratima Solanki, C. M. Pandey, Manoj Patel and all the members of the Biomedical Instrumentation Section, NPL, for discussions.

References

1 S. Chou, *J. Appl. Phys.*, 1994, **76**, 6673.
2 D. Schaadt, *J. Vac. Sci. Technol., A*, 2000, **18**, 1834.
3 K. Mosbach and L. Andersson, *Nature*, 1977, **270**, 259–261.
4 D. K. Yi, S. S. Lee and J. Y. Ying, *Chem. Mater.*, 2006, **18**, 2459–2461.
5 C. B. Catherine and S. G. C. Adam, *J. Phys. D: Appl. Phys.*, 2003, **36**, R198.
6 E. Amstad, M. Textor and E. Reimhult, *Nanoscale*, 2011, **3**, 2819–2843.
7 S. Laurent, D. Forge, M. Port, A. Roch, C. Robic, L. Vander Elst and R. N. Muller, *Chem. Rev.*, 2008, **108**, 2064–2110.
8 T. Osaka, T. Matsunaga, T. Nakanishi, A. Arakaki, D. Niwa and H. Iida, *Anal. Bioanal. Chem.*, 2006, **384**, 593–600.
9 R. Weissleder, H.-C. Cheng, A. Bogdanova and A. Bogdanov, *J. Magn. Reson. Imaging*, 1997, **7**, 258–263.
10 F. Cengelli, D. Maysinger, F. Tschudi-Monnet, X. Montet, C. Corot, A. Petri-Fink, H. Hofmann and L. Juillerat-Jeanneret, *J. Pharmacol. Exp. Ther.*, 2006, **318**, 108–116.
11 F. Sonvico, S. p. Mornet, S. b. Vasseur, C. Dubernet, D. Jaillard, J. Degrouard, J. Hoebeke, E. Duguet, P. Colombo and P. Couvreur, *Bioconjugate Chem.*, 2005, **16**, 1181–1188.
12 M. Mahmoudi, A. Simchi, M. Imani and U. O. Halfeli, *J. Phys. Chem. C*, 2009, **113**, 8124–8131.
13 A. Petri-Fink, M. Chastellain, L. Juillerat-Jeanneret, A. Ferrari and H. Hofmann, *Biomaterials*, 2005, **26**, 2685–2694.
14 A. K. Gupta and S. Wells, *IEEE Trans. NanoBiosci.*, 2004, **3**, 66.
15 J. Li, R. Yuan and Y. Chai, *Microchim. Acta*, 2011, **173**, 369–374.
16 J. Wang, Z. Zhu, A. Munir and H. S. Zhou, *Talanta*, 2011, **84**, 783–788.
17 H. Li, Q. Wei, J. He, T. Li, Y. Zhao, Y. Cai, B. Du, Z. Qian and M. Yang, *Biosens. Bioelectron.*, 2011, **26**, 3590–3595.
18 I. M. Hsing, Y. Xu and W. Zhao, *Electroanalysis*, 2007, **19**, 755–768.
19 G. Zhao, J. J. Feng, Q. L. Zhang, S. P. Li and H. Y. Chen, *Chem. Mater.*, 2005, **17**, 3154–3159.
20 H.-H. Yang, S.-Q. Zhang, X.-L. Chen, Z.-X. Zhuang, J.-G. Xu and X.-R. Wang, *Anal. Chem.*, 2004, **76**, 1316–1321.
21 K. Souza, J. Ardisson and E. Sousa, *J. Mater. Sci.: Mater. Med.*, 2009, **20**, 507–512.
22 T. Sen, A. Sebastianelli and I. J. Bruce, *J. Am. Chem. Soc.*, 2006, **128**, 7130–7131.
23 W. Xian-Wen, Z. Guo-Xing, X. Chuan-Jun and Y. Yin, *Nanotechnology*, 2006, **17**, 4307.
24 I. Zhitomirsky, *J. Mater. Sci.*, 2006, **41**, 8186–8195.
25 L. Besra and M. Liu, *Prog. Mater. Sci.*, 2007, **52**, 1–61.
26 Y. S. Kang, S. Risbud, J. F. Rabolt and P. Stroeve, *Chem. Mater.*, 1996, **8**, 2209–2211.
27 T. J. Daou, G. Pourroy, S. Begin-Colin, J. M. Greneche, C. Ulhaq-Bouillet, P. Legare, P. Bernhardt, C. Leuvrey and G. Rogez, *Chem. Mater.*, 2006, **18**, 4399–4404.
28 Y. Li, T. Leng, H. Lin, C. Deng, X. Xu, N. Yao, P. Yang and X. Zhang, *J. Proteome Res.*, 2007, **6**, 4498–4510.
29 X. Shouhu, H. Lingyun, J. Wanquan, G. Xinglong, H. Yuan and C. Zuyao, *Nanotechnology*, 2007, **18**, 035602.
30 J. Li and C.-Y. Liu, *New J. Chem.*, 2009, **33**, 1474–1477.
31 Y. Lu, Y. Yin, B. T. Mayers and Y. Xia, *Nano Lett.*, 2002, **2**, 183–186.

32 Z. X. Sun, F. W. Su, W. Forsling and P. O. Samskog, *J. Colloid Interface Sci.*, 1998, **197**, 151–159.
33 M. Jarlbring, L. Gunneriusson, B. Hussmann and W. Forsling, *J. Colloid Interface Sci.*, 2005, **285**, 212–217.
34 T. J. Daou, G. Pourroy, J. M. Greneche, A. Bertin, D. Felder-Flesch and S. Begin-Colin, *Dalton Trans.*, 2009, 4442–4449.
35 M. L. Fisher, M. Colic, M. P. Rao and F. F. Lange, *J. Am. Ceram. Soc.*, 2001, **84**, 713–718.
36 P. R. Solanki, S. K. Arya, S. P. Singh, M. K. Pandey and B. D. Malhotra, *Sens. Actuators, B*, 2007, **123**, 829–839.
37 Z. Matharu, G. Sumana, S. K. Arya, S. P. Singh, V. Gupta and B. D. Malhotra, *Langmuir*, 2007, **23**, 13188–13192.
38 L. Yonglan, *Mater. Lett.*, 2007, **61**, 1039–1041.
39 L. Huo, W. Li, L. Lu, H. Cui, S. Xi, J. Wang, B. Zhao, Y. Shen and Z. Lu, *Chem. Mater.*, 2000, **12**, 790–794.
40 T. D. Waite and D. M. Sherman, *Am. Mineral.*, 1985, **70**, 1262–1269.
41 T. A. Egerton and I. R. Tooley, *Int. J. Cosmet. Sci.*, 2012, **34**, 117–122.
42 S. L. Westcott, S. J. Oldenburg, T. R. Lee and N. J. Halas, *Langmuir*, 1998, **14**, 5396–5401.
43 Y. Kobayashi, V. Salgueirino-Maceira and L. M. Liz-Marzan, *Chem. Mater.*, 2001, **13**, 1630–1633.
44 K. Tao, H. Dou and K. Sun, *Chem. Mater.*, 2006, **18**, 5273–5278.
45 W. Cai and J. Wan, *J. Colloid Interface Sci.*, 2007, **305**, 366–370.
46 J. Sun, S. Zhou, P. Hou, Y. Yang, J. Weng, X. Li and M. Li, *J. Biomed. Mater. Res., Part A*, 2007, **80**, 333–341.
47 O. N. Shebanova and P. Lazor, *J. Raman Spectrosc.*, 2003, **34**, 845–852.
48 J. Tang, M. Myers, K. A. Bosnick and L. E. Brus, *J. Phys. Chem. B*, 2003, **107**, 7501–7506.
49 W. Feitknecht and K. J. Gallagher, *Nature*, 1970, **228**, 548–549.
50 J. Morales, L. Sanchez, F. Martin, F. Berry and X. L. Ren, *J. Electrochem. Soc.*, 2005, **152**, A1748–A1754.
51 P. Guardia, J. Perez-Juste, A. Labarta, X. Batlle and L. M. Liz-Marzan, *Chem. Commun.*, 2011, **46**, 6108–6110.
52 B. M. Kabyemela, T. Adschiri, R. M. Malaluan and K. Arai, *Ind. Eng. Chem. Res.*, 1999, **38**, 2888–2895.
53 Q. Wang, H. Li, L. Chen and X. Huang, *Carbon*, 2001, **39**, 2211–2214.
54 C. Adina, F. Florinela, T. Abdelmoumen and S. Carmen, *Rom. Biotechnol. Lett.*, 2010, **15**, 5738–5744.
55 A. Azioune, A. Ben Slimane, L. Ait Hamou, A. Pleuvy, M. M. Chehimi, C. Perruchot and S. P. Armes, *Langmuir*, 2004, **20**, 3350–3356.
56 D. Kandpal, S. Kalele and S. Kulkarni, *Pramana*, 2007, **69**, 277–283.
57 P. Pramod, S. T. S. Joseph and K. G. Thomas, *J. Am. Chem. Soc.*, 2007, **129**, 6712–6713.
58 Z. Matharu, P. Pandey, M. K. Pandey, V. Gupta and B. D. Malhotra, *Electroanalysis*, 2009, **21**, 1587–1596.
59 T. Sen, A. Sebastianelli and I. J. Bruce, *J. Am. Chem. Soc.*, 2006, **128**, 7130–7131.
60 J. L. Campbell, J. Arora, S. F. Cowell, A. Garg, P. Eu, S. K. Bhargava and V. Bansal, *PLoS One*, 2011, **6**, e21857.
61 L. L. Vatta, J. Kramer and K. R. Koch, *Sep. Sci. Technol.*, 2007, **42**, 1985–2002.
62 A. A. Ansari, A. Kaushik, P. R. Solanki and B. D. Malhotra, *Electrochem. Commun.*, 2008, **10**, 1246–1249.
63 A. A. Ansari, A. Kaushik, P. R. Solanki and B. D. Malhotra, *Electroanalysis*, 2009, **21**, 965–972.
64 S. P. Singh, S. K. Arya, P. Pandey, B. D. Malhotra, S. Saha, K. Sreenivas and V. Gupta, *Appl. Phys. Lett.*, 2007, **91**, 063901–063903.
65 P. R. Solanki, A. Kaushik, A. A. Ansari and B. D. Malhotra, *Appl. Phys. Lett.*, 2009, **94**, 143901–143903.
66 G. Kouassi, J. Irudayaraj and G. McCarty, *J. Nanobiotechnol.*, 2005, **3**, 1.

Point Based Features for Contact-less Palmprint Images

Anil Singh Parihar[1], Amoiy Kumar[2], Om Prakash Verma[1], Ankita Gupta[1], Prerana Mukherjee[1], and Deepika Vatsa[1]

[1]Department of Information Technology, Delhi Technological University, New Delhi, India
[2]Department of Electrical Engineering, Indian Institute of Technology, New Delhi, India
parihar.anil@gmail.com, amioy.iitd@gmail.com, opverma.dce@gmail.com, ankita.gupta.mail@gmail.com, mukherjee.prerana@gmail.com, vatsa.deepika@gmail.com

Abstract— **In this paper, feature extraction and authentication scenarios for contact-based and contact-less palmprint images are investigated. The point-based feature extraction techniques like: Scale Invariant Feature Transform (SIFT), Harris corner detector, and Histogram of Gradient (HOG) in combination to Gabor filter are experimented for contact-based and contact-less palmprint authentication. In our experiments, we have used publicly available IITD database consisting of unconstrained contact-less palmprint images and compared its performance on these features with HongKong PolyU database acquired under constant illumination and constrained conditions. The presented work establishes that majority of the previous methods for palm print authentication, may work well with contact-based images, (with constrained environment) but fail to produce substantial results with unconstrained natural contact-less palmprint images. The proposed techniques give high recognition rate (97.5% and 93% GAR with Harris and SIFT respectively) for contact-less palmprint database. The experimental results in this paper have shown significant improvement for contact-based palmprint as well.**

Key words: palmprint, contact-based, contact-less, constrained, ROI

I. INTRODUCTION

Biometric authentication refers to the automatic identification of a person based on human physiological (e.g., fingerprint, iris) or behavioural (e.g., signature) or chemical (e.g. chemical composition of human perspiration) characteristics or traits [34]. The traditional methods require the pin number or the password to be remembered for identification/authentication and thus are more vulnerable to attacks. As a result, biometric systems are being deployed to enhance security and reduce financial fraud [34][43]. Various biometric traits are being used for real-time recognition, the most popular being fingerprint, face and iris [41][44]. Among the various biometric techniques used for authentication, hand based biometrics is well established trait, with some advantages over the already prevalent competitor techniques. It is so, because of the textural details which can be extracted from hand based features for authentication is high and the human hand data acquisition is convenient and user-friendly. Also, it is less exposed to anatomic variations and environmental artifacts. Higher recognition rates in most hand based modalities rely on a contact device with pegs for image acquisition[5].Hand-based biometrics has been used in personal identification by using fingerprint[44],palmprint [5][29-33], hand geometry [15][35], 3-D finger geometry [36-37], hand vein [38-40] and finger knuckles [6-9]. Fingerprint is a widely used and reliable modality since it is easy to use and gives accurate results. However, as investigated by NIST, approximately 2% of the population do not have useful and accessible fingerprints thus fingerprint identification is useless for such people [1]. Palmprint is a highly accurate biometric modality as there is a larger surface area for feature extraction, and thus they carry more information for personal identification. Moreover, capture devices are much low in cost and memory requirement is less for the storage of low resolution palm images.

The literature works show that, most of the available efforts are on contact-based palmprint acquisition. There is growing concern over using contact-based (constrained) palmprint images as it does not give a user friendly real life scenario. It has resulted in inclination of research interest towards constrained free natural contact-less palmprint authentication. The contacts-less palmprint acquisition systems are more convenient to the user and have negligible hygiene issues. However, a contact-less palmprint acquisition may suffer from scale, rotation, occlusion and translational variations which can reduce authentication accuracy. The available approaches for palmprint authentication can be categorized into following categories: (i) texture-based approaches (Gabor filter, Discrete Fourier Transform) [5][21-22] (ii) line-based approaches (Line matching, Morphological Operators) [23-24], and (iii) appearance-based approaches(PCA, LDA)[25-27]. Most of the reported works have shown satisfactory results on constrained images. The difficulties faced by user in contact-based system, are mainly due to constrained applied like application of pegs, limitation in orientations, and necessity of contact with surface, which may be unhygienic. Nowadays, a growing trend towards the idea of peg-free, contact-less, hand biometrics has emerged. The contact-less imaging increases user convenience [28] [30][37][39], enhances real life scenario and results in less imposter attacks. There are various challenges in designing a contact-less system. It involves a careful selection of distance between the hand and input sensor and adds variations like rotational variations, translational variations, scale variations, blurring etc., since there is no restriction on hand placement during image acquisition [42].Therefore, the usage of traditional palmprint feature extraction methods on contact-less imaging schemes remains questionable and hence most of

the popular palmprint feature extraction methods may not be useful in contact-less frameworks.

Considerably, less work has been reported using the contact-less images in the literature. Cui Xin *et al.* have done work on contact-less hand shape identification system [11]. Analysis of 3-D finger geometry features has been done by Malassiotis *et al.* using peg-free imaging [37].Morales *et al.* has also done some significant work on contact less palmprint images [42]. Tee Connie *et al.* [10] have given a robust approach on knuckle and palmprint recognition using contact-less databases. Badrinath *et al.* used SIFT to extract features from constrained palmprint images [12]. Julien Doublet *et al* used skin color and hand shape information to classify users into imposter and genuine [45]. In this work some methods have been proposed which can be used for contact-less databases. The proposed methods Gabor –SIFT and Gabor-Harris give highly improved the authentication rate of the PolyU database (contact-based palmprint), though other approach Gabor-HOG results are comparable .The proposed approaches degrades the performance with the IITD database (contact-less) as compare to earlier approaches. But, SIFT, Harris and HOG give efficient results for IITD database. Thus the work establishes that Gabor based approaches are not suitable for contact-less palmprints, but improves authentication results remarkably for contact-based palmprints. So, the authentication schemes that can efficiently detect rotation and scale invariant features has been used in the proposed approach. The basic steps in palmprint authentication are: pre-processing, feature extraction, matching.

The organization of rest of this paper is as follows; Section 2 describes the process of feature extraction, Section 3 details the proposed approaches, and section 4 presents results and discussion. Finally the conclusion of this work is summarized in section 5.

II. FEATURE EXTRACTION

Feature point detection is the vital step in palmprint authentication in which the input data captured is transformed into a reduced representation of feature vector set on which different similarity measure like Euclidean distance, L-norm, cosine similarity are used. The visual features comprise of domain specific features (e.g. fingerprints, human faces) or general features (viz. color, texture and shape). The most popular and intuitive choice for similarity measure, the cosine function is considered for this work. The experiments have shown that most of the existing approaches are not so promising with contact less databases, there is a need for such detectors which can deal with the images having variations and gives the best authentication results. The detectors explained below will address these variations. Here, the acquisition is considered to be done under constant fluorescent illumination circumstances. Interesting features are extracted from the pre-processed image i.e. ROI. Every image consists of some particular features, points or key points that need to be extracted from the image.

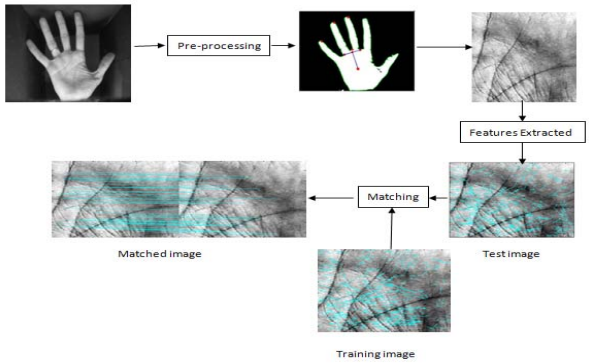

Fig. 1: Basic Steps of palm print authentication system

The palm consists of principal lines, wrinkles (secondary lines) and epidermal ridges. Detectors used for extracting these features are SIFT, HARRIS, AND HOG. SIFT is an approach for detecting and extracting local feature descriptor which are invariant to scale and rotation. HARRIS is an approach to detect and extract corners from the palmprint image which are invariant to scale and illumination. HOG are feature descriptors that represent occurrences of gradient orientation in localized portions of an image. Descriptor is anything which describes the properties of an image like color, orientation, texture, pixel intensity, edges etc. In palmprint, unique properties can be texture, orientation, scale etc. Descriptor with edge orientation information (SIFT, HOG) in this work have been used. Local feature descriptors of palmprint images are then matched using cosine similarity measure.

III. PROPOSED APPROACHES FOR PALMPRINT AUTHENTICATION

In the proposed approach, Gabor filter is utilized to improve the features in palmprints. SIFT feature detector is used with Gabor to result the Gabor-SIFT approach, which is experimented with contact-based and contact-less palmprints. HARRIS, feature detector, which were earlier used for contact-based palmprints is experimented for contact-less database. The system with combination of Gabor and HARRIS, called Gabor-HARRIS, is also proposed. In this approach SIFT descriptor is used for describing the feature obtained through HARRIS. Another feature detector HOG is also experimented for both type of uses i.e. alone and combination with Gabor (Gabor-HOG).

A. Gabor SIFT: Gabor Scale Invariant Feature Transform

Scale-invariant feature transform (SIFT) is a powerful detector extensively used in the pattern recognition and computer vision fields. The pre-processed palm print ROIs are used in SIFT feature extraction. In case of palmprint authentication, features consist of principal lines, wrinkles (secondary lines) and epidermal ridges. However, these principal lines are not sufficient to represent the uniqueness of each individual's palmprint because different people may have similar principal lines in their palmprints as in Fig. 2.

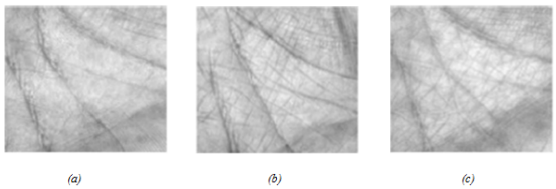

Fig. 2: ROI's of different users having similar *principal lines*

Therefore in the proposed approach, to extract texture features especially, fine features of palmprint images, Gabor filter (Gab) is applied for enhancement of textural features.

$$Gab(x, y, \theta, u, \sigma)=\left(\frac{1}{2\Pi\sigma^2}\exp\left(-\frac{x^2+y^2}{2\sigma^2}\right)x\exp(2\Pi i(ux\cos\theta + uy\sin\theta))\right) \quad (1)$$

Where 'u' is the frequency of the sinusoidal wave, 'θ' controls the orientation of the function 'σ' is the standard deviation of the Gaussian envelope and (x, y) is any location in the image plane. The images obtained after applying Gabor filter are called as Gabor enhanced images (GROI) as shown in Fig. 3.

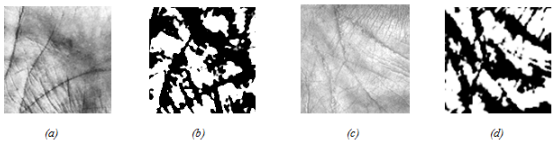

Fig. 3: a) ROI of the left palm print of a user (IITD database), (b) GROI of (a), (c) ROI of the left palm print of a user (PolyU database), (b) GROI of (c).

Each image is convolved with Gabor filter to enhance the details of the image and to increase the number of key points detected. The image obtained is the pre-processed image. This image can now be used for feature detection. The scale space of an image is defined as a function, Lap(x, y, σ), this is produced from the convolution of a variable-scale Gaussian function, Gauss(x, y,σ), with an input image, I(x, y): as in

$$Lap(x,y,\sigma)=Gauss(x,y,\sigma)*I(x,y) \quad (2)$$

where '∗' represents the convolution operation and the Gaussian function is given by:

$$Gauss(x,y,\sigma)=\frac{1}{2\pi\sigma^2}\exp\left(-\frac{x^2+y^2}{2\sigma^2}\right) \quad (3)$$

Detection process is then done by selecting key locations at local maxima and minima of a Difference of Gaussian (DoG) function applied in scale space, which is computed by successively down sampling the input image. Maxima and minima of this scale space function are determined by comparing each pixel to its neighbors. The scale of the key point is used to select the Gaussian smoothened image with the closest scale. For each image sample, at this scale, the gradient magnitude, *mag(x, y),* and orientation, *arg(x, y)*, are precomputed using pixel differences:

$$mag(x,y)=\sqrt{\left(Lap(x+1,y)-Lap(x-1,y)\right)^2+\left(Lap(x,y+1)-Lap(x,y-1)\right)^2} \quad (4)$$

$$arg(x,y)=\tan^{-1}\left(\frac{Lap(x,y+1)-Lap(x,y-1)}{Lap(x+1,y)-Lap(x-1,y)}\right) \quad (5)$$

Orientations are assigned to each key point location based on local image gradient directions and orientation histogram obtained. The peaks in the orientation histogram amount to dominant directions of local gradients. Any local peak that is within 80% of the highest peak is used to create a key point with that orientation. More detail description of this process can be found in Lowe [16]. Fig. 4 shows sample palm print SIFT extraction results.

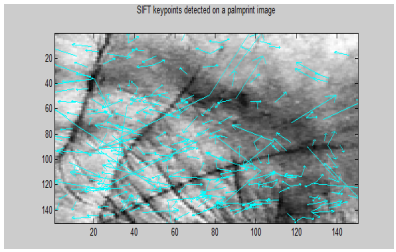

Fig. 4: SIFT keypoints detected in a palmprint ROI

B. Gabor-Harris Corner Detector

The Harris corner detector is a popular interest point detector that addresses the issues like invariance to rotation, scale, illumination variation and image noise. In the proposed approach Gabor filter is used for enhancement of the fine features similar to the Gabor-SIFT approach. The Harris corner detector [48] is based on the local auto-correlation function of a signal, where the local auto-correlation function measures the local changes of the signal with patches shifted by a small amount in different directions. Given a shift (Δx, Δy) and a point (x, y), the auto-correlation function is defined as,

$$c(x,y)=\sum w(I(x_i,y_i)-I(x_i+\Delta x,y_i+\Delta y))^2 \quad (6)$$

where $I(x_i,y_i)$ denotes the image function and (x_i,y_i) is i^{th} point window (Gaussian) w centred at (x,y). The shifted image is approximated by a Taylor expansion truncated to the first order terms,

$$I(x_i+\Delta x,y_i+\Delta y)\approx I(x_i,y_i)+[\,I_x(x_i,y_i)\;\;I_y(x_i,y_i)][\,\Delta x\;\Delta y]^T \quad (7)$$

where $I_x(x_i,y_i)$ and $I_y(x_i,y_i)$ denote the partial derivatives with respect to x and y, respectively. Using (6) and (7) and various mathematical operations we get

$$c(x,y) = [\Delta x\;\Delta y]c(x,y)[\Delta x\;\Delta y]^T \quad (8)$$

Where updated matrix c(x,y) captures the intensity structure of the local neighborhood. The Eigen values for matrix c(x,y) are calculated and if both eigen values are high and the local auto-correlation function is sharply peaked, then shifts in any direction will result in a significant increase; this indicates a corner. Once the corners are detected then Sift descriptor is applied, as described by David Lowe to get feature vectors [16]. Harris Corners are described in Fig. 5.

A. Gabor-HOG-Gabor Histogram of Gradients

Originally HOG has been first proposed by Dalal and Triggs, as an image descriptor for localizing pedestrians in complex images. Here in this approach, Gabor filter is applied to palmprint images as done in Gabor-SIFT and Gabor-HARRIS approaches to enhance the features of the palmprint image. The HOG descriptor [46] represents an image by a set of local

histograms which count occurrences of gradient orientation in a local cell of the image. In this the image is divided into small spatial regions (cells), for each cell accumulating a local 1-D histogram of gradient directions or edge orientations over the pixels of the cell. The gradients can be computed using the Eqn. 9. The combined histogram entries represent the whole image. For invariance to illumination, the local responses are contrast normalised before using them. This is done by accumulating a measure of local histogram energy over larger spatial regions called blocks.

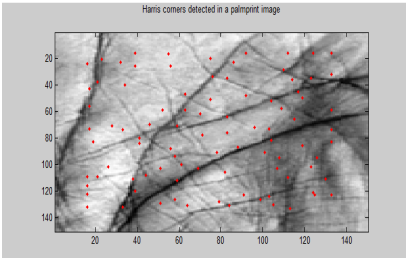

Fig. 5: Harris Corners detected in a palmprint ROI

These results are used to normalize all the cells in the block using any of the normalization schemes like *L2 - norm, L1-sqrt, L2- Hys* etc[46].

$$g(x,y)=\sqrt{g_x(x,y)^2 + g_y(x,y)^2} \quad (9)$$

Here, g_x and g_y represent 1-D filters. HOG had been used as a detector as well as a descriptor which divides the images into blocks and cells, and then return its full feature vector which is used for authenticating the palmprint images.

IV. RESULTS AND DISCUSSIONS

The experimentation in this work is carried out on Hong Kong Polytecnic University(PolyU) palmprint database[49] and IITD database[48]. The characteristics of both the databases are shown in the table 1. Zhang's *et al* method [5] gave promising results with contact-based images, PolyU images(GAR=99.7 at FAR=0.01) but the result were not that satisfactory for the contact-less database, IITD images (GAR=60 at FAR=0.01). So there was a need for better authentication schemes particularly for contact-less images. ROCs of this experiment are given in Fig. 6.

Table 1: Characteristics of IITD and PolyU Database

Characteristics	IITD database	PolyU database
No of Users	235	345
No of Samples	7(1645 in total)	7(2415 in total)
Hands Acquired	Left	Left
Acquisition Method	Contact-less, Unconstrained(Pegs free)	Contact-based, Constrained
Background	Uncontrolled	Controlled
ROI size	150 × 150	128 × 128

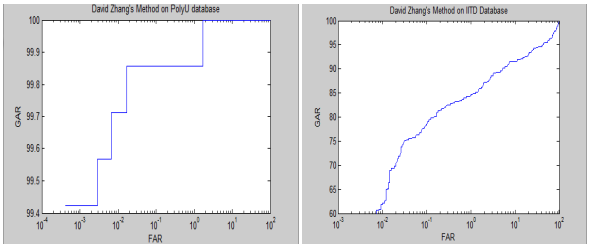

Fig. 6: ROC for IITD and PolyU database using Zhang's et al method.

Throughout our experimentation process, values used for the Gabor filter are $\theta = \pi/4, \sigma = 5.6179, u = 0.0916$ .The images obtained after convolving Gabor filter are named as GROI(Gabor-Region of Interest). First we explain the experiments designed to assess the robustness and capabilities of the different region detectors and the descriptors. PolyU images are contact-based palm images. The results after application of SIFT on GROI images of contact-based database were considerably good(97.5% GAR) although it was very low(51% GAR) for images that were not convolved with the Gabor filter. However the results after application of SIFT on IITD GROI images were not significantly improved (70% GAR). The ROC curves are shown in figure 7 and 8. The Red curve is the curve for original images (WOG- WithoutGabor) and the Blue Curve is for GROI images (WG- With Gabor). This color notation for curves is used throughout this paper.

In the second set of experiments, the Harris corner points are detected at different scales and are described at different scales. The range of scale taken is 's'∈ (4, 12). As the scale is further increases the number of keypoints detected are less and it gradually decreases the matching performance also. The performance at different scales is cited in table 2 and ROC plots are shown in figure 9, 10 and 11. By observing the ROCs at different scales it was found that GAR was maximum for scale 8(GAR=87 at FAR=0.01) for IITD database.

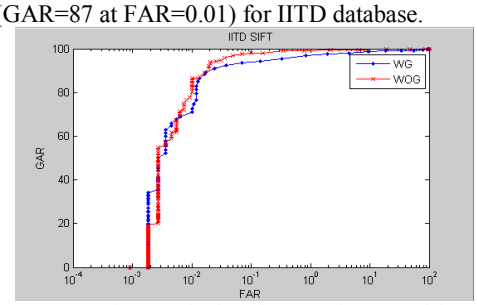

Fig. 7: ROC curve for IITD database for GROI images and the original images using SIFT detector.

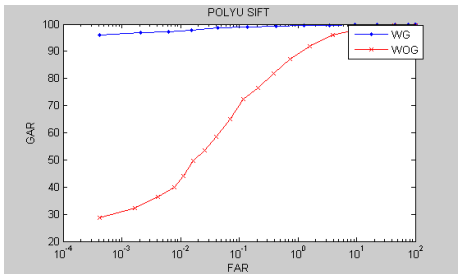

Fig. 8: ROC curve for PolyU database for GROI images and the original images using SIFT detector.

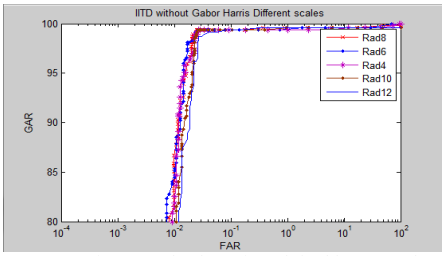

Fig. 9: ROC curve for IITD database for original images. The curve is obtained for Harris detector at different scales (4,6,8,10 and 12).

Table 2: IITD database without Gabor performance measures using Harris detector with different scales Characteristics of IITD and PolyU Database

Harris scale	FAR	GAR
4	0.01	82
6	0.01	85
8	0.01	87
10	0.01	78
12	0.01	70

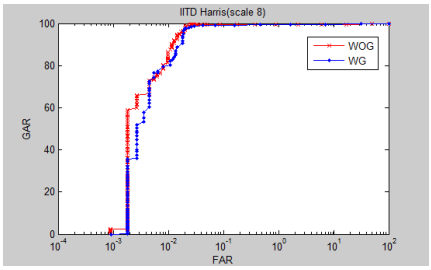

Fig. 10: ROC curve for IITD database for images convolved with GROI images and the original images using Harris detector.

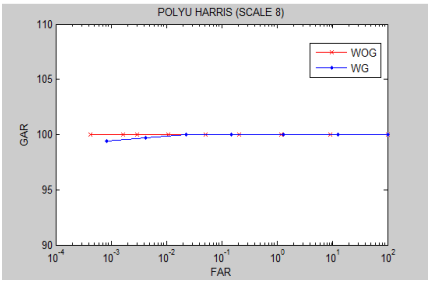

Fig. 11: ROC curve for PolyU database for images convolved with GROI images and the original images using Harris detector.

Harris also proved a very good and better technique for contact-based giving GAR = 100. In the third set of experiments, the results using HOG on GROI images of PolyU database were considerably good (99.4% GAR) although it were also good (99.2% GAR) for images that were not convolved with the Gabor filter. However, the results after application of HOG on IITD GROI images were low (60% GAR). The ROC curves are shown in figure 12 and 13.

The performance measures of different detectors on both the databases are shown in table 3 and 4.

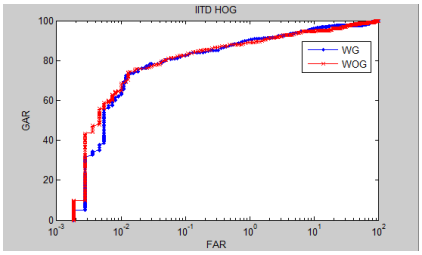

Fig. 12: ROC curve for IITD database for images convolved with GROI images and the original images using HOG.

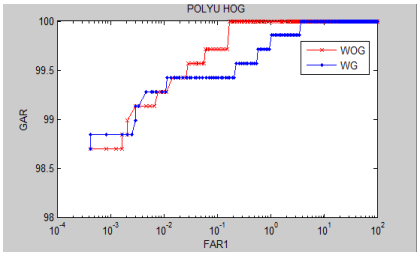

Fig. 13: ROC curve for PolyU database for images convolved with GROI images and the original images using HOG.

Table 3: IITD Database performance measures using different detectors

Different Detectors	With Gabor (WG)		Without Gabor (WOG)	
	GAR (at FAR 0.1)	*GAR (at FAR 0.02)*	*GAR (at FAR 0.1)*	*GAR (at FAR 0.02)*
SIFT	94	90	98	93
HARRIS	99	97	99.3	97.5
HOG	83	76	83	76

Table 4: PolyU Database performance measures using different detectors

Different Detectors	With Gabor (WG)		Without Gabor (WOG)	
	GAR (at FAR 0.1)	*GAR (at FAR 0.02)*	*GAR (at FAR 0.1)*	*GAR (at FAR 0.02)*
SIFT	99	98.1	70	51
HARRIS	100	99.97	100	100
HOG	99.7	99.5	98	99.4

V. CONCLUSIONS

All these techniques discussed above could work well for the contact-less databases. An interesting point to note is that application of Gabor on contact-less database did not improve the results but it worked quite efficiently for contact-based database. This has also been proved by the prior method of Zhang [5] which incorporated the use of Gabor on the databases and matching was done by hamming distance. The results on PolyU database were high but not so good for IITD database which supports the fact that Gabor is not efficient for contact-less databases. In fact applying Gabor on PolyU database the results were significantly improved for SIFT and Harris but it remained almost the same for HOG. From the above experiments it was also found that out of all these three techniques Harris corner detector worked best for both the palmprint databases viz. PolyU and IITD. The experimental results on Harris detector can be summarised as: GAR 97.5%

for IITD database and GAR=100% for PolyU. Second in performance is SIFT followed by HOG. It could be concluded that the point based features like Harris (GAR=97.5%) and SIFT (GAR=93%) were most successful in detecting the features for contact-less palmprint images (IITD). For further improvement of the performance of these feature detectors, our future work will focus primarily on finding new and more efficient techniques for contact-less databases which can also work with other biometric modalities like vein, knuckle etc.

REFERENCES

[1] A.Kumar and T. Chan, "Robust ear identification using sparse representation of local texture descriptors", Pattern recognition, vol. 46, pp 73-85, 2012.

[2] K.Chang, K.Bowyer and P.Flynn "Multiple nose region matching for 3D face recognition under varying facial expressions", IEEE Transactions on Pattern Analysis and Machine Intelligence, vol. 28, no. 10, 2006.

[3] V.Blanz and T. Vetter, "Face recognition based on fitting a 3D morphable model", IEEE transactions on pattern analysis and machine intelligence, vol. 25, no. 9, 2003.

[4] A.Abate, M.Nappi, D.Riccio and G.Sabatino, "2D &3D Face recognition: A Survey", Pattern recognition letters, vol. 28, 2007.

[5] D. Zhang, A. W.-K. Kong, J. You, and M. Wong, "Online palmprint identification",IEEE Transaction on Pattern Analysis and Machine Intelligence, vol. 25, no. 9, pp. 1041–1050, Sep. 2003.

[6] L.Zhang, L. Zhang and D. Zhang, "Finger knuckle print: A new biometric identifier", IEEE, ICIP,pp-1981-1984, 2009.

[7] L.Zhang, L. Zhang, D. Zhang and H. Zhu, "Online finger knuckle print verification for personal authentication", Pattern Recognition, vol.43, pp-2560-2571, 2010.

[8] J. Daugman, "High confidence visual recognition of persons by a test of statistical independence", IEEE Transactions on Pattern Analysis and machine intelligence, Vol.15, no. 11, pp. 1148-1161, 1993.

[9] A. Kumar, "Personal identification using finger knuckle imaging", IITD Techn. Rep. IITD-BRL-07-2,2007.

[10] G.Michael , T. Connie andA. Jin, "Robust Palm Print and Knuckle Print Recognition System Using a Contact-less Approach" , 5th IEEE Conference on Industrial Electronics and Applications, pp. 323-329, 2010.

[11] C.Xin, X. Wu, Z. Qiushi and T.Youbao , "A Contact-less Hand Shape Identification System", 3rd International Conference on Advanced Computer Control (lCACC), pp. 561-565, 2011.

[12] G.Badrinath and P. Gupta , " Palmprint Verification using SIFT features", In Proceedings of International workshop on Image Processing Theory, Tools and Applications (IPTA), pp. 1-8, November, 2008.

[13] L. Brown, B. Morrissey and M. Gudale, "Vision in the palm of your hand", Neuropsychologia, vol.47, pp. 1621-1626, 2009.

[14] A. K. Jain and J. Feng, "Latent palmprint matching",IEEE Transactions on Pattern Analysis and Machine Intelligence, vol. 31, no.6, pp. 1032-1047, 2009.

[15] A. Kumar and D. Zhang, "Hand geometry recognition using entropy based discretization", IEEE Transactions on Information Forensics and Security, vol. 2, no. 2, pp. 181-187, 2007.

[16] D. Lowe, "Distinctive Image Features from Scale-Invariant Keypoints", International Journal of Computer Vision, vol. 60, pp. 1-28, 2004.

[17] A. Kumar and D. Zhang, "Personal recognition using hand shape and texture", IEEE Transactions on Image Processing, vol. 15, no.8, pp. 2454-2461, 2006.

[18] A.Kumar and D. Zhang, "Incorporating user quality for performance improvement in hand identification", in Proc. 10th ICARCV, Hanoi, Vietnam , pp. 1133-1136, 2008.

[19] X. Jiang, W. Xu, L. Sweeney, Y. Li, R. Gross and D. Yurovsky, "New directions in contact free hand recognition", in Proc. ICIP, pp.-389-392, 2007.

[20] A. Kumar, D.C.M. Wong, H.Shen and A.K. Jain, "Personal authentication using hand images", Pattern Recognition Letter, vol. 27, no.13, pp. 1478-1486, 2006.

[21] A.Kumar and H.C Shen, "Palmprint identification using palmcodes," in Proceedings Of the Internatinal Conference on Image & Graphics, ICIG, pp. 258-261, 2004.

[22] W.Li, D. Zhang and Z.Xu, "Palmprint identification by Fourier transform," International Journal on Pattern Recognition & Artificial Intelligence, vol. 16, no. 4, pp. 417-432, 2002.

[23] D. Zhang and W. Shu, "Two novel characteristics in palmprint verification: datum point invariance and line feature matching", Pattern Recognition, vol. 32 (4) pp. 691–702, 1999.

[24] C.-C. Han, H.-L. Cheng, C.-L. Lin and K.-C. Fan, "Personal authentication using palm-print features", Pattern Recognition, vol. 36, pp. 371–381, 2003.

[25] G. Lu, D. Zhang and K. Wang, "Palmprint recognition usingeigenpalm-like features", Pattern Recognition Letter, vol. 24, pp.1473–1477, 2003.

[26] X. Lu, D. Zhang and K. Wang, "Fisherpalms based palmprint recognition", Pattern Recognition Letter, vol. 24,pp. 829–838, 2003.

[27] T. Connie, A.Teoh, M. Goh and D. Ngo, "Palmhashing: a novel approach for cancelable biometrics", Information Processing Letter, vol. 93, pp. 1–5, 2005.

[28] Y. Hao, Z. Sun, T. Tan and C. Ren, "Multispectral Fusion for Accurate contact free palmprint recognition", IEEE, ICIP, pp. 281-284,2008.

[29] P. H. Hennings-Yeomans, B. V. K. Kumar, and M. Savvides, "Palmprint classification using multiple advanced correlation filters and palm-specific segmentation",IEEE Transactions on Information Forensics and Security, vol. 2, no. 3, pp. 613–622, Sep. 2007.

[30] A. Kumar and D. Zhang, "Personal recognition using hand shape and texture",IEEE Transactions on Image Processing, vol. 15, no. 8, pp. 2454–2461,Aug. 2006.

[31] S. Ribaric and I. Fratric, "A biometric identification system based on eigenpalm and eigenfinger features",IEEE Transactions on Pattern Analysis and Machine Intelligence, vol. 27, no. 11, pp. 1698–1709, Nov. 2005.

[32] X. Lu, D. Zhang, and K. Wang, "Fisherpalms based palmprint recognition",Pattern RecognitionLetter, vol. 24, pp. 2829–2838, 2003.

[33] A. Kumar and D. Zhang, "Personal authentication using multiple palmprint representation",Pattern Recognition, vol. 38, pp. 1695–1704, Mar.2005.

[34] A.K. Jain, A. Ross and S. Prabhakar, "An Introduction to Biometric Recognition", IEEE Transactions on Circuits and System for Video Technology,vol. 14, no. 1, pp. 4-20, 2004.

[35] H. G. Sanchez Paper, R. Sanchez-Reillo, C. Sanchez-Avila, and A. Gonzalez-Macros, "Biometric identification through hand geometry measurements", IEEE Transactions on Patter*n* Analysis and Machine Intelligence, vol. 22, no. 10, pp. 1168–1171, Oct. 2000.

[36] D. L. Woodard and P. J. Flynn, "Finger surface as a biometric identifier",Computer Vision and Image Understanding, vol. 100, pp. 357–384, Aug. 2005.

[37] S. Malassiotis, N. Aifanti, and M. G. Strintzis, "Personal authentication using 3-D finger geometry",IEEE Trans. Information Forensics and Security, vol.1, no. 1, pp. 12–21, Mar. 2006.

[38] J.-G.Wang, W.-Y. Yau, A. Suwandy, and E. Sung, "Person recognition by fusing palmprint and palm vein images based on "Laplacianpalm"representation",Pattern Recognition, vol. 41, pp. 1531–1544, 2008.

[39] A. Kumar and K. V. Prathyusha, "Personal authentication using hand vein triangulation", in Proceedings of SPIE Biometric Technology for HumanIdentification, Orlando, FL, vol. 6944, p. 69440E, 2008.

[40] C.L. Lin and K-C. Fan, "Biometric verification using thermal images of palm-dorsa vein patterns",IEEE Transactions on Circuits and System for Video Technology,vol. 14, no. 2, pp. 199–213, 2004.

[41] J. Daugman, "How Iris Recognition Works", International conference on Image Processing, vol. 1, pp. I-33-I-36, 2002.

[42] A. Morales, M.A. Ferrer and A. Kumar, "Towards contact-less palmprint authentication", IET Computer Vision, vol. 5, no. 6, pp. 407–416, 2011.

[43] N. Ratha, J. Connell and R. Bolle, "Enhancing security and privacy in biometrics-based authentication systems", IBM Systems Journal, vol. 40, pp. 614-634, 2001.

[44] Y. Chen, S. Dass and A. Jain, "Fingerprint quality indices for predicting authentication performance", 5th International Conference, AVBPA, Springer, vol. 3546, pp. 160-170,2005.

[45] J. Doublet, M.Revenu, and O.Lepetit, "Robust grayscale distribution estimation for contact-less palmprint recognition", In Biometrics: Theory, Applications, and Systems, 2007. BTAS 2007 , IEEE, pp. 1-6,2007

[46] N. Dalal and B. Triggs, "Histogram of oriented gradients for human detection", Computer Vision and Pattern Recognition, vol. 1, pp. 886-893, 2005.

[47] C. Harris and M. Stephens, "A Combined Corner and Edge Detector", In Proceedings of the Fourth Alvey Vision Conference, pp. 147-151, 1988

[48] http://www4.comp.polyu.edu.hk/~csajaykr/IITD/Database_Palm.htm

[49] http://www4.comp.polyu.edu.hk/~biometrics/2D_3D_Palmprint.htm

ARTICLE IN PRESS

Available online at www.sciencedirect.com

ScienceDirect

Ceramics International ▮ (▮▮▮▮) ▮▮▮–▮▮▮

CERAMICS INTERNATIONAL

www.elsevier.com/locate/ceramint

Pr^{3+} doped lead tungsten tellurite glasses for visible red lasers

M. Venkateswarlu[a], M.V.V.K.S. Prasad[a], K. Swapna[a], Sk. Mahamuda[a], A. Srinivasa Rao[a,b,*], A. Mohan Babu[c], D. Haranath[d]

[a]*Department of Physics, KL University, Green Fields, Vaddeswaram 522502, AP, India*
[b]*Department of Applied Physics, Delhi Technological University, Bawana Road, New Delhi 110042, India*
[c]*Department of Physics, Chadalawada Ramanamma Engineering College, Tirupati 517502, India*
[d]*CSIR – National Physical Laboratory, Dr. K.S. Krishnan Road, Pusa Road, New Delhi 110012, India*

Received 6 September 2013; received in revised form 31 October 2013; accepted 15 November 2013

Abstract

Lead tungsten tellurite (LTT) glasses doped with Pr^{3+} (0.01, 0.1, 0.5, 1.0 and 1.5 mol%) ions were prepared by the conventional melt quenching technique. The glasses were characterized by X-ray diffraction, optical absorption and photoluminescence spectra. The glassy nature of LTT host glass has been confirmed through XRD measurements. From the measured intensities of various absorption bands of these glasses, the three phenomenological Judd–Ofelt (J–O) intensity parameters (Ω_2, Ω_4 and Ω_6) have been evaluated by using the standard as well as modified J–O theory. The J–O parameters measured from the modified J–O theory were used to characterize the absorption and luminescence spectra of these glasses. From this theory, various radiative properties like radiative transition probability (A_R), total transition probability (A_T), branching ratio (β_R) and radiative lifetime (τ_R) have been evaluated for the fluorescent levels of Pr^{3+} in these glasses. The emission spectra show five emission bands in visible region for which the effective band widths ($\Delta\lambda_P$) and emission cross-sections (σ_{se}) have been evaluated. Among all the five emission transitions, a transition $^3P_0 \rightarrow {}^3F_2$ is more intense and falls in red region. The visible emission spectra, stimulated emission cross-sections and branching ratios observed for all these glasses suggest the feasibility of using these glasses as lasers in red region. The CIE chromaticity co-ordinates were also evaluated from the emission spectra to understand the suitability of these materials for red emission. From the absorption, emission and CIE chromaticity measurements, it was found that 1 mol% of Pr^{3+} ion concentration is quite suitable for LTT glasses to develop bright red lasers from these glasses.

Keywords: Glasses; Optical absorption; JO parameters; Photoluminescence

1. Introduction

In recent years rare-earth doped glasses have fascinated several researchers because of their potential applications in the development of several optical devices like optical amplifiers, solid state lasers, laser wave guides, light converters, sensors, three dimensional displays, color display devices, biomedical diagnostics and up conversion lasers [1–9]. The spectral characteristics of rare-earth ions are reliant on host glass composition, concentration of dopant ion and ambient temperatures [10]. Heavy metal oxide glasses are suitable candidates for the development of non-linear optical devices, electro-optic modulators, electro-optic switches, solid state laser materials and IR technologies because of their high density, refractive index and low phonon energy [11–14]. Tellurium oxide being a conditional glass former can form a stable glass in presence of certain glass modifiers like tungsten trioxide (WO_3). Tellurium based glasses can be prepared at relatively low temperatures with phonon energies as low as $\sim 800\ cm^{-1}$ in comparison to phosphate, borate and silicate glasses. Glasses with low phonon energies offer less non-radiative relaxation rates and high fluorescence quantum efficiencies. Tellurium based glasses have slow crystallization rate, owing to good transparency in a wide spectral region from visible to NIR region. Relatively good mechanical strength, chemical stability and high refractive indices make them as the best host materials for obtaining efficient luminescence from trivalent rare-earth ions [15,16].

*Corresponding author at: Department of Applied Physics, Delhi Technological University, Bawana Road, New Delhi 110042, India. Tel.: +91 85860 39007.
E-mail address: drsrallam@yahoo.co.in (A.S. Rao).

0272-8842/$ - see front matter © 2013 Published by Elsevier Ltd and Techna Group S.r.l.
http://dx.doi.org/10.1016/j.ceramint.2013.11.084

Tungsten trioxide (WO_3) besides being a transition-metal oxide, is a very good semi-conducting oxide that has attracted attention for several years. It is the most investigated and used material for electro-chromic and photochromic devices in which coloration and bleaching can be reversibly obtained by an electro-chemical process [17] and has wide applications in smart windows, display devices and sensors. The TeO_2–WO_3 glasses have low transition temperature, low crystallization ability, chemically inactive, high refractive index and also are transparent in the visible and near infrared region [18,19]. Addition of fluoride compounds to tellurite based glasses can reduce phonon energies, since the maximum phonon energies of the additives are 340 cm^{-1}, which are less than the phonon energies of tellurite based glasses $\sim$800 cm^{-1}. Addition of fluoride compounds can help to remove OH group from glasses by reacting with OH group to form HF group [20,21]. This reduces the phonon energies of glasses to relatively lower values (200–400 cm^{-1}). Hence addition of PbF_2 to a tellurite based glass can decrease the phonon energy and there by reduces the non-radiative decay process.

Pr^{3+} doped glasses with low phonon energy are used very much for compact solid state lasers emitting in visible region. Pr^{3+} ions in glasses have relatively good number of absorption bands in the vis–NIR regions due to which they have various technological applications as functional photonic materials like optical fiber amplifiers, lasers and wavelength converting devices. Pr^{3+} is a significant optical activator with its several meta-stable states that offer stimulated emissions in blue, green, orange, red and infrared regions [22]. In the present work, lead tungsten tellurite (LTT) glasses were prepared by varying Pr^{3+} concentration to study the optical and luminescent properties to identify the better glass for visible solid state laser devices.

2. Experimental

2.1. Glass preparation

Lead tungsten tellurite glasses doped with different concentrations of Pr^{3+} ions were prepared by the melt quenching technique. All chemicals used to prepare the LTT glasses were analar grade with 99.9% purity. The glass composition of LTT glasses and their labeling are given in Table 1. All the reagents are thoroughly mixed in an agate mortar for 2 h to get uniform mixing and then melted using a silica crucible at 735 °C in a programable furnace for about 25 min. The resultant melts were rotated 3–4 times before quenching to achieve homogenous mixture. Such melts were then poured on a preheated brass mold and pressed quickly with another brass plate. The samples were annealed in another furnace for about 1 h to remove thermal strains that are produced due to sudden quenching. The glasses thus obtained were highly grounded to achieve a uniform thickness of 0.2 cm.

2.2. Physical and optical measurements

The densities for the prepared glasses were measured by using Archimedes's principle with xylene as an immersion liquid. The refractive indices of all glasses were measured by using Brewster's angle method with He–Ne laser operating at 632 nm. Using density and refractive indices, some other physical properties were also measured using suitable formulae [23] and are given in Table 2. In the present study the physical properties are changing from glass to glass with increase in the concentration of Pr^{3+} ions, indicating the change in environment around the doped Pr^{3+} ions. The optical absorption spectra were measured for all the glass samples from 440 to 2400 nm at room temperature with a spectral resolution of 0.1 nm using a Jasco V-670 UV–vis–NIR spectrometer. The luminescence spectra were measured by using a PL spectrometer Perkin-Elmer LS55 with a xenon arc lamp as radiation source. In order to check the amorphous nature of the prepared glasses, the XRD spectral measurement was taken for undoped glasses using a Bruker X-ray diffractometer (model D8Advance) which operates at 40 KV and 40 mA current and is shown in Fig. 1. The broad hump observed in the XRD spectrum, characteristic of an amorphous material confirms the glassy nature of the prepared glasses.

3. Results and discussion

3.1. Optical absorption spectra

Optical absorption spectra of Pr^{3+} ions doped LTT glasses were recorded at room temperature in vis–NIR region. Fig. 2 shows the optical absorption spectra recorded for glass D along with the assignment of the absorption bands. The spectra for other glasses are alike with slight difference in intensity of various absorption bands and hence spectra of the remaining glasses were not shown. The band assignments are in good agreement with earlier reports [24,25]. Pr^{3+} ion doped LTT glasses contain nine absorption bands (except glass A) corresponding to the transitions between the $^3H_4$ ground level and the excited states $^3P_2$, $^3P_1$, $^3P_0$, $^1D_2$,$^1G_4$, $^3F_4$, $^3F_3$,$^3F_2$ and $^3H_6$ belonging to the $4f^2$ configuration of the Pr^{3+} ions. The absorption bands are assigned to different transitions according to the Carnal report [26] on Pr^{3+} ion and the corresponding peak wavelength is given in Table 3. In glass A, six absorption bands are only observed in vis–NIR regions which may be due to very low concentration of Pr^{3+} ions (0.01 mol%) in that glass. The experimental oscillator strengths (f_{exp}) for the electric dipole transitions were calculated from [27].

$$f_{exp} = 4.32 \times 10^{-9} \int \varepsilon(\nu) d\nu$$

here $\varepsilon(\nu)$ is the molar extinction coefficient corresponding to the energy (ν cm^{-1}) and $d\nu$ is the half-band width of the absorption band. Quite often in glasses the absorption bands need not show a Gaussian shape. In such cases the value of $\int \varepsilon(\nu) d\nu$ is evaluated by using the area method. In the present work, for all the absorption bands, the intensities were measured by the area method. Of all the transitions, the transitions $^3H_4 \rightarrow {}^3P_2$ and $^3H_4 \rightarrow {}^3F_3$ are known as hypersensitive transitions whose intensities strongly depends on the

Please cite this article as: M. Venkateswarlu, et al., Pr^{3+} doped lead tungsten tellurite glasses for visible red lasers, Ceramics International (2013), http://dx.doi.org/10.1016/j.ceramint.2013.11.084

Table 1
LTT glass composition with different concentrations of Pr^{3+} ions (in mol%).

Name of the glass	TeO_2	WO_3	PbF_2	Pr_6O_{11}
Base glass	60	25	15	–
Glass A	59.99	25	15	0.01
Glass B	59.9	25	15	0.1
Glass C	59.5	25	15	0.5
Glass D	59	25	15	1
Glass E	58.5	25	15	1.5

Table 2
Various physical properties of Pr^{3+} doped LTT glasses.

Physical properties	Glass A	Glass B	Glass C	Glass D	Glass E
Density ρ (g cm^{-3})	6.606	6.607	6.612	6.616	6.622
Refractive index (n_d)	2.305	2.306	2.307	2.308	2.309
Average molecular weight $\overline{M}$ (g)	135.1	135.2	135.9	136.8	137.6
Pr^{3+} ion concentration N (10^{21} ions/cm^3)	0.294	2.941	14.643	29.122	43.451
Mean atomic volume (g/cm^3/atom)	6.629	6.296	6.308	6.324	6.338
Dielectric constant (ε)	5.315	5.320	5.325	5.329	5.334
Optical dielectric constant (ε^1)	4.315	4.320	4.325	4.330	4.334
Reflections loss (R) (%)	0.155	0.156	0.156	0.156	0.156
Molar refraction (R_m) (cm^{-3})	13.97	13.99	14.06	14.14	14.22
Polaron radius (r_P) (Å)	0.210	0.066	0.029	0.021	0.017
Inter ionic distance (r_i) (Å)	15.034	6.981	4.088	3.251	2.845
Molecular electronic polarizability, α (10^{-23} cm^3)	137.5	13.76	2.762	1.388	0.930
Field strength (10^{22} cm^{-2})	0.675	6.744	33.57	66.77	99.63
Optical basicity (Λ_{th})	0.540	0.541	0.542	0.544	0.545

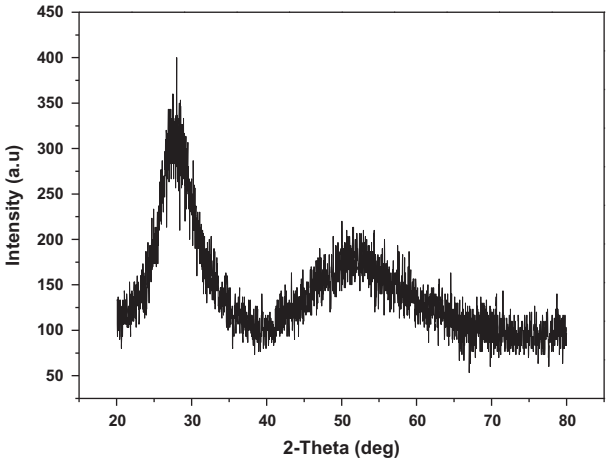

Fig. 1. XRD spectrum of an undoped LTT glass.

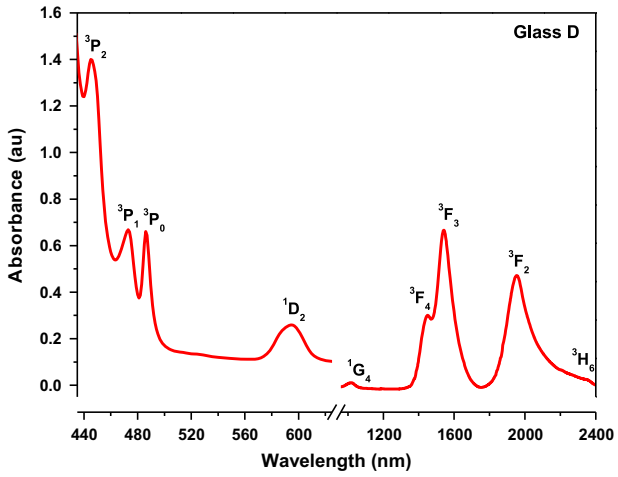

Fig. 2. Absorption spectrum of 1 mol% of Pr^{3+} ions in LTT glass (glass D) with strong absorption bands in the NIR region.

neighboring ligands [28]. The hypersensitive transitions are observed in other RE ions and exhibit anomalous nature irrespective of matrix elements and follows selection rules $\Delta S=0$, $\Delta L\leq 2$ and $\Delta J\leq 2$. Judd and Ofelt independently derived expressions for the oscillator strengths of induced electric dipole transitions for the f^N configurations [29,30]. The basic idea of the Judd–Ofelt (J–O) theory is that the intensity of the forbidden f–f electric dipole transitions can arise from the admixture of the $4f^N$ configurations with the excited configurations of opposite parity. The calculated oscillator strengths (f_{cal}) of the $\psi_J \rightarrow \psi'_{J'}$ transition are determined by using the expression given in the J–O theory [29,30].

It is well known that, the application of the J–O theory to the 4f transitions of Pr^{3+} ion gives poor agreement between the

Table 3
Assignment of absorption bands, experimental (f_{exp}) (10^{-6}), calculated oscillator strengths (f_{cal}) (10^{-6}) and r.m.s. deviation (δ_{rms}) (10^{-6}) of Pr^{3+} ions doped LTT glasses using standard and modified J–O theories.

Transition from	λ (nm)	Glass A			Glass B			Glass C			Glass D			Glass E		
$^3H_4 \rightarrow$		f_{exp}	f_{cal}	f^*_{cal}	f_{exp}	f_{cal}	f^*_{cal}	f_{exp}	f_{cal}	f^*_{cal}	f_{exp}	f_{cal}	f^*_{cal}	f_{exp}	f_{cal}	f^*_{cal}
$^3P_2$	445	–	–	–	–	–	–	6.49	5.61	**7.45**	8.87	6.06	**8.80**	6.33	4.70	**6.26**
$^3P_1$	473	–	–	–	5.37	8.03	**7.66**	4.59	6.34	**6.33**	7.31	7.54	**7.67**	5.11	6.19	**6.27**
$^3P_0$	486	–	–	–	2.02	7.91	**7.47**	3.79	6.25	**6.18**	4.32	7.42	**7.49**	4.13	6.10	**6.12**
$^1D_2$	596	1.26	1.20	**1.47**	2.30	1.56	**1.91**	3.62	1.88	**2.27**	3.92	2.04	**2.47**	3.09	1.55	**1.88**
$^1G_4$	1024	0.62	0.33	**0.35**	1.12	0.43	**0.47**	1.02	0.53	**0.57**	1.25	0.57	**0.62**	1.04	0.43	**0.47**
$^3F_4$	1453	3.16	3.17	**3.17**	1.37	4.21	**4.70**	4.16	5.76	**6.05**	4.69	6.12	**6.46**	3.31	4.59	**4.87**
$^3F_3$	1541	8.05	8.05	**8.05**	12.4	10.5	**10.1**	12.7	11.9	**11.5**	13.6	13.0	**12.7**	10.4	9.89	**9.61**
$^3F_2$	1956	8.36	8.35	**8.35**	14.2	14.3	**14.3**	15.1	15.1	**15.1**	16.7	16.7	**16.7**	11.1	11.11	**11.1**
$^3H_6$	2357	0.73	0.71	**0.67**	0.70	0.88	**0.86**	1.62	1.12	**1.07**	1.82	1.21	**1.16**	1.58	0.93	**0.89**
δ_{rms}		± 0.11		± **0.13**	± 2.61		± **2.54**	± 1.35		± **1.36**	± 1.64		± **1.40**	± 1.19		± **1.08**

f_{cal} – calculated oscillator strengths from the standard J–O theory and f^*_{cal} – calculated oscillator strengths from the modified J–O theory.

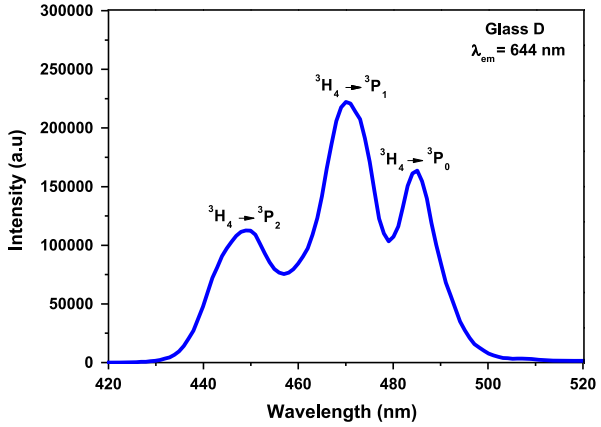

Fig. 3. Excitation spectrum of 1 mol% of Pr^{3+} ions in LTT glass (glass D).

theoretical and experimental oscillator strengths [31–34]. This poor agreement between experimental and calculated oscillator strengths is expected because of small energy difference between $4f^2$ and 4f5d levels. By applying the modified J–O theory, it is possible to get reasonably good agreement between theoretical and experimental oscillator strengths with less r.m.s. deviation including hypersensitive transition [35]. According to the modified J–O theory, the experimental oscillator strengths (f_{exp}) for electric dipole transitions were calculated using the following expression:

$$f_{exp} = \frac{8\pi^2 mc\vartheta}{3h(2J+1)} \frac{(n^2+2)^2}{9n} \times \sum_{\lambda=2,4,6} \Omega_\lambda [1+2\alpha(E_J + E_{J'} - 2E_{f^0})](\psi_J \| U^\lambda \| \psi J'_{J'})^2$$

Here E_J is the energy of the ground state, $E_{J'}$ is the energy of excited state, E_{f^0} is the energy of the center of gravity of the $4f^2$ configuration ($\sim$10,000 cm^{-1}) and $\alpha = \frac{1}{2}[E(4f5d) - E(4f)]$. The parameter α has a value of 10^{-5} cm^{-1}, but in practice it is treated as an additional fitting parameter. The calculated oscillator strengths measured by using standard as well as modified J–O theories including $^3H_4 \rightarrow {}^3P_2$ hypersensitive transition are tabulated in Table 3 along with the experimental oscillator strengths. From Table 3 it is observed that, for most of the LTT glasses, the modified J–O theory gives good approximation between experimental and calculated oscillator strengths with less r.m.s. deviation than the standard J–O theory. Table 4 gives the J–O parameters measured for all the LTT glasses using the standard and modified J–O theories along with their trend. Significant improvement in the J–O intensity parameters can be observed after applying the modified J–O theory. Except for glass A, the trend followed by the J–O intensity parameters is the same ($\Omega_2 > \Omega_4 > \Omega_6$) for all LTT glasses in both standard as well as modified J–O theories. From both the J–O theories, the Ω_2 parameter is found to be maximum for all the LTT glasses.

It is well known fact that the magnitude of the J–O intensity parameters is related to the physical and chemical properties such as viscosity and covalent character of the chemical bonds. In general, Ω_2 values for the rare earth ions in glasses are intermediate between crystalline oxides and chelating ligands [36–38]. In glasses, the rare earth ions are randomly distributed

Please cite this article as: M. Venkateswarlu, et al., Pr^{3+} doped lead tungsten tellurite glasses for visible red lasers, Ceramics International (2013), http://dx.doi.org/10.1016/j.ceramint.2013.11.084

Table 4
Judd–Ofelt intensity parameters Ω_2, Ω_4 and Ω_6 (10^{-20} cm^2) and their trend for Pr^{3+} doped LTT glasses with standard and modified J–O theories.

Name of the glass sample	Standard J–O theory			Trend	Modified J–O theory			Trend
	Ω_2	Ω_4	Ω_6		Ω_2	Ω_4	Ω_6	
Glass A	4.782	6.148	2.208	$\Omega_4 > \Omega_2 > \Omega_6$	5.402	6.609	2.318	$\Omega_4 > \Omega_2 > \Omega_6$
Glass B	11.06	7.156	2.854	$\Omega_2 > \Omega_4 > \Omega_6$	13.90	5.557	3.641	$\Omega_2 > \Omega_4 > \Omega_6$
Glass C	12.88	5.648	4.412	$\Omega_2 > \Omega_4 > \Omega_6$	15.43	4.590	5.041	$\Omega_2 > \Omega_6 > \Omega_4$
Glass D	13.89	6.70	4.606	$\Omega_2 > \Omega_4 > \Omega_6$	16.69	5.559	5.305	$\Omega_2 > \Omega_4 > \Omega_6$
Glass E	8.309	5.503	3.481	$\Omega_2 > \Omega_4 > \Omega_6$	10.30	4.542	4.045	$\Omega_2 > \Omega_4 > \Omega_6$

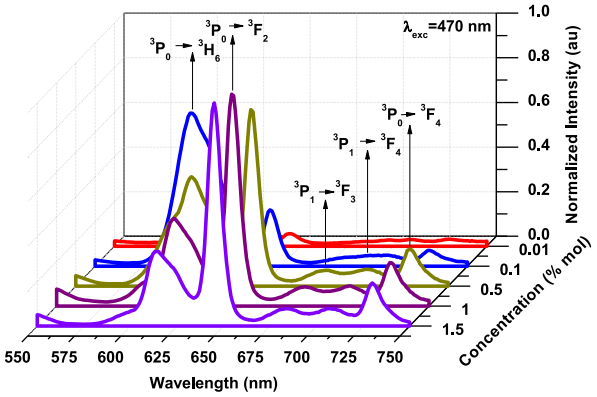

Fig. 4. Emission spectra of Pr^{3+} ions in LTT glasses.

over non-equivalent sites with a wide distribution of crystal fields. In such cases, a distribution of large number of rare earth ions occupying sites with non-centrometric potential will contribute significantly to the changes in the Ω_2 value [39]. The large Ω_2 parameter values are indicators of the covalent character of the chemical bonds among the glass matrix and rare earth ions. The Ω_2 parameter depends mainly on the asymmetry of the sites in the neighborhood of rare earth ion. The higher the Ω_2 parameter, the higher is the degree of asymmetry around the rare earth ion and stronger the covalence of rare earth ion–oxygen bond. The intensity parameters Ω_4 and Ω_6 are related to the bulk properties such as viscosity and dielectric of the media and are also affected by the vibronic transitions of the rare earth ions bound to the ligand atoms [40,41] and less sensitive to the medium in which the ions are situated. From Table 4, it is observed that, the J–O intensity parameters are found to be high for glass D, indicating that it is more asymmetric, more covalent and more rigid than the other LTT glasses.

3.2. Photoluminescence properties

To analyze the photoluminescence properties of the LTT glasses doped with Pr^{3+} ion, it is necessary to know the excitation wavelength of Pr^{3+} ion. The excitation wavelength plays an important role in recording the emission spectra of rare-earth ions doped luminescent materials. Fig. 3 shows the excitation spectra of glass D when emission is monitored at 644 nm. The excitation spectra consist of three bands corresponding to the transitions $^3H_4 \rightarrow {}^3P_2$, $^3H_4 \rightarrow {}^3P_1$ and $^3H_4 \rightarrow {}^3P_0$. Among all these transitions, a transition $^3H_4 \rightarrow {}^3P_1$ corresponding to 470 nm is more intense and is used as an excitation wavelength to record the emission spectra. The emission spectra recorded at room temperature for LTT glasses doped with different concentrations of Pr^{3+} ions in the spectral range 550–750 nm are shown in Fig. 4. The emission spectra consist of five emission bands at 613, 644, 683, 707 and 730 nm corresponding transitions to $^3P_0 \rightarrow {}^3H_6$, $^3P_0 \rightarrow {}^3F_2$, $^3P_1 \rightarrow {}^3F_3$, $^3P_1 \rightarrow {}^3F_4$ and $^3P_0 \rightarrow {}^3F_4$ respectively.

Fluorescence quenching is observed in all the emission transitions with increase in the concentration of Pr^{3+} ions. The quenching of intensity is the same for all the emission transitions except for $^3P_0 \rightarrow {}^3H_6$ transition. Fluorescence quenching for all the emission transitions begins at 1.0 mol% but for $^3P_0 \rightarrow {}^3H_6$ transition, the quenching began at 0.1 mol% of Pr^{3+} ion concentration itself. This may be due to the energy transfer through cross-relaxation between Pr^{3+} ions. Fig. 4 also shows that, with increase in Pr^{3+} ion concentration, a significant red shift has been observed for $^3P_0 \rightarrow {}^3H_6$ emission transition. The peak position of $^3P_0 \rightarrow {}^3H_6$ transition in LTT glasses observed at 600, 602, 611, 613 and 614 nm for 0.01, 0.1, 0.5, 1.0 and 1.5 mol% of Pr^{3+} ion concentration respectively indicates a red shift of that peak. This red shift may be attributed to the site distribution of Pr^{3+} ions in the vicinity of ligand fields [42]. However, for the other transitions namely $^3P_0 \rightarrow {}^3F_2$, $^3P_1 \rightarrow {}^3F_3$, $^3P_0 \rightarrow {}^3F_3$ and $^3P_0 \rightarrow {}^3F_4$ no red shift has been observed because of negligible emission intensities of the respective emission bands. Fig. 5 represents the energy level diagram depicting the various lasing transitions for 1 mol% of Pr^{3+} ions in LTT glass (glass D). From Fig. 5, it is observed that the emission occurs only from $^3P_0$, which indicates that $^3P_1$ state is thermally populated.

In order to predict the emission performance of LTT glasses doped with Pr^{3+} ions, the radiative parameters such as radiative transition probability (A_R), total radiative transition probability (A_T), radiative lifetime (τ_R), branching ratio (β_R) and stimulated emission cross-section (σ_{se}) were measured for the observed fluorescent levels using the J–O parameters derived from the modified J–O theory. The necessary mathematical expressions needed to measure the above radiative parameters were collected from our previous paper [43]. The radiative parameters thus evaluated are given in Tables 5–7. In addition to these

Please cite this article as: M. Venkateswarlu, et al., Pr^{3+} doped lead tungsten tellurite glasses for visible red lasers, Ceramics International (2013), http://dx.doi.org/10.1016/j.ceramint.2013.11.084

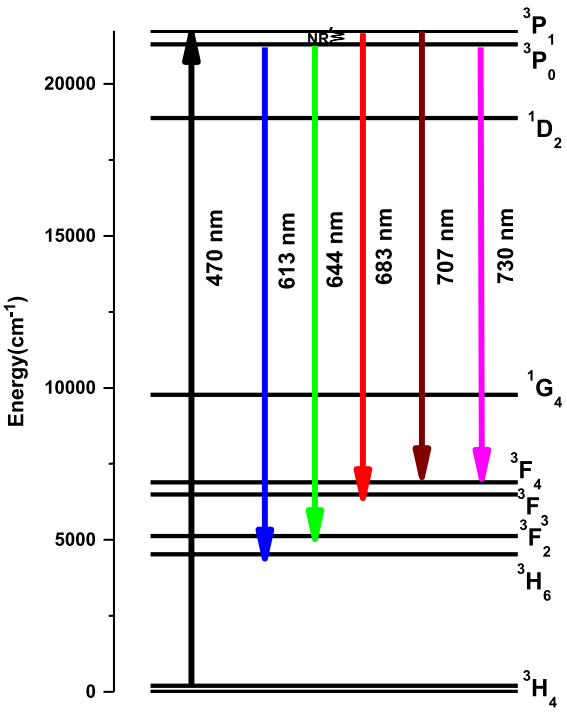

Fig. 5. Energy level scheme for emission process of 1 mol% Pr^{3+} ions in LTT glass (glass D).

parameters, the other radiative parameters like gain band width ($\sigma_{se} \times \Delta\lambda_P$) and optical gain parameters ($\sigma_{se} \times \tau_R$), which are also important to identify a laser active medium, are evaluated and included in Table 7.

Table 5 gives the transition probability (A_R), total transition probability (A_T) and radiative lifetimes (τ_R) for the observed emission transitions of Pr^{3+} ions doped LTT glasses. Large transition probability value obtained for glass D for $^3P_1 \rightarrow {}^3F_3$ fluorescent level gives the potentiality of glass D over the other LTT glasses. Table 6 represents the measured and experimental branching ratios (β_R) observed for all the emission transitions of Pr^{3+} doped LTT glasses. The emission transitions with higher magnitude of β_R are more competent for laser action than the other transitions originating from a given excited state. From Table 6, it can be observed that β_R value for $^3P_0 \rightarrow {}^3F_2$ transition is more than the other transitions in all LTT glasses. This gives the potentiality of this energy level for laser emission at 644 nm in these LTT glasses. From Table 6, it can also be observed that the β_R and β_{exp} are in good agreements with each other for all the transitions in LTT glasses. Table 7 gives the emission peak wavelength (λ_P), effective band widths ($\Delta\lambda_P$), stimulated emission cross-sections (σ_{se}), gain band width ($\sigma_{se} \times \Delta\lambda_P$) and optical gain parameter ($\sigma_{se} \times \tau_R$) for the emission transitions of Pr^{3+} ions doped LTT glasses. Stimulated emission cross-section which signifies the energy extraction for the material is an important parameter to estimate laser performance of a material. From Table 7, it is observed that among all the emission transitions, $^3P_0 \rightarrow {}^3F_2$ (644 nm) and $^3P_0 \rightarrow {}^3H_6$ (602 nm) transitions possess highest and least stimulated emission cross-sections respectively. This may be due to the variation of in-homogenous line

Table 5
Transition probabilities (A_R) (s^{-1}), total transition probability (A_T) (s^{-1}) and radiative lifetimes (τ_R) (μs) for the observed prominent emission transitions of Pr^{3+} doped LTT glasses.

Transition	Glass A			Glass B			Glass C			Glass D			Glass E		
	A_R	A_T	τ_R	A_R	A_T	τ_R	A_R	A_T	τ_R	A_R	A_T	τ_R	A_R	A_T	τ_R
$^3P_1 \rightarrow {}^3F_4$	16,914	175,196	5	14,294	245,767	4	11,787	249,880	4	14,300	280,367	3	11,703	195,693	5
$^3P_1 \rightarrow {}^3F_3$	45,984	175,196	5	94,941	245,767	4	102,262	249,880	4	112,030	280,367	3	71,559	195,693	5
$^3P_0 \rightarrow {}^3F_4$	18,598	190,419	5	15,720	26,9284	3	12,960	27,2646	3	15,723	306,094	3	12,868	212,646	4
$^3P_0 \rightarrow {}^3F_2$	59,343	190,419	5	152,956	269,284	3	170,080	272,646	3	184,281	306,094	3	113,919	212,646	4
$^3P_0 \rightarrow {}^3H_6$	7492	19,0419	5	11,788	269,284	3	16,348	272,646	3	17,234	306,094	3	13,163	212,646	4

Please cite this article as: M. Venkateswarlu, et al., Pr^{3+} doped lead tungsten tellurite glasses for visible red lasers, Ceramics International (2013), http://dx.doi.org/10.1016/j.ceramint.2013.11.084

Table 6
Measured (β_R) and experimental (β_{exp}) branching ratios of different concentrations of Pr^{3+} ions doped LTT glasses.

Transition	Glass A		Glass B		Glass C		Glass D		Glass E	
	β_R	β_{exp}	β_R	β_{exp}	β_R	β_{exp}	β_R	β_{exp}	β_R	β_{exp}
$^3P_1 \rightarrow {}^3F_4$	0.096	0.050	0.058	0.283	0.047	0.315	0.051	0.050	0.059	0.032
$^3P_1 \rightarrow {}^3F_3$	0.262	0.191	0.386	0.109	0.409	0.304	0.399	0.409	0.365	0.456
$^3P_0 \rightarrow {}^3F_4$	0.097	0.044	0.058	0.034	0.047	0.052	0.051	0.062	0.060	0.067
$^3P_0 \rightarrow {}^3F_2$	0.311	0.146	0.568	0.231	0.623	0.248	0.602	0.166	0.535	0.103
$^3P_0 \rightarrow {}^3H_6$	0.039	0.067	0.043	0.042	0.060	0.080	0.056	0.112	0.061	0.012

Table 7
Emission peak wavelength (λ_P) (nm), effective band widths ($\Delta\lambda_P$) (nm), stimulated emission cross-sections (σ_{se}) (10^{-20}) (cm^2), gain band width ($\sigma_{se} \times \Delta\lambda_p$) ($10^{-25}$) ($cm^3$) and optical gain parameters ($\sigma_{se} \times \tau_R$) ($10^{-25}$) ($cm^2$ s) for the emission transitions of Pr^{3+} doped LTT glasses.

Spectral parameters	Glass A	Glass B	Glass C	Glass D	Glass E
$^3P_0 \rightarrow {}^3H_6$					
λ_p	600	602	611	613	614
$\Delta\lambda_p$	16.3	8.11	12.0	13.0	16.3
σ_{se}	1.49	4.76	4.73	4.66	2.83
$\sigma_{se} \times \Delta\lambda_p$	0.24	0.38	0.56	0.60	0.46
$\sigma_{se} \times \tau_R$	0.74	1.43	1.42	1.40	1.14
$^3P_0 \rightarrow {}^3F_2$					
λ_p	644	644	644	644	644
$\Delta\lambda_p$	7.61	6.52	5.43	4.89	5.43
σ_{se}	33.5	101.0	134.0	161.0	89.8
$\sigma_{se} \times \Delta\lambda_p$	2.55	6.57	7.29	7.90	4.88
$\sigma_{se} \times \tau_R$	16.8	30.2	40.3	48.4	35.9
$^3P_1 \rightarrow {}^3F_3$					
λ_p	683	683	683	683	683
$\Delta\lambda_p$	8.11	6.76	9.46	4.05	9.46
σ_{se}	30.8	76.3	58.7	150.0	41.0
$\sigma_{se} \times \Delta\lambda_p$	2.50	5.16	5.55	6.07	3.88
$\sigma_{se} \times \tau_R$	15.4	30.5	23.5	45.0	20.5
$^3P_1 \rightarrow {}^3F_4$					
λ_p	707	707	707	707	707
$\Delta\lambda_p$	14.9	13.5	12.5	12.2	13.5
σ_{se}	7.08	6.60	5.87	7.30	5.39
$\sigma_{se} \times \Delta\lambda_p$	1.06	0.89	0.73	0.89	0.72
$\sigma_{se} \times \tau_R$	3.54	2.64	2.35	2.19	2.70
$^3P_0 \rightarrow {}^3F_4$					
λ_p	730	730	730	730	730
$\Delta\lambda_p$	9.46	10.8	8.11	6.76	8.11
σ_{se}	13.9	10.3	11.3	16.5	11.2
$\sigma_{se} \times \Delta\lambda_p$	1.32	1.11	0.91	1.11	0.91
$\sigma_{se} \times \tau_R$	6.97	3.09	3.39	4.94	4.49

widths of the two transitions. In the present LTT glasses, the glass D with 1 mol% of Pr^{3+} ions possesses highest stimulated emission cross-section for all the transitions. In glass D, $^3P_0 \rightarrow {}^3F_2$ transition (644 nm) possesses highest stimulated emission cross-section over the other transitions in the same glass. Hence glass D is said to be having enough competency to emit bright red laser at 644 nm. The gain parameters ($\sigma_{se} \times \tau_R$) and gain band width ($\sigma_{se} \times \Delta\lambda_p$) are used to obtain a laser host material with highest stability [44]. In the present work, the gain properties of $^3P_0 \rightarrow {}^3F_2$ level are found to be maximum for all the LTT glasses. Among all the glasses, glass D possesses higher values of these parameters. Based on the measured radiative parameters, it is suggested that glass D doped with 1 mol% of Pr^{3+} ions can be used for red laser

Please cite this article as: M. Venkateswarlu, et al., Pr^{3+} doped lead tungsten tellurite glasses for visible red lasers, Ceramics International (2013), http://dx.doi.org/10.1016/j.ceramint.2013.11.084

Table 8
CIE chromaticity co-ordinates of Pr^{3+} ions doped LTT glasses

Name of the glass	Color co-ordinates	
	X-co-ordinates	*Y*-co-ordinates
Glass A	0.6343	0.3564
Glass B	0.6423	0.3523
Glass C	0.6646	0.3345
Glass D	0.6512	0.2785
Glass E	0.6435	0.2764

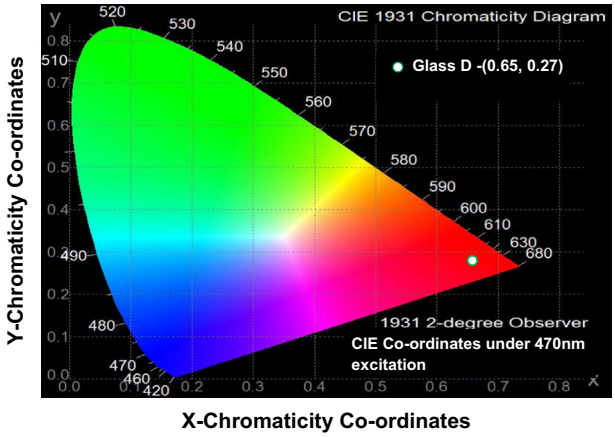

Fig. 6. CIE 1931 chromaticity diagram for 1 mol% of Pr^{3+} ions in LTT glass (glass D).

emission at 644 nm corresponding to the transitions $^3P_0 \rightarrow {}^3F_2$ and also for optical amplification.

3.3. CIE chromaticity co-ordinates

The CIE co-ordinates are used to find the color of the light emitted by the material under excitation. They are measured from the emission spectra given by the materials under investigation. Such CIE co-ordinates measured from the emission spectra of LTT glasses doped with Pr^{3+} ions using the CIE system are presented in Table 8. The emission spectra contain three parts. The first part is orange to red, second part is red and the third part is NIR. The CIE color co-ordinates for all the samples were found to be in the bright red region. Among all the glass samples, particularly glass D color co-ordinates ($x=0.65$, $y=0.27$) are falling in the bright red region corresponding to $^3P_0 \rightarrow {}^3F_2$ (644 nm) transition. Fig. 6 represents the CIE plot with color co-ordinates for 1 mol% of Pr^{3+} in LTT glass (glass *D*) excited at 470 nm wavelength. Hence glass D with 1 mol% of Pr^{3+} ions is quite suitable to give bright red color laser at 644 nm.

4. Conclusion

Lead tungsten tellurite (LTT) glasses doped with different concentrations of Pr^{3+} ions were prepared by using the conventional melt quenching technique. The amorphous nature of the prepared LTT glasses was confirmed by XRD spectrum recorded for an undoped LTT glass. The modified J–O theory has been applied to analyze the absorption spectra of Pr^{3+} ions doped LTT glasses. The J–O intensity parameters calculated by using the modified J–O theory give less r.m.s. deviation between experimental and calculated oscillator strengths. In the present work, the J–O intensity parameters (Ω_2, Ω_4 and Ω_6) are found to be high for glass D indicating that it is more asymmetric, more covalent and more rigid than the other glasses. Using the J–O parameters obtained from the modified J–O theory, the radiative properties such as transition probability (A_R), radiative lifetime (τ_R) and branching ratios (β_R) are evaluated. The emission spectra recorded at different concentrations of Pr^{3+} ions show five emission bands at 613, 644, 683, 707 and 730 nm corresponding transitions to $^3P_0 \rightarrow {}^3H_6$, $^3P_0 \rightarrow {}^3F_2$, $^3P_1 \rightarrow {}^3F_3$, $^3P_1 \rightarrow {}^3F_4$ and $^3P_0 \rightarrow {}^3F_4$ respectively. Among these five emission transitions observed, $^3P_0 \rightarrow {}^3F_2$ is more intense and is falling in red region. Based on visible emission spectra, the high stimulated emission cross-section and branching ratios observed for $^3P_0 \rightarrow {}^3F_2$ transition for all these glasses suggest the feasibility of using these materials as lasers in red region. The CIE chromaticity co-ordinates evaluated from the emission spectra recorded at 470 nm excitation for all LTT glasses confirm the suitability of these glassy materials for red emission. From the measured emission cross-sections and CIE chromaticity co-ordinates, it was found that 1 mol% of Pr^{3+} ions in LTT glasses (glass D) is aptly suitable for the development of bright visible red lasers to operate at 644 nm from these LTT glasses.

Acknowledgments

One of the authors, M. Venkateswarlu is very much thankful to Koneru Satyanarayana (President, KL University) for his motivation and support. Two of the authors, Swapna Koneru (File no.: SR/WOS-A/PS-35/2011) and Mahamuda Shaik (File no.: SR/WOS-A/PS-53/2011) are very much thankful to the Department of Science and Technology (DST), Government of India, New Delhi, for awarding them with a Women Scientist's scheme under DST-WOS(A) Program.

References

[1] T. Som, B. Karmakar, Optical properties of Eu^{3+} doped antimony oxide based low phonon disordered matrices, J. Phys. Condens. Matter 22 (2010) 035603.
[2] B. Lai, J. Wang, Q. Su, Ultraviolet and visible up-conversion emission in Tb^{3+}/Yb^{3+} co-doped fluorophosphate glasses, Appl. Phys. B 98 (2010) 41–47.
[3] R.S. Chaliha, K. Annapurna, A. Tarafder, V.S. Tiwari, P.K. Gupta, B. Karmakar, Luminescence and dielectric properties of nano-structured Eu^{3+}:K_2O–Nb_2O_5–SiO_2 glass ceramics, Solid State Sci. 11 (2009) 1325–1332.
[4] B.J. Chen, E.Y.B. Pun, H. Lin, Photoluminescence and spectral parameters of Eu^{3+} in sodium–aluminum–tellurite ceramics, J. Alloys Compd. 479 (2009) 352–356.

[5] Y.N. Savvin, N.V. Babayevskaya, S.S. Oleinik, O.N. Bezkrovnaya, A.V. Tolmachev, Luminescent properties of europium-activated yttrium gadolinium phosphates, Inorg. Mater. 45 (2009) 423–427.
[6] M. Mattarelli, M. Montagna, L. Zampedri, M. Bouazaoui, B. Capoen, S. Turrell, M. Ferrari, G.C. Righini, Effect of Eu^{3+} and Ce^{3+} codoping on the relaxation of Er^{3+} in silica–hafnia and tellurite glasses, Phys. Status Solidi 4 (3) (2007) 793–796.
[7] A. Ivankov, J. Seekamp, W. Bauhofer, Optical properties of Eu^{3+}-doped zinc borate glasses, J. Lumin. 121 (2006) 123–131.
[8] R. Balda, J. Fernandez, L.M. Lacha, M.A. Arriandiaga, J.M. Fernandez-Navarro, Energy transfer studies in Eu^{3+}-doped lead–niobium germanate glasses, Opt. Mater. 27 (2005) 1776–1780.
[9] C. Cascales, R. Balda, J. Fernandez, M.A. Arriandiaga, J.M. Fdez-Navarro, Site selective spectroscopy of Eu^{3+} in heavy-metal oxide glasses, J. Non-Cryst. Solids 352 (2006) 2448–2451.
[10] H.J. Lozykowski, W.M. Jadwisienczak, I. Brown, Photoluminescence and cathodoluminescence of GaN doped with Pr, J. Appl. Phys. 88 (2000) 210–222.
[11] Poulain Marcel, Advanced glasses, Ann. Chim. Sci. Mater. 28 (2003) 87–94.
[12] J. Yang, S. Dai, Y. Zhou, L. Wen, L. Hu, Z.H. Jiang, Spectroscopic properties and thermal stability of erbium-doped bismuth-based glass for optical amplifier, J. Appl. Phys. 93 (2) (2003) 977–983.
[13] E. Culea, L. Pop, S. Simon, Spectroscopic and magnetic behaviour of xGd_2O_3–$(1–x)(Bi_2O_3 \cdot PbO)$ glasses, Mater. Sci. Eng. B 112 (2004) 59–63.
[14] R. Balda, I. Saez de Ocariz, J. Fernandez, J.M. Fdez. Navarro, M. A. Arriandiga, Spectroscopy and orange-blue frequency upconversion in Pr^{3+}-doped GeO_2–PbO–Nb_2O_5 glass, J. Phys.: Condens. Matter 12 (2000) 10623–10632.
[15] H. Nii, K. Ozaki, M. Herren, M. Morita, Up-conversion fluorescence of Er^{3+} and Yb^{3+}-doped TeO_2-based oxide glass and single crystals, J. Lumin. 76-77 (1998) 116–119.
[16] A. Mori, Y. Ohishi, S. Sudo, Erbium-doped tellurite glass fibre laser and amplifier, Electron. Lett. 33 (1997) 863–864.
[17] D. Barreca, S. Bozza, G. Carta, G. Rossetto, E. Tondello, P. Zanella, Structural and morphological analyses of tungsten oxide nanophasic thin films obtained by MOCVD, Surf. Sci. 532 (2003) 439–443.
[18] T. Kosuge, Y. Benino, V. Dimitrov, R. Sato, T. Komatsu, Thermal stability and heat capacity changes at the glass transition in K_2O–WO_3–TeO_2 glasses, J. Non-Cryst. Solids 242 (1998) 154–164.
[19] I. Shaltout, Y. Tang, R. Braunstein, E.E. Shaisha, FTIR spectra and some optical properties of tungstate tellurite glasses, J. Phys. Chem. Solids 57 (1996) 1223–1230.
[20] M.R. Sahar, A.K. Jehnu, M.M. Karim, TeO_2-ZnO-$ZnCl_2$ glasses for IR transmission, J. Non-Cryst. Solids 213–214 (1997) 164–167.
[21] B. Bridge, T.E. Bavins, D. Woods, T. Woolven, on the preparation and composition of the glass formation range of the system TeO_2–$ZnCl_2$, J. Non-Cryst. Solids 88 (1986) 262–270.
[22] A.A. Kaminskii, in: Laser Crystals, second ed., Springer-Verlag, Berlin, 1990.
[23] A. Srinivasa Rao, B. Rupa Venkateswara Rao, M.V.V.K.S. Prasad, J.V. Shanmukha Kumar, M. Jayasimhadri, J.L. Rao, R.P.S. Chakradhar, Spectroscopic and optical properties of Nd^{3+} doped fluorine containing alkali and alkaline earth zinc aluminophospate optical glasses, Physica B 404 (2009) 3717–3721.
[24] D.V.R. Murthy, B.C. Jamalaiah, T. Sasikala, L. Rama Moorthy, M. Jayasihmadri, Kiwan Jang, H.o. Sueb Lee, Soung Soo Yi, Jung Hyun Jeong, Optical absorption and emission characteristics of Pr^{3+}-doped RTP glasses, Physica B 405 (2010) 1095–1100.
[25] A.Mendioroz Balda, J. Fernandez, M.A. arriandiaga, L.S. Grisom, J.L. Adam, Laser spectroscopy and up-conversion studies of Pr^{3+}-doped halide modified sulfide glasses, Opt. Mater. 16 (2001) 249–254.
[26] W.T. Carnall, P.R. Fields, K. Rajnak, Electronic energy levels in the trivalent lanthanide aquo-ions. I. Pr^{3+}, Nd^{3+}, Pm^{3+}, Sm^{3+}, Dy^{3+}, Ho^{3+}, Er^{3+}, and Tm^{3+}, J. Chem. Phys. 49 (1968) 4424–4442.
[27] W.T. Carnall, J.P. Hessler, F. Wagner Jr., Transition probabilities in the absorption and fluorescence spectra of lanthanides in molten lithium nitrate–potassium nitrate eutectic, J. Phys. Chem. 82 (1978) 2152–2158.
[28] C.K. Jorgensen, B.R. Judd, Hypersensitive pseudo-quadrupole transitions in lanthanides, Mol. Phys. 8 (1964) 281–290.
[29] B.R. Judd, Optical absorption intensities of rare-earth ions, Phys. Rev. 127 (1962) 750–761.
[30] G.S. Ofelt, Intensities of crystal spectra of rare-earth ions, J. Chem. Phys. 37 (1962) 511–520.
[31] J. Hormadaly, R.J. Reisfeld, Intensity parameters and laser analysis of Pr^{3+} and Dy^{3+} in oxide glasses, J. Non-Cryst. Solids 30 (1979) 337–348.
[32] S.V.J. Lakshman, L. Rama Moorthy, Optical absorption spectrum of Pr^{3+} in aprotic $POCl_3$–$SnCl_4$ laser liquid, J. Quant. Spectrosc. Radiat. Transfer 29 (1983) 439–444.
[33] G. Amarnath, S. Buddhudu, Optical properties of rare-earth doped HMF glasses, J. Non-Cryst. Solids 143 (1992) 252–256.
[34] M.A. Bunuel, R. Cases, M.A. Chamarro, J. Alcala, Optical properties of Pr^{3+}IN ZnF_2–CdF_2, Phys. Chem. Glasses 33 (1992) 16.
[35] A.A. Kornienko, A.A. Kaminskii, E.B. Dunina, Dependence of the line strength of f–f transitions on the manifold energy. II. Analysis of Pr^{3+} in $KPrP_4O_{12}$, J. Phys. Status Solidi A 157 (1990) 267–273.
[36] A.F. Kirbey, R.A. Palmer, Hypersensitive transition probability in tris (1,3-diphenyl-1, 3-propanedionato) aquo lanthanides(III), Inorg. Chem. 20 (1981) 4219–4222.
[37] A.F. Kirbey, R.A. Palmer, Single-crystal electronic absorption of tris (1,3-diphenyl-1, 3-propanedionato) aquoneodymium (III): oscillator strength of the $^4I_{9/2} \rightarrow {}^4G_{5/2}$ hyper-sensitive transition, Inorg. Chem. 20 (1981) 1030–1033.
[38] R. Reisfeld, C.K. Jorgenson, in: Lasers and Excited States of Rare Earths, Springer, New York, 1977.
[39] K.B. Yatsimirskii, N.K. Davidenko, Absorption spectra and structure of lanthanide co-ordination compounds in solution, Coord. Chem. Rev. 27 (1979) 223–273.
[40] W.F. Krupkee, Optical absorption and fluorescence intensities in several rare-earth doped Y_2O_3 and LaF_3 single crystals, Phys. Rev. 145 (1966) 325–337.
[41] C. GorllerWalrand, K. Binnemas, Spectral intensities of f–f transitions, in: K.A. Gschneidner Jr., L. Eyring (Eds.), Hand Book of Physics and Chemistry of Rare Earths, vol. 25, Elsevier, Netherlands, 1998, p. 101.
[42] X.J. Wang, H.R. Zheng, D. Jia, S.H. Huang, R.S. Meltzer, M.J. Dejneka, W.M. Yen, Spectroscopy of different sites in Pr^{3+} doped oxy-fluoride glass ceramics, Microelectron. J. 34 (2003) 549–551.
[43] Sk. Mahamuda, K. Swapna, A. Srinivasa Rao, T. Sasikala, L. Rama Moorthy, Reddish-orange emission from Pr^{3+} doped zinc alumino bismuth borate glasses, Physica B 428 (2013) 36–42.
[44] M. Liao, Z. Duan, L. Hu, Y. Fang, L. Wen, Spectroscopic properties of Er^{3+}/Yb^{3+} co-doped fluorophosphate glasses, J. Lumin. 126 (2007) 139–144.

Please cite this article as: M. Venkateswarlu, et al., Pr^{3+} doped lead tungsten tellurite glasses for visible red lasers, Ceramics International (2013), http://dx.doi.org/10.1016/j.ceramint.2013.11.084

International Journal of Scientific & Engineering Research, Volume 4, Issue 8, August 2013
ISSN 2229-5518

Prediction of Resonant Frequencies of Rectangular, Circular and Triangular Microstrip Antennas using a Generalized RBF Neural Model

Taimoor Khan and Asok De

Abstract—Microstrip antennas have proved to be the excellent radiators for many applications. It is so because of their numerous advantages such as light weight, low profile, conformable to planar and non-planar surface, low fabrication cost because of printed-circuit technology, integrability with other microwave integrated circuits (MICs) on the same substrate etc. Because of inherent characteristic of microstrip antennas to operate in the vicinity of resonant frequency, this resonant frequency needs to be calculated accurately. This paper presents a simple, accurate and fast approach based on radial basis function (RBF) neural networks for predicting the resonant frequencies of rectangular, circular and triangular microstrip antennas, simultaneously. The computed results are in very good agreement with their measured counterparts.

Index Terms— Resonant Frequencies, microstrip antennas, rectangular patch, circular patch, triangular patch, generalized approach and RBF neural networks.

1 INTRODUCTION

The conventional methods [1-3] like: transmission line model, cavity model, and full wave analysis are popularly used in analyzing and designing the microstrip antennas (MSAs). For the purpose, three stages are basically, involved in applying these methods on the electromagnetic (EM) problems. Firstly, the problem is formulated by creating a set of system equations to be solved. The geometry, describing the problem with necessary discretization into smaller elements, is created in the second stage and finally, these equations are solved using the method of choice. There are various circumstances like optimizing the problem geometry for optimum outputs, where repetitive computation of EM field is required. A minor alteration in the geometry requires a different discretization which itself is a time consuming exercise. Further, all these techniques have their own strong and weak points and require elaborate mathematics in applying on EM problems. Recently, the artificial neural networks (ANNs) have acquired tremendous utilization in analyzing and designing the MSAs [4-13]. It is so because the neural-models are computationally much more efficient than conventional models and require lesser time to model a circuit. A neural-model is trained off-line using few patterns generated through measurement, simulation and/or analytical model suitable for a problem. Once it is trained for a specified error then it returns the results for every infinitesimal changes in the input patterns within a fraction of a second and thus, completely bypasses the repetitive use of conventional models as the conventional models need re-discretization for every infinitesimal changes in the geometry which itself is a lingering and time-consuming exercise. Karaboga et. al. [5] have used a structure of two hidden layers with five neurons in each layer and a gradient descent with momentum backpropagation algorithm for training their neural model. Using this algorithm, they have calculated the resonant frequencies of electrically thin and thick rectangular MSAs with an average absolute error of 16.33 MHz. Nurhan Turker et. al. [6] have proposed multi-layered perceptron neural networks model of two hidden layers too. They have calculated the resonant frequencies of the rectangular MSAs with an average absolute error of 50 MHz. Ouchar et. al. [7] have used multi-layered perceptron artificial neural networks model with backpropagation training algorithm for calculating the resonant frequencies of the circular MSAs and the average absolute error in this model is calculated as 34.61MHz. Sagiroglu et. al. [8] have calculated the resonant frequencies of the circular MSAs using neural approach. They have used standard backpropagation algorithm with learning coefficient of 0.08 and the momentum coefficient of 0.10. The average absolute error in this model is calculated as 1.85 MHz. Sagiroglu and Guney [9] have used gradient-descent with momentum backpropagation algorithm for computing the resonant frequencies of equilateral triangular MSAs. Using this model, they have calculated the resonant frequencies of equilateral triangular MSAs with an average absolute error of 1.53 MHz. Thus the neural models [5-9] have been used for computing only single parameter i.e. the resonant frequencies of rectangular, circular and triangular microstrip antennas, respectively.

Recently the concept of using generalized neural models has been proposed for computing the resonant frequencies of rectangular, circular and triangular MSAs, simultaneously [10-13]. In these models the equivalent patch dimensions for the circular and triangular MSAs have been obtained by equating the patch areas of the circular and triangular MSAs to that of an equivalent rectangular MSA. Guney et. al. [10] have used two hidden layers with twelve and six neurons, respectively. Thus structural configuration of this neural model is complex and the calculated results by this model are also not in good agreement with their measured counterparts. Further, the Tabu search algorithm [11], ANFIS method [12] and CNFS method [13] have also been used for getting more accurate results but these approaches are also very complex. In present work, a very simple approach has been proposed for getting more accurate results than that of generalized models [10-13]. The proposed method based on radial basis function (RBF) neural networks is so simple that it can be trained from the measured, simulated and/or calculated results but to understand the novelty of the proposed work initially, it has been decided to use the measured results [14-26] as training and testing patterns. Once it is tested and validated successfully, it can be generalized on measured, simulated and/or calculated patterns.

Authors are working with department of electronics and communication engineering, Delhi Technological University (Formerly Delhi College of Engineering), Delhi-110042, India, E-mail: ktaimoor@gmail.com.

2. RBF NEURAL NETWORKS

The radial basis function neural networks (RBFNN) and the multi-layered perceptron neural networks (MLPNN) are the two popular models used in different applications of microwave domain [5-13]. A RBF neural networks consists of three layered feed-forward neural networks with entirely different tasks. The input layer is made-up of source nodes which connect the network to the outside environment. A multi-variate Gaussian non-linear transformation is used as an activation function in the hidden layer and the output layer supplies the response of the network and does not have any activation function. During training process, a RBFNN model is developed by learning from the available patterns. The aim of training process is to minimize the error between actual output and calculated output from the RBFNN model. As far as training is concerned, RBFNN is much faster than MLPNN. It is so because the training process in RBFNN has two stages and both the stages are made more efficient by using appropriate training algorithm. That is the reason of using RBFNN instead of MLPNN in many applications. Once the model is trained for a specified error, then it returns the results for every infinitesimal changes in the applied input patterns within a fraction of a second. In general three common steps are used in applying neural networks for instantly predicting the desired performance parameter; resonant frequency of rectangular, circular or triangular MSAs. Firstly, the training and testing patterns are generated and the structural configuration of hidden layer neurons is selected for training in the second step. And finally, training algorithm is applied on RBFNN model in the third step. The detailed description of each step involved is being discussed in the subsequent sub-sections below:

2.1 Generation of Patterns

A microstrip antenna, in its simplest configuration, consists of a radiating conductive patch on one side of a dielectric substrate of relative permittivity 'ε_r' and of thickness 'h' having a ground plane on the other side [1-3]. The side-view of a microstrip antenna and different radiating patches used in present work are shown in Fig. 1

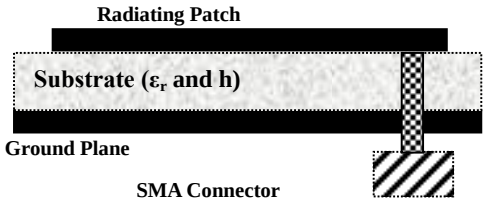

(a) Side-view

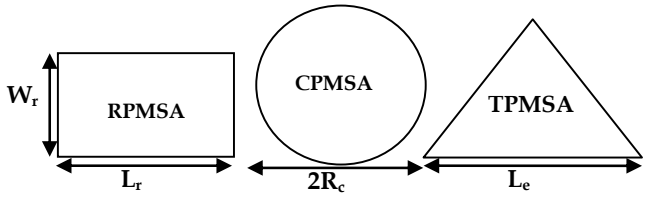

(b) Different Radiating patches

Fig. 1: Microstrip Patch Antennas

In Fig.1, RPMSA corresponds to a rectangular patch of physical dimensions 'W_r' and 'L_r', CPMSA to a circular patch of radius 'R_c' and TPMSA to an equilateral triangular patch of side-length 'L_e'. It is clear from the literature [14-26] that the resonant frequency of a microstrip antenna is the function of physical dimension(s), relative permittivity, dielectric thickness and mode of propagation. Total 81 data patterns (46 for RPMSA, 20 for CPMSA and 15 for TPMSA) have been arranged from the literature [14-17], [18-24] and [25-26], respectively. It is clear from Table 1 that the calculating parameter of a radiating patch is the function of five input parameters (x_1, x_2, x_3, x_4, and x_5) of the patch in three different cases. To distinguish them, an arbitrary parameter, 'x_6', is also included in 5-dimensional input patterns where x_6 = 1, 2 and 3 corresponds to the resonant frequency of RPMSAs, resonant frequency of CPMSAs and resonant frequency of TPMSAs, respectively.

Table 1: Input-Output Patterns for RBFNN Training

CASE I: Resonant Frequency of RPMSA (x_6=1)

Patch Parameters	ANN Inputs	ANN Output (GHz)
Width of the Patch (cm)	x_1	Resonant Frequency of RPMSA (Total patterns=46) **[14-17]**
Length of the Patch (cm)	x_2	
Dielectric Thickness (cm)	x_3	
Dielectric Constant (ε_r)	x_4	
Mode of Propagation (m&n)	x_5	

CASE II: Resonant Frequency of CPMSA (x_6=2)

Patch Parameters	ANN Inputs	ANN Output (GHz)
Radius of the Patch (cm)	x_1	Resonant Frequency of CPMSA (Total patterns=20) **[18-24]**
Dielectric Thickness (cm)	x_2	
Dielectric Constant (ε_r)	x_3	
Mode of Propagation (m)	x_4	
Mode of Propagation (n)	x_5	

CASE III: Resonant Frequency of TPMSA (x_6=3)

Patch Parameters	ANN Inputs	ANN Output (GHz)
Side-Length of Patch (cm)	x_1	Resonant Frequency of TPMSA (Total patterns=15) **[25-26]**
Dielectric Thickness (cm)	x_2	
Dielectric Constant (ε_r)	x_3	
Mode of Propagation (m)	x_4	
Mode of Propagation (n)	x_5	

2.2 Proposed ANN Structure and Algorithms

Selecting the structural configuration of RBF neural networks and neurons in the hidden layer is the prime requirement before applying training algorithm on the neural networks [4]. The training performance of the neural networks is observed by varying the number of neurons in the hidden layer and finally, it is optimized with sixteen neurons for the best performance. Further, the proposed RBF neural networks is trained with seven different algorithms [27-29]; BFGS quasi-Newton backpropagation (BFG), Bayesian regulation backpropagation (BR), scaled conjugate gradient backpropagation (SCG), Powell-Beale conjugate gradient backpropagation (CGP), conjugate gradient backpropagation with Fletcher-Peeves (CGP), one step secant backpropagation (OSS), and Levenberg-

Marquardt backpropagation (LM) and only the LM backpropagation [29] is proved to be the fastest converging training algorithm and produced the results with least error as can be confirmed from Table 2. Total 81 measured samples are divided into 66 training samples (37 for resonant frequencies of RPMSA, 17 for CPMSA and 12 for TPMSA) whereas remaining 15 samples are validated during the testing of the RBF neural networks. All initial weights and bias values are selected randomly and rounded-off between -1.0 and +1.0. The mean square error (MSE), learning rate, momentum coefficient and spread value is taken as: 5×10^{-7}, 0.1, 0.5 and 0.5, respectively and epochs required for getting a MSE of 5×10^{-7} is only 958. After getting training successfully, one can predict the resonant frequency of any arbitrary patch; rectangular, circular or equilateral triangular for the given arbitrary set of input parameters within their specified ranges. This is shown in Fig. 2.

Table 2: Comparison of Error vs. Training Algorithm

Training Algorithm [27-29]	Average Absolute Error in analysis			Iteration Required
	RPMSAs (MHz)	CPMSAs (MHz)	ETMSAs (MHz)	
BFG	2.244	17.155	9.680	2241
BR	6.337	16.370	7.687	2863
SCG	4.374	14.265	13.093	2312
CGP	4.683	15.260	19.487	2101
CGF	3.754	11.985	19.273	2161
OSS	3.085	11.575	20.180	2160
LM	1.922	1.145	1.553	958

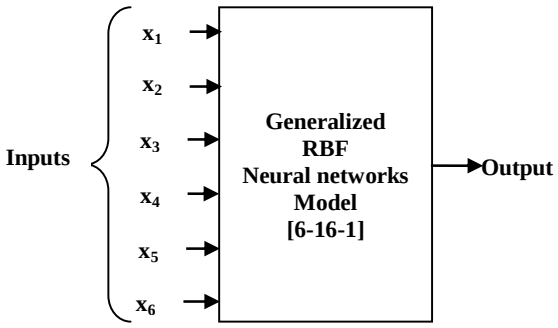

Fig. 2: Proposed GRBFNN

3. CALCULATED RESULTS AND DISCUSSION

The resonant frequencies calculated using the generalized neural model for rectangular, circular and triangular MSAs are listed in Table 3, Table 4 and Table 5, respectively. For comparison, the neural results obtained by Karaboga et al [5], Turker et. al. [6] and Guney and Sarikaya [12-13] are given in Table 3, by Oucher et. al. [7], Guney et. al. [8] and Guney and Sarikaya [12-13] in Table 4**,** by Guney and Sarikaya [12-13], Guney et. al. [10] and Sagiroglu and Guney [9] in Table 5 for resonant frequencies of rectangular, circular and triangular MSAs, respectively. Table 3 shows that in the models [5], [6], [12], and [13] the average absolute error for resonant frequencies of rectangular MSAs is calculated as 16.33MHz, 50.0MHz, 6.1697MHz and 16.8818MHz whereas in the present model it is only 1.922MHz. In case of circular MSAs, the present method is having the average absolute error of 1.145MHz whereas in the models [12], [13], [10], [8] and [7], it is calculated as 4.60MHz, 5.84MHz, 23.09MHz, 0.550MHz and 4.60MHz, respectively**.** For triangular MSAs, the models [12], [13], [10] and [9] are having the average absolute error as 1.773MHz, 1.873MHz, 18.127MHz and 1.533MHz, respectively whereas in the present method, it is only 1.553MHz.

Further illustrating the proposed work, the average absolute errors between the measured and calculated results are also compared in Tables 4-6. It is clear from these three tables that the results in the proposed method are closer with their measured counterparts as compared to the previous ANN results [5, 6, 7, 8, 9, 10, 11, 12 and 13] in all three different computing parameters. A very good convergence between the measured and calculated results supports the validity of the generalized neural method. It is clear from Table 4 that the present approach is less accurate than the approach proposed by Sagiroglu et. al. [8] in case of circular MSAs but the model [8] is calculating only one parameter whereas the present model is calculating the resonant frequencies in three different MSAs.

4. CONCLUSION

The generalized neural method based on radial basis function has been presented to accurately and simultaneously computing the resonant frequencies of the rectangular, circular, and triangular MSAs as such an accurate and simple approach is rarely available in the literature. The RBF neural model has been trained with seven different training algorithms and only Levenberg-Marquardt training algorithm is proved to be the most accurate. The results of the proposed method are in very good agreement with their measured counterparts, and has the better accuracy with respect to the neural models proposed in the literature [5-13]. The main advantage of the proposed method is that the single hidden layer structure with only 16 neurons is used for calculating the three different parameters of three different microstrip antennas. The proposed approach offers an accurate and efficient single alternative to the independent neural models [5-9]. The quick, accurate and efficient computation feature of the proposed method recommends developing some embedded neural simulators on microcontrollers, DSP processors or on FPGA platforms that would open some novel paradigms in the microwave community for effectively utilizing the artificial neural networks on some sort of hardware. Further, the approach can also be included in antenna computer-aided designs because of computing three different parameters of three different microstrip antennas accurately and simultaneously.

REFERENCES

[1] R.F. Munson, "Conformal microstrip antennas and microstrip phased arrays", *IEEE Trans. on Antennas and Propagation*, vol. 22, pp. 74-78. 1974.

[2] Y.T. Lo, D. Solomon and W.F. Richards, "Theory and experiment on microstrip antennas", *IEEE Trans. Antennas Propagat.*, Vol. AP-27, pp. 137–145, 1979.

[3] K.R. Carver and E.L. Coffey, "*Theoretical investigation of the microstrip antennas*", Tech. Rept. PT-00929, Physical Science Laboratory New Maxico State University, Las Cruces New Mexico, 1979.

[4] Q.J. Zhang and K. C. Gupta, "*Neural Networks for RF and Microwave Design*", Artech House Publishers, 2000.

[5] D. Karaboga, K. Guney, S. Sagiroglu, and M. Erler, "Neural com putation of resonant frequency of electrically thin and thick rectangular microstrip antennas", Microwaves, Antennas and Propaga-

tion, IEEE Proceedings, vol. 146, no. 2, pp. 155-159, 1999.

Table 3: Calculated Results for Rectangular MSAs and Comparison with Previous ANN Results

W_r (cm)	L_r (cm)	h (cm)	ε_r	Mode	Measured *f_r(GHz)	Calculated #f_{rn}(GHz)	Previous ANN Results			
							Ref. [5]	Ref. [6]	Ref. [12]	Ref. [13]
5.7000	3.8000	0.3175	2.3300	TM_{10}	2.3100	2.3107	2.3090	2.3109	-	-
4.5500	3.0500	0.3175	2.3300	TM_{10}	2.8900	2.8687	2.8900	2.8881	-	-
2.9500	1.9500	0.3175	2.3300	TM_{10}	4.2400	4.2413	4.2240	4.2061	-	-
1.9500	1.3000	0.3175	2.3300	TM_{10}	5.8400	5.8400	5.8410	5.8890	-	-
1.7000	1.1000	0.3175	2.3300	TM_{10}	6.8000	6.8003●	6.8320	6.6959	-	-
1.4000	0.9000	0.3175	2.3300	TM_{10}	7.7000	7.6909	7.7040	7.7950	-	-
1.2000	0.8000	0.3175	2.3300	TM_{10}	8.2700	8.2654	8.2700	8.3661	-	-
1.0500	0.7000	0.3175	2.3300	TM_{10}	9.1400	9.1381	9.1460	9.0720	-	-
1.7000	1.1000	0.9525	2.3300	TM_{10}	4.7300	4.7310	4.7280	4.6867	-	-
1.7000	1.1000	0.1524	2.3300	TM_{10}	7.8700	7.8702	7.8390	-	-	-
4.1000	4.1400	0.1524	2.5000	TM_{10}	2.2280	2.2279	2.2260	-	-	-
6.8580	4.1400	0.1524	2.5000	TM_{10}	2.2000	2.2010●	2.1900	-	-	-
10.8000	4.1400	0.1524	2.5000	TM_{10}	2.1810	2.1809	2.1810	-	-	-
0.8500	1.2900	0.0170	2.2200	TM_{10}	7.7400	7.7383	7.7360	-	7.7438	7.7400
0.7900	1.1850	0.0170	2.2200	TM_{10}	8.4500	8.4496●	8.4140	-	8.4555	8.2640
2.0000	2.5000	0.0790	2.2200	TM_{10}	3.9700	3.9681	3.9660	-	3.9711	3.9700
1.0630	1.1830	0.0790	2.5500	TM_{10}	7.7300	7.7271	7.7250	-	7.7266	7.7300
0.9100	1.0000	0.1270	10.2000	TM_{10}	4.6000	4.6003	4.6000	-	4.5988	4.6000
1.7200	1.8600	0.1570	2.3300	TM_{10}	5.0600	5.0599	5.0580	5.0259	5.0575	5.0599
1.8100	1.9600	0.1570	2.3300	TM_{10}	4.8050	4.8049●	4.8280	-	4.8426	4.8324
1.2700	1.3500	0.1630	2.5500	TM_{10}	6.5600	6.5597	6.5420	-	6.5598	6.5599
1.5000	1.6210	0.1630	2.5500	TM_{10}	5.6000	5.5991	5.5810	-	5.5947	5.6003
1.3370	1.4120	0.2000	2.5500	TM_{10}	6.2000	6.2001●	6.1890	-	6.1813	6.1936
1.1200	1.2000	0.2420	2.5500	TM_{10}	7.0500	7.0493	7.0230	-	7.0489	7.0501
1.4030	1.4850	0.2520	2.5500	TM_{10}	5.8000	5.7948	5.8010	-	5.8007	5.7994
1.5300	1.6300	0.3000	2.5000	TM_{10}	5.2700	5.2681	5.2660	-	5.2776	5.2702
0.9050	1.0180	0.3000	2.5000	TM_{10}	7.9900	7.9889	7.9670	-	7.9916	7.9900
1.1700	1.2800	0.3000	2.5000	TM_{10}	6.5700	6.5680	6.5540	-	6.5701	6.5702
1.3750	1.5800	0.4760	2.5500	TM_{10}	5.1000	5.0968●	5.1570	-	5.0978	4.8378
0.7760	1.0800	0.3300	2.5500	TM_{10}	8.0000	7.9962	7.9900	-	7.9980	8.0000
0.7900	1.2550	0.4000	2.5500	TM_{10}	7.1340	7.1339	7.1070	7.0603	7.1349	7.1339
0.9870	1.4500	0.4500	2.5500	TM_{10}	6.0700	6.0684	6.0670	6.0940	6.0726	6.0698
1.0000	1.5200	0.4760	2.5500	TM_{10}	5.8200	5.8181●	5.8470	5.8600	5.8632	5.8323
0.8140	1.4400	0.4760	2.5500	TM_{10}	6.3800	6.3750	6.3920	6.4234	6.3803	6.3802
0.7900	1.6200	0.5500	2.5500	TM_{10}	5.9900	5.9851	5.9500	5.9439	5.9900	5.9899
1.2000	1.9700	0.6260	2.5500	TM_{10}	4.6600	4.6600	4.6320	-	4.6592	4.6600
0.7830	2.3000	0.8540	2.5500	TM_{10}	4.6000	4.6001	4.6020	-	4.6063	4.6000
1.2560	2.7560	0.9520	2.5500	TM_{10}	3.5800	3.5805●	3.5100	-	3.6005	3.5428
0.9740	2.6200	0.9520	2.5500	TM_{10}	3.9800	3.9802	3.9540	-	3.9721	3.9796
1.0200	2.6400	0.9520	2.5500	TM_{10}	3.9000	3.9031	3.8820	-	3.9070	3.9003
0.8830	2.6760	1.0000	2.5500	TM_{10}	3.9800	3.9812	3.9780	-	3.9845	3.9801
0.7770	2.8350	1.1000	2.5500	TM_{10}	3.9000	3.9002	3.9820	-	3.8947	3.9000
0.9200	3.1300	1.2000	2.5500	TM_{10}	3.4700	3.4702	3.4600	-	3.4725	3.4699
1.0300	3.3800	1.2810	2.5500	TM_{10}	3.2000	3.2002●	3.1870	-	3.1949	3.2224
1.2650	3.5000	1.2810	2.5500	TM_{10}	2.9800	2.9809	2.9630	-	2.9794	2.9800
1.0800	3.4000	1.2810	2.5500	TM_{10}	3.1500	3.1501	3.1410	-	3.1485	3.1501
Average Absolute Error (MHz) →						**1.9220**	16.330	50.000	6.1697	16.882

*f_r→Measured Results [21-24], #f_{rn}→Calculated GRBFNN Results and ●→Testing Results.

[6] Turker, Nurhan, Gunes, Filiz and Yildirim, Tulay, "Artificial neural design of microstrip antennas", *Turk J Elec. Engin*, vol. 14, no. 3, 2006.

[7] A. Qucher, R. Aksas, and H. Baudrand, "Artificial neural network for computing the resonant frequency of circular patch antennas", *Microw and Opt Technol Lett*, vol. 4, pp. 564-566, 2005.

[8] Sagiroglu Seref, Guney Karim and Erler Mehmet, "Resonant frequency calculation for circular microstrip antennas using artificial neural networks", *Int J RF, Microw and CAE*, vol. 8, 1998.

[9] S. Sagiroglu and K. Guney, "Calculation of resonant frequency for an equilateral triangular microstrip antennas with the use of artificial neural networks", *Microw and Opt. Technol. Lett.* vol. 14, no. 2, pp. 89-93, 1997.

[10] Karim Guney, Seref Sagiroglu and Mehmet Erler, "Generalized neural method to determine resonant frequencies of various microstrip antennas", *International Journal of RF and Microwave Computer Aided Engineering*, vol. 12, pp 131-139, 2002.

[11] S. Sagiroglu and A. Kalinli, "Determining resonant frequencies of various microstrip antennas within a single neural model trained using parallel Tabu search algorithm," *Electromagnetics*, vol. 25, pp. 551–565, 2005.

[12] K. Guney and N. Sarikaya, "A hybrid method based on combining artificial neural network and fuzzy interference system for simultaneous computation of resonant frequencies of rectangular, circular, and triangular microstrip antennas", *IEEE Trans. on Antenna and Propag.*, vol. 55, no. 3, 2007.

Table 4: Calculated Results for Circular MSAs and Comparison with Previous ANN Results

Input Parameters				Measured	Calculated	Previous ANN Results				
R_c (cm)	h(cm)	ε_r	Mode	*f_c (GHz)	#f_{cn} (GHz)	Ref. [12]	Ref. [13]	Ref. [10]	Ref. [8]	Ref. [7]
6.80000	0.08000	2.32000	TM_{11}	0. 8350	0.8351	0.8346	0.8356	0.8229	0.835	0.8351
6.80000	0.15900	2.32000	TM_{11}	0.8290	0.8289●	0.8233	0.8241	0.8202	0.828	0.8301
6.80000	0.31800	2.32000	TM_{11}	0.8150	0.8152	0.8158	0.8166	0.8145	0.815	0.8144
5.00000	0.15900	2.32000	TM_{11}	1.1280□□ □□□	1.1283	1.1280	1.1282	1.1081	1.128	1.1284
3.80000	0.15240	2.49000	TM_{11}	1.4430	1.4428	1.4444	1.4447	1.4404	1.443	1.4443
4.85000	0.31800	2.52000	TM_{11}	1.0990	1.0991	1.0977	1.0985	1.1096	1.099	1.0986
3.49300□ □□	0.15880	2.50000	TM_{11}	1.5700	1.5685	1.5703	1.5728	1.5655	1.570	1.5678
1.27000□ □□	0.07940	2.59000	TM_{11}	4.0700	4.0709	4.0707	4.0703	4.1443	4.070	4.0703
3.49300□ □□	0.31750	2.50000	TM_{11}	1.5100□□	1.5102	1.5100	1.5115	1.5617	1.510	1.5117
4.95000□ □□□	0.23500	4.55000	TM_{11}	0.8250	0.8253	0.8248	0.8257	0.8824	0.825	0.8250
3.97500	0.23500	4.55000	TM_{11}	1.0300	1.0307	1.0305	1.0323	1.0280	1.030	1.0313
2.99000	0.23500	4.55000	TM_{11}	1.3600	1.3591	1.3603	1.3593	1.3126	1.361	1.3592
2.00000	0.23500	4.55000	TM_{11}	2.0030	2.0030●	2.0348	2.0321	1.9791	2.003	2.0048
1.04000	0.23500	4.55000	TM_{11}	3.7500	3.7481	3.7495	3.7501	3.7322	3.750	3.4980
0.77000	0.23500	4.55000	TM_{11}	4.9450	4.9425	4.9429	4.9450	4.9655	4.945	4.9458
1.15000	0.15875	2.65000	TM_{11}	4.4250	4.4257	4.4242	4.4243	4.4287	4.425	4.4209
1.07000	0.15875	2.65000	TM_{11}	4.7230	4.7131	4.7204	4.7226	4.7123	4.723	4.7292
0.96000	0.15875	2.65000	TM_{11}	5.2240	5.2236	5.2253	5.2247	5.1980	5.224	5.2249
0.74000	0.15875	2.65000	TM_{11}	6.6340	6.6322	6.6718	6.7014	6.6625	6.634	6.2523
0.82000	0.15875	2.65000	TM_{11}	6.0740	6.0738●	6.0715	6.0734	6.0450	6.074	6.1084
Average Absolute Error (MHz) →					**1.1450**	4.6000	5.8400	23.100	0.550	4.6000

*f_c→Measured Results [25-31], #f_{cn}→ Calculated GRBFNN Results and ●→Testing Results.

Table 5: Calculated Results for Triangular MSAs and Comparison with Previous ANN Results

Input Parameters				Measured	Calculated	Previous ANN Models			
L_e(cm)	h(cm)	ε_r	Mode	*f_e(GHz)	#f_{en}(GHz)	Ref. [12]	Ref. [13]	Ref. [10]	Ref. [9]
4.1000	0.0700	10.5000	TM_{10}	1.5190	1.5185●	1.5175	1.5191	1.5270	1.5260
4.1000	0.0700	10.5000	TM_{11}	2.6370	2.6365	2.6358	2.6340	2.6235	2.6370
4.1000	0.0700	10.5000	TM_{20}	2.9950	2.9957	2.9968	2.9957	2.9833	2.9950
4.1000	0.0700	10.5000	TM_{21}	3.9730	3.9741	3.9730	3.9732	3.9921	3.9730
4.1000	0.0700	10.5000	TM_{30}	4.4390	4.4392	4.4386	4.4387	4.4245	4.4390
8.7000	0.0780	2.3200	TM_{10}	1.4890	1.4885●	1.4888	1.4899	1.5037	1.4780
8.7000	0.0780	2.3200	TM_{11}	2.5960	2.5943	2.5958	2.5954	2.6006	2.5960
8.7000	0.0780	2.3200	TM_{20}	2.9690	2.9704	2.9695	2.9679	2.9866	2.9690
8.7000	0.0780	2.3200	TM_{21}	3.9680	3.9671	3.9774	3.9776	3.9456	3.9680
8.7000	0.0780	2.3200	TM_{30}	4.4430	4.4441	4.4423	4.4424	4.4402	4.4430
10.0000	0.1590	2.3200	TM_{10}	1.2800	1.2838	1.2804	1.2787	1.2577	1.2800
10.0000	0.1590	2.3200	TM_{11}	2.2420	2.2425	2.2424	2.2429	2.2241	2.2420
10.0000	0.1590	2.3200	TM_{20}	2.5500	2.5409	2.5494	2.5506	2.5009	2.5500

10.0000	0.1590	2.3200	TM_{21}	3.4000	3.4013	3.3982	3.4001	3.4165	3.4000
10.0000	0.1590	2.3200	TM_{30}	3.8240	3.8247●	3.8315	3.8321	3.8612	3.8290
Average Absolute Error (MHz) ⟶					**1.5530**	1.7730	1.8730	18.127	1.5330

*f_e→Measured Results [32-33], #f_{en}→ Present Method Results ●→Testing Results.

[13] K. Guney and N. Sarikaya, "Concurrent neuro-fuzzy systems for resonant frequency computation of rectangular, circular, and triangular microstrip antennas", *Progress In Electromagnetic Research*, vol. 84, pp. 253-277, 2008.

[14] E. Chang, S.A. Long and W.F. Richards, "An experimental investigation of electrically thick rectangular microstrip antennas," *IEEE Trans on Antennas and Propagat*, AP-34, pp.767-772, 1986.

[15] K.R. Carver, "Practical analytical techniques for the microstrip antenna" *Proc-workshop on printed circuit antenna technology*, New Mexico State University, Las Cruces 1979. P.7.1-7.20.

[16] M. Kara, "The resonant frequency of rectangular microstrip antenna elements with various substrate thicknesses" *Microw Opt Technol Lett*, vol.11, no.2, pp 55-59, 1996.

[17] M. Kara, "Closed-form expressions for the resonant frequency of rectangular microstrip antenna elements with thick substrates" *Microw Opt Technol Lett*, vol. 12, no.3, pp.131-136, 1996.

[18] J.S. Dahele and K.F. Lee "Effect of substrate thickness on the performance of a circular-disk microstrip antenna", *IEEE Trans Antenna and Propagat*, vol. 31, no. 2, pp. 358-364, 1983.

[19] J.S. Dahele and K.F. Lee, "Theory and experiment on microstrip antennas with air-gaps", IEE Proc, vol. 132, no. 7, pp 455-460, 1985.

[20] K.R. Carver, "Practical analytical techniques for the microstrip antenna", *Proc. Workshop on Printed Circuit Antennas*, New Mexico State University, pp. 7.1-7.20, 1979.

[21] K. Antoszkiewicz, and L. Shafai, "Impedance characteristics of circular microstrip patches", *IEEE Trans Antenna and Propag*, vol. 38, no. 6, pp.942-946, 1990.

[22] J.Q. Howell, "Microstrip antennas", *IEEE Trans Antenna and Propagat*, vol. 23, pp. 90-93, 1975.

[23] T. Itoh and R. Mittra, "Analysis of a microstrip disk resonator", *Arch Electron Ubertrugungs, v*ol. 27, no. 11, pp.456-458, 1973.

[24] F. Abboud, J.P. Damiano and A. Papiernik, "New determination of resonant frequency of circular disc microstrip antenna: application to thick substrate", Electron Lett, vol. 24, no. 1, pp.1104-1106, 1988.

[25] W. Chen, K.F. Lee and J.S. Dahele, "Theoretical and experimental studies of the resonant frequencies of the equilateral triangular microstrip antenna", *IEEE Trans on Antennas and Propag*, vol. 40, no.10, pp.1253-1256, 1992.

[26] J.S. Dahele and K.F. Lee, "On the resonant frequencies of the triangular patch antenna", *IEEE Trans on Antenna and Propag*, vol 35, no. 1, pp.100-101, 1987.

[27] P.E. Gill, W. Murray, and M. H. Wright, *Practical Optimization*, New York: Academic Press, 1981.

[28] L.E. Scales, *Introduction to Non-Linear Optimization*, New York: Springer-Verlag, 1985.

[29] M.T. Hagan and M. Menhaj, "Training feed forward networks with the Marquardt algorithms", *IEEE Trans. on Neural Networks*, vol 5, pp. 989-993, 1994.

Preparation and characterization of self-assembled layer by layer $NiCo_2O_4$-reduced graphene oxide nanocomposite with improved electrocatalytic properties

Manish Srivastava, Md. Elias Uddin, Jay Singh, Nam Hoon Kim, Joong Hee Lee

PII: S0925-8388(13)03090-9
DOI: http://dx.doi.org/10.1016/j.jallcom.2013.12.111
Reference: JALCOM 30175

To appear in:

Received Date: 20 September 2013
Revised Date: 11 December 2013
Accepted Date: 12 December 2013

Please cite this article as: M. Srivastava, Md. Elias Uddin, J. Singh, N.H. Kim, J.H. Lee, Preparation and characterization of self-assembled layer by layer $NiCo_2O_4$-reduced graphene oxide nanocomposite with improved electrocatalytic properties, (2013), doi: http://dx.doi.org/10.1016/j.jallcom.2013.12.111

Preparation and characterization of self-assembled layer by layer $NiCo_2O_4$-reduced graphene oxide nanocomposite with improved electrocatalytic properties

Manish Srivastava[a], Md. Elias Uddin[a], Jay Singh[b], Nam Hoon Kim[a], Joong Hee Lee[a,c,*]

[a] Advanced Materials Research Institute for BIN Fusion Technology (BK Plus Global Program), Department of BIN Fusion Technology, Chonbuk National University, Jeonju, Jeonbuk, 561-756, Republic of Korea.

[b]Department of Applied Chemistry, Delhi Technological University, Shahbad Daulatpur, Main Bawana Road, Delhi 110042, India

[c] Advanced Wind Power System Research Center, Department of Polymer & Nano Engineering, Chonbuk National University, Jeonju, Jeonbuk, 561-756, Republic of Korea.

***Correspondence Author: Joong Hee Lee (jhl@chonbuk.ac.kr)**
Tel: +82 63 270 2342; Fax: +82 63 2702341

Abstract

$NiCo_2O_4$ nanoparticles dispersed on reduced graphene oxide (RGO) are prepared by simultaneously reducing graphene oxide (GO), nickel and cobalt nitrate via a hydrothermal method assisted by post annealing at low temperature. The method involves formation of hydroxides on GO using ammonia under hydrothermal conditions. Subsequent thermal treatment at 300 ºC led to the conversion of hydroxides into single-phase $NiCo_2O_4$ atop the RGO. The synthesized products are characterized through several techniques including X-ray diffraction (XRD), ultraviolet-visible spectroscopy (UV-Vis), Fourier transform infrared spectroscopy (FT-IR), Raman spectroscopy (RS), field emission scanning electron microscopy (FE-SEM), transmission electron microscopy (TEM) and X-ray photoelectron spectroscopy (XPS). The FE-SEM investigations reveal the growth of a layer by layer assembly of $NiCo_2O_4$-RGO (2:1) nanocomposite, where the $NiCo_2O_4$ nanoparticles are tightly packed between the layers of RGO. Further, the catalytic properties of the $NiCo_2O_4$-RGO nanocomposite are investigated for the oxygen evolution reaction (OER) through cyclic voltammetry (CV) measurements. It is observed that the special structural features of the $NiCo_2O_4$-RGO (2:1) nanocomposite, including layer by layer assembly, integrity and excellent dispersion of the $NiCo_2O_4$ nanoparticles atop the RGO, produced a synergistic effect and therefore significantly improved the electrochemical performance. The oxidation potential (0.135 V) of $NiCo_2O_4$-RGO (2:1) nanocomposite was observed to be lower than that of bare $NiCo_2O_4$ nanoparticles (0.33 V), whereas the corresponding current densities were measured to be 4.1 mA/cm^2 and 3.11 mA/cm^2, respectively.

Keywords: Graphene; nanocomposite materials; nickel-cobaltite; catalyst.

1. Introduction

Graphene, a carbon allotrope consisting of a single layer of carbon atoms with a hexagonal packed lattice structure, has aroused great interest within the scientific community. Graphene exhibits several unique properties such as excellent optical and mechanical properties, good thermal conductivity, high surface area and high carrier mobility [1]. Owing to these attractive properties, graphene and its composites have shown potential for applications in different research fields including environmental pollution remediation and energy storage/conversion devices such as supercapacitors, lithium ion batteries and fuel cells [2-3].

Usually, nanoparticles are combined with graphene to produce different types of composite materials for catalytic applications. However, poor dispersion of nanoparticles over the graphene and aggregation of graphene may reduce the catalytic activity [4]. On the other hand, though GO may exhibit better dispersibility and anchoring of the nanoparticles, GO is insulating, making it unsuitable for fabrication of catalyst [5]. In contrast, reduction of GO to fabricate reduced graphene oxide (RGO)/nanoparticle composites has stimulated intense research as RGO can combine the advantages of graphene and GO in terms of both conductivity and dispersibility. Therefore, various types of RGO/nanoparticle composites have been widely studied for potential applications including in supercapacitors, lithium ion batteries, catalyst, biosensors, reinforced composites, photocatalysts and semiconductor devices [6-12].

Among the various types of metal oxides, nickel-cobaltite ($NiCo_2O_4$) is a low cost environmentally-friendly transition metal oxide that has been used as an electrocatalyst for water splitting (oxygen evolution) [13], as a photocatalyst [14], in supercapacitors [15] and in lithium ion batteries [16]. Generally, $NiCo_2O_4$ is regarded as a mixed metal oxide consisting of a spinel

type crystal structure, where the nickel cations occupy octahedral sites and cobalt cations are randomly distributed over the tetrahedral and octahedral sites. The redox couples Ni^{+3}/Ni^{+2} and Co^{+3}/Co^{+2} present in the crystal structure provide notable electrocatalytic properties. Furthermore, the electronic conductivity of $NiCo_2O_4$ has been reported to be much higher than those of nickel oxide and cobalt oxide. Therefore, $NiCo_2O_4$ is expected to show better catalytic properties compared to the single-component metal oxide due to rich redox reactions originating from Ni and Co cations which are present in different valance states [17]. Nevertheless, it has been observed that, due to the high surface area, nanoparticles tend to aggregate and form large clusters, which reduce the catalytic activity. It is well known that the catalytic activity relies highly on an electrochemically activate surface area and the kinetic features of the material. Therefore, enhancing the kinetics of ions on the electrode and electrode/electrolyte interface combined with a highly electro-active surface area is crucial [18]. Catalytic activity can be enhanced by size reduction and uniform dispersion of the nanoparticles, which can provide high surface area. Strategies have been created to design high performance catalysts by introducing a conducting substrate which can afford a smooth electron pathway and a short diffusion length [19-20]. Compared to one-dimensional carbon nanotubes, graphene is a more suitable substrate for the nanoparticles because of a large surface area and higher conductivity.

In response to the needs of modern society and increased pollution, one of the major challenges is to provide clean and renewable energy sources. Therefore, this field has prompted extensive research activity. Among the different types of renewable energy sources, hydrogen (H_2), an environment friendly and clean fuel, is expected to be one of the most promising power sources in the future. The methods of H_2 production include photochemical, electrochemical, thermal and thermal-chemical techniques. However, water electrolysis is one of the most

promising and most progressive methods. Nevertheless, the main challenges in the development of water electrolysis devices are to improve the efficiency of H_2 production and reduce the cost of components. Therefore, development of an electrocatalyst having high stability, high efficiency, low cost, and a low overpotential for oxygen and hydrogen evolution reaction is required. The oxygen evolution reaction (OER) involves an anodic reaction employed in electrolysis cells and may also be helpful to balance solar fuel synthesis reactions.

Though RuO_2 and IrO_2 are considered to be the best catalysts for OER in acidic and basic media, respectively, they suffer from poor chemical stability. Additionally, being the rarest metal oxides, they are expensive and therefore not of practical interest for large-scale applications. On the other hand, oxides of transition metals, particularly copper, nickel and cobalt, exhibit better catalytic properties than other metal oxides. However, inferior electrocatalytic activities for OER have been observed with these metal oxides. Furthermore, in highly acidic and basic media, metal and metal oxide nanoparticles also suffer from corrosion effects, which cause a short cycling life of the electrode. In view of the above mentioned issues, considerable research efforts have been devoted to synthesis and characterization of anode materials (catalyst) for OER. Recently, teflon-bonded Ti/Co_3O_4 [21], iron, nickel phthalocyanines/multi-walled carbon nanotubes [22], MnO_2 nanorods [23], lithium-doped Co_3O_4 [24], Co_3O_4/Co_2MnO_4 nanocomposites [25], $CaMn_4O_x$ [26], nitrogen-doped graphene [27], $NiCo_2S_4$/graphene [28], WO_3/graphene [29], and cobalt phosphate/GO nanocomposites [30] have been studied for OER.

In this study, we report synthesis of a $NiCo_2O_4$-RGO nanocomposite, where $NiCo_2O_4$ acts as the active catalytic species. A simple hydrothermal method assisted by low temperature annealing was adopted to synthesize $NiCo_2O_4$-RGO nanocomposites. Simultaneous reduction of GO in the presence of nickel and cobalt metal precursors was achieved under hydrothermal

conditions. It was concluded that in-situ growth of $NiCo_2O_4$ on RGO improved the dispersibility and therefore improved the charge transfer ability. Furthermore, this method is eco-friendly, since it avoids the use of toxic reagents like hydrazine. Combining the catalytic ability of $NiCo_2O_4$ nanoparticles and the high electron transfer ability of RGO, the $NiCo_2O_4$-RGO nanocomposites exhibited much better catalytic ability than that of bare $NiCo_2O_4$ nanoparticles toward the OER.

2. Experimental

2.1 Chemicals

Natural graphite flakes were purchased from Sigma–Aldrich, Steinheim, Germany. H_2SO_4, H_2O_2 and HCl were purchased from Samchun Pure Chemical Co. Ltd. (Pyeongtaek-si, Korea). $KMnO_4$ (Junsei Chemical Co. Ltd., City, Japan), 25 % NH_4OH, cobalt nitrate (II) hex-hydrate [$Co(NO_3)_2.6H_2O$] and nickel nitrate (III) nonahydrate [$Ni(NO_3)_2.6H_2O$], procured from Sigma Aldrich, were used as received**.**

2.2 Experimental Procedure

2.2.1 Synthesis of GO

A modified Hummers method was used to synthesize GO [31]. In a typical procedure, 23 ml of H_2SO_4 (98%) was added to 1 gm of natural graphite flake in a round bottom flask, followed by vigorous stirring in an ice bath. Then, 3 gm of $KMnO_4$ was carefully added at a controlled rate. The mixture was vigorously stirred for 2h while maintaining the temperature of the reaction < 5 ºC. Subsequently, the mixture continued to react at 35 ºC for 6h immersed in a preheated oil bath. Further, 45 ml of deionized (DI) water was added and stirred for another 2h. Then, the obtained mixture was transferred into a 5 L beaker, and H_2O_2 (35 %) was gradually added until the mixture turned yellow. In order to remove the excess manganese salt, dilute HCl

solution (5% by volume) was also added. The obtained suspension of GO afforded a brown dispersion. Finally, GO was washed several times using DI water until the pH of the dispersion was neutral.

2.2.2 Synthesis of $NiCo_2O_4$-RGO composite

$NiCo_2O_4$-RGO nanocomposite was synthesized by a hydrothermal method. Synthesis involves the following steps: 100 mg of GO was dispersed in 40 ml of DI water using ultrasonication for a period of 30 min. Then, 0.298 gm of nickel nitrate and 0.582 gm of cobalt nitrate were dissolved in 10 ml of DI water. The above prepared solution of metal salts was gradually added into the solution of GO over 1h under vigorous magnetic stirring to obtain a uniform solution. After that, NH_4OH (25 %) was dropped into the above prepared solution under a constant-rate of magnetic stirring while maintaining the pH of the solution at ~11. After stirring for 5h, the as-prepared solution was transferred into a 100 ml Teflon vessel and placed into a stainless steel tank. The reaction was carried out at 180 ºC for 24h. Once the reaction was complete, the autoclave was allowed to cool to room temperature. The obtained product was washed several times using DI water, ethanol and was further dried at 70 ºC in vacuum for two days. The obtained product was further calcined at 300 ºC for 4h under an argon atmosphere to obtain the final product, which was labeled $NiCo_2O_4$-RGO (2:1). A schematic diagram of the synthesis procedure is shown in Scheme.1. Following the above mentioned steps, bare $NiCo_2O_4$, RGO and $NiCo_2O_4$-RGO nanocomposites with two ratios of $NiCo_2O_4$ to RGO (1:1, 4:1) were also synthesized.

2.2.3 Growth mechanism

The synthesis method involves electrostatic interactions between the metal cations and GO. Precipitation of metal precursors was achieved using ammonia solution on GO via a

hydrothermal treatment, which can reduce the post calcination process at high temperature to produce a single-phase $NiCo_2O_4$-RGO composite. Scheme 1 also illustrates that the metal cations were coordinated with the functional groups of GO to form a mixture of metallic ion/GO, where these metal cations were converted to a cluster of metal hydroxides by adjusting the pH of the mixture using ammonia. Furthermore, the hydrothermal treatment assisted by calcination can yield crystallite growth of $NiCo_2O_4$ nanoparticles on RGO.

3. Measurements and Characterization

3.1 Characterization

Crystalline features and phase formation of the synthesized samples were investigated through powder X-ray diffraction (XRD) using a D/Max 2500V/PC (Cu Kα, λ = 1.5406 Å; Rigaku Corporation, Tokyo, Japan). Diffraction patterns were recorded at a scan rate of 1° min^{-1} in the 2 θ range of 5 - 90º. Fourier transform infrared spectra (FT-IR) of the samples were recorded over a wave-number range of 400–4000 cm^{-1} using a Nicolet 6700 spectrometer (Thermoscientific, USA). For FT-IR measurements, samples were prepared by mixing the powder form into KBr and preparing a pellet. Optical properties and energy band gap measurements were performed through UV–visible spectroscopy using a UVS-2100 SCINCO spectrophotometer. Raman spectra were recorded in the range of 100-3000 cm^{-1} at room temperature using a Nanofinder 30 (Tokyo Instruments Co., Osaka, Japan). Field emission transmission electron microscopy (JEOL JEM-2200 FS, Japan) was used to study the shape, size, and crystal structure of the synthesized material through imaging, selected area electron diffraction pattern (SAED) and high resolution transmission electron microscope (HR-TEM). Elemental compositions and extent of reductions in RGO and $NiCo_2O_4$/RGO composite were investigated through X-ray photoelectron spectroscopy (XPS) (Axis-Nova, Kratos Analytical

Ltd., Manchester, UK), at KBSI Jeonju center. Nitrogen adsorption-desorption isotherms data were measured through Brunauer-Emmett–Teller apparatus (BET) [BEL Japan] and the specific surface area (SSA) have been determined by BET method.

3.2 Electrochemical measurements

The catalytic activities of the synthesized materials were tested via potentiostat/galvanostat CHI660A using a three-electrode electrochemical cell. A platinum wire and saturated Ag/AgCl (sat. KCl) were used as the counter and reference electrode, respectively, whereas the modified glassy carbon electrode (GCE) was used as the working electrode. The measurements were performed at room temperature using the aqueous solution of 1 M KOH as the electrolyte.

3.3 Electrode preparation

The working electrode was prepared as follows. First, GCE was carefully polished on a clean polishing cloth using alumina paste (0.05 μm). After that, the polished electrode was rinsed with acetone and DI water followed by ultrasonication for 20 min and then drying at 30 ºC in a vacuum oven. A solution containing 2.5 mg of catalyst was prepared in ethanol (100 μL) as the solvent and Nafion (3 wt %) as the binder, followed by ultrasonic treatment for 30 min. A volume of 20 μL of the as prepared solution was carefully casted onto the surface of GCE and was dried at 30 ºC in a vacuum oven to obtain the modified GCE. All the working electrodes were prepared following the same procedure. The GCE electrodes modified by $NiCo_2O_4$ and $NiCo_2O$-RGO composites were labeled as $NiCo_2O_4$-GCE and $NiCo_2O$-RGO-GCE, respectively.

4. Results and discussion

4.1 XRD analysis

Figure 1 shows the XRD patterns of as synthesized GO, RGO, $NiCo_2O_4$ and $NiCo_2O_4$-RGO composites. It can be clearly seen that the XRD pattern of GO exhibits a characteristic diffraction

peak at a 2θ value of 10.60º, corresponding to the (002) plane, which was shifted toward the higher 2θ value, ~25.09º in the case of RGO. This phenomena is attributed to the reduction of GO, which causes a decreased interlayer spacing of GO layers. However, the interlayer spacing of 3.60 A˚ is observed to be slightly larger than that of ordered graphite (3.40 A˚) [S-1], suggesting the presence of oxygen-containing functional groups in RGO. The XRD patterns of $NiCo_2O_4$ and $NiCo_2O_4$-RGO composites exhibit diffraction peaks corresponding to (111), (220), (311), (400), (422), (511), (440), and (533) planes. These diffractions peaks were indexed to a cubic and face centered spinel type $NiCo_2O_4$ structure (JCPDS-73-1702) [13, 17]. Additionally, in the case of $NiCo_2O_4$-RGO composite, a diffraction peak of low intensity ~25.30 º was also observed, possibly due to the presence of RGO in the composite.

4.2 FT-IR study

Figure 2 shows the FT-IR spectra of GO, RGO, $NiCo_2O_4$ and $NiCo_2O_4$-RGO composites. The FT-IR spectrum of GO shows characteristic peaks of C = O corresponding to stretching vibrations from a carbonyl group at ~1732 cm^{-1}. The band at ~1580 cm^{-1} is attributed to the stretching of aromatic C = C bonds but also may arise from the deformation of O – H bonds (presence of water molecules). The peaks at ~1225 cm^{-1} and 857 cm^{-1} were ascribed to epoxy groups in GO, and the band at ~1052 cm^{-1} corresponds to deformation of C - O bonds [32]. Only absorption bands at ~1634 cm^{-1} and 1560 cm^{-1} were observed in the FT-IR spectrum of RGO, indicating the elimination of oxygen-containing functional groups from GO. The FT-IR spectra of $NiCo_2O_4$ and $NiCo_2O_4$-RGO nanocomposites exhibit a wide band at ~3440 cm^{-1}, corresponding to O-H stretching vibrations. Moreover, presence of two intense bands at ~650 cm^{-1} and ~550 cm^{-1} were also seen in the spectra of $NiCo_2O_4$ and $NiCo_2O_4$-RGO composites. These bands are the feature of a metal-oxygen bond in a spinel-type crystal

structure. Two different positions of metal-oxygen bands are due to the difference in bond length between the metal cations and oxygen anions present on tetrahedral and octahedral sites [33].

4.3 UV-Vis spectroscopy

The optical properties of the synthesized sample were investigated through UV-Vis spectroscopy. Figure 3 (a) compares the UV-Vis spectra of GO and RGO. The UV-vis spectrum of GO exhibits an intense peak at ~235 nm, along with a shoulder at ~305 nm, which are attributed to the $\pi \rightarrow \pi^*$ transition of aromatic C-C bonds and the $n \rightarrow \pi^*$ transition of C = O, respectively. Comparatively, for the UV-Vis spectra of RGO, only a broad peak at ~270 nm was seen, while the shoulder at ~305 nm disappeared. This red shift in the absorption peak from 235 to 270 nm suggests the restoration of π electronic conjugation within the RGO [34].

Figure 3 (b) shows UV-Vis spectra of $NiCo_2O_4$ and $NiCo_2O_4$-RGO composites. It can be seen that, in the wavelength range of 300-550 nm, both the spectra show high absorption of light. The optical energy band gap was determined by Tauc's plot, following [Eq.1]:

$$(\alpha h\upsilon) = K(h\upsilon - E_g)^n \quad (1)$$

where hυ is the photon energy, α is the absorption coefficient, *K* is the proportionality coefficient and E_g is the energy band gap. The direct band gap (n = ½) was calculated by plotting the graph $[(\alpha h\upsilon)^2$ vs. hυ], as shown in Figure 3 (c). Extrapolation of the linear portion of the $[(\alpha h\upsilon)^2$ vs. hυ] graph to the (hυ) axis at zero gives the value of the band gap. The energy band gap was calculated to be 2.55 eV and 2.60 eV for $NiCo_2O_4$ and $NiCo_2O_4$-RGO composites, respectively. It is well known that the band gap of semiconductor nanoparticles increases as the size decreases (quantum confinement) [35]. Slightly higher values of band gap in the case of $NiCo_2O_4$-RGO composites may arise due to the slightly smaller size of the particles compared to the bare $NiCo_2O_4$. These observations are consistent with an earlier study [14].

4.4 Raman study

To further evaluate the phase formation and structural features (order/disorder), samples were characterized through Raman spectroscopy. Raman spectra of GO, RGO and $NiCo_2O_4$-RGO composite are presented in Figure 4. Usually, the Raman spectrum of graphene exhibits vibrational peaks around ~1342 cm^{-1} and ~1580 cm^{-1}, which can be assigned to the D and G bands, respectively [8]. The D band is associated with the vibrational mode of the k-point phonons of A_{1g} symmetry, and the G band is related to the E_{2g} phonon of the Csp^2 atoms. Moreover, the D band is related to disorder and defects in the hexagonal lattice, whereas the G band is associated with vibrations of sp^2-bonded carbon atoms in a 2D hexagonal lattice. By calculating the intensity ratio (I_D/I_G) and/or area ratio (A_D/A_G) of D and G bands, information about the degree of graphitization and defects can be obtained. The value of (I_D/I_G) and the positions of D and G bands for GO, RGO and $NiCo_2O_4$/RGO composites are summarized in Table 1. The I_D/I_G ratio of RGO was found to be higher than that of GO, suggesting a higher degree of defects in RGO than in GO. However, the I_D/I_G ratio for $NiCo_2O_4$-RGO composites was slightly lower than RGO but higher than GO. In addition, (I_D/I_G) and (A_D/A_G) were correlated with the sp^2 domain size of the graphene [S-2] [36-37]. Furthermore, in the Raman spectrum of the $NiCo_2O_4$-RGO composite, additional peaks below a wavenumber of 700 cm^{-1} were also observed and could be assigned to vibrational modes of spinel phases [38-40]. It was also observed that, in the case of $NiCo_2O_4$-RGO nanocomposites, D and G bands were blue-shifted compared to RGO. This phenomenon can be associated with the charge transfer between the RGO and $NiCo_2O_4$ nanoparticles. Similar observations have also been reported in earlier studies [41-42].

4.5 FE-SEM / TEM investigations

Surface morphologies of the synthesized material were probed using FE-SEM. Figure 5 (a-d) shows FE-SEM images of $NiCo_2O_4$, RGO, and $NiCo_2O_4$-RGO composites. $NiCo_2O_4$ nanoparticles are uniformly distributed over the whole region with a grain size of 20-30 nm. The FE-SEM image of RGO reveals curled and entangled sheets together with layers showing a paper-type morphology. Low magnification FE-SEM images of $NiCo_2O$-RGO composites clearly show that some of the $NiCo_2O$ nanoparticles adhere to RGO, while most of the particles are confined between the RGO sheets, exhibiting a layer by layer structure. Additionally, the high magnification FE-SEM of $NiCo_2O$-RGO composite also demonstrates that the nanoparticles are densely packed, indicating a strong interaction between the RGO sheet and $NiCo_2O$ nanoparticles [S-3].

Figure 6 (a-b) show TEM images of $NiCo_2O_4$ nanoparticles, with sizes in the range of 10-30 nm along with some agglomeration. HR-TEM images of the nanoparticles exhibit grains aligned in different directions, and the interference fringes are clearly observed with d-spacings of 0.29 nm and 0.46 nm, corresponding to the (220) and (111) planes of the crystal, respectively. The selected area electron diffraction (SAED) pattern [inset of Figure 6(a)] displays a series of diffraction rings corresponding to crystal planes of $NiCo_2O_4$, suggesting the polycrystalline nature of the $NiCo_2O_4$ nanoparticles. A TEM image of the RGO, as shown in Figure 6 (c), exhibits a crumpled surface and scrolling edges. In addition, the SAED pattern of RGO clearly exhibits six bright dots arranged in the hexagonal geometry, demonstrating the features of graphene [inset Figure 6 (c)]. The HR-TEM images of the RGO taken at the edge of the sheet shows that the RGO consists of 3-4 layers [Figure 6 (d)]. From the TEM image [Figure 6 (e)] of $NiCo_2O_4$-RGO composites, it can be seen that the $NiCo_2O_4$ nanoparticles are well dispersed on

the surface of RGO, and the agglomeration of the particles is effectively prevented compared to bare $NiCo_2O_4$ nanoparticles [43]. It is expected that the well dispersed nanoparticles on the surface of the RGO will inhibit the restacking of RGO, avoiding the loss of high active surface area in the composite. The corresponding SAED [inset, Figure 6 (e)] pattern also displays diffraction rings, signifying the polycrystalline nature of the $NiCo_2O_4$-RGO composite. The HR-TEM images [Figure 6 (f)] of $NiCo_2O_4$-RGO composites display interference fringes with d-spacings of 0.20 nm, 0.29 nm and 0.46 nm, corresponding to the (400), (220) and (111) planes of the $NiCo_2O_4$ crystal, respectively and also suggest that $NiCo_2O_4$ nanoparticles are grown on the surface of RGO. The contrast difference can be seen in dark-field TEM image Figure 6 (g).

4.6 XPS analysis

In order to achieve a better understanding of the catalytic effect, the elemental composition and oxidation states of metal cations were investigated through XPS studies. Figure 7 (a) shows a wide range survey spectrum of RGO and $NiCo_2O_4$-RGO composites. The XPS survey spectrum of RGO exhibits characteristic peaks corresponding to C 1s and O 1s components, whereas, for $NiCo_2O_4$-RGO nanocomposites, peaks correspond to C 1s, O 1s, Ni 2p and Co 2p, suggesting the formation of a composite phase. In the case of RGO, the atomic ratio of C/O was found to be ~9.12, which was much higher than that of GO (2.3) [44], suggesting the removal of the oxygen-containing functional groups and the reduction of GO. In the $NiCo_2O_4$-RGO composite, the C/O atomic ratio was found to be ~1.16, including the content of oxygen from $NiCo_2O_4$. These observations further suggest that most of the oxygen-containing functional groups from GO were removed in RGO, whereas a few of the residual functional groups provide a stable dispersion of nanoparticles in the $NiCo_2O_4$-RGO nanocomposite [45]. Additionally, in the $NiCo_2O_4$-RGO composite, the Ni to Co atomic ratio was ~0.497, which is nearly the same as that at the initial

stage of the preparation. The obtained results indicate a good stoichiometry of Ni and Co in $NiCo_2O_4$ nanoparticles. The deconvoluted C 1s spectra of RGO and $NiCo_2O_4$-RGO composites are shown in Figure 7 (b) and (c), respectively. The deconvoluted C 1s spectra of RGO and $NiCo_2O_4$-RGO show peaks corresponding to C – C, C – O, O = C - O and O = C – OH groups. It is well known that, in spinel $NiCo_2O_4$, Ni and Co may exist in different ionic states. As shown in Figure 7 (d), the Ni 2p spectrum was fitted (Gaussian-Lorentzian) with two spin-orbit doublets (Ni $2P_{3/2}$ & Ni $2p_{1/2}$), characteristic of Ni^{3+} and Ni^{2+}, along with two shakeup satellite (identified as "Sat."). Similarly, the Co 2p spectrum [Figure 7 (e)] was also fitted with two spin–orbit doublets (Co $2P_{3/2}$ & Co $2P_{1/2}$), characteristic of Co^{2+} and Co^{3+}, along with two shakeup satellites. These observations further suggest that the $NiCo_2O_4$-RGO composite contains Ni^{3+}, Ni^{2+}, Co^{2+} and Co^{3+}. These results are in agreement with an earlier study [46]. A schematic representation of the crystal structure of cubic spinel $NiCo_2O_4$ is shown in Figure 7 (f). It is expected that the nickel and cobalt cations are present in different valance states and may provide adequate catalytic properties compared to their single-component metal oxides i.e., Ni/Co oxides [14, 16, 47].

4.7 Electrochemical studies

4.7.1 Cyclic voltammetry

In order to examine the catalytic properties of the synthesized products, electrocatalytic measurements were performed using CV. The CV results of the $NiCo_2O_4$-GCE and $NiCo_2O_4$-RGO-GCE electrodes in the presence of 1 M KOH, measured at scan rate of 50 mV s^{-1}, are shown in Figure 8 (a). As shown, the CV curves of $NiCo_2O_4$-RGO-GCE and $NiCo_2O_4$-GCE electrodes exhibit a pair of redox peaks. These redox peaks can be correlated with reversible oxidation of Co (II) and the reduction of Ni (III). Further, the anodic peaks could be associated

with the oxidation of Co (II) to Co (III) to Co (IV), whereas cathodic peaks correspond to the reduction of Co (IV) to Co (III) to Co (II) and Ni(III) to Ni(II). It has been reported that the redox potential of Co (III)/Co (IV) is very close to Ni (II)/Ni (III) [17]. This type of CV behavior has also been reported in earlier studies [48]. The current density of the $NiCo_2O_4$-RGO-GCE electrodes is much higher than that of the $NiCo_2O_4$-GCE electrode, suggesting better catalytic properties of $NiCo_2O_4$-RGO composites. Additionally, for $NiCo_2O_4$-RGO-GCE electrode, the oxidation potentials were observed to be lower than those of the $NiCo_2O_4$-GCE. These phenomena can be correlated with a synergistic effect between the $NiCo_2O_4$ nanoparticles and RGO sheets. It was observed that the different ratio of $NiCo_2O_4$ to RGO leads to variation in current density and oxidation potential. Among the three samples, the oxidation potential for the $NiCo_2O_4$-RGO (2:1) nanocomposite was found to be lowest. The value of oxidation potential for $NiCo_2O_4$-GCE, $NiCo_2O_4$-RGO-GCE (1:1), $NiCo_2O_4$-RGO-GCE (2:1) and $NiCo_2O_4$-RGO-GCE (4:1) electrodes were found to be 0.33 V, 0.288 V, 0.135 V and 0.247 V, respectively. On the other hand the corresponding current densities were measured to be 3.11 mA/cm^2, 4.8 mA/cm^2, 4.1 mA/cm^2 and 4.92 mA/cm^2, respectively. This phenomenon can be further correlated with surface area and dispersion of the nanoparticles in the $NiCo_2O_4$-RGO nanocomposites, which influence the electroactive site and therefore improve the electrochemical performance [S-5]. The well dispersed nature of the $NiCo_2O_4$ nanoparticles over the highly conducting RGO sheets and unique layer by layer structure of the $NiCo_2O_4$-RGO (2:1) nanocomposite are expected to provide better catalytic properties. In alkaline solutions, the oxygen evolution reaction can be described through the following equation:

$$4OH^- \rightarrow O_2 + 2H_2O + 4\ e- \qquad (2)$$

The CV response of $NiCo_2O_4$-RGO nanocomposite was also investigated at different scan rates, and the obtained result is shown in Figure 8 (b). Both the anodic and cathodic peaks shifted toward higher potential values with increasing scanning rate. The plot of anodic peak current with the square root of scanning potential is shown in Figure 8 (c). A linear response of the graph suggests that the electrochemical reaction is diffusion controlled. Furthermore, the $NiCo_2O_4$-RGO nanocomposite also exhibits excellent cycling stability [S-4].

The obtained result demonstrated better catalytic properties of the $NiCo_2O_4$-RGO composite compared to those of IrO_2-based binary metal oxides [49], nickel hydroxide [50-52], metal oxide-based thin films [53], lithium-doped Co_3O_4 [24], Ru functionalized carbon surfaces [54], teflon-bonded Ti/Co_3O_4 [21], iron/nickel phthalocyanines supported on multi-walled carbon nanotubes [22], nitrogen-doped graphene [27], $NiCo_2S_4$/graphene [28], and core–ring structured $NiCo_2O_4$ nanoplatelets. Moreover, the oxidation potential was found to be lower than that of the $NiCo_2O_4$/graphene composite [55].

4.7.2 Chronoamperometry measurements

To further investigate the performance and long term stability of $NiCo_2O_4$-RGO-GCE and $NiCo_2O_4$-GCE electrodes, chronoamperometric measurements were also performed. Figure 8 (d) compares the current-time response of the prepared electrodes. The measurements were performed for 2000 sec at a fixed potential of 0.5 V in the presence 1 M KOH. The initial high current density is attributed to a double layer charging process and various active sites on the electrode. As expected, during the entire testing time, the current density of the $NiCo_2O_4$-RGO-GCE electrode was much higher than that of the $NiCo_2O_4$-GCE electrodes. The higher current density of the $NiCo_2O_4$-RGO-GCE electrode directly reflects the lower resistivity of the composite catalyst. Additionally, the $NiCo_2O_4$-RGO-GCE electrode exhibited a lower current

declining rate [56]. These phenomena clearly suggest a better catalytic performance of the $NiCo_2O_4$-RGO-GCE compared to the $NiCo_2O_4$-GCE electrode. The chronoamperometry measurements were supported by CV results.

4.7.3 EIS measurements

EIS is an effective way to understand the charge transfer characteristics of an electrode. Nyquist plots of the EIS measurements for $NiCo_2O_4$-GCE and $NiCo_2O_4$-RGO-GCE electrodes are shown in Figure 8 (e-f). EIS spectra may include a semicircle part in the high frequency range, attributed to the charge transfer, whereas a linear part in the low frequency region corresponds to the diffusion process. The diameter of the semicircle is a measure of the charge transfer resistance (R_{ct}) which depends on the dielectric and insulating properties of the electrode/electrolyte interface. Smaller diameter semicircles indicate lower R_{ct} values for the corresponding electrode. The lower R_{ct} value in the case of the $NiCo_2O_4$-RGO-GCE electrode suggests a higher electrochemical activity compared to the $NiCo_2O_4$-GCE electrode. Additionally, the straight line in the EIS spectra also suggests the diffusion limiting step of the electrochemical process. Further, it can be concluded that the $NiCo_2O_4$-RGO nanocomposite exhibits synergistic effects, and the lowest R_{ct} value is the consequence of the facile electron transfer ability and excellent conductivity of RGO [57]. The RGO effectively enhances the charge transfer rate between the electrode and electrolyte.

5. Conclusions

In summary, we have synthesized $NiCo_2O_4$-RGO nanocomposites by hydrothermal methods assisted by a low temperature calcination process. The physical properties of the synthesized products were probed through several characterization techniques. FE-SEM results suggest the formation of a layer by layer structure of $NiCo_2O_4$-RGO (2:1) nanocomposites with dense

packing of $NiCo_2O_4$ nanoparticles between the layers of RGO. TEM investigations also suggest that the nanoparticles do not experience agglomeration. It was concluded that the unique structural features of the $NiCo_2O_4$-RGO (2:1) nanocomposite, including layer by layer assembly, tight packing and dispersibility of the nanoparticles atop the RGO, cause a synergistic effect between $NiCo_2O_4$ nanoparticles and RGO, which significantly improved the electrochemical performance for OER relative to that of bare $NiCo_2O_4$ nanoparticles. The synthesis method adopted in the present study is advantageous since it avoids the use of toxic reducing agents like hydrazine. Therefore, it is eco-friendly and is simple as well. The improved electrochemical performance demonstrates that $NiCo_2O_4$-RGO nanocomposites represent promising electrocatalysts for various applications.

Acknowledgement

This study was supported by the Converging Research Center Program (2013K000404) through the Ministry of Science, ICT & Future Planning and the Basic Science Research Program through the National Research Foundation (NRF) funded by the Ministry of Education of Korea (NRF-2013R1A1A2011608).

References

1 X. Huang, X. Qi, F. Boey, H. Zhang, Chem. Soc. Rev. 41 (2012) 666-686.

2 G. Zhao, T. Wen, C. Chen, X. Wang, RSC Adv. 2 (2012) 9286-9303.

3 H. J. Choi, S. M. Jung, J. M. Seo, D. W. Chang, L. Dai, J. B. Baek, Nano Energy 1 (2012) 534-551.

4 S. M. Bak, K. W. Nam, C. W. Lee, K. H. Kim, H. C. Jung, X. Q. Yang, K. B. Kim, J. Mater. Chem. 21 (2011) 17309-17315.

5 W. Zhou, J. Liu, T. Chen, K. S. Tan, X. Jia, Z. Luo, C. Cong, H. Yang, C. M. Li, T. Yu, Phys. Chem. Chem. Phys. 13 (2011) 14462-14465.

6 P. D. Tran, S. K. Batabyal, S. S. Pramana, J. Barber, L. H. Wong, S. C. J. Loo, Nanoscale 4 (2012) 3875-3878.

7 W. Ma, X. Lv, D. Han, F. Li, X. Dong, L. Niu, J. Electroanal. Chem. 690 (2013) 111-116.

8 T. Kuila, S. Bose, A. K. Mishra, P. Khanra, N. H. Kim, J. H. Lee, Prog. Mater. Sci. 57 (2012) 1061-1105.

9 T. Kuila, S. Bose, P. Khanra, A. K. Mishra, N. H. Kim, J. H. Lee, Biosens Bioelectron. 26 (2011) 4637-4648.

10 S. Bose, T. Kuila, A. K. Mishra, R. Rajasekar, N. H. Kim, J. H. Lee, J. Mater. Chem. 22 (2012) 767–784.

11 T. Kuila, A. K. Mishra, P. Khanra, N. H. Kim, J. H. Lee, Nanoscale 5 (2013) 52- 71.

12 N. H. Kim, T. Kuila, J. H. Lee, J. Mater. Chem. A 1 (2013) 1349-1358.

13 B. Cui, H. Lin, J. B. Li, X. Li, J. Yang, J. Tao, Adv. Funct. Mater. 18 (2008) 1440–1447.

14 B. Cui, H. Lin, Y. Z. Liu, J. B. Li, P. Sun, X. C. Zhao, C. J. Liu, J. Phys. Chem. C 113 (2009) 14083–14087.

15 C. Yuan, J. Li, L. Hou, X. Zhang, L. Shen, X. W. Lou, Adv. Funct. Mater. 22 (2012) 4592–4597.

16 J. Li, S. Xiong, Y. Liu, Z. Ju, Y. Qian, ACS Appl. Mater. Interfaces 5 (2013) 981–988.

17 T. Y. Wei, C. H. Chen, H. C. Chien, S. Y. Lu, C. C. Hu, Adv. Mater. 22 (2010) 347–351.

18 K. H. Chang, Y. F. Lee, C. C. Hu, C. I. Chang, C. L. Liua, Y. L. Yang, Chem. Commun. 46 (2010) 7957-7959

19 A. Nouralishahi, A. A. Khodadadi, A. M. Rashidi, Y. Mortazavi, J. Colloid Interface Sci. 393 (2013) 291-299.

20 Y. Lin, S. Zhang, S. Yan, G. Liu, Electrochim. Acta 66 (2012) 1–6.

21 S. Palmas, F. Ferrara, M. Mascia, A. M. Polcaro, J. R. Ruiz, A. Vacca, G. Piccaluga, Int. J. Hydrogen Energy 34 (2009) 1647-1654.

22 A. Abbaspour, E. Mirahmadi, Electrochim. Acta 105 (2013) 92-98.

23 S. Chen, T. Zhai, X. H. Lu, M. Z. Zhang, Z. Y. Li, C. W. Xu, Y. Tong, Int. J. Hydrogen Energy 37 (2012) 13350-13354.

24 X. Wu, K. Scott, Int. J. Hydrogen Energy 38 (2013) 3123-3129.

25 D. Wang, X. Chen, D. G. Evans, W. Yang, Nanoscale 5 (2013) 5312-5315.

26 Y. Gorlin, T. F. Jaramillo, J. Am. Chem. Soc. 132 (2010) 13612–13614.

27 Z. Lin, G. H. Waller, Y. Liu, M. Liu, C. Wong, Carbon 53 (2013) 130-136.

28 Q. Liu, J. Jin, J. Zhang, ACS Appl. Mater. Interfaces 5 (2013) 5002−5008.

29 J. Guo, Y. Li, S. Zhu, Z. Chen, Q. Liu, D. Zhang, W. J. Moon, D. M. Song, RSC Adv. 2 (2012) 1356-1363.

30 J. Tian, H. Li, A. M. Asiri, A. O. A. Youbi, X. Sun, Small, 9 (2013) 2709- -2714.

31 W. S. Hummers, R. E. Offeman, J Am Chem. Soc. 80 (1958) 1339.

32 Y. Liu, J. Zhou, X. Zhang, Z. Liu, X. Wan, J. Tian, T. Wang, Y. Chen, Carbon 47 (2009) 3113–3121.

33 P. Bhunia, G. Kim, C. Baik, H. Lee, Chem. Commun. 48 (2012) 9888–9890.

34 Q. Shou, J. Cheng, L. Zhang, B. J. Nelson, X. Zhang, J. Solid State Chem. 185 (2012) 191-197.

35 H. S. Mansur, A. A. P. Mansur, Mater. Chem. Phys. 125 (2011) 709–717.

36 S. P. Lima, N. M. Huanga, H. N. Lim, Ceram. Int. 39 (2013) 6647–6655.

37 J. W. Lee, A. S. Hall, J. D. Kim, T. E. Mallouk, Chem. Mater. 24 (2012) 1158−1164.

38 Z. Z. Lazarevic, C. Jovalekic, A. Milutinovic, D. Sekulic, V. N. Ivanovski, A. Recnik, B. Cekic, N. Z. Romcevic, J. Appl. Phys. 113 (2013) 187221.

39 G. V. M. Jacintho, A. G. Brolo, P. Corio, P. A. Z. Suarez, J. C. Rubim, J. Phys. Chem. C 113 (2009) 7684–7691.

40 Z. Q. Liu, K. Xiao, Q. Z. Xu, N. Li, Y. Z. Su, H. J. Wang, S. Chen, RSC Adv. 3 (2013) 4372–4380.

41 M. Srivastava, A. K. Das, P. Khanra, M. E. Uddin, N. H. Kim, J. H. Lee, J. Mater. Chem. A 1 (2013) 9792–9801.

42 L. Jiang , M. Yao , B. Liu , Q. Li , R. Liu, H. Lv, S. Lu, C. Gong, B. Zou, T. Cui, B. Liu, J. Phys. Chem. C 116 (2012) 11741–11745.

43 J. C. Meyer, A. K. Geim, M. I. Katsnelson, K. S. Novoselov, T. J. Booth, S. Roth, Nature 446 (2007) 60-63.

44 T. Kuila, S. Bose, P. Khanra, A. K. Mishra, N. H. Kim, J. H. Lee, Carbon 50 (2012) 914–921.

45 B. Zhang, Q. B. Zheng, Z. D. Huang, S. W. Oh, J. K. Kim, Carbon 49 (2011) 4524 – 4534.

46 S. Huang, G. N. Zhu, C. Zhang, W. W. Tjiu, Y. Y. Xia, T. Liu, ACS Appl. Mater. Interfaces 4 (2012) 2242−2249.

47 R. Zou, K. Xu, T. Wang, G. He, Q. Liu, X. Liu, Z. Zhang, J. Hu, J. Mater. Chem. A 1 (2013) 8560-8566.

48 H. W. Wang, Z. A. Hu, Y. Q. Chang, Y. L. Chen, H. Y. Wu, Z. Y. Zhang, Y. Y. Yang, J. Mater. Chem. 21 (2011) 10504-10511.

49 C. Felix, T. Maiyalagan, S. Pasupathi, B. Bladergroen, V. Linkov, Int. J. Electrochem. Sci. 7 (2012) 12064 – 12077.

50 D. Cibrev, M. Jankulovska, T. L. Villarreal, R. Gomez, Int. J. Hydrogen Energy 38 (2013) 2746–2753.

51 M. E. G. Lyons, L. Russell, M. O. Brien, R. L. Doyle, I. Godwin, M. P. Brandon, Int. J. Electrochem. Sci., 7 (2012) 2710 – 2763.

52 I. J. Godwin, M. E. G. Lyons, Electrochem. Commun. 32 (2013) 39-42.

53 L. Trotochaud, J. K. Ranney, K. N. Williams, S. W. Boettcher, J. Am. Chem. Soc. 134 (2012) 17253−17261.

54 L. Tong, M. Gothelid, L. Sun, Chem. Commun. 48 (2012) 10025–10027.

55 D. U. Lee, B. J. Kim, Z. Chen, J. Mater. Chem. A, 1 (2013) 4754-4762.

56 X. Wang, X. Li, D. Liu, S. Song, H. Zhang, Chem. Commun. 48 (2012) 2885-2887.

57 D. Carriazo, J. Patino, M.C. Gutierrez, M.L. Ferrer, F. D. Monte, RSC Adv 3 (2013) 13690-13695.

Figure Captions

Scheme 1 Schematic illustration of the synthesis procedure for $NiCo_2O_4$-RGO nanocomposite.

Figure 1 XRD pattern of GO, RGO, $NiCo_2O_4$ and $NiCo_2O_4$-RGO (2:1) nanocomposites.

Figure 2 FT-IR spectra of GO, RGO, $NiCo_2O_4$ and $NiCo_2O_4$-RGO (2:1) nanocomposites.

Figure 3 UV-Vis spectra of GO and RGO **(a)**, $NiCo_2O_4$ and $NiCo_2O_4$-RGO (2:1) nanocomposites **(b),** Tauc plot {(hν) versus $(\alpha h\nu)^2$} for $NiCo_2O_4$ and $NiCo_2O_4$-RGO (2:1) nanocomposites **(c).**

Figure 4 Raman spectra of GO, RGO, $NiCo_2O_4$ and $NiCo_2O_4$-RGO (2:1) nanocomposites.

Figure 5 FE-SEM images of $NiCo_2O_4$ [inset shows high magnification image, bar length is 500 nm] **(a)**, RGO **(b)**, low **(c)** and high magnifications **(d)** images of $NiCo_2O_4$-RGO (2:1) nanocomposites.

Figure 6 TEM micrographs of $NiCo_2O_4$ nanoparticles [inset show SAED pattern] **(a)**, HR-TEM image of $NiCo_2O_4$ nanoparticles **(b),** TEM micrograph of RGO [inset is the SAED pattern] **(c),** HR-TEM of RGO **(d)**, TEM micrograph of $NiCo_2O_4$-RGO (2:1) nanocomposite [inset shows SAED pattern] **(e)**, HR-TEM image of $NiCo_2O_4$-RGO (2:1) nanocomposite **(f)** dark field image of $NiCo_2O_4$-RGO (2:1) nanocomposite **(g)**.

Figure 7 XPS survey spectra of RGO and $NiCo_2O_4$-RGO (2:1) nanocomposites **(a),** C 1s deconvoluted spectra of RGO **(b),** C1s deconvoluted spectra of $NiCo_2O_4$-RGO (2:1) nanocomposite **(c),** deconvoluted spectra of Ni 2p **(d),** deconvoluted spectra of Co 2p **(e),** and representation for cubic spinel type crystal structure of $NiCo_2O_4$ **(f)**.

Figure 8 CV of $NiCo_2O_4$ and $NiCo_2O_4$-RGO nanocomposites modified GCE, recorded in the presence of 1 M KOH at a scan rate of 50 mV s^{-1} **(a),** CV responses of $NiCo_2O_4$-RGO (2:1) catalyst in 1 M KOH recorded at different scan rates **(b),** square root of potential versus anodic peak current graph **(c)**, chronoamperograms of $NiCo_2O_4$ and $NiCo_2O_4$-RGO (2:1) modified GCE in 1 M KOH at a fixed potential of 0.5 V **(d),** EIS of $NiCo_2O_4$ **(e),** and $NiCo_2O_4$-RGO (2:1) **(f),** and modified GCE in 1 M KOH measured at a perturbation potential of 50 mV.

Table 1. Raman results of GO, RGO and $NiCo_2O_4$-RGO (2:1) nanocomposites.

Sample	**Position of D band (cm^{-1})**	**Position of G band (cm^{-1})**	**Intensity ratio (I_D/I_G)**
GO	1345.60	1582.81	0.96
RGO	1351.00	1578.06	1.02
$NiCo_2O_4$-RGO (2:1)	1539.53	1571.84	0.97

Scheme 1

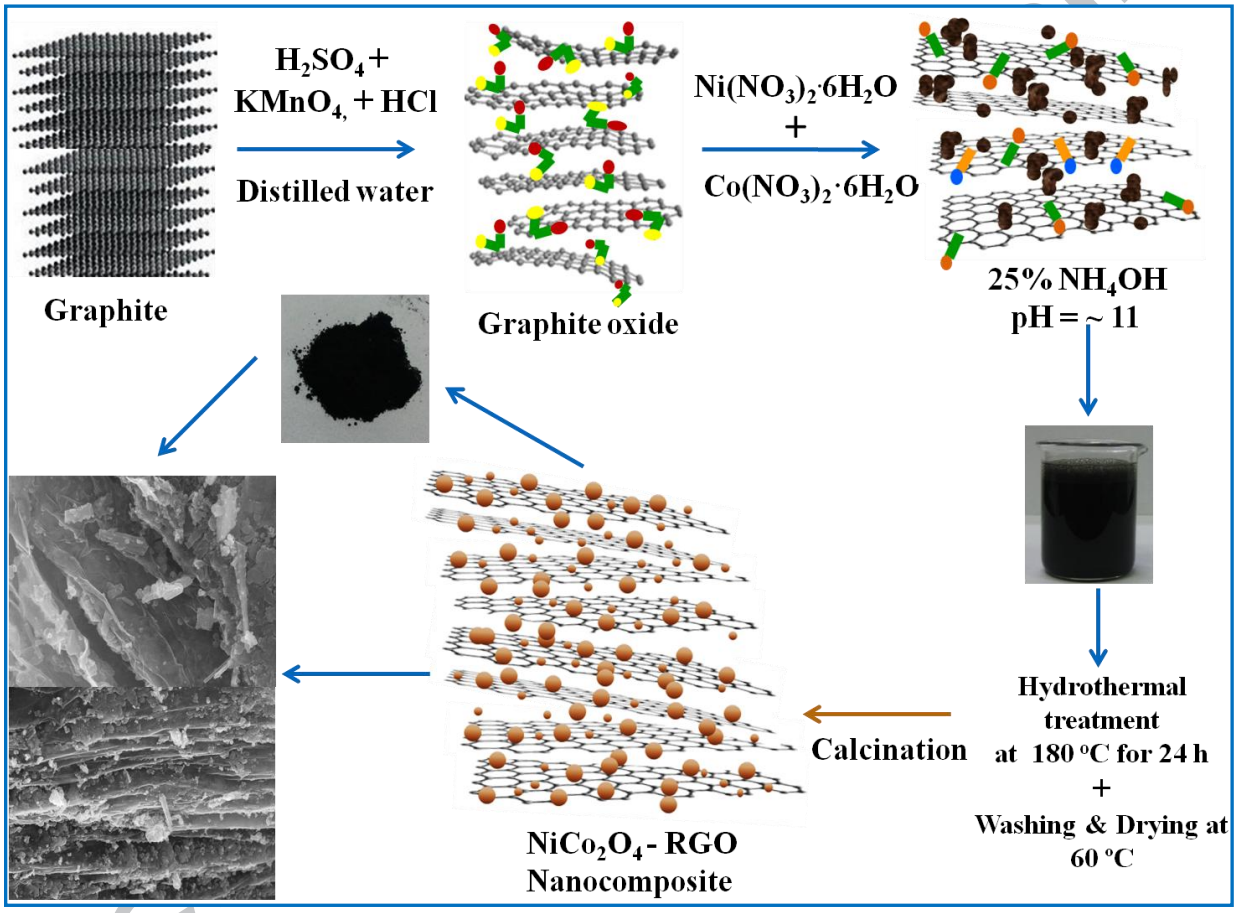

Figure 1

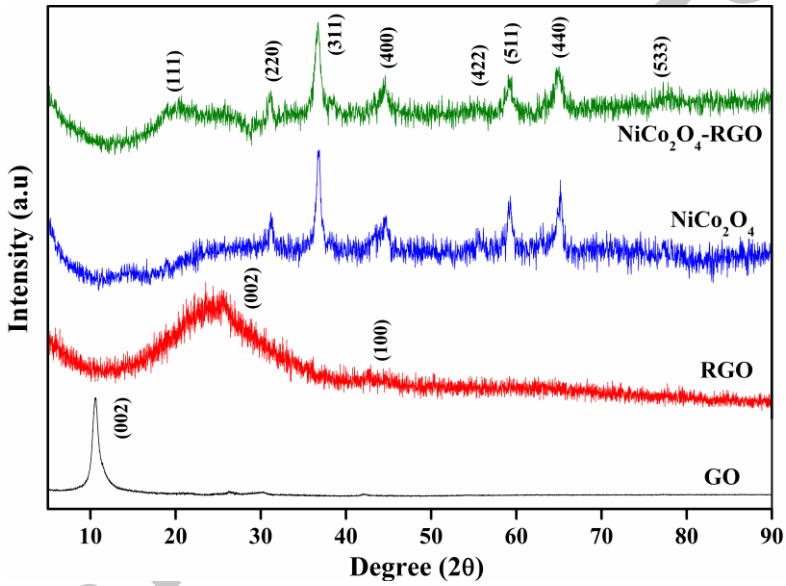

Figure 2

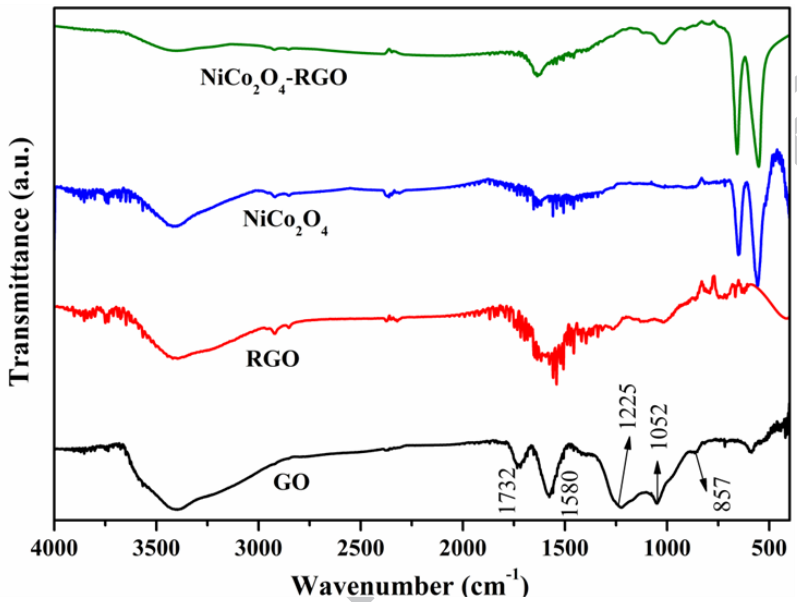

Figure 3

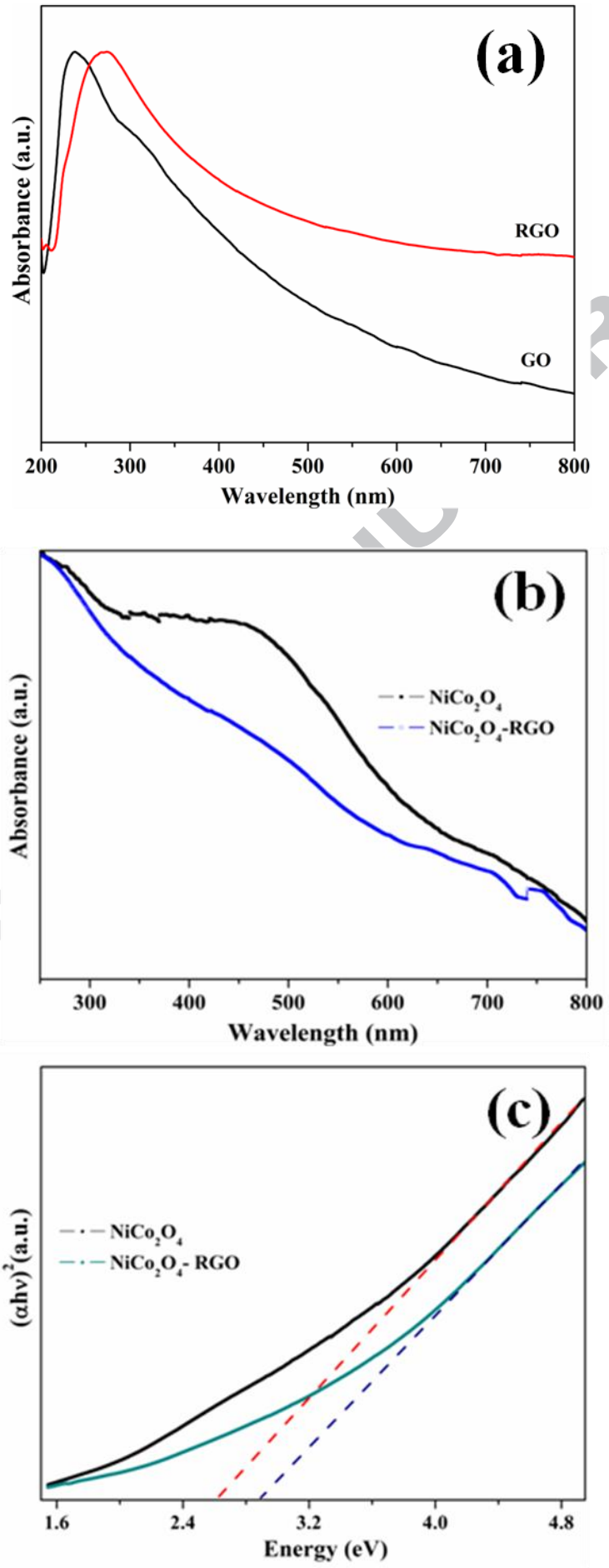

Figure 4

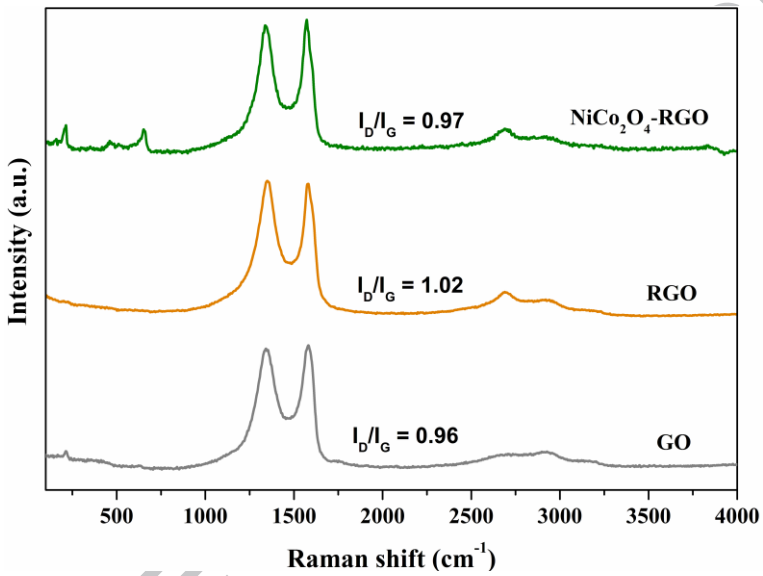

Figure 5

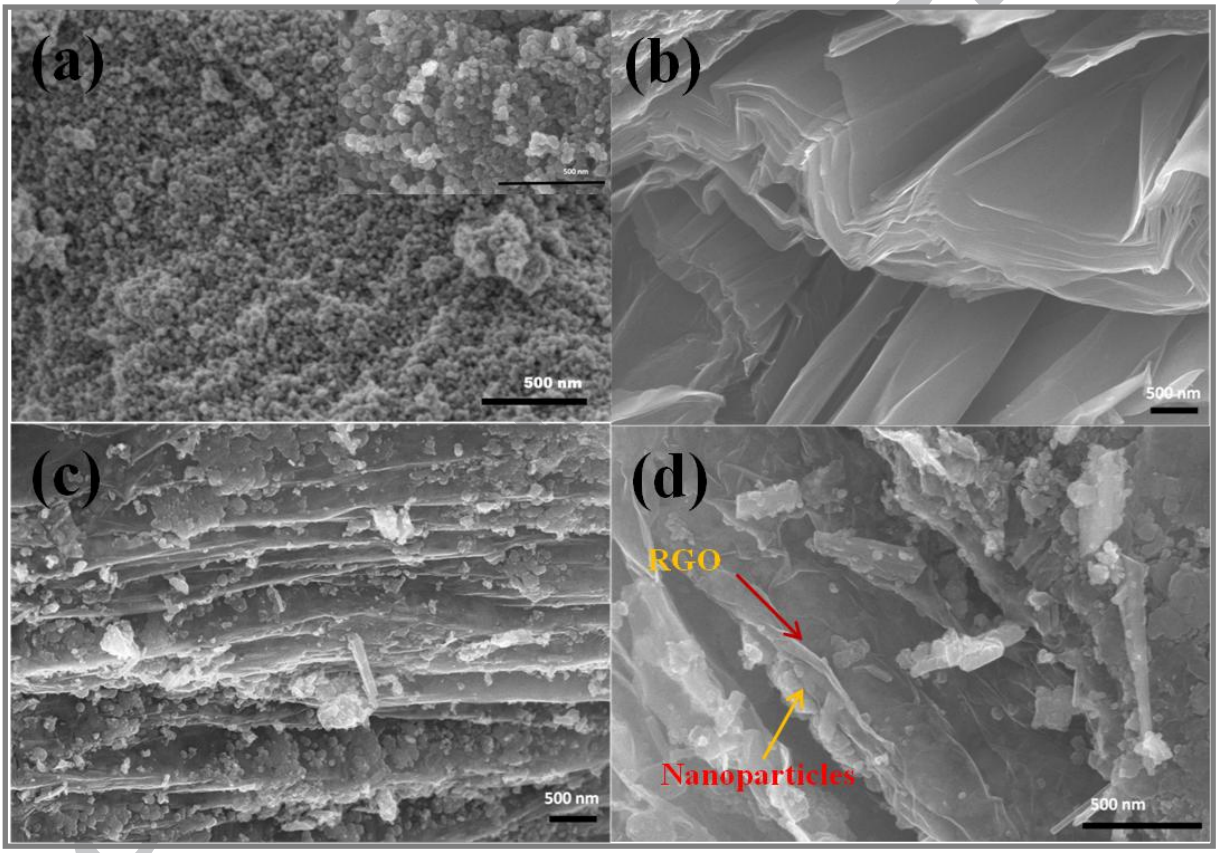

Figure 6

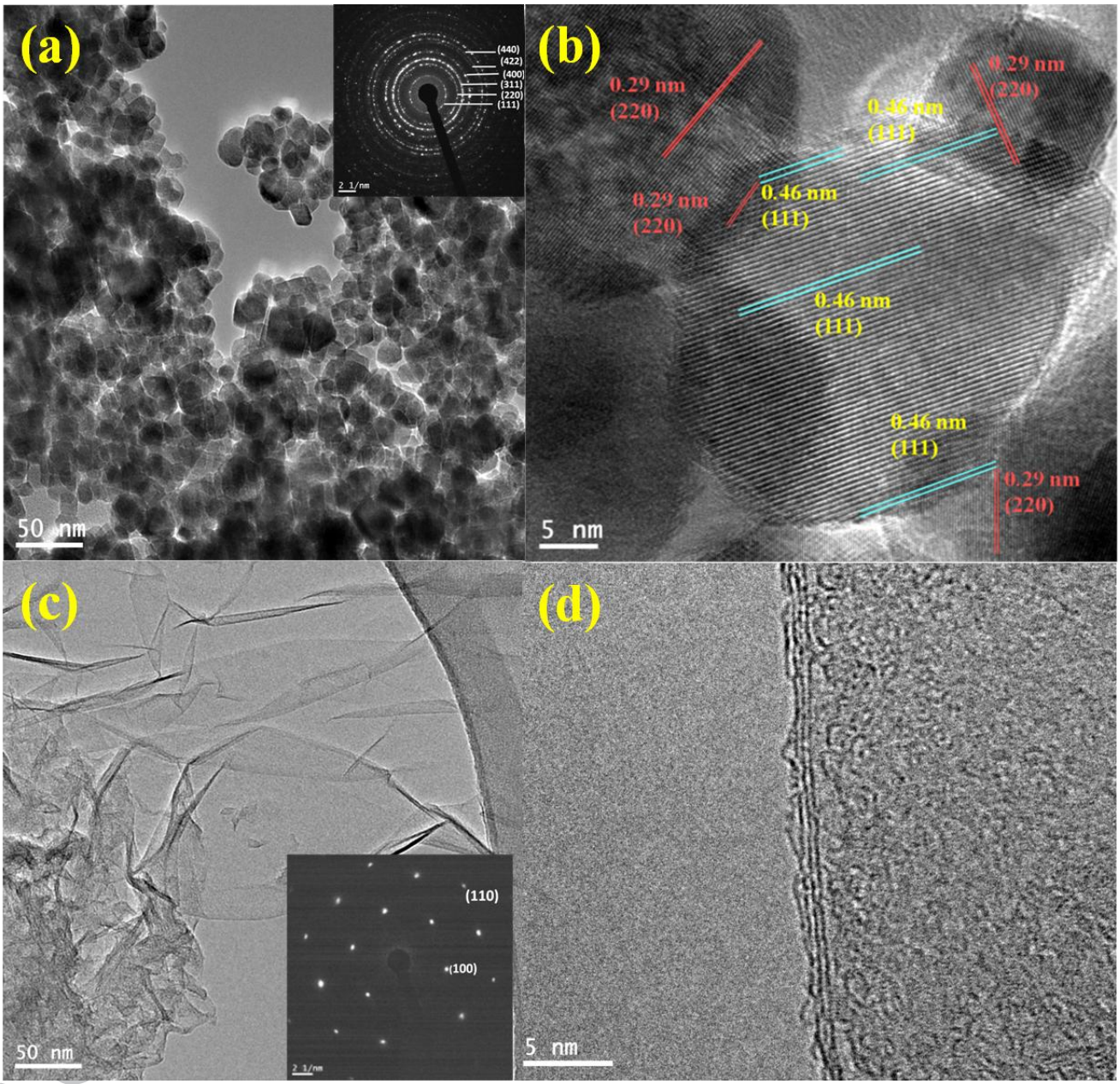

Contd….

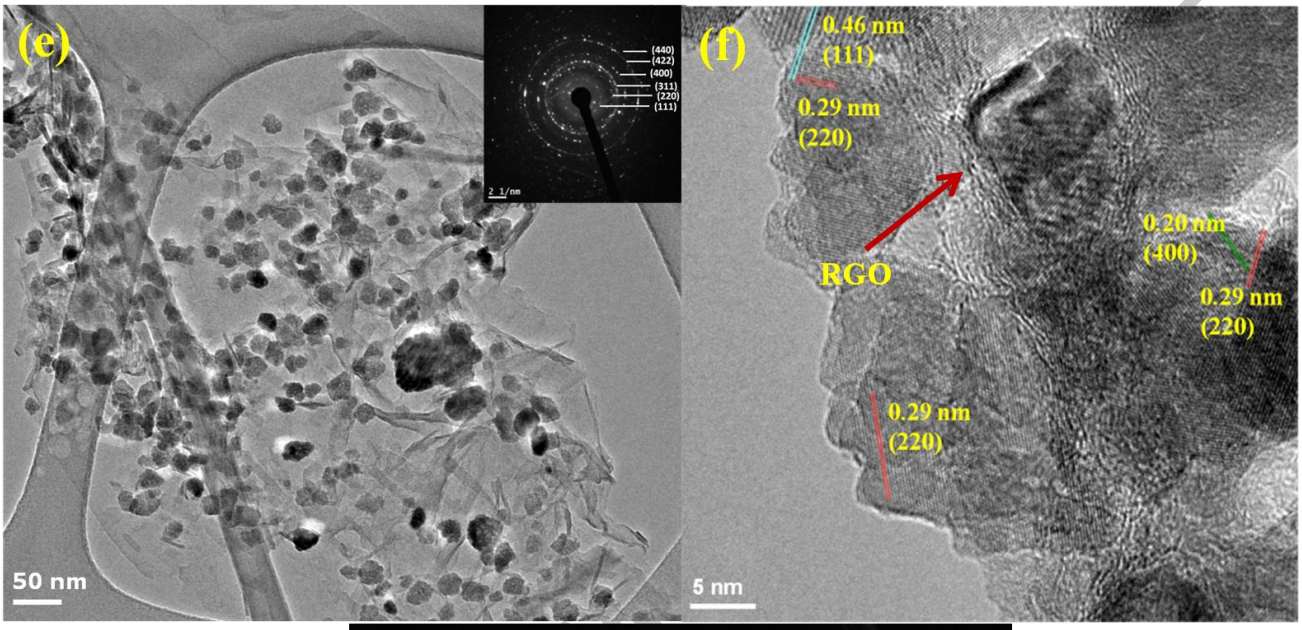

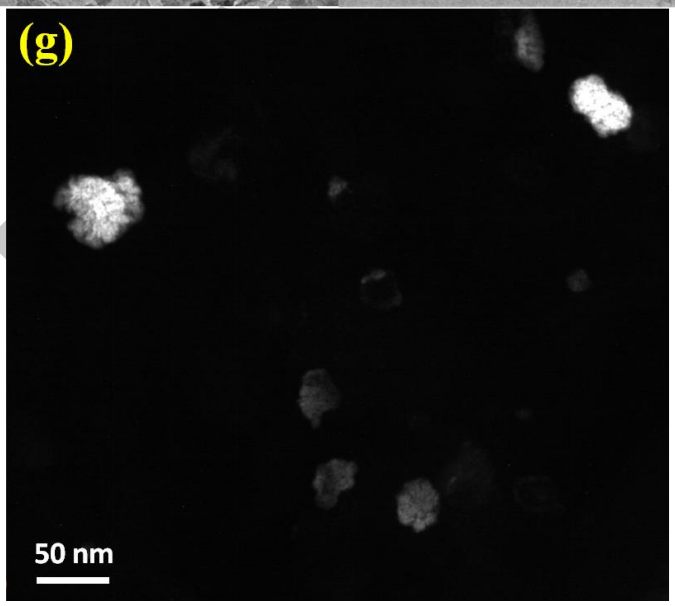

Figure 7

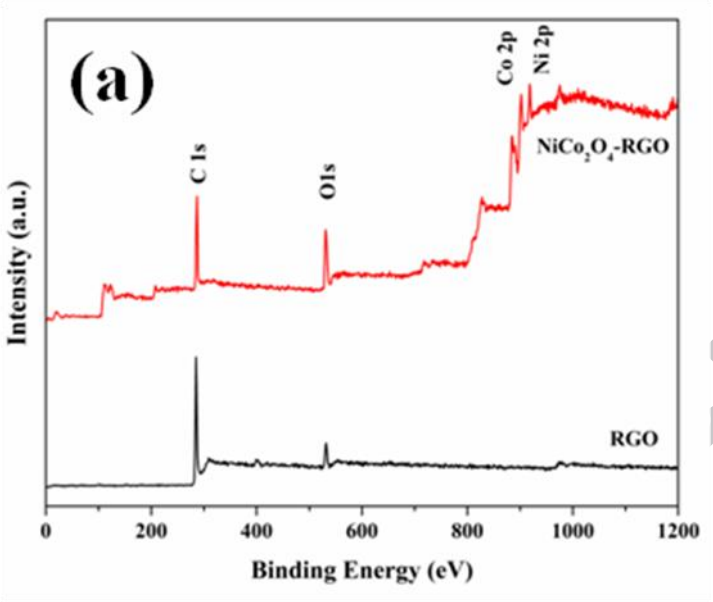

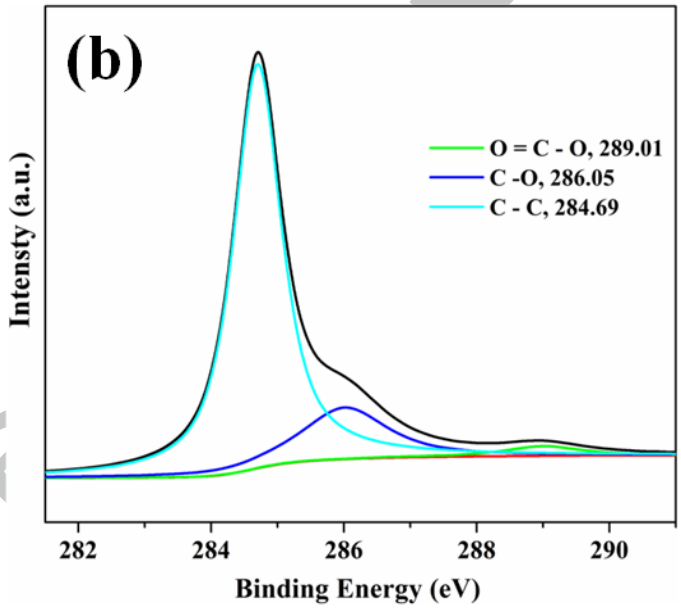

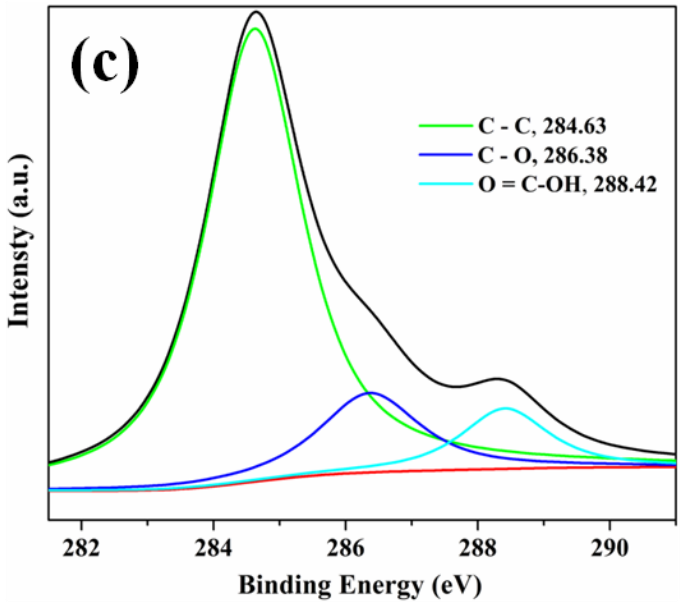

Contd….

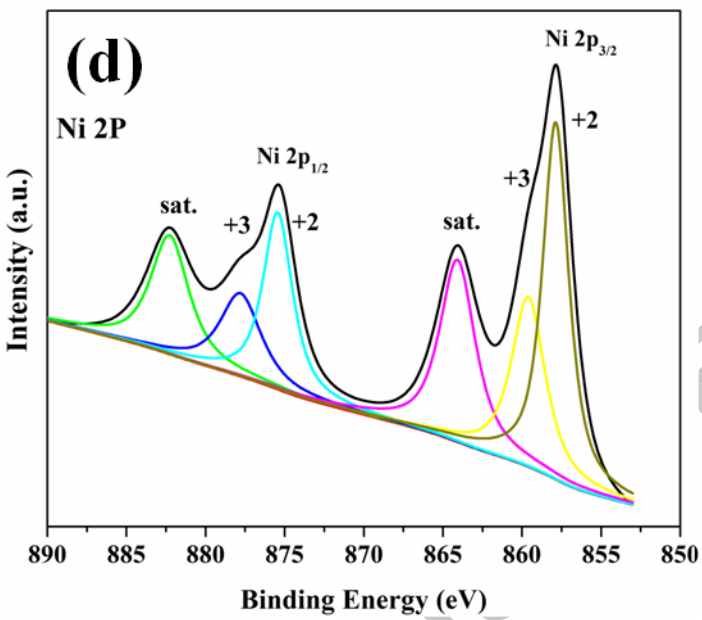

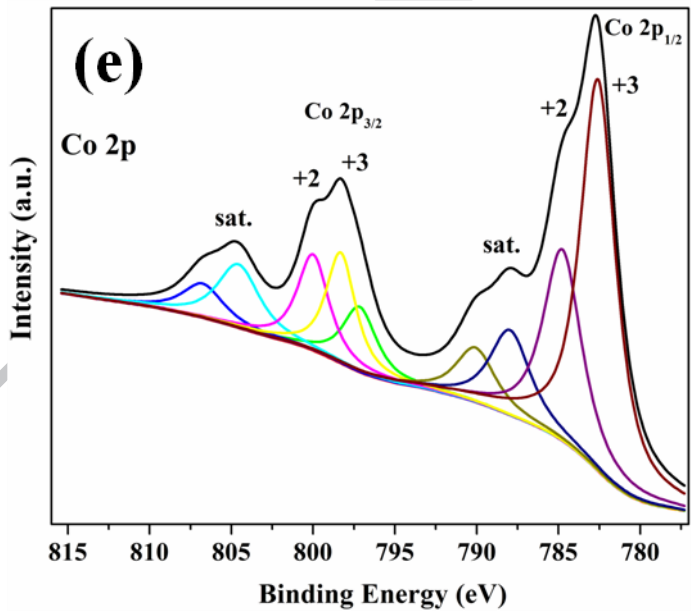

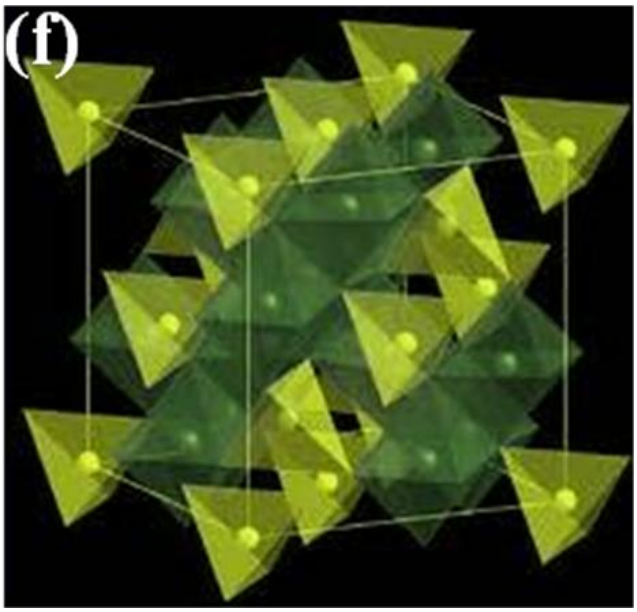

Figure 8

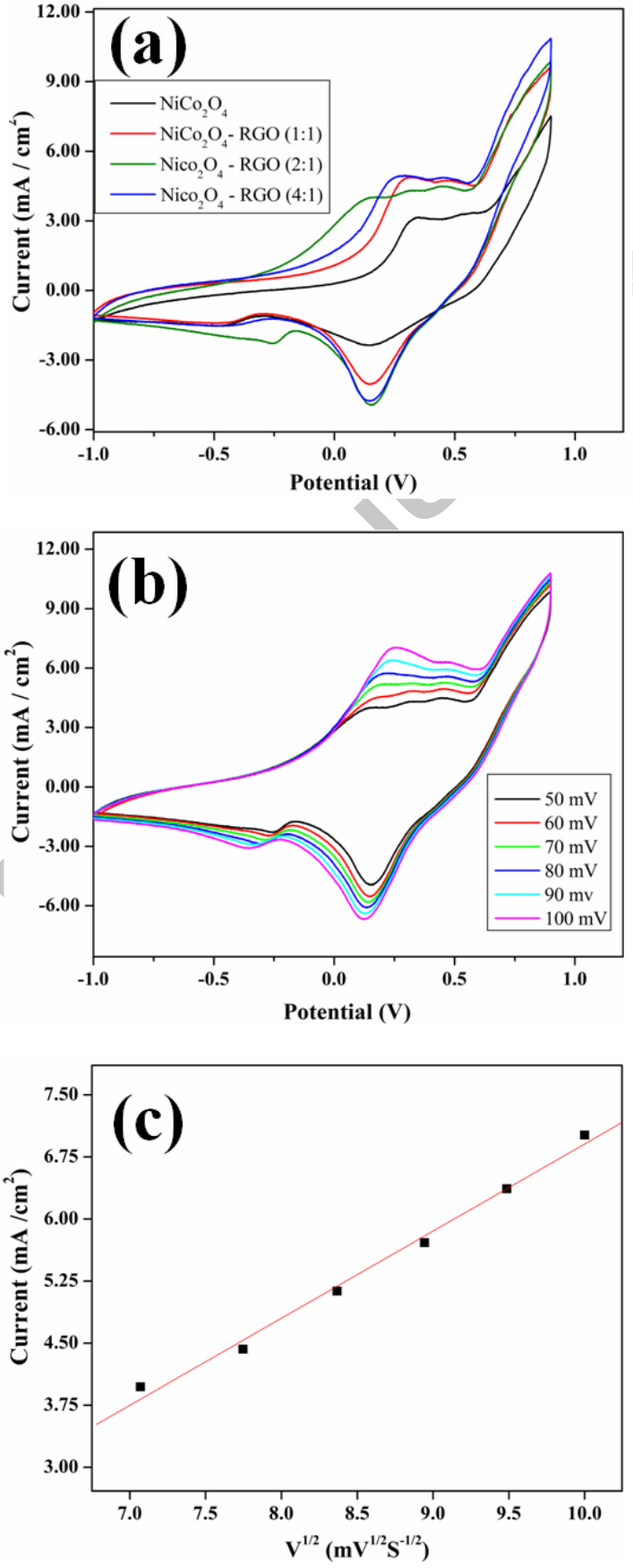

Contd…..

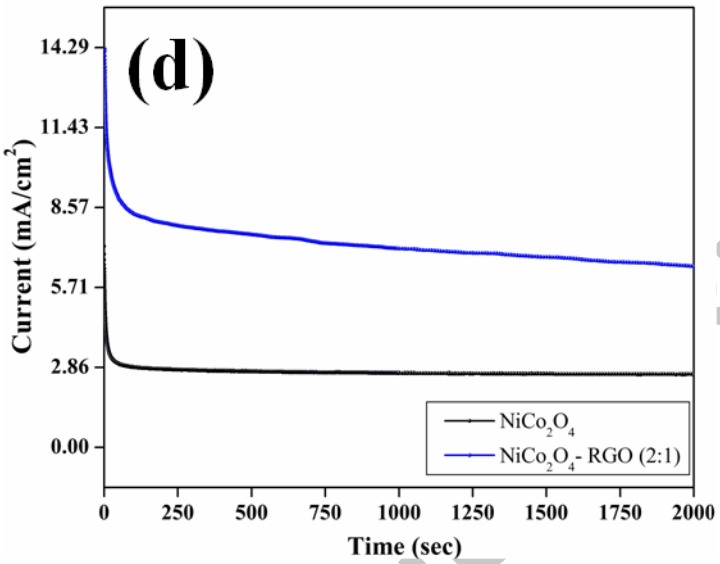

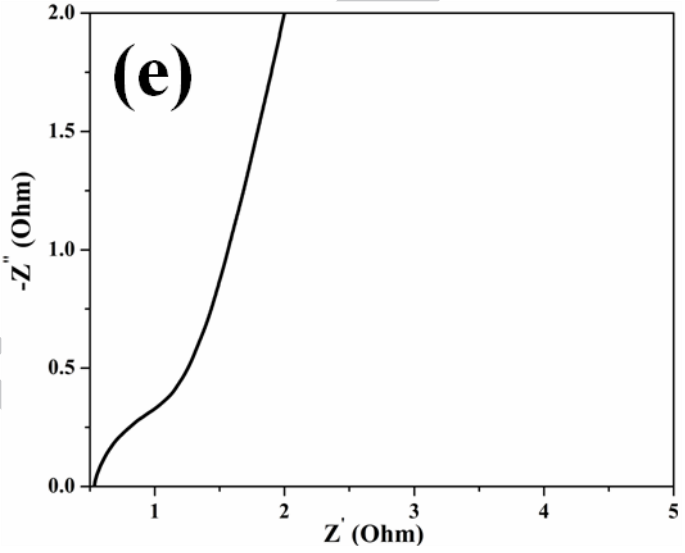

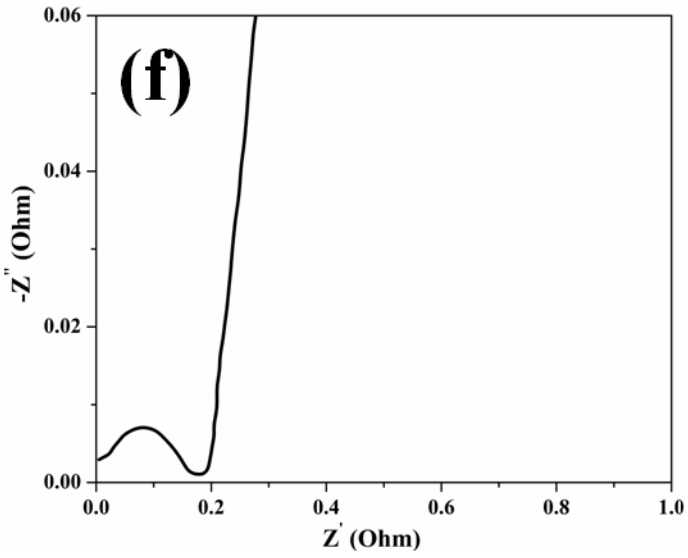

Graphical Abstract

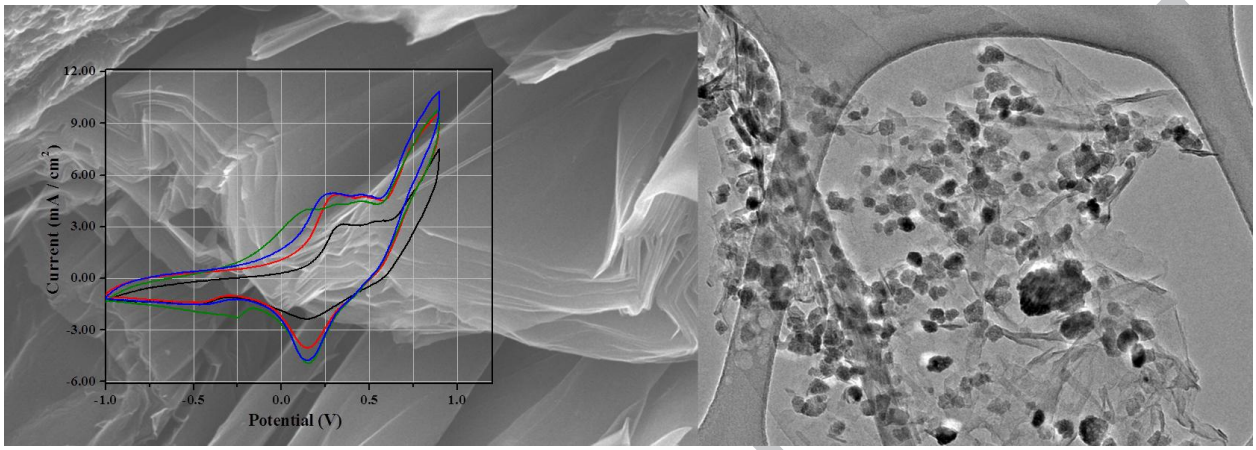

- $NiCo_2O_4$ were grown RGO by in-situ synthesis process.
- FE-SEM investigation revealed self assembled layer by layer growth of $NiCo_2O_4$-RGO nanocomposite.
- $NiCo_2O_4$-RGO nanocomposite exhibited synergetic effect between $NiCo_2O_4$ nanoparticles and RGO and therefore a better electrochemical performance compared to bare $NiCo_2O_4$ nanoparticles for OER.

Highlight

- $NiCo_2O_4$ were grown RGO by in-situ synthesis process.
- FE-SEM investigation revealed self assembled layer by layer growth of $NiCo_2O_4$-RGO nanocomposite.
- $NiCo_2O_4$-RGO nanocomposite exhibited synergetic effect between $NiCo_2O_4$ nanoparticles and RGO and therefore a better electrochemical performance compared to bare $NiCo_2O_4$ nanoparticles for OER.

Realization of CDTA Based Frequency Agile Filter

Neeta Pandey[1], Rajeshwari Pandey[2], Richa Choudhary[3], Aseem Sayal [4], Manan Tripathi[5]
[1,2] Department of Electronics and Communication Engineering,[3,4,5]Department of Electrical Engineering
Delhi Technological University, Delhi, INDIA
[1]n66pandey@rediffmail.com, [2]rajeshwaripandey@gmail.com,[3]dce.richa@gmail.com, [4]aseem.sayal@gmail.com,
[5]manantripathi1990@gmail.com,

***Abstract*— This paper presents frequency agile filter based on current difference transconductance amplifier (CDTA). The agile filters used in this work provide high agilty, tunability and quality factor while they are fully integrated configurations and not discrete systems. The use of grounded capacitors and resistor makes these structures suitable for integration. The functional verification is exhibited through extensive SPICE simulations using 0.25µm TSMC CMOS technology model parameters. The performance evaluation is made in terms of power dissipation, signal to noise ratio (SNR) and output noise.**

***Index Terms*-- Current difference transconductance amplifier (CDTA), Frequency agile filter (FAF), Power Dissipation, Signal to Noise Ratio (SNR).**

I. INTRODUCTION

There is an increasing demand for presenting a one-fits-all "analog" front end solution due to rapid evolution of wireless services form simple voice/text to recently multimedia [1]. These services use different standards and therefore necessitate development of multi-standard transceivers. An integrated multi-standard transceiver results in reduction of size, price, complexity, power consumption etc. Its architecture has parameters that can be modified in order to be able to adapt to the specifications of each standard [1]. The transceivers can be designed by using the practical approach of connecting the elements in parallel that handle various standards or using reconfigurable elements. The reconfigurable filters are integral components of multi-standard transceiver. The recently introduced frequency agile filter (FAF) [1]-[10] may be used in transceivers and is characterized by adjustment range; reconfigurability against tunability, and agility. The literature survey shows that a limited number of topologies of active FAF are available and are based on opamp [1] and current mode active block [2]-[3] and CMOS [4].

There is a wide range of current mode building blocks available in open literature. Among these blocks current difference transconductance amplifier (CDTA) [17] has received considerable interest as it is free from input capacitance. Many applications such as filters, oscillators based on CDTA have been reported in the literature [11]-[18]. The main intention of this paper is to present a CDTA based frequency agile filter. The filter uses grounded capacitors and is suitable for integration. The terminology associated with FAF and its implementation scheme is briefly reviewed in Section II. The proposed CDTA based implementation of FAF is given next in Section III. Simulation results are provided in Section IV to substantiate the proposed FAF. The performance evaluation of class *0* and class *1* agile filters is presented in Section V. The paper is concluded in section VI.

II. TERMINOLOGIES AND IMPLEMENTATION SCHEME

This section first describes the basic terminologies related to frequency agile filter [2]. Thereafter, the implementation scheme for class *0*, class *1* & class *n* agile filter [2] is put forward.

A. Basic Terminologies

The basic terminologies related to agile filter [2] are described below:

1.) Adjustment Range: It is necessary to make adjustment to the center frequency of filters for congruous tuning of multi-standard transceivers. The range of adjustment of center frequency (f_0) for filters is termed as adjustment range. If the filter center frequency is considered as f_0 , then this frequency can be adjusted between two frequencies i.e. f_{0min} and f_{0max}. Then, the adjustment range of filter starts from f_{0min} to f_{0max}.

2.) Tunability: The tuning ratio of filter is given by (1).

$$n = \frac{f_{0\max}}{f_{0\min}} \tag{1}$$

The tunable filter is defined as filter in which tuning of center frequency f_0 in short specific range is possible to nullify the effect of drift i.e. the value of n is small.

978-1-4673-6190-3/13/$31.00 ©2013 IEEE

3.) Reconfigurability: The reconfigurable filters are the tunable filter in which center frequency is varied over a wide frequency range i.e. the tuning ratio has large value.

4.) Agility: A frequency agile filter (Hoping Filter) is a reconfigurable filter which can switch over two frequencies f_1 and f_2 very quickly.

B. Implementation Scheme of FAF

The implementation scheme of frequency agile filter (FAF) is described in this section.

1.) Class Zero FAF: The implementation of FAF is based on a classical second order filter having one input (I_{IN}) and two outputs, band pass output (I_{BP}) and low pass output (I_{LP}) as depicted in Fig. 1 [3]. This second order filter is called Class Zero FAF.

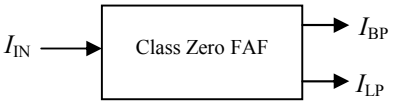

Fig. 1. Class Zero FAF

The transfer functions of class *0* FAF are given by (2)-(3).

$$T_{BP}(s) = \frac{I_{BP}}{I_{IN}} = \frac{ps}{1+as+bs^2} \tag{2}$$

$$T_{LP}(s) = \frac{I_{LP}}{I_{IN}} = \frac{q}{1+as+bs^2} \tag{3}$$

The center frequency and quality factor of the filter are represented by (4)-(5) respectively.

$$f_0 = \frac{1}{2\pi\sqrt{b}} \tag{4}$$

$$Q = \frac{\sqrt{b}}{a} \tag{5}$$

2.) Class 1 FAF: In class *1* filter, the low pass output of the class *0* FAF is amplified (with variable gain *A*) and fed back to the input. The basic block diagram of class *1* FAF is shown in Fig. 2.

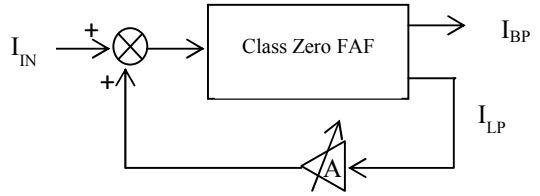

Fig. 2. Class 1 FAF

The characteristic frequency of Class *1* FAF is given by (6).

$$f_{0A} = f_0\sqrt{(1+Aq)} \tag{6}$$

where f_0 is center frequency of class *0* FAF and *A* is gain of amplifier. The Q-factor, Q_A of class *1* FAF is given by (7).

$$Q_A = Q\sqrt{(1+Aq)} \tag{7}$$

3.) Class n FAF: The method outlined for class *1* FAF realization can be extended for class *n* FAF implementation. Fig. 3 shows the implementation of class *n* FAF. This will require *n* amplifiers to be placed in *n* feedback paths obtained in the same way as done in class *1* implementation. It is noticeable that only adjustable-gain amplifiers with gain *A* are required along with class *0 FAF*. The characteristic parameters of n^{th} class FAF are given by (8)-(9).

$$f_{0An} = f_{0An-1}\sqrt{(1+Aq)} = f_0(1+Aq)^{\frac{n}{2}} \tag{8}$$

$$Q_{An} = Q_{An-1}\sqrt{(1+Aq)} = Q(1+Aq)^{\frac{n}{2}} \tag{9}$$

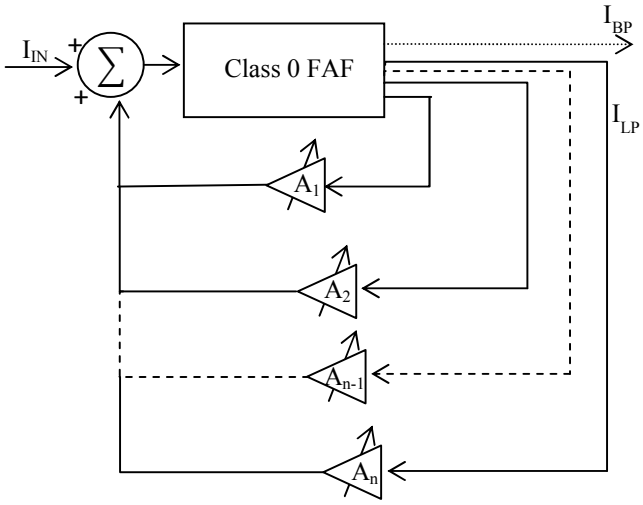

Fig. 3. Class *n* FAF [3]

III. DESIGN OF CDTA BASED FAF

This section first describes the CDTA operation and its internal structure. Thereafter, the design of current mode CDTA based class *0* and class *1* frequency agile filters is proposed.

A. CDTA

CDTA [11]-[18] is an active and versatile circuit element which is free from parasitic input capacitances and can operate in a wide frequency range due to its current-mode operation. It consists of a unity-gain current source controlled

by the difference of the input currents and a multi-output transconductance amplifier providing electronic tunability through its transconductance gain. The CDTA symbol is shown in Fig. 4 and its terminal characteristic in matrix form are given by (10).

$$\begin{bmatrix} V_p \\ V_n \\ I_z \\ I_{x+} \\ I_{x-} \end{bmatrix} = \begin{bmatrix} 0 & 0 & 0 & 0 & 0 & 0 \\ 0 & 0 & 0 & 0 & 0 & 0 \\ 1 & -1 & 0 & 0 & 0 & 0 \\ 0 & 0 & g_m & 0 & 0 & 0 \\ 0 & 0 & -g_m & 0 & 0 & 0 \end{bmatrix} \begin{bmatrix} I_p \\ I_n \\ V_z \\ V_{x+} \\ V_{x-} \end{bmatrix} \quad (10)$$

where, g_m is transconductance of the CDTA. The CMOS implementation of CDTA [16] is given in Fig. 5. It comprises of a current difference (Mc1–Mc17) [16] which is followed by transconductance amplifier (Mc18–Mc26). The value of transconductance (g_m) is expressed as

$$g_m = \sqrt{2\mu C_{ox}(W/L)_{19,21} I_{Bias}} \quad (11)$$

which can be adjusted by bias current I_{Bias} of CDTA.

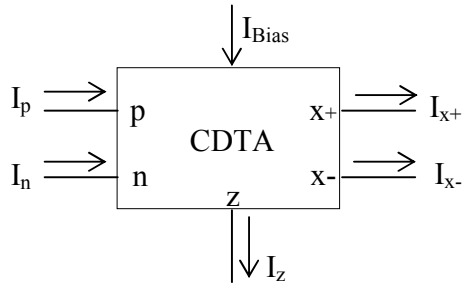

Fig. 4. Symbol of CDTA

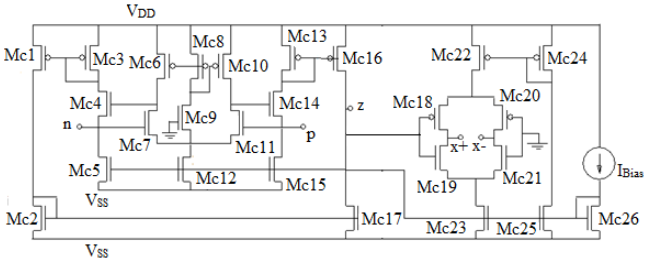

Fig. 5. CMOS implementation of CDTA

The CDTA based current mode FAF is presented in next section. The simulation results of these circuits are placed in section IV.

B. Design of CDTA based class zero FAF

The single CDTA based second order filter presented in [14] provides both low pass and band pass responses. Therefore it can be used as class zero FAF. The circuit is shown in Fig. 6. which employs a single CDTA block, two grounded capacitors and one resistor [14]. The low pass and band pass transfer functions of CDTA based class *0* Frequency agile filter are given by (12)-(13) respectively.

$$\frac{I_{LP}}{I_{IN}} = \frac{g_1}{R_1C_1C_2s^2 + sC_2 + g_1} \quad (12)$$

$$\frac{I_{BP}}{I_{IN}} = \frac{sC_2}{R_1C_1C_2s^2 + sC_2 + g_1} \quad (13)$$

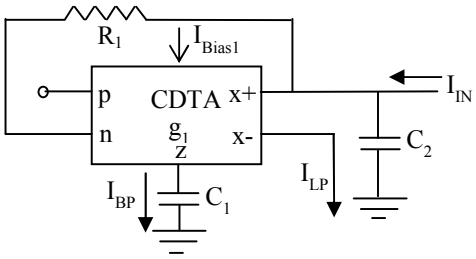

Fig. 6. CDTA based Class *0* FAF [14]

The center frequency and quality factor of class *0* FAF are:

$$f_0 = \frac{1}{2\pi}\sqrt{\frac{g_1}{R_1C_1C_2}} \quad (14)$$

$$Q = \sqrt{\frac{g_1R_1C_1}{C_2}} \quad (15)$$

C. Design of CDTA based Class 1 FAF

Fig. 7. shows the CDTA based current mode class 1 FAF implementation. The CDTA block in the feedback path is used as amplifier with tunable gain A. The expression of gain A of CDTA based amplifier is given by (16).

$$A = g_2R_2 \quad (16)$$

This gain is adjusted by varying I_{Bias2} to obtain central frequency f_{0A} higher than f_0. In the realization of class *1* FAF, the bias current of class *0* FAF is kept constant while amplifier's gain is varied by changing I_{Bias2} to obtain different center frequencies. The CDTA based class *1* FAF employs two CDTA blocks, two grounded capacitors and two resistors.

The center frequency and quality factor of the CDTA based class *1* FAF are expressed by (17)-(18) respectively.

$$f_{0A} = \frac{1}{2\pi}\sqrt{\frac{g_1}{RC_1C_2}}\sqrt{(1+g_2R_2)} \quad (17)$$

$$Q_A = \sqrt{\frac{g_1RC_1}{C_2}}\sqrt{(1+g_2R_2)} \quad (18)$$

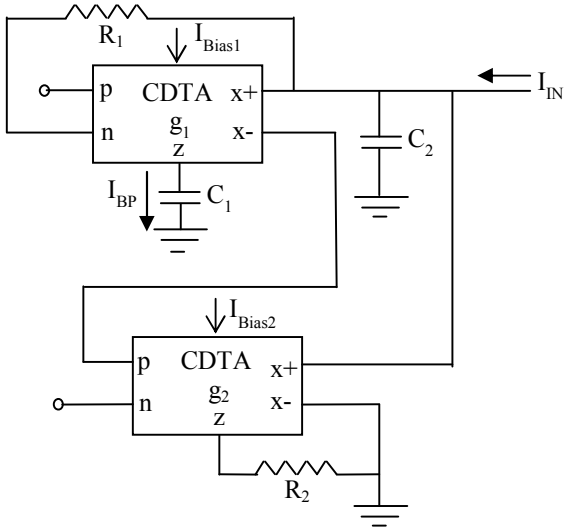

Fig. 7. CDTA based Class *1* FAF

IV. Simulation Results

The theoretical proposition has been verified through SPICE simulations using TSMC 0.25µm CMOS process model parameters. The CMOS schematic of Fig. 5 is used for CDTA and the MOS dimensions of the transistors in CDTA that were used in the implementation of the CDTA-based FAF structure are given in Table I. The supply voltages of $V_{DD} = -V_{SS} = 1.8$ V are used.

TABLE I. MOS Dimensions of CDTA

MOSFETs	***W(µm)/L(µm)***
Mc26	7.0/0.7
Mc1	9.8/0.7
Mc2, Mc3, Mc13,Mc16, Mc17	10.5/0.7
Mc19, Mc21	16.1/0.7
Mc6, Mc20	28.0/0.7
Mc8, Mc10, Mc18	28.7/0.7
Mc15, Mc12, Mc5	35.0/0.7
Mc4, Mc14	42.0/0.7
Mc22, Mc23, Mc25	56.0/0.7
Mc24	58.8/0.7
Mc7, Mc9, Mc11	70.0/0.7

A. Simulation of CDTA based Class 0 FAF

The frequency response of CDTA based Class Zero FAF topology is illustrated in Fig. 8. The responses are obtained by varying bias current I_{Bias1} to 1µA, 10 µA and 50µA. It can be clearly noticed that center frequency f_0 increases on increasing the bias current I_{Bias1}. The tunability of class zero filter is 2.5 when the input bias current I_{Bias1} is varied from 1µA to 50µA. The performance of the proposed CDTA based class *0* FAF is shown in Figs. 9-10. Fig. 9 depicts the Signal to Noise Ratio (SNR) for the CDTA based class *0* FAF topology. The noise behavior of CDTA based class *0* FAF for different values of input bias current I_{Bias1} is given in Fig. 10. The circuit elements for CDTA based FAF are listed in Table II. Table III lists the values of central frequency (f_0), quality factor (Q) and bandwidth for different values of bias current I_{Bias1}.

TABLE II. Circuit Parameters of Class *0* FAF

Circuit Parameter	**Value**
R_1	30KΩ
C_1	5pF
C_2	10pF

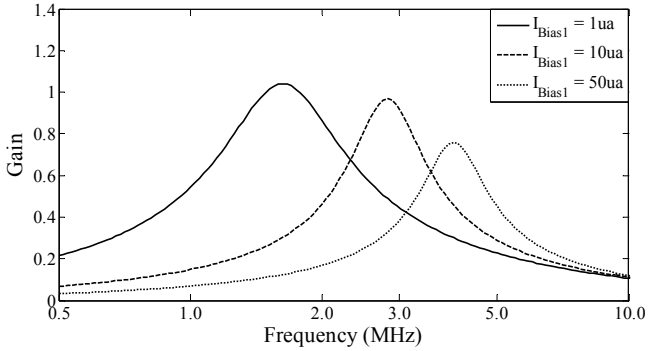

Fig. 8. Frequency response of CDTA based class *0* FAF

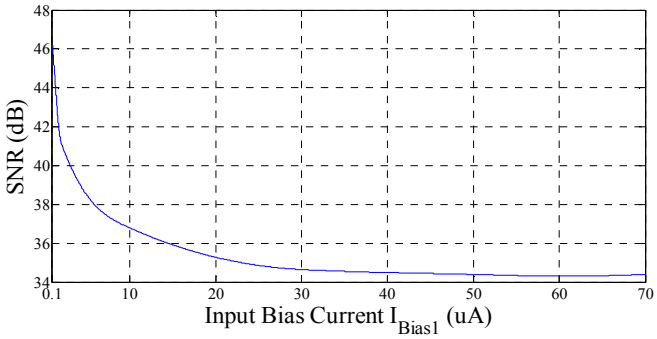

Fig. 9. SNR of CDTA based class *0* FAF

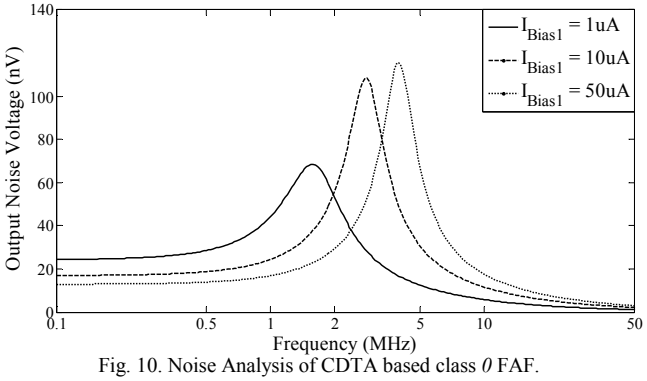

Fig. 10. Noise Analysis of CDTA based class *0* FAF.

TABLE III. Parameters of CDTA Based Class *0* FAF

I_{Bias1}	f_0	**Bandwidth**	Q
1µA	1.62MHz	1.087MHz	1.49
10µA	2.8MHz	1.005MHz	2.78
50µA	4.0MHz	1.365MHz	2.93

B. Simulation of CDTA based Class 1 FAF

The frequency response of proposed CDTA based class *1* FAF topology is illustrated in Fig. 11. The responses are obtained by setting bias current I_{Bias1} to 0.5µA and varying I_{Bias2} to 1µA, 10 µA and 25µA. It can be clearly noticed that center frequency f_0 increases on increasing the bias current I_{Bias2}. The tunability of class 1 filter is 1.7 when the input bias current I_{Bias2} is varied from 1µA to 25µA. The performance of the proposed CDTA based class *1* FAF is shown in Figs. 12-13. Fig. 12 depicts the Signal to Noise Ratio (SNR) for the CDTA based class *1* FAF topology. The noise behavior of CDTA based class *1* FAF for different values of input bias current I_{Bias2} is given in Fig. 13. The circuit elements for CDTA based FAF are listed in Table IV. Table V lists the values of central frequency (f_0), quality factor (Q) and bandwidth for different values of bias current I_{Bias2}.

TABLE IV. CIRCUIT PARAMETERS OF CLASS *1* FAF

Circuit Parameter	Value
R_1	30KΩ
R_2	10KΩ
C_1	5pF
C_2	10pF

TABLE V. PARAMETERS OF CDTA BASED CLASS *1* FAF

I_{Bias2}	f_0	Bandwidth	Q
1µA	1.73MHz	0.86MHz	2.01
10µA	2.56MHz	0.67MHz	3.82
25µA	2.94MHz	0.57MHz	5.157

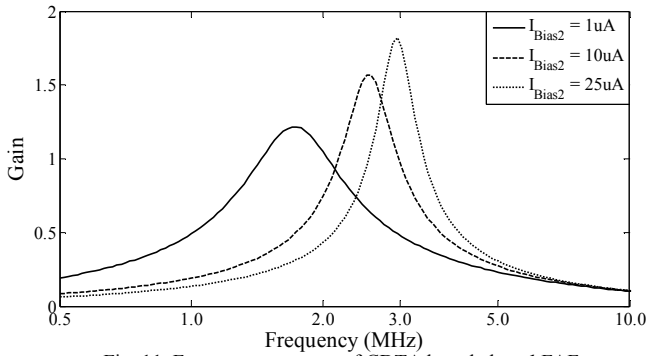

Fig. 11. Frequency response of CDTA based class *1* FAF.

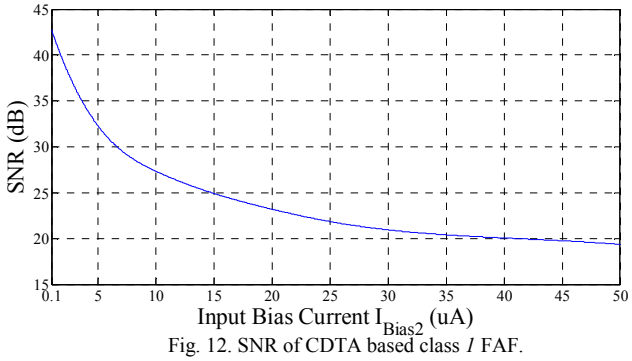

Fig. 12. SNR of CDTA based class *1* FAF.

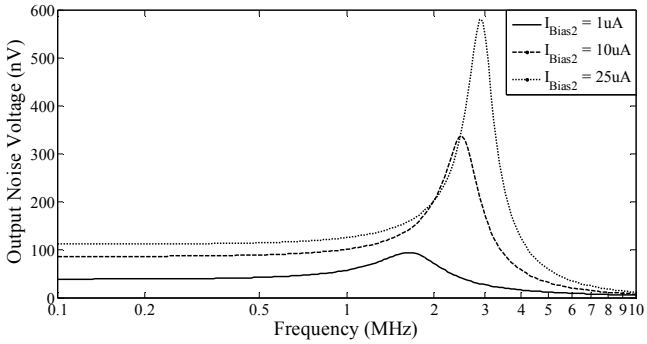

Fig. 13. Noise Analysis of CDTA based class *1* FAF.

V. PERFORMANCE CHARACTERISTICS

The performance of proposed CDTA based FAF circuits is studied in terms of output noise, power dissipation, total and signal to noise ratio (SNR) and are summarized in Table VI and VII respectively. Maximum output noise voltage is calculated from Noise Analysis Curve of CDTA based class 0 and class1 FAF (Fig.10 and Fig 13 respectively) .The maximum value of SNR is taken from Fig. 9 and Fig. 12.The power dissipation is obtained through simulations

TABLE VI. PERFORMANCE CHARACTERISTICS OF CLASS 0 FAF

Parameters	I_{Bias1} = 1µA	I_{Bias1} = 10µA	I_{Bias1} = 50µA
Power Dissipation	0.15mW	1.56mW	7.79mW
SNR	46.40dB	35.40dB	34.40dB
Max. Output Noise	68.35nV	108.50nV	115.60nV

TABLE VII. PERFORMANCE CHARACTERISTICS OF CLASS 1 FAF

Parameters	I_{Bias2} = 1µA	I_{Bias2} = 10µA	I_{Bias2} = 25µA
Power Dissipation	0.23mW	1.63mW	3.98mW
SNR	42.75dB	27.75dB	21.80dB
Max. Output Noise	93.70nV	337.00nV	570.00nV

VI. CONCLUSION

In this paper, a detailed examination of current difference transconductance amplifier (CDTA) based frequency agile filter is performed. The agile filter topologies use grounded capacitors and are suitable from integration point of view. The simulation results are included to demonstrate the workability of the circuits. The filter configurations in class 0 and class 1 are evaluated in terms of power dissipation, SNR and noise performance. The increment is observed in power dissipation with increase in bias current

REFERENCES

[1] Pui-In Mak, Seng-Pan U and Rui Paulo Martins, "Analog – baseband architecture and circuits for multistandard and low voltage wireless transceivers", Analog Circuits and Signal Processing, Springer, 2007.

[2] Yahya Lakys, Alain Fabre, "Multistandard transceivers: state of the art and a new versatile implementation for fully active frequency agile filters", Analog Integrated Circuits and Signal Processing, Vol. 74, No. 1, pp. 63-78, Springer, 2013.

[3] Yahya Lakys, Alain Fabre , “A fully active frequency agile filter for multistandard transceivers”, International Conference on Applied Electronics, pp. 1-7, 2011.
[4] Stefan Kaehlert, Dirk Bormann, Tobias D. Werth, Muh-Dey Wei, Lei Liao and Stefan Heinen, “Design of frequency agile filters in RF frontend circuits”, Radio and Wireless Symposium (RWS), pp. 13- 16, IEEE, 2012.
[5] Alan J. X. Chen. Yang Wu, Justin Hodiak, and Paul K. L. Yu, “Frequency Agile Digitally Tunable Microwave Photonic Filter”, International Topical Meeting on Microwave Photonics, pp. 89-92, IEEE, 2003.
[6] Guru Subramanyam, Frederick W. Van Keuls, Félix A. Miranda, “A K-Band-Frequency Agile Microstrip Bandpass Filter Using a Thin- Film HTS/Ferroelectric/Dielectric Multilayer Configuration”, IEEE Transactions on Microwave Theory and Techniques, Vol. 48, No. 4, 2000.
[7] Hengky Chandrahalim, Sunil A. Bhave, Ronald G. Polcawich, Jeff Pulskamp, Roger Kaul, “A Pb(Zr0.55Ti0.45)O3-Transduced Fully Differential Mechanically Coupled Frequency Agile Filter”, IEEE Electron Device Letters, Vol. 30, No. 12, 2009.
[8] Mark W. Wyville, Russell C. Smiley, James S. Wight, “Frequency Agile RF Filter for Interference Attenuation”, Radio and Wireless Symposium (RWS),IEEE, pp 399- 402, 2012.
[9] Hjalti H. Sigmarsson, Juseop Lee, Dimitrios Peroulis, William J. Chappell, “Reconfigurable-Order Bandpass Filter for Frequency Agile Systems”, International Microwave Symposium Digest, pp. 1756-1759, IEEE, 2010.
[10] Yahya Lakys, Balwant Godara, Alain Fabre, “Cognitive and Encrypted Communications, Part 2 : A New Approach to Active Frequency-Agile Filters and Validation Results for an Agile Bandpass Topology in SiGe-BiCMOS”, International Conference on Electrical and Electronics Engineering, pp. II-16 –II-29, IEEE, 2009.
[11] Atilla Uygur, Hakan Kuntman, Ali Zeki, “Multi-Input Multi-Output CDTA-Based KHN Filter”, International Microwave Symposium Digest, pp. 1756-1759, IEEE, 2010.
[12] D. Biolek, V Biolkova, Z Kolka, “Current-mode biquad emploting single CDTA”, Indian Journal of Pure & Applied Physics, Vol. 47, 2009.
[13] Montree Kumngern, Punnavich Phatsornsiri, Kobchai Dejhan, “Four Inputs and One Output Current-Mode Multifunction Filter Using CDTAs and All-Grounded Passive Components”, IEEE Tenth International Conference on ICT and Knowledge Engineering, pp. 59-62, IEEE, 2012.
[14] Sunil Kumar Pandey, Abhay Pratap Singh, Manish Kumar, Sumit Dubey,Pallavie Tyagi, “A Current Mode Second Order Filter Using Dual Output CDTA”, International Journal of Computer Science & Communication Networks, Vol. 2(2), pp. 210-213, 2012.
[15] F. Kacar, H. Kuntman, “A New CMOS Current Differencing Transconductance Amplifier (CDTA) and its Biquad Filter Application,” IEEE EUROCON’09, pp. 189-196, 2009.
[16] D. Biolek, E. Hancioglu, A. U. Keskin, “High-performance current differencing transconductance amplifier and its application in precision current-mode rectification,” International Journal on Electronics and Communications, (AEU), 62, 92 – 96, 2008.
[17] D. Biolek, “CDTA-building block for current-mode analog signal processing,” Proceedings of the ECCTD’03, vol. III, Krakow, Poland, pp. 397–400, 2003.
[18] W. Chiu, S. I. Liu, H. W. Tsao, J. J. Chen, “CMOS differential difference current conveyor and their applications,” IEE Proceedings on Circuits Devices Systems, 143, pp. 91- 96, 1996.

Retrieval of FAQs based on SMS-input through phonetic equivalence

Akhil Lohchab Amanpreet Singh Ashish Mahajan Ritu Agarwal

Delhi Technological University Delhi Technological University Delhi Technological University Asst. Prof., Delhi Technological University

Abstract : Short Messaging Service(SMS) has become really popular in the present day and presents a unique opportunity to make automated query response reach a wider audience.Public information systems such as passenger query systems and patient query systems in a hospital can prove to be quite useful when implemented this way. In this paper, we have addressed the problem of mapping the user queries on government portals in the form of SMSes to their equivalent plain text frequently asked questions (FAQs) stored in the database by generating phonetic equivalents of both the queries and the FAQs. Lucene indexer has been used to index the FAQs and the score for a document is determined by primarily by the number of tokens in the SMS query that have a high similarity score with an FAQ. Experiments show high success rate on the new unseen SMSes.

1. Introduction

The number of mobile users is growing at an amazing rate. In India alone a few million subscribers are added each month with the total subscriber base now crossing 370 million. The anytime anywhere access provided by mobile networks and portability of handsets coupled with the strong human urge to quickly find answers has fueled the growth of information based services on mobile devices. These services can be simple advertisements, polls, alerts or complex applications such as browsing, search and e-commerce. The latest mobile devices come equipped with high resolution screen space, inbuilt web browsers and full message keypads, however a majority of the users still use cheaper models that have limited screen space and basic keypad. On such devices, SMS is the only mode of text communication.[1]

Language usage over SMSes differs significantly from the language of communication from person-to-person. The characteristic features of the mobile devices have brought about the unique ways of communication, notably in its usage is the restriction in the number of characters/words engaged by the user to communicate because of the memory space, pad structures of the design and writing skills of the query and bandwidth issue . Its construction is based on convenience of spelling and homophony of the wordings. Regardless of the range of the handsets (low, medium or high end).This nature of texting language makes it difficult to build automated question answering systems around SMS technology. This is true even for questions whose answers are well documented in a FAQ database.

In this paper we present a SMS query-based FAQ retrieval system that allows the query to be input in the SMS texting language. Our goal is to accept the queries and respond by finding the most appropriate FAQ from a corpus of FAQs.

2. Our Approach

Our initial idea was to use term correction and find the closest words to SMS-tokens based on edit distance from the FAQ-list and then use these corrected SMS tokens to calculate a similarity score with the FAQs. After a few preliminary experiments, it was observed that certain words rarely had any effect on the list or the ranks of the FAQs retrieved. Hence, a stop word list was added that removes all the words within the file from the SMSes as well as the FAQs. However, this approach did not cater well to the 'Speech_queries' and a different direction was sought, namely phonetic equivalents where the Metaphone library was used to generate phonetic equivalents.

We indexed all FAQs using Lucene. Lucene is a public domain search utility that builds an inverted index on the given document set. Whenever a search is made on some keywords, this index is searched.

Every FAQ document was tokenized and phonetic key was generated for each token using the Metaphone library with a maximum possible length of key. All SMS queries were also tokenized and converted to phonetic equivalent tokens.

Metaphone uses a set of rules to code a token by using the 16 consonant symbols 0BFHJKLMNPRSTWXY, where '0' represents "th" (as an ASCII approximation of Θ), 'X' represents "sh" or "ch", and the others represent their usual English pronunciations.

Once, the FAQs have been tokenized, stop words removed, the phonetic equivalents of the tokens are generated and committed to the index. A similar procedure allowed the phonetic equivalents of the tokenized SMS query to be generated. The index was then searched with each token of the SMS query, and a score for each document with respect to the SMS token is calculated. A list of top scoring documents is then compiled and a maximum of 5 documents are selected. Selection of the documents is filtered by a threshold function.

3. Results

Text-Only queries:

No. of In-domain Queries	200
No. of Out of Domain Queries	99
In Domain correct	179/200 (0.895)
Out of Domain correct	58/99(0.58)
Total Score	0.7926421

Mean Reciprocal Rank (MRR): 0.95936835

Overall :

No. of In-domain Queries	392
No. of Out of Domain queries	148
In Domain Correct	180/392 (0.4591)
Out of Domain correct	83/148 (0.5608108)
Total Score	0.48703703

Mean Reciprocal Rank (MRR): 0.6298412

4. Future Work and Conclusion

Given the problem of retrieving an FAQ based on SMS query, we obtained a good accuracy on the text queries and although our attempt at mapping the 'Speech_queries' fared poorly, one can consider trying other approaches. In particular, using a synonym lookup dictionary to improve the matching of SMS tokens to FAQ tokens is something one can try.

5. References

1. SMS based Interface for FAQ Retrieval. Govind Kothari. IBM India Research Lab gokothar@in.ibm.com. Sumit Negi. IBM India Research Lab sumitneg@in.ibm.

2. A Query-Based SMS Translation in Information Access System. Ademola O. Adesina, Kehinde K. Agbele, Nureni A. Azeez, Ademola P. Abidoye, International Journal of Soft Computing and Engineering (IJSCE) 2011.

3. E. Prochasson, Christian Viard-Gaudin, Emmanuel Morin. 2007. Language Models for Handwritten Short Message Services, In Proceedings of the 9th International Conference on Document Analysis and Recognition.

4. E. Sneiders. 1999. Automated FAQ Answering: Continued Experience with Shallow Language Understanding, Question Answering Systems. Papers from the 1999 AAAI Fall Symposium. Technical ReportFS-99−02, November 5−7, North Falmouth, Massachusetts,

5. Dr. Hadeel Showket Al-Obaidy, "Building Ontology Web Retrieval System Using Data Mining," ed.

International Journal of Current Engineering and Technology
ISSN 2277 - 4106

Available at http://inpressco.com/category/ijcet

Case Study

Total Productive Maintenance Review: A Case Study in Automobile Manufacturing Industry

Jagtar Singh [Á], Vikas Rastogi [Ḃ] and Richa Sharma [Ċ*]

[Á] Mechanical Engineering Department, SLIET Longowal-148106, Distt. Sangrur, Punjab, India
[Ḃ] Department of Mechanical &Production Engineering, Delhi Technological University Delhi-110042
[Ċ] Department of Mechanical & Automation Engineering, Amity University, Noida-201301

Accepted 25 November 2013, Available online 15 December 2013, **Vol.3, No.5 (December 2013)**

Abstract

This paper will review all the Total Productive Maintenance (TPM) Pillars, TPM Implementation methodology and the contribution of TPM towards improving manufacturing performance.. It will also focus on calculating the Overall Equipment Effectiveness (OEE) in one of the two wheeler automobile Industry in India. The relationship between various TPM implementation dimensions and manufacturing performance improvements have been evaluated by applying OEE. The study establishes that focused TPM implementation over a reasonable time period can strategically contribute towards realization of significant manufacturing performance enhancements. Set of various techniques like Single Minute Exchange Die (SMED), computer maintenance management system, production planning were suggested to the industry after calculating the overall equipment effectiveness to improve their maintenance procedures and improve the productivity.

Keywords: *Total Productive Maintenance, Overall Equipment Effectiveness, Availability, Performance Efficiency.*

1. Introduction

TPM is a unique Japanese philosophy which has been developed based on the productive maintenance concepts and methodologies. Total Productive Maintenance is an innovative approach to maintenance that optimizes equipment effectiveness, eliminates breakdowns and promotes autonomous maintenance by operators through day-to-day activities involving total workforce (Bhadury, 2000). TPM is a production driven improvement methodology that enhance the equipment reliability and ensure effectual management of plant assets using employee involvement and empowerment, by linking maintenance, manufacturing and engineering functions (Ahuja and Khamba. 2008). The key objective of an effective TPM initiative is to bring critical maintenance skilled trades and production workers together (A.W. Labib,1999) with its three ultimate goals: Zero breakdown, Zero defects and Zero accidents (P. Willmott. 1994), (M.Noon *et al* 2000). Another US advocate of TPM, (Wireman 1991) suggests that TPM is maintenance that involves all employees in the organization and accordingly includes everyone from top management to the line employee and indicates:
it encompasses all departments including, maintenance, operations, facilities, design engineering, project engineering, instruction engineering, inventory and stores, purchasing, accounting finances, plant /site management

There are many different definitions for TPM and the reason behind this diversity in definition is found in the way of adoption this strategy, some industries focus on the group working more than equipment management, and other focus on equipment effectiveness, this diversity shows how important implementing TPM in company that it is covers all factors may affect the production process (D.Hutchins. 1998)

This paper is organized in following sections: section two presents Pillars of TPM , section three presents the implementing the TPM methodology, section four represents the contribution of TPM towards improving manufacturing performance, section five describe the Overall Equipment Effectiveness, section six presents the case study in an Automobile Manufacturing Organization and conclusion is discussed in section seven.

2. TPM Pillars

Total Productive Maintenance (TPM) is classified into eight pillars, all of which are supported by 5S include Autonomous Maintenance, Focused Improvement, Planned Maintenance, Quality Maintenance, Education & Training, Office TPM Pillar, Safety Health & Environment and Development Management Pillar. (Ireland & Dale, 2001; Shamsuddin *et al*, 2005)

Dr. Jagtar Singh and **Dr. Vikas Rastogi** are working as Professor; *Corresponding author **Richa Sharma** is working as Assistant Professor

5S Concept

TPM starts with 5S. It is a systematic process of housekeeping to achieve a serene environment in the work place involving the employees with a commitment to sincerely implement and practice housekeeping. Problems cannot be clearly seen when the work place is unorganized. Cleaning and organizing the workplace helps the team to uncover problems. Making problems visible is the first step of improvement. 5S is a foundation program before the implementation of TPM..

5S is the name of a workplace organization method that uses a list of five Japanese words: *seiri*, *seiton*, *seiso*, *seiketsu*, and *shitsuke*. There are five primary 5S phases: sorting, set in order, systematic cleaning, standardizing, and sustaining. Refer to the Figure 1 for 5S meaning

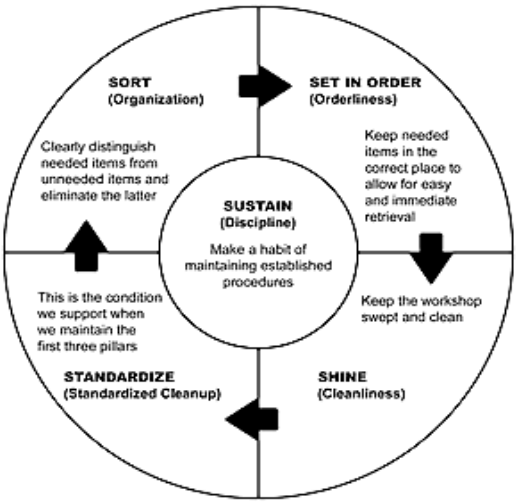

Figure 1: 5S Meaning

Pillar1. Autonomous Maintenance

Autonomous Maintenance follows a structured approach to increase the skill levels of personnel so that they can understand, manage and improve their equipment and processes. The goal is to change operators from being reactive to working in a more proactive way, to achieve optimal conditions that eliminate minor equipment stops as well as reducing defects and breakdowns. The Autonomous Maintenance pillar activity is broken down into three phases and is owned by the team who use the equipment on a daily basis.

The first phase establishes and maintains basic equipment conditions through restoration and eliminating causes of forced deterioration and sources of contamination. Standards are introduced for cleaning, inspection, tightening and lubrication to ensure the conditions are sustained.

The second phase increases the capabilities of the team by training them in the detailed operating principles of the equipment and then improving the standard basic condition.

During the third phase, the operators take total ownership of the equipment as self-directed teams, continuously improving equipment condition and performance to further reduce losses.

Pillar 2: Focused Improvement

Focused improvement includes all activities that maximize the overall effectiveness of equipment, processes, and plants through uncompromising elimination of losses* and improvement of performance.The objective of Focused Improvement is for equipment to perform as well every day as it does on its best day. The better our machines run, the more productive our shop floor, andthe more successful our business. The driving concept behind Focused Improvement is Zero Losses. Maximizing equipment effectiveness requires the complete elimination of failures, defects, and other negative phenomena – in other words, the wastes and losses incurred in equipment operation.(Nakajima 1988). Overall Equipment Effectiveness (OEE) is the key metric of Focused Improvement. Focused Improvement is characterized by a drive for Zero Losses, meaning a continuous improvement effort to eliminate any effectiveness loss. Equipment losses may be either chronic (the recurring gap between the equipment'sactual effectiveness and its optimal value) or sporadic (the sudden or unusual variation or increase in efficiency loss beyond the typical and expected range), (Tajiri and Gotoh 1992)

Pillar 3: Planned Maintenance

Planned Maintenance aims to achieve zero breakdowns. It follows a structured approach to establish a management system that extends the equipment reliability at optimum cost.

It is aimed to have trouble free machines and equipment producing defects free products for total customer satisfaction. The Planned Maintenance pillar activities are normally led by the maintenance team. The initial phase prioritises equipment and involves evaluating current maintenance performance and costs to set the focus for the pillar activity. Support is provided to the Autonomous Maintenance pillar to establish a sustainable standard basic condition and the team focusses on eliminating the causes of breakdowns

Pillar 4: Quality Maintenance

Quality Maintenance aims to assure zero defect conditions. It does this by understanding and controlling the process interactions between manpower, material, machines and methods that could enable defects to occur. The key is to prevent defects from being produced in the first place, rather than installing rigorous inspection systems to detect the defect after it has been produced. Quality Maintenance is implemented in two phases. The first phase aims to eliminate quality issues by analysing the defects, so that optimum conditions can be defined that prevent defects occurring. Then, the current state is investigated and improvements are implemented. The second phase ensures that quality is sustained, by

standardising the parameters and methods to achieve a zero defect system.

Pillar 5: Early Management

Early Management is the fifth pillar of TPM and aims to implement new products and processes with vertical ramp up and minimized development lead time. It is usually deployed after the first four pillars as it builds on the learning captured from other pillar teams, incorporating improvements into the next generation of product and equipment design. There are two parts to the Early Management pillar: Early Equipment Management and Early Product Management. Both approaches focus on using the lessons from previous experiences to eliminate the potential for losses through the planning, development and design stages.

For Early Equipment Management, the goal is to introduce a loss and defect free process so that equipment downtime is minimal (zero breakdowns), and maintenance costs are all considered and optimized, from commissioning onwards.

Early Product Management aims to shorten development lead times, with teams working on simultaneous activities so that vertical start up can be achieved with zero quality loss (zero defects).

Pillar 6: Education and Training

It is aimed to have multi-skilled revitalized employees whose morale is high and who has eager to come to work and perform all required functions effectively and independently. Education is given to operators to upgrade their skill. It is not sufficient know only Know-How by they should also learn Know-why. By experience they gain, Know-How to overcome a problem what to be done. This they do without knowing the root cause of the problem and why they are doing so. Hence it become necessary to train them on knowing Know-why. The employees should be trained to achieve the four phases of skill. The goal is to create a factory full of experts. The different phase of skills are:-

1. Do not Know
2. Know the theory but cannot do
3. Can do but cannot teach
4. Can do and also teach

Pillar 7: Office TPM

Office TPM should be started after activating four other pillars of TPM (Autonomous Maintenance, Focused Improvement, Planned Maintenance and Quality Maintenance).Office TPM concentrates on all areas that provide administrative and support functions in the organization. The pillar applies the key TPM principles in eliminating waste and losses from these departments. The pillar ensures that all processes support the optimisation of manufacturing processes and that they are completed at optimal cost. Office TPM benefits organizations by eliminating losses in the administrative systems across the whole organization and into the extended supply chain. This delivers cost reductions in the organisation's overheads as well as supporting improvement and sustainability of the manufacturing process efficiency.

Pillar 8: Safety, Health and Environment

Safety, Health and Environment (SHE) implements a methodology to drive towards the achievement of zero accidents. It is important to note that this is not just safety related but covers zero accidents, zero overburden (physical and mental stress and strain on employees) and zero pollution. SHE pillar activities aim to reactively eliminate the root causes of incidents that have occurred, to prevent reoccurrence, and proactively reduce the risk of future potential incidents by targeting near misses and potential hazards. The pillar team target three key areas: people's behaviours, machine conditions and the management system. All SHE pillar activities should be aligned to relevant external quality standards and certifications. The immediate benefits of implementing the SHE pillar are to prevent reoccurrence of lost time accidents and reduce the number of minor accidents as well as preventing environmental system failure. This has a direct financial saving in the cost of containment, investigation and compensation as well as reputational impact.

3. TPM Implementation Methodology

In a non-TPM organization, a lot of changes are invited in order to have a full-blown TPM system. So, it cannot be attained overnight. Depending on the size of the organization in terms of number of equipment, complexity of equipment handling, and availability of skilled manpower, it takes 1-3 years to create a „total" TPM organization. However, a strategic plan is required for its proper implementation. The major elements of its implementation in order are the understanding and development of awareness about TPM, identification and classification of problems, development of human resources and formation of small groups, collection of data on losses and flow of information, identification of engineering methods for their minimization, implementation of those methods and evaluation by statistical analysis and interpretation, documentation, and measures for further improvement. Following are the twelve steps for the implementation of TPM:-

Step 1: Announcement of TPM - Top management needs to create an environment that will support the introduction of TPM. Without the support of management, skepticism and resistance will kill the initiative.

Step 2: Launch a formal education program. This program will inform and educate everyone in the organization about TPM activities, benefits, and the importance of contribution from everyone.

Step 3: Create an organizational support structure. This group will promote and sustain TPM activities once they begin. Team-based activities are essential to a TPM effort. This group needs to include members from every level of

the organization from management to the shop floor. This structure will promote communication and will guarantee everyone is working toward the same goals.
Step 4: Establish basic TPM policies and quantifiable goals. Analyze the existing conditions and set goals that are SMART: Specific, Measurable, Attainable, Realistic, and Time-based.
Step 5: Outline a detailed master deployment plan. This plan will identify what resources will be needed and when for training, equipment restoration and improvements, maintenance management systems and new technologies.
Step 6: TPM kick-off. Implementation will begin at this stage.
Step 7: Improve effectiveness of each piece of equipment. Project Teams will analyze each piece of equipment and make the necessary improvements.
Step 8: Develop an autonomous maintenance program for operators. Operators routine cleaning and inspection will help stabilize conditions and stop accelerated deterioration.
Step 9: Develop a planned or preventive maintenance program. Create a schedule for preventive maintenance on each piece of equipment.
Step 10: Conduct training to improve operation and maintenance skills. Maintenance department will take on the role of teachers and guides to provide training, advice, and equipment information to the teams.
Step 11: Develop an early equipment management program. Apply preventive maintenance principles during the design process of equipment.
Step 12: Continuous Improvement - As in any Lean initiative the organization needs to develop a continuous improvement mindset

4. Contributions Of TPM Towards Improving Manufacturing Performance

Manufacturing is considered to be an important element in a firm's endeavor to improve firm Performance(Skinner, 1982; Hayes & Wheelwright,1984). TPM is a highly structured approach, which uses a number of tools and techniques to achieve highly effective plants and machinery. With competition in manufacturing industries rising relentlessly TPM has proved to be the maintenance improvement philosophy preventing the failure of an organization (Eti et al., 2006). Today, an effective TPM strategy and programs are needed, which can cope with the dynamic needs and discover the hidden but unused or under utilized resources (human brainpower, man-hours, machine-hours). TPM methodology has the potential to meet the current demands. A well conceived TPM implementation program not only improve the equipment efficiency and effectiveness but also brings appreciable improvements in other areas of the manufacturing enterprise.

Kutucuoglu et al. (2001) have stated that equipment is the major contributor to the performance and profitability of manufacturing systems. (Seth & Tripathi 2005) have investigated the strategic implications of TQM and TPM in an Indian manufacturing set-up. (Thun 2006) has described the dynamic implications of TPM by working out interrelations between various pillars of TPM to analyze the fundamental structures and identifies the most appropriate strategy for the implementation of TPM considering the interplay of different pillars of this maintenance approach. (Ahuja & Khamba 2008a) have investigated the significant contributions of TPM implementation success factors like top management leadership and involvement, traditional maintenance practices and holistic TPM implementation initiatives towards affecting improvements in manufacturing performance in the Indian industry.

5. Overall Equipment Effectiveness

The goal of the TPM is to maximize equipment effectiveness. OEE provides an effective way of measuring and analyzing the efficiency of a single machine/cell or an integrated manufacturing system. The six major losses that can result from faulty equipment or operation, whose elimination is the major objective of the TPM, are as shown in Table 1, can results in a dramatic improvement in the Overall Equipment Efficiency (OEE). The calculation of OEE is performed by obtaining the product of availability of the equipment, performance efficiency of the process and rate of quality products.

OEE= Availability (A) x Performance Efficiency (P) x Rate of Quality

Table 1: Big Equipment Losses and OEE

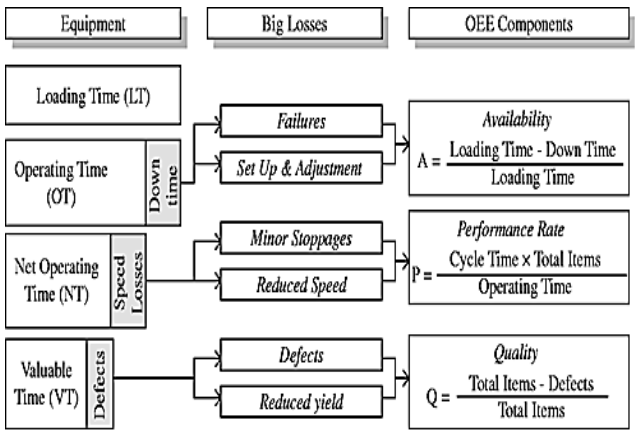

It provides a systematic method for establishing production targets, and incorporates practical management tools and techniques in order to achieve a balanced view of process availability, performance efficiency and rate of quality .As stated earlier that an overall 85 percent benchmark OEE is considered as world-class performance. However, it is desirable to find the gaps between the existing performance levels and desired performance levels. Calculating the OEE following mathematical models (Sohal et.al. 2010) is adopted. The high level of effectiveness OEE will be achieved only, when all the three indexes are very high. OEE is calculated by obtaining the product of availability of the equipment,

performance efficiency of the process and rate of quality products expressed by (Jostes and Helms 1994):

5.1.1 Availability

The available time can be defined as the time of production to operate the equipment minus the other planned downtime like breaks, meetings etc. The down time can be defined as the actual time for which the equipment is down for repairs or changeovers. This time is also sometimes known as the breakdown time. The output of this formula gives the true availability of the equipment. This value is used also in the overall equipment effectiveness formula to measure the effectiveness of the equipment. The availability is calculated as the required available time minus the downtime and then divided by the required available time. This can be written in the form of formula as (Almeanazel, 2010 and Afefy, 2012):-

$$\text{Availability} = \frac{\text{Total Loading time} - \text{Total downtime} \times 100}{\text{Total Loading Time}}$$

5.1.2 Performance Efficiency

The performance efficiency can be defined as the ideal or design cycle time to produce the item multiplied by the output of the equipment and then divided by the operating time. This will give the performance efficiency rate of the equipment. The formula to calculate the performance rate can be expressed as (Gomaa, 2003):

$$\text{PE} = \frac{\text{Total Actual Amount of Product} \times 100}{\text{Target amount of Product}}$$

5.1.3 Quality Rate

The quality rate can be expressed as the process quantity minus the volume or number of defective quantity then divided by processed quantity. The quality rate can be expressed in a formula as [24] (Chana et al., 2005):

$$\text{Quality Rate} = \frac{\text{Processed Quantity} - \text{Defective Quantity} \times 100}{\text{Processed Quantity}}$$

Where, the quality defects mean the amount of products which are below the quality standards i.e. the rejected items after the production process. This formula is very helpful to calculate the quality problems in the production process (Mobley, 2002).

5.1.4 World Class OEE

Table 2: Percentage of World Class OEE

OEE Factors	OEE World Class
A%	90.0
PE%	95.0
QR%	99.9
OEE%	85.0

World class OEE is a standard which is used to compare the OEE of the firm. The percentage of World Class OEE is given in Table I (Kailas, 2009).

6. Case Study in Automobile Manufacturing Organization

In this section, the TPM implementation is demonstrated through a case study in an automobile manufacturing organization. Section 6.1 gives a brief review of case organization and then the TPM implementation procedure is discussed in section 6.2

6.1 Automobile Manufacturing Organization

The case study reported in this paper has been conducted at an automobile manufacturing two wheeler plant in SIDCUL, Haridwar. The management of the company observed that maintenance costs increased for 30-40 percent of the production costs and emergency repairs were three times more expensive then the same job done in pre-planned manner. Since the plant facilities and manufacturing processes were extremely equipment intensive and the data collection and analysis process revealed that the total idle time for the critical process equipment was observed to be extremely high which was not at all acceptable under the prevailing circumstances. Thus, the need for fostering an efficient TPM implementation program was felt fundamentally necessary

6.2 TPM Implementation in Automobile Manufacturing

TPM implementation started with the selection of key model machines and measurement of TPM effectiveness with initiation of four activities – 5S Implementation, Autonomous Maintenance, focused improvement, planned maintenance and OEE have been implemented. A maintenance plan have also been prepared.

(i)Selection of Machines

The first step of this work is selection of machines on which the study is carried out. To start with TPM, a few machines have been selected for implementation of TPM, which is known as TPM model machine. In that Organization, there are seven shops. Four machines have been selected from Light Machine Shop (LMS) i.e. 2 Broaching machines, 1 Cylindrical Grinder and 1 Surface Grinder for TPM implementation. This section was named as TPM model section in Light Machine Shop. Shop. These machines are used in production of components like bull gear, shafts for power transmission etc. A code is assigned to each machine for ease of identification. Each machine is studied thoroughly to identify each part and to understand the working of every component.. OEE is calculated for all the machines before and after implementation as shown in Table 3, 4 and Table 5.

OEE for Broaching Machine I

Table 3: OEE for Broaching Machine I Before TPM Implementation

Before TPM Implementation		
A	Shift Time (General)	450
B	Planned Downtime	60
C	Running Time (A-B)	390
D	Running Time Losses	78
E	Operating Time (C-D)	312
F	**Availability (E/C)x 100**	80%
G	Output	180
H	Machine Speed(No. of Components per year	0.75
I	Expected Output (H x E)	234
J	**Efficiency (Gx 100)/I**	76.9%
K	Rejection	8
L	**Quality (G-K x 100)/G**	95.5%
OEE= Availability x Performance Efficiency x Quality Rate 80% x 76.9% x 95.5% 58.7%		

Table 4: OEE for Broaching Machine I After TPM Implementation

After TPM Implementation		
A	Shift Time (General)	450
B	Planned Downtime	60
C	Running Time (A-B)	390
D	Running Time Losses	58
E	Operating Time (C-D)	332
F	**Availability (E/C)x 100**	85.1%
G	Output	207
H	Machine Speed(No. of Components per year	0.75
I	Expected Output (H x E)	249
J	**Efficiency (Gx 100)/I**	83.1%
K	Rejection	2
L	**Quality (G-K x 100)/G**	99%
OEE= Availability x Performance Efficiency x Quality Rate 85.1% x 83.1% x 99 % = 70%		

Similarly OEE is calculated for rest of the machines at LMS section of the Machine Shop Floor as shown in Table 5

Table 5: OEE Improvement Before and After TPM Implementation

Name of Machine	OEE %	
	Before	After
Broaching Machine I	59	70
Broaching Machine I	60	69
Cylindrical Grinder	53	67
Surface Grinder	50	65

Conclusion

It can be seen that OEE has shown a progressive growth as shown in Table 5, which is an indication of increase in equipment availability, decrease in rework, rejection and increase in rate of performance. Today, with competition in industry at an all time high, TPM may be the only thing that stands between success and total failure for some companies TPM can be adapted to work not only in industrial plants, but also in construction, building maintenance, transportation, and in variety of other situations. Employees must be educated and convinced that TPM is not just another program of the month and that management is totally committed to the program and the extended time frame is necessary for full implementation. If everyone involved in a TPM program does his or her part, a usually high rate of return compared to resources invested may be expected. TPM success requires strong and active support from management, clear organizational goals and objectives for TPM implementation.

References

Bhadury,B.(2000). Management of Productivity through TPM. *Productivity*, 41 (2), 240-51.

Ahuja and Khamba, TPM: Literature Review and directions, *International Journal of Quality & Reliability Management*, Vol 25, pp 709-756, 2008.

A.W. Labib, A framework for benchmarking appropriate productive maintenance, *Management Decision*, Vol. 37, No. 10, pp 792-799, 1999.

P. Willmott,Total Quality with teeth. *The TQM Magazine*, Vol 6, No.4, pp 48-50, 1994.

M.Noon, S.Jenkins and M.M. Lucio, FADS techniques and control: the competing agendas of TPM and Tecax at the Royal Mail (UK), *Journal of Management Studies*, vol 37, no.4, pp 499-519, 2000.

Wireman T, Computerized Maintenance Management systems, 1994, 2nd ed, New York, USA.

D.Hutchins, Introducing TPM, *Manufacturing Engineer*, Vol 77, no.1, pp 34-7, 1998

Ireland,F. &Dale,B.G.(2001). A study of total productive maintenance. Implementation. *Journal of Quality in Maintenance Engineering*, 7(3), 183-197.

Shamsuddin,A.,Hassan,M.H.&Taha,Z.(2005).TPM can go beyond maintenance excerpt from a case implementation: *Journal of Quality in Maintenance Engineering*, 11(1), 19-42.

Nakajima, S.(1988). Introduction to TPM (TPM). Productivity Press. Portland, OR.\TPM Implementation- A Japanese Approach, Tajiri, Gotah, Publishing *Mcgraw-Hill* (1992-06).

Skinner,W.(1982).Getting physical: new strategic leverage from operations: *Journal of Business Strategy*, 3(4), 74-79.

Hayer,R.H.&Wheelwright,S.C.(1984). Matching process technology with product/market requirements.In:Hayes,R.H. and Wheelwright, S.C. (Eds.),Restoring our competitive edge: Competing through manufacturing.*Wiley*,New York,NY.

Eti,M.C.,Ogaji,S.O.T. & Probert,S.D. (2006). Reducing the cost of preventive maintenance (PM) through adopting a proactive reliability- focused culture. *Applied Energy*, 83,1235-1248.

Kutucuoglu,K.Y., Hamali,J.,Irani,Z.& Sharp, J.M. (2001) A framework for managing maintenance using performance measurement systems. *International Journal of Operations & Production Management*, 21 (1/2), 173-19

Seth,D.&Tripathi,D.(2005).Relationship between TQM and TPM implementation factors and business performance of manufacturing industry in Indian context. *International Journal of Quality & Reliability Management*, 22(2/3), 256-277.

Thun,J.H. (2006). Maintaining preventive maintenance and maintenance prevention analyzing the dynamic implications of total productive maintenance.*System Dynamics Review*, 22(2), 163-179.

Ahuja,I.P.S.,Khamba, J.S. (2008a). An evaluation of TPM initiatives in indian industry for enhanced manufacturing performance. *International Journal of Quality & Reliability Management*, 25(2), 147-72

Sohal Amrik, Neill Peter O, Olhager Jan and Prajogo (2010).,Implementation of OEE issues and challenges, Paper presented at the *International Conference on advanced in production management systems*, Oct 11-13, 2010, Cemobbio, Como, Itlay.

Josfes Roberts., Helms.Total Productive Maintenance and its link to Total Quality Management, *Work Study*, Vol 43, Iss:7, pp 18-20.

Almeanazel O.T., (2010), Total Productive Maintenance Review and Overall Equipment Effectiveness Measurement *Jordan Journal of Mechanical and Industrial Engineer*, 4, 517-522.

Afetfy H., (2012)., Maintenance planning based on computer Aided Preventive Maintenance Policy, *International Multi Conference of Engineers and Scientists*, VolII. March 14-16.

GomaaH.(2003), Maintenance Planning and Management, A Literature Study, *American University in Cairo*

Channa F.T.S., Lanb H.C.W, Ipc R.W.L.,Chana H.K. Konga.S.(2005), Implementation of Total Productive Maintenance: A Case Study, *International Journal of Production Economics*, 96, 71-94

Mobley R.K. (2002), An Introduction to maintenance, Linded, USA.

Kailas S.C., (2009), Modern approach to Overall equipment effectiveness (OEE). Seminar Report.

Osama Taisir R.Almeanazel, (2010), Total Productive Maintenance Review and Overall Equipment Effectiveness Measurement *Jordan Journal of Mechanical and Industrial Engineering*, Vol4, No.4, pp 517-522.

Dunn,R. (1988). Maintenance update-88. Plant Engineering, 42(8), 60-62.

Nakajima,S.(1989). TPM Development program:Implementing total productive maintenance: *Productivity Press*, Portland,OR.

Yoshida,K.,Hongo,E., Kimura,Y., Ueno,Y.,Kaneda,M.& Morimoto,T. (1990). In: NachiFujikoshi Corporation and JIPM (Eds.), Training for TPM: A manufacturing success story, *Productivity Press*, Portland, OR.